EBM Experimental Biology and Medicine

Volume 249 | Issue 6

Experimental Biology and Medicine

Interim Editor in Chief

Nicola Conran
University of Campinas, Brazil

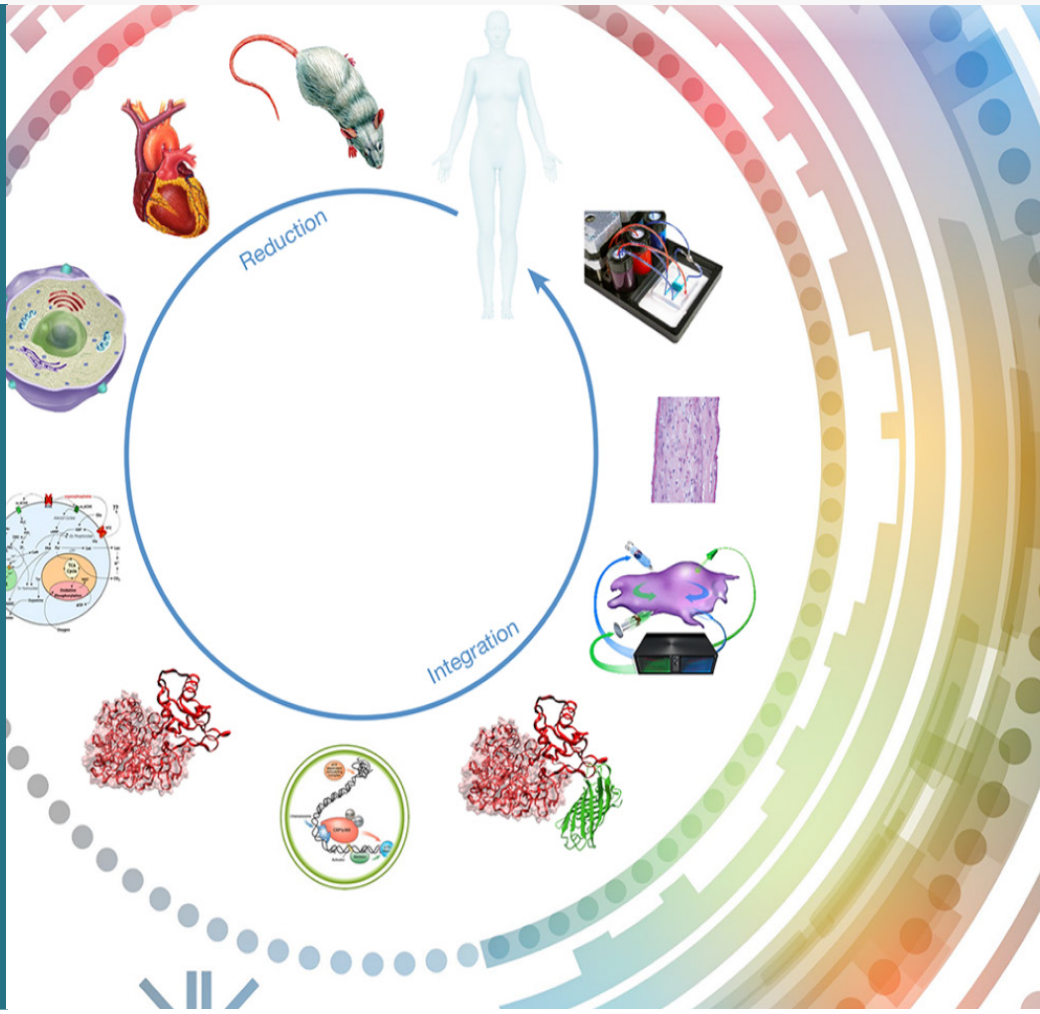

ISBN 978-2-8325-5718-1
DOI 10.3389/978-2-8325-5718-1

frontiers | Publishing Partnerships

SEBM Executive Council

Publication Committee

Society for Experimental Biology and Medicine
3220 N Street NW, #179
Washington DC 20007, USA
Executive Director – ed@sebm.org
Assistant to Editor-in-Chief – bzimmer@sebm.org

www.sebm.org

EBM Experimental Biology and Medicine

Editorial Board

ISSN 1535-3699
ISBN 978-2-8325-5718-1
DOI 10.3389/978-2-8325-5718-1

EBM Experimental Biology and Medicine

2024 | Volume 249 | Issue 6 | ISSN 1535-3699

Table of contents

Original Research

Neuroscience

Correction

EBM Experimental Biology and Medicine

TYPE Editorial
PUBLISHED 10 September 2024
DOI 10.3389/ebm.2024.10346

OPEN ACCESS

*CORRESPONDENCE
Steven R. Goodman,
sgoodma5@uthsc.edu

RECEIVED 17 August 2024
ACCEPTED 26 August 2024
PUBLISHED 10 September 2024

CITATION
Goodman SR (2024) Experimental Biology and Medicine: a global journal with rigorous publication standards. *Exp. Biol. Med.* 249:10346. doi: 10.3389/ebm.2024.10346

Experimental Biology and Medicine: a global journal with rigorous publication standards

Steven R. Goodman*

Department of Pediatrics, University of Tennessee Health Science Center (UTHSC), Memphis, TN, United States

KEYWORDS

biomedical, journal, global, review process, paper mills

Roughly 10 months ago the Society of Experimental Biology and Medicine (SEBM) Council approved its journal *Experimental Biology and Medicine* (EBM) opening an office on the continent of Australia/Oceania, with Sulev Koks, MD/PhD at Murdoch University becoming our new Global Editor from this continent. With the opening of the Australia/Oceania office, and the existing offices in the United States, Taiwan, China, the United Kingdom, Brazil, and Ghana, EBM now has offices and Global Editors on all six habitable continents. We also have twenty-two scientific categories covering the breadth of modern biomedical research and all Translational stages from T0 to T4 spanning basic, translational, clinical, clinical trial and population research.

Exactly 2 weeks after our addition of the Australia/Oceania office, we began accepting manuscripts though the Frontiers portal on 4th November 2023, with our first papers accepted for publication in January 2024. We have used the same rigorous single blind review process that EBM has been known for since our first published issue in 1904. Our standards remain the same and our acceptance rate since changing publishers to Frontiers in 2024 has been 18%, which is lower than the acceptance rate with our prior publisher which ranged from 20% to 30% annually. We have added to our workflow rigorous checks and standard operating procedures to screen out any manuscripts that have the possibility of being generated by a paper mill, which has become a common pervasive problem for all biomedical research journals. We have gone beyond typical procedures by having our new Deputy Editor Nicola Conran, PhD prescreening manuscripts with paper mill characteristics and checking raw data supplied by authors when deemed necessary. We go through this stringent process to assure our readers and ourselves that manuscripts accepted for publication in EBM can be trusted to be honest and important contributions to advancing biomedical research. If we find any of our published articles that do not meet these standards due to any form of research misconduct, they are swiftly retracted.

As Editor-in-Chief of EBM for over 18 years, you can be assured that bringing the research community important and honest contributions to the scientific record is always foremost on my mind. In my academic university career, I have served as a Research Integrity Officer, a Vice President for Research, and a Vice Chancellor for Research. In each of these roles, I was overseeing all research integrity for my Academic Health Center. I believe that this long overlapping experience in dealing with Research misconduct issues at Academic Institutions and journal publications, places EBM in a unique position to be worthy of your trust.

Author contributions

The author confirms being the sole contributor of this work and has approved it for publication.

Conflict of interest

The author declared no potential conflicts of interest with respect to the research, authorship, and/or publication of this article.

EBM Experimental Biology and Medicine

TYPE Original Research
PUBLISHED 14 October 2024
DOI 10.3389/ebm.2024.10084

OPEN ACCESS

*CORRESPONDENCE
Ming Qi,
qiming0509.2008@163.com

RECEIVED 28 December 2023
ACCEPTED 02 September 2024
PUBLISHED 14 October 2024

CITATION
Zhu Y, He Q and Qi M (2024) Exosomal circPTPRK promotes angiogenesis after radiofrequency ablation in hepatocellular carcinoma.
Exp. Biol. Med. 249:10084.
doi: 10.3389/ebm.2024.10084

Exosomal circPTPRK promotes angiogenesis after radiofrequency ablation in hepatocellular carcinoma

Yufeng Zhu[1,2], Qianru He[3] and Ming Qi[4]*

[1]Department of General Surgery, The First Affiliated Hospital of Jinzhou Medical University, Jinzhou, Liaoning, China, [2]Liaoning Provincial Key Laboratory of Clinical Oncology Metabonomics, Jinzhou, Liaoning, China, [3]Zhuhai People's Hospital Affiliated With Jinan University, Zhuhai, Guangdong, China, [4]Department of Ultrasound, The First Affiliated Hospital of Jinzhou Medical University, Jinzhou, Liaoning, China

Abstract

Radiofrequency ablation (RFA) is an effective treatment for hepatocellular carcinoma (HCC), but the recurrence rate remains high due to angiogenesis in residual cancer cells. We used thermal stimulation to simulate the post-RFA microenvironment. The expression profile of circRNAs between normal control HCC cell-derived exosomes and exosomes after heat stimulation were analyzed by RNA sequencing. Quantitative real-time PCR was applied to evaluate the expression of circPTPRK in exosomes and human umbilical vein endothelial cells (HUVECs). Then, the functions of heat-stimulated HCC cell-derived exosomes and exosomal circPTPRK on HUVECs were unveiled. Transcriptome sequencing was utilized to determine targeted genes of circPTPRK. Heat-stimulated HCC cell-derived exosomes augmented cell proliferation, migration, and angiogenesis of HUVECs. In total, 229 differentially expressed circRNAs were obtained, including 211 upregulated circRNAs and 18 downregulated circRNAs in heat-stimulated HCC cell-derived exosomes. The expression of circPTPRK was remarkably increased in heat-stimulated HCC cell-derived exosomes and the HUVECs incubated with them. Heat-stimulated HCC cell-derived exosomes with circPTPRK knockdown significantly inhibited cell proliferation, migration, and angiogenesis of HUVECs. Mechanistic studies indicated that PLA2G4E is a downstream target of circPTPRK, and PLA2G4E overexpression reversed the inhibitory effect of circPTPRK knockdown on HUVEC angiogenesis. Our results indicated that exosomal circPTPRK activated HUVEC angiogenesis by upregulating PLA2G4E expression.

KEYWORDS

hepatocellular carcinoma, exosome, circPTPRK, radiofrequency ablation, angiogenesis

Impact statement

In this study, 229 differentially expressed circRNAs were obtained, including 211 upregulated circRNAs and 18 downregulated circRNAs in heat-stimulated HCC cell-derived exosomes. The expression of circPTPRK was remarkably increased in heat-stimulated HCC cell-derived exosomes and the HUVECs incubated with them. Heat-stimulated HCC cell-derived exosomes with circPTPRK knockdown significantly inhibited cell proliferation, migration, and angiogenesis of HUVECs. Mechanistic studies indicated that PLA2G4E is a downstream target of circPTPRK, and PLA2G4E overexpression reversed the inhibitory effect of circPTPRK knockdown on HUVEC angiogenesis. Our results indicated that exosomal circPTPRK activated HUVEC angiogenesis by upregulating PLA2G4E expression.

Introduction

Hepatocellular carcinoma (HCC) is the most common primary liver cancer and the predominant cause of cancer death globally [1, 2]. At present, there are many treatments for HCC, but the prognosis remains relatively poor [3]. Furthermore, the incidence and mortality of HCC remain high. Radiofrequency ablation (RFA) has become one of the key approaches to prolonging the survival of HCC patients due to its minimally invasive, safe, and convenient use [4]. Studies have shown that thermal stimulation of RFA could promote angiogenesis of residual cancer. Therefore, the poor prognosis of some patients after ablation may be attributed to the abnormally vigorous angiogenesis under thermal stimulation, leading to the higher invasion of this part of the tumor [5]. Angiogenesis is the basic pathological feature of malignant tumors and performs a vital role in the development, metastasis, and occurrence of tumors [6]. Therefore, the elucidation of the mechanism of angiogenesis after RFA in HCC patients is of great value to improve the long-term efficacy of RFA.

Circular RNAs (circRNAs) are a type of noncoding RNA that are synthesized by "end-to-end" splicing of RNAs [7]. CircRNAs inhibit or promote cellular function by sponging microRNAs. Many studies have pointed out that circRNAs are closely associated with tumor progression. Guo et al. showed that circITCH (has-circ-0001141) acted as a repressor to inhibit HCC malignancy by sponging miR-184 [8]. Zhan et al. revealed that circRNA hsa_circRNA_103809 facilitated HCC development by modulating the miR-377-3p/FGFR1/ERK axis [9]. Moreover, it was shown that hsa_circRNA_100084 can be used as a miR-23a-5p sponge to stimulate IGF2 expression in HCC cells [10]. Notably, circRNAs can be identified in the blood and urine of patients, indicating that circRNAs may be diagnostic markers for human cancer [7]. However, limited studies have been conducted on circPTPRK, and its association with HCC remains unclear, meaning it requires further investigation.

Exosomes are extracellular vesicles with a diameter of 30–100 nm [11]. A large body of research has proven that exosomes are the communication bridge between cells and play an important role in the tumor microenvironment [12]. Exosomes participate in cancer-associated biological functions, such as cell proliferation, migration, and angiogenesis [13]. Exosomal circRNAs have been reported to play a crucial role in the development of numerous cancers, including gastric, colorectal, and pancreatic cancer [14]. For example, Exosomal circSTRBP derived from cancer cells promoted gastric cancer progression by modulating the miR-1294/miR-593-3p/E2F2 axis [15]. Exosomal circTUBGCP4 induced vascular endothelial cell tipping to foster angiogenesis and tumor metastasis through activation of the Akt signaling pathway [16]. Moreover, exosomal circRNAs are also closely related to the development of HCC. It has been shown that exosomal ANGPT2 secreted by HCC cells promoted tumor angiogenesis [17]. Evidence from recent studies has indicated that transfection of exosomal circRNA-100338 into recipient HUVECs could promote angiogenesis and subsequently affect HCC [18]. Adipocytes secreted exosomal circRNAs, which accelerated HCC tumor growth by repressing miR-34a and triggering the USP7/Cyclin A2 pathway [19]. Recently, exosomal lncRNA ASMTL-AS1 was reported to exacerbate the malignancy in residual HCC after insufficient RFA [20]. However, the effects of exosomal circRNA on angiogenesis after RFA remain obscure.

In the present study, we aimed to determine the role and regulatory mechanism of HCC cell-derived exosomal circRNAs in angiogenesis after RFA. We explored the role of MHCC-97H cell-derived exosomes after heat stimulation (HS-exo) in angiogenesis of human umbilical vein endothelial cells (HUVECs). RNA sequencing was carried out to determine differentially expressed circRNAs (DEcircRNAs) between normal control exosomes (NC-exo) and HS-exo. The function and mechanism of exosomal circPTPRK in HUVEC angiogenesis was determined via cell experiments and RNA sequencing. Our study may provide a hopeful therapeutic strategy for HCC recurrence after RFA.

Materials and methods

Cell culture and treatment

The human HCC cell lines (MHCC-97H and HepG2) and HUVECs were acquired from iCell Bioscience Inc. (Shanghai, China). MHCC-97H cells were cultivated in Dulbecco's modified Eagle's medium (DMEM) (CORNING, United States). HepG2 cells were cultivated in minimum Eagle's medium (MEM) (CORNING, United States). The HUVECs were cultivated in endothelial cell medium (ScienCell, United States). MHCC-97H and HUVECs were appended with 10% fetal bovine serum (GIBCO, United States), 100 μg/mL streptomycin, and 100 U/mL penicillin in a 37°C incubator of 5% CO_2.

To simulate the tumor microenvironment after RFA *in vitro*, MHCC-97H cells were cultivated at 42°C for 24 h (heat stimulation) according to a previous report [21], with some modification.

Isolation of exosomes

Exosomes were extracted by the ultracentrifugation method in accordance with the previous report [18], with some changes. The collected medium was centrifuged at 300 g for 10 min at 4°C to remove the cell pellet. Afterwards, the supernatant was centrifuged at 2,000g for 10 min at 4°C and then 10,000 g for 10 min at 4°C to eliminate the dead cells and cell debris. Finally, the supernatant was centrifuged at 120,000 g for 2 h at 4°C. The precipitate was resuspended in pre-cooled 1×PBS and preserved at −80°C. The concentration of isolated exosomes was measured by the BCA kit (Beyotime, P0010S).

Internalization of exosomes

MHCC-97H cells in the NC group and HS group were cultured at 37°C and 42°C for 24 h, respectively. Serum-free medium was replaced and supernatants were collected after 48 h culture to obtain exosomes via ultracentrifugation. Subsequently, the exosomes were supplemented with 1 μL of DiI fluorescent dye and incubated for 20 min at room temperature. HUVECs were incubated with exosomes labeled with DiI for 48 h. DAPI (Sangon) was used to stain cell nuclei. Finally, fluorescence microscope (NIKON, Japen) was employed to confirm the internalization of exosomes in HUVECS.

RNA sequencing

TRIzol reagent was applied to separate total RNA from the collected NC-exo (20 μg/mL) and HS-exo (20 μg/mL). Construction of a cDNA library was conducted by utilizing TruSeq RNA Sample Prep Kit (Illumina, United States) and RNA sequencing was conducted on the Illumina HiSeq 2500 platform. Fast-QC was employed for sequencing raw data to evaluate the overall quality. Clean reads were mapped to GRCh38 with HISAT2 software. The differentially expressed circRNAs (DEcircRNAs) were acquired by utilizing DESeq2 with *P*-value <0.05 and $|\log_2(\text{Fold change})| > 1$. Miranda/RNAhybird was applied to predict the target genes of DEcircRNAs. Gene ontology (GO) and Kyoto encyclopedia of genes and genomes (KEGG) enrichment analysis was used to analyze the function and enrichment pathways of target genes of DEcircRNAs. To determine the downstream targets of circPTPRK, RNA sequencing was performed with si-NC and si-circPTPRK HUVECs (n = 3). The differentially expressed genes were acquired by utilizing DESeq2 with *P*-value <0.05 and $|\log_2(\text{Fold change})| > 1$. GO and KEGG enrichment analysis was employed to analyze the function and enrichment pathways of target genes of circPTPRK.

Cell transfection

Small interfering (si) RNAs targeting circPTPRK (circPTPRK siRNA-1/2/3), siRNA negative control (si-NC), and PLA2G4E overexpression plasmid were acquired from Shanghai GenePharma Co., Ltd. (China). Cells were placed in 6-well plates with 30×10^4 cells each well. Transfection was executed by employing Lipofectamine 2000 (Invitrogen, United States) in line with the manufacturer's protocol.

Quantitative real-time PCR (qRT-PCR)

Total RNA was segregated with TRIzol reagent (Invitrogen). Reverse transcription reaction was conducted using Thermo Scientific RevertAid First Strand cDNA Synthesis Kit (Thermo). The qRT-PCR reaction was conducted with the SYBR Green PCR kit (Roche) on the Applied Biosystems Q6 real-time PCR system (United States). The reaction conditions consisted of 95°C for 10 min, followed by 40 cycles of 95°C for 15 s, and 60°C for 60 s. GAPDH was regarded as an internal control. The relative expression of circRNA and genes was detected using the $2^{-\Delta\Delta CT}$ method. The primers are listed in Supplementary Table S1.

Cell counting kit-8 (CCK-8) assay

Cell proliferation was evaluated by CCK-8. HUVEC were placed in 6-well plates and co-cultured with exosomes (20 μg/mL) for 48 h. Afterward, 10 μL of CCK8 (Beyotime, China) solution was appended to each well. After 2 h of incubation at 37°C, the absorbance was read out with a microplate spectrophotometer (Bio-Rad, United States) at 450 nm.

Transwell assay

Transwell migration assays were conducted in 24-well plates (Corning, United States). HUVECs and exosomes (20 μg/mL) were plated on the upper chambers. Endothelial cell medium comprising 10% FBS was appended to the lower chambers. After incubation for 48 h, cells were fixed with 4% paraformaldehyde, and subsequently dyed with crystal violet

solution. In the end, the cells were photographed and counted using a microscope.

Wound scratch assay

The transfected cells were seeded in 6-well plates, reaching a cell density exceeding 90%. After 24 h, scratches were drawn on the cells with a pipette tip, followed by washing the cells twice with PBS. Subsequently, images were captured at 0 and 24 h using a Nikon microscope.

Tube formation assay

The impact of HS-exo and exosomal circPTPRK on angiogenesis was examined by the tube formation assay. HUVECs were incubated in serum-free medium for 12 h and subsequently transferred to 48-well plates precoated with matrigel (356230, Corning) for 10 h. Exosomes (20 μg/mL) from different treatments were added into HUVEC and incubated for 48 h. The formation of blood vessels was observed by utilizing a microscope, and the vascular branches were analyzed by utilizing ImageJ software.

Statistical analysis

Statistical analysis was conducted by utilizing GraphPad Prism 9. Data were displayed as mean ± standard deviation (SD). The differences between the two groups were compared by student t-test, and the three groups were determined by the one-way ANOVA. A *P*-value less than 0.05 was considered as statistically significant.

Results

HCC cell-derived exosomes produced after heat stimulation promote HUVEC proliferation, migration, and tube formation

In order to determine whether HS-exo regulate endothelial cell function, we first performed exosome tracer experiments. The results displayed that HS-exo were absorbed by endothelial cells (Figure 1A). Then, we used CCK8, transwell, wound scratch assay, and tube formation cell function experiments to examine their effects on HUVEC proliferation, migration, and tube formation capacity. The results showed that HS-exo dramatically boosted HUVEC proliferation (1.04-fold), migration (1.28-fold in transwell assay, and 1.55-fold in wound scratch assay), and tube formation capacity (1.84-fold) relative to NC-exo (Figures 1B–E). Together, HS-exo promoted endothelial cell proliferation, migration, and tube formation.

Analysis of differentially expressed circRNAs in exosomes after heat stimulation

We conducted RNA sequencing of normal control HCC cell-derived exosomes and exosomes produced after thermal stimulation. The comparison of total RNA vs. cirRNA in NC-exo and HS-exo is shown in Figure 2A. In comparison with the normal control exosomes, 229 circRNAs were differentially expressed in the exosomes produced after heat stimulation. Among them, 211 circRNAs were strikingly up-regulated, whereas 18 were obviously down-regulated in exosomes produced after thermal stimulation (Figure 2B). GO analysis revealed that target genes of DEcircRNAs were principally implicated in the mRNA metabolic process, cellular response to heat, and gene expression (Figure 2C). KEGG enrichment analysis unveiled that target genes of DEcircRNAs were primarily enriched in Protein processing in endoplasmic reticulum, Pentose phosphate pathway, and HIF−1 signaling pathways (Figure 2D).

circPTPRK was up-regulated in exosomes after heat stimulation

To determine the pivotal circRNAs that modulate angiogenesis, a "circRNAs—target genes—angiogenesis-related pathways" network was constructed (Figure 3A). Five circRNAs (circABR, circUBAP2, circPTPRK, circESYT2, and circMTUS1) were picked for qRT-PCR validation. The results showed that circPTPRK was significantly upregulated in HS-exo with 2.58-fold change, showing the largest fold difference (Figure 3B). Therefore, circPTPRK was selected for subsequent experiments. Sanger sequencing verified the circular structure of circPTPRK (Figure 3C). circPTPRK expression was remarkably enhanced in HUVECs incubated by HS-exo (Figure 3D). In order to explore whether exosomal circPTPRK can regulate the function of endothelial cells, circPTPRK siRNA-1/2/3 and si-NC were transfected into MHCC-97H cells. qRT-PCR results uncovered that the expression of circPTPRK was dramatically down-regulated in MHCC-97H cells transfected with circPTPRK siRNA-3 with the largest difference (Figure 3E). Therefore, circPTPRK siRNA-3 was selected to knockdown circPTPRK.

Exosomal circPTPRK promotes HUVEC proliferation, migration, and tube formation

We further investigated whether exosomes produced after heat stimulation function on endothelial cells by carrying circPTPRK.

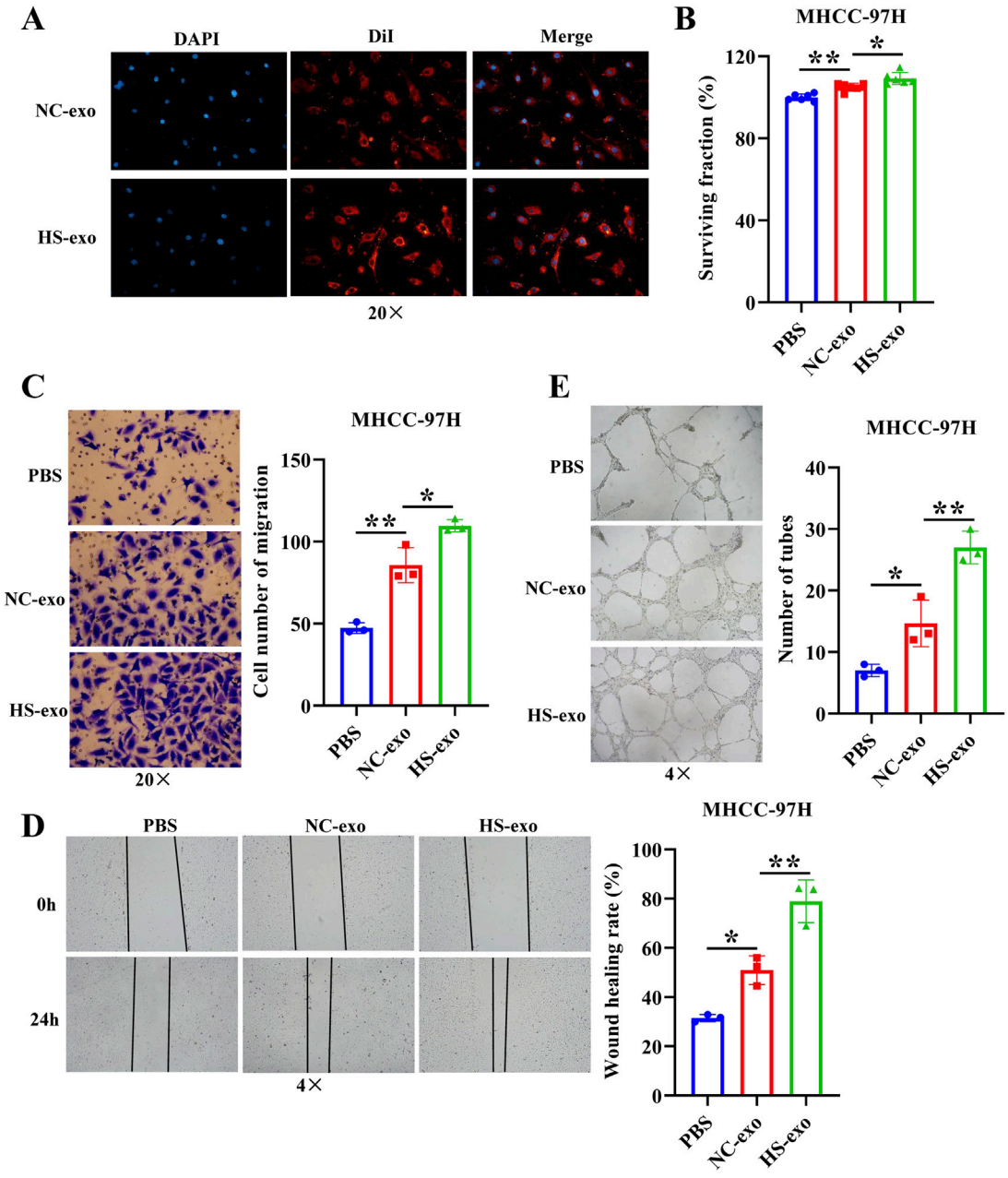

FIGURE 1
Effects of exosomes produced after heat stimulation on HUVEC function. **(A)** Exosome absorption by HUVECs was observed by fluorescence microscope. n = 3. **(B)** The effect of exosomes produced after thermal stimulation on HUVEC proliferation was detected by CCK-8. n = 6. Transwell assay **(C)** and wound scratch assay **(D)** were applied to examine the effect of exosomes produced after thermal stimulation on HUVEC migration. n = 3. **(E)** Tube formation assay was employed to examine the impact of exosomes produced after thermal stimulation on tube formation ability of HUVECs. n = 3. NC-exo: Normal control exosomes derived from human hepatocellular carcinoma cell line MHCC-97H. HS-exo: Exosomes produced after thermal stimulation. *$p < 0.05$; **$p < 0.01$.

qRT-PCR results verified that circPTPRK expression was markedly diminished in circPTPRK knockdown exosomes relative to the normal control group (Figure 4A). circPTPRK expression was also prominently diminished in HUVECs incubated with circPTPRK knockdown exosomes compared with control exosome-incubated HUVECs (Figure 4B). Next, we used CCK8, transwell, wound scratch assay, and tube formation cell function experiments to examine the role of two cell line (MHCC-97H and HepG2)-derived exosomal circPTPRKs in HUVEC proliferation, migration, and tube formation. Results

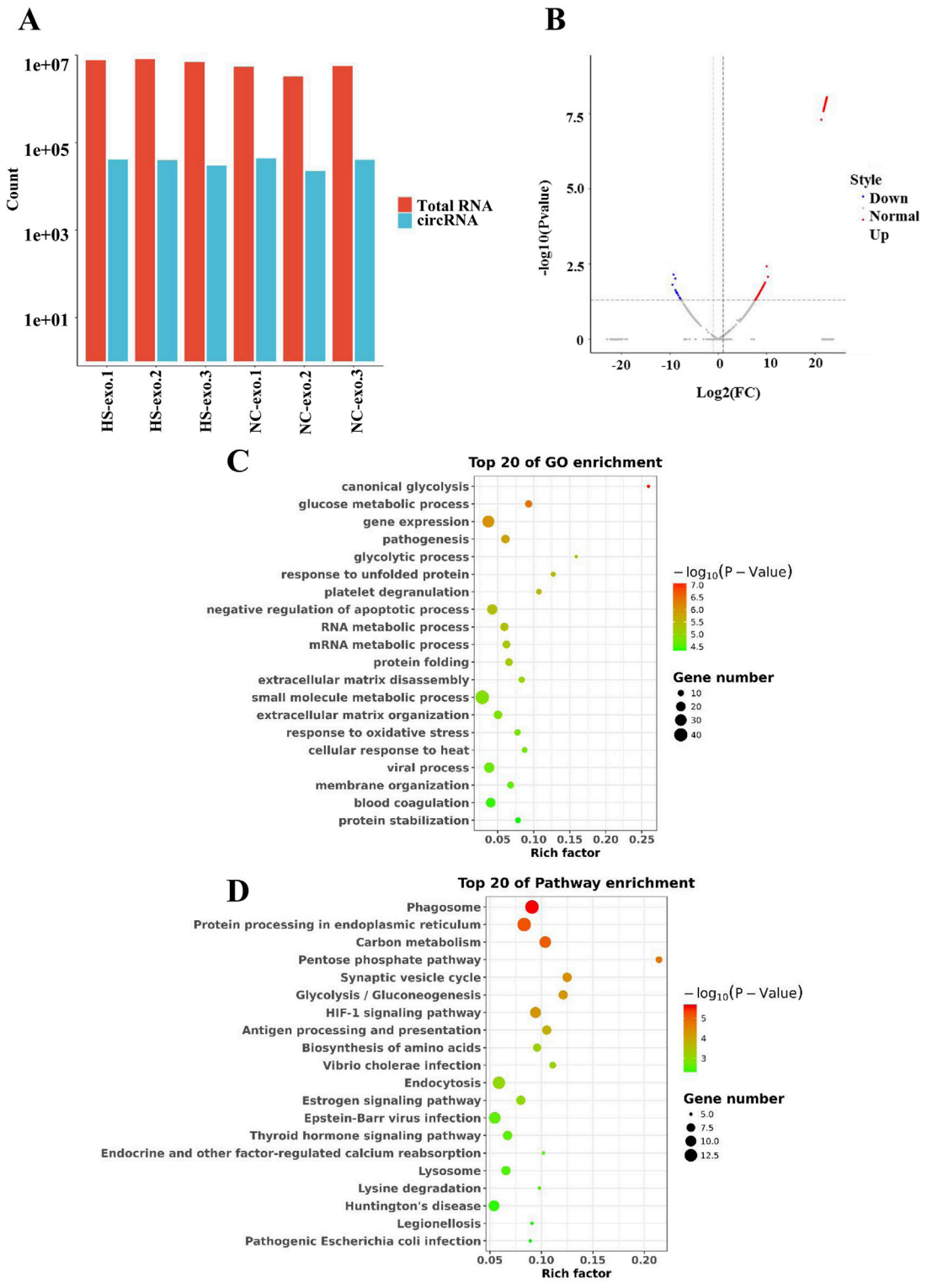

FIGURE 2
Analysis of differentially expressed circRNAs (DEcircRNAs) in exosomes after heat stimulation. **(A)** The comparison of total RNA vs. cirRNA in NC-exo and HS-exo. **(B)** Volcano plot of DEcircRNAs between NC-exo and HS-exo (n = 3). **(C)** GO analysis of target genes of DEcircRNAs. **(D)** KEGG analysis of target genes of DEcircRNAs.

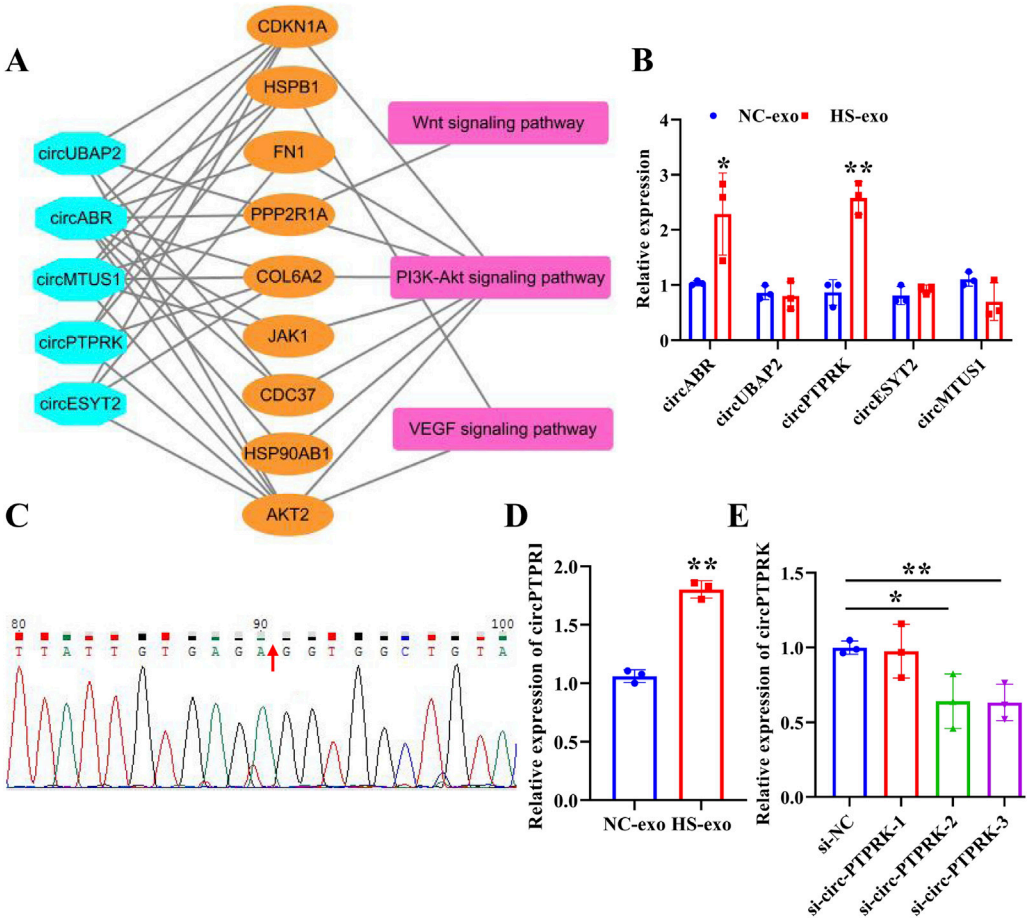

FIGURE 3
circPTPRK expression was up-regulated in exosomes after heat stimulation. **(A)** The network diagram of circRNAs-mRNAs-pathways. **(B)** qRT-PCR was employed to examine the expression of candidate circRNAs in NC-exo and HS-exo. n = 3. **(C)** Sanger sequencing confirmed the circular structure of circPTPRK. **(D)** Expression of circPTPRK was tested by qRT-PCR in HUVECs incubated with exosomes produced after heat stimulation. n = 3. **(E)** The interference efficiency of circPTPRK was confirmed in MHCC-97H cells by qRT-PCR. n = 3. *$p < 0.05$; **$p < 0.01$.

showed that MHCC-97H cell-derived exosomes with circPTPRK knockdown remarkably reduced HUVEC proliferation, migration, and tube formation relative to the control exosomes (Figures 4C–F). The same results were observed in HUVECs after HepG2 cell-derived exosomes with circPTPRK knockdown treatment (Figures 5A–D). In conclusion, exosomes produced by heat stimulation augmented HUVEC proliferation, migration, and tube formation through circPTPRK.

Analysis of circPTPRK target genes

Transcriptome sequencing was carried out on circPTPRK knockdown and control HUVECs. In contrast with the control group, 305 target genes were differentially expressed in circPTPRK knockdown HUVECs. Among them, 195 target genes were up-regulated and 110 target genes were down-regulated after circPTPRK knockdown (Supplementary Figures S1A, B). To discover the biological function of differentially expressed target genes, we conducted functional enrichment and pathway analysis of target genes. GO analysis showed that these differentially expressed target genes were chiefly implicated in hormone biosynthesis and phosphorylation regulation (Supplementary Figure S1C). KEGG enrichment analysis displayed that differentially expressed target genes were principally enriched in T cell receptor, VEGF, and TGF-beta signaling pathways (Supplementary Figure S1D).

Overexpression of PLA2G4E reverses the effect of exosomal circPTPRK knockdown on proliferation, migration, and tube formation of HUVECs

To determine the regulatory mechanism of circPTPRK in HUVEC angiogenesis, we screened target genes enriched in

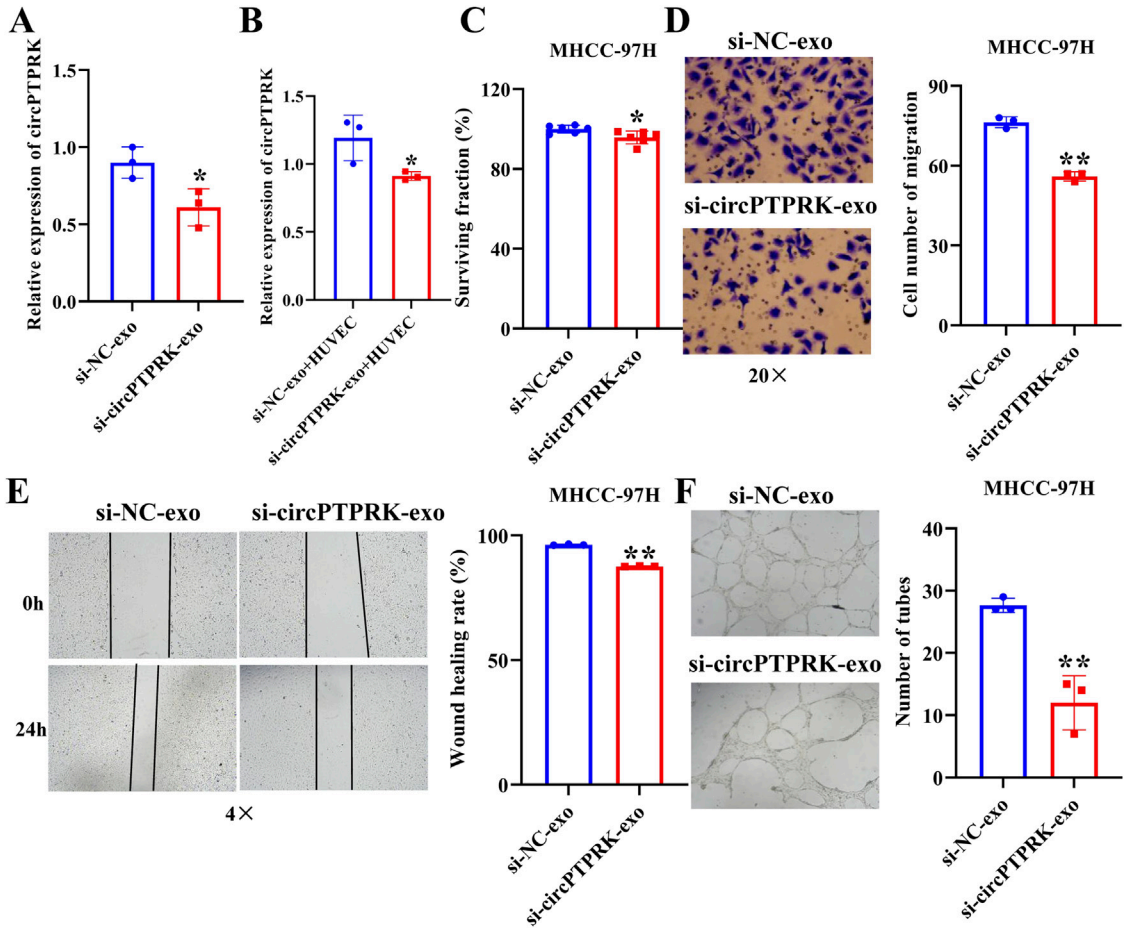

FIGURE 4
Heat-stimulated MHCC-97H cell-derived exosomes regulate HUVEC function through circPTPRK. **(A)** The expression of circPTPRK in circPTPRK knockdown exosomes was assessed via qRT-PCR. n = 3. **(B)** circPTPRK expression was tested by qRT-PCR in circPTPRK knockdown exosome-incubated HUVECs. n = 3. **(C)** The impact of circPTPRK on cell proliferation of HUVECs was evaluated via CCK-8. n = 6. The effect of circPTPRK on cell migration of HUVECs was detected by transwell assay **(D)** and wound scratch assay **(E)**. n = 3. **(F)** Tube formation assay was utilized to evaluate the impact of circPTPRK on tubular formation ability of HUVECs. n = 3. *$p < 0.05$; **$p < 0.01$.

angiogenesis-related pathways through RNA sequencing data (Figure 6A) and selected four target genes with large differences and high expression levels for qRT-PCR validation. The results revealed that the expression of PLA2G4E and CBLC was in line with the transcriptome sequencing results. circPTPRK knockdown significantly decreased PLA2G4E expression, while it increased CBLC expression in HUVECs (Figure 6B). PLA2G4E was selected for subsequent studies. To further investigate whether MHCC-97H cell-derived exosomal circPTPRK regulates HUVEC angiogenesis by targeting PLA2G4E, we performed rescue experiments. The results showed that exosomal circPTPRK knockdown remarkably repressed proliferation, migration, and tube formation of HUVECs, which was partly reversed by PLA2G4E overexpression (Figures 7A–D). Overall, exosomal circPTPRK knockdown inhibited HUVEC angiogenesis by regulating PLA2G4E expression.

Discussion

HCC is a common tumor worldwide, with high morbidity and mortality [22]. In this study, we discovered that HCC cell-derived exosomes produced after thermal stimulation promoted cell proliferation, migration, and tube formation of HUVECs. Moreover, circPTPRK was markedly upregulated in the HS-exo group relative to the NC-exo group. Exosomal circPTPRK knockdown could significantly suppress proliferation, migration, and tube formation of HUVECs. Mechanistically, circPTPRK targeted PLA2G4 and exosomal circPTPRK knockdown repressed HUVEC angiogenesis by regulating PLA2G4E expression (Figure 8). Therefore, we believe that exosomal circPTPRK could be a potential therapeutic target for HCC.

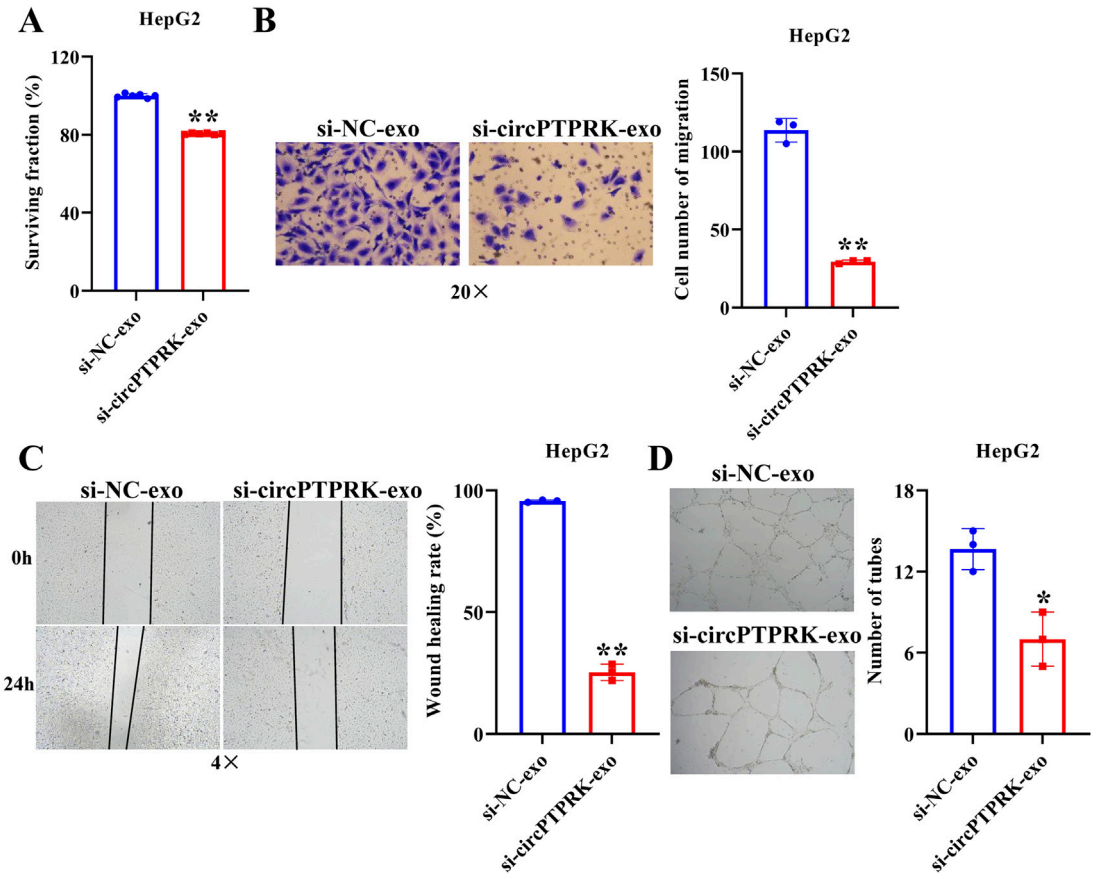

FIGURE 5
HepG2 cell derived-exosomal circPTPRK promotes HUVEC angiogenesis. **(A)** The impact of circPTPRK on proliferation of HUVECs was evaluated via CCK-8. n = 6. The effect of circPTPRK on the migration of HUVECs was detected by transwell assay **(B)** and wound scratch assay **(C)**. n = 3. **(D)** Tube formation assay was utilized to evaluate the impact of circPTPRK on tubular formation ability of HUVECs. n = 3. *$p < 0.05$; **$p < 0.01$.

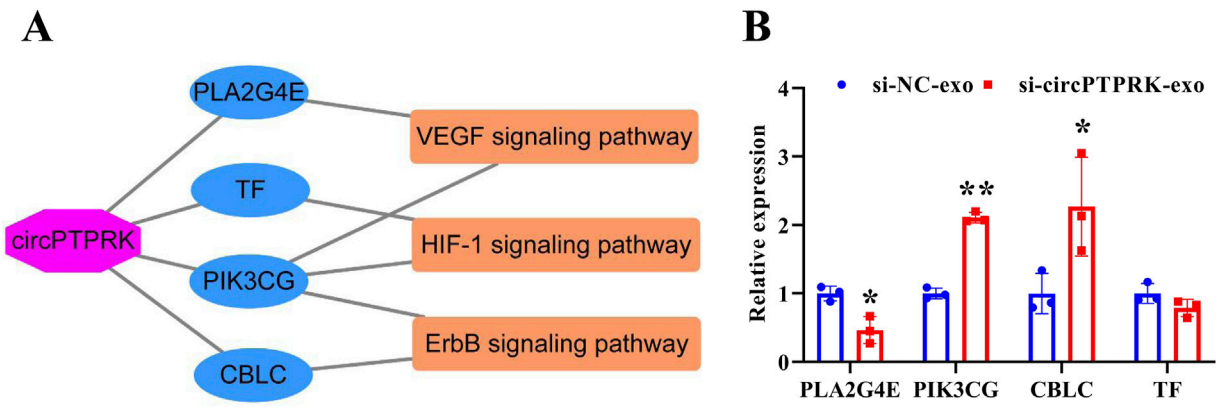

FIGURE 6
Screening of circPTPRK target genes. **(A)** The network of circPTPRK-target gene-angiogenesis-related signaling pathway. **(B)** qRT-PCR was applied to test the expression of candidate target genes in circPTPRK knockdown HUVECs. n = 3, *$P < 0.05$; **$P < 0.01$.

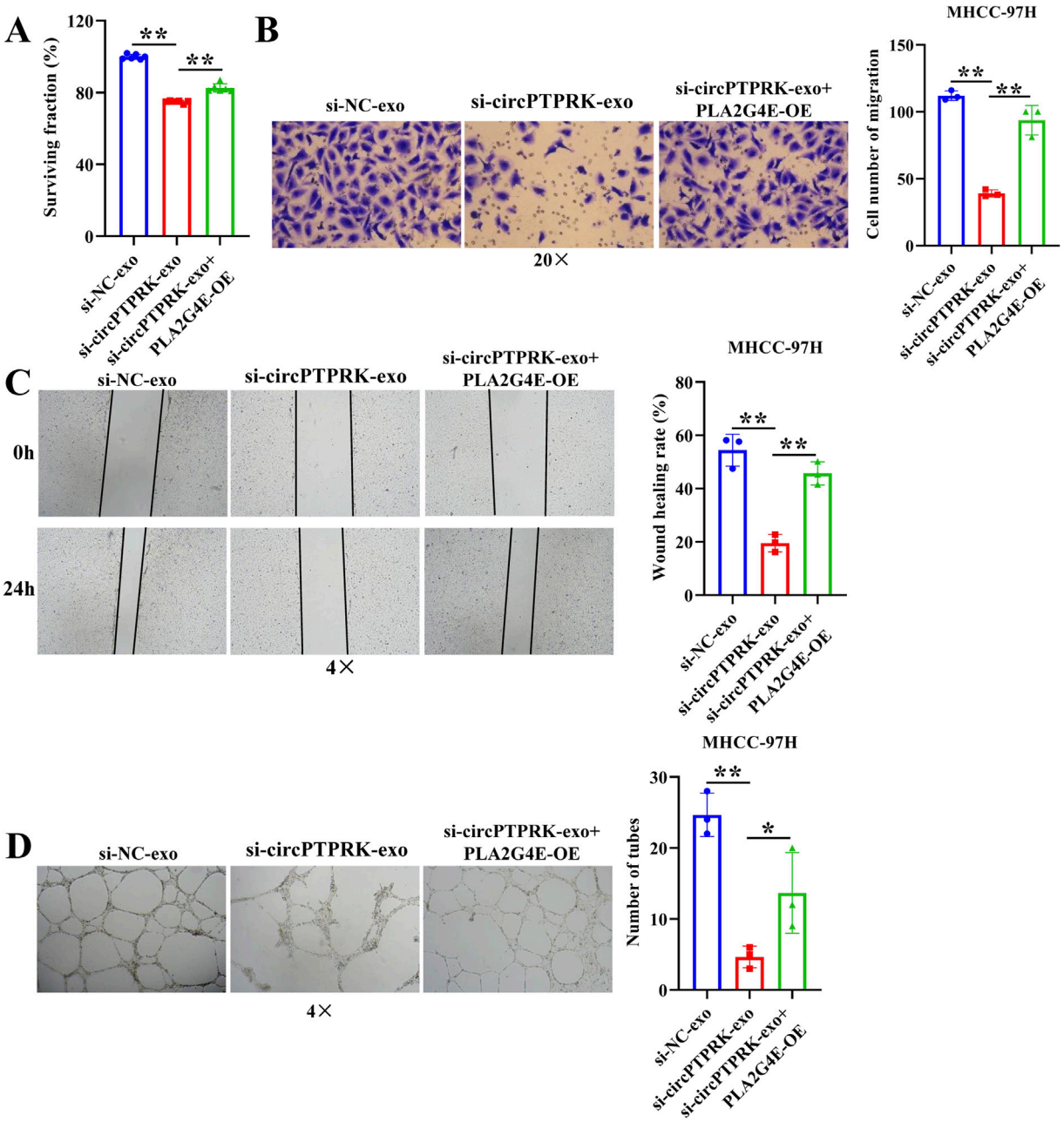

FIGURE 7
MHCC-97H cell-derived exosomal circPTPRK promotes HUVEC angiogenesis by modulating PLA2G4E expression. **(A)** The impact of exosomal circPTPRK knockdown and PLA2G4E overexpression on cell proliferation of HUVECs was evaluated via CCK-8. n = 6. The effect of exosomal circPTPRK knockdown and PLA2G4E overexpression on cell migration of HUVECs was detected by transwell assay **(B)** and wound scratch assay **(C)**. n = 3. **(D)** Tube formation assay was utilized to evaluate the impact of exosomal circPTPRK knockdown and PLA2G4E overexpression on tubular formation ability of HUVECs. n = 3. $*p < 0.05$; $**p < 0.01$.

Angiogenesis is defined as a marker in HCC progression and can be used as a therapeutic target [23]. In our study, we discovered that exosomal circPTPRK could be transported to HUVECs and play its role in promoting angiogenesis. Evidence has shown that exosomal circRNAs can regulate angiogenesis by enhancing the communication between HCC cells and HUVECs [18]. Additionally, exosomes regulated cell-to-cell communication, changed the tumor microenvironment,

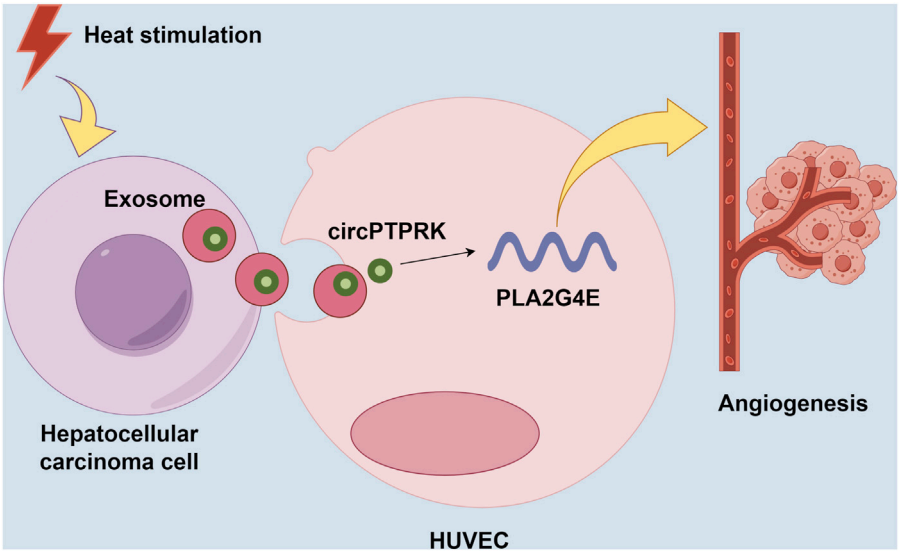

FIGURE 8
Schematic model for the mechanism by which exosomal circPTPRK promotes angiogenesis after radiofrequency ablation in hepatocellular carcinoma.

and stimulated angiogenesis through proteins, nucleic acids, and other substances [24]. Similarly, anti-angiogenesis has shown great potential in the treatment of other malignancies. The results of Yu et al. displayed that exosomal circATP10A was a biomarker for angiogenesis in multiple myelomas [25]. Previous research indicated that circCCAC1 participated in cholangiocarcinoma progression, induced angiogenesis, and damaged vascular endothelial barriers [26]. Li et al. pointed out that gastric-cancer-derived exosomal circ29 promoted angiogenesis by modulating the miR-29a/VEGF axis in endothelial cells [27]. Given the vital role of angiogenesis in tumor progression and the negative impact of existing anti-angiogenic drugs, there is an urgent need to continuously search for new anti-angiogenic targets in the future.

In this study, we discovered that target genes of circPTPRK were mainly involved in VEGF and TGF-beta signaling pathways. VEGF is a crucial modulator of angiogenesis and exerts a vital role in angiogenesis [28]. A recent study reported that PinX1 inhibited renal cancer angiogenesis via the VEGF signaling pathway [29]. Another study found that TRPV3 facilitated angiogenesis via the HIF-1α-VEGF signaling pathway in non-small-cell lung cancer [30]. The TGF-beta pathway is also vital to tumor angiogenesis. Chen et al. found that Prrx1 contributed to stemness and angiogenesis via the TGF-β/smad pathway in glioma [31]. Therefore, we presumed that exosomal circPTPRK promoted angiogenesis via VEGF and TGF-beta signaling pathways in HCC.

CircRNAs primarily function in cancers via targeting miRNAs to increase the expression of mRNAs. For example, circCRIM1 contributed to the development of esophageal squamous cell carcinoma by upregulating TCF12 [32]. Silencing of circCCNB1 repressed cervical cancer development by increasing SOX4 expression [33]. circABCC4 accelerated the malignant behavior of prostate cancer by sponging miR-1182 to upregulate FOXP4 expression [34]. In our study, we found that exosomal circPTPRK knockdown inhibited HUVEC angiogenesis by downregulating PLA2G4E expression.

Certainly, there were a few limitations in our study. First, the effect of exosomal circPTPRK *in vivo* remains unknown. Second, the molecular mechanism of circPTPRK in angiogenesis should be studied further.

In conclusion, our study suggested that HS-exo participated in the modulation of HUVEC proliferation, migration, and angiogenesis by transmitting circPTPRK. Consequently, circPTPRK is considered a potential therapeutic target for HCC treatment after RFA.

Author contributions

YZ performed experiments and the methodology and wrote the manuscript. QH collected and analyzed the data. MQ designed the study. All authors contributed to the article and approved the submitted version.

Data availability

All the data obtained and materials analyzed in this research are available from the corresponding author upon reasonable request.

Ethics statement

This study was approved by the Ethics Committee of The First Affiliated Hospital of Jinzhou Medical University.

Funding

The authors declare that financial support was received for the research, authorship, and/or publication of this article. This work was supported by the National Natural Science Foundation of China (grant number 81903130).

Conflict of interest

The authors declared no potential conflicts of interest with respect to the research, authorship, and/or publication of this article.

Supplementary material

The Supplementary Material for this article can be found online at: https://www.ebm-journal.org/articles/10.3389/ebm.2024.10084/full#supplementary-material

SUPPLEMENTARY FIGURE S1
Expression and functional analysis of circPTPRK target genes. **(A)** Volcano plot of circPTPRK-targeted genes. Transcriptome sequencing was performed on circPTPRK knockdown and control HUVECs (n = 3). **(B)** Cluster map of circPTPRK-targeted genes. **(C)** GO analysis of differentially expressed circPTPRK target genes. **(D)** KEGG analysis of differentially expressed circPTPRK target genes.

References

1. Margini C, Dufour J. The story of HCC in NAFLD: from epidemiology, across pathogenesis, to prevention and treatment. *Liver Int* (2016) **36**:317–24. doi:10.1111/liv.13031

2. Bosetti C, Turati F, La Vecchia C. Hepatocellular carcinoma epidemiology. *Best Pract and Res Clin Gastroenterol* (2014) **28**:753–70. doi:10.1016/j.bpg.2014.08.007

3. Aliya S, Lee H, Alhammadi M, Umapathi R, Huh Y. An overview on single-cell technology for hepatocellular carcinoma diagnosis. *Int J Mol Sci* (2022) 23. doi:10.3390/ijms23031402

4. Thayer D, Noda C, Charalel R, Mills A, Chang R, Tao Y, et al. Survival comparison of hepatocellular carcinoma patients treated with radioembolization versus nonoperative/interventional treatment. *J Comp effectiveness Res* (2018) **7**:343–56. doi:10.2217/cer-2017-0064

5. Fernandez M, Semela D, Bruix J, Colle I, Pinzani M, Bosch J. Angiogenesis in liver disease. *J Hepatol* (2009) **50**:604–20. doi:10.1016/j.jhep.2008.12.011

6. Onishi M, Ichikawa T, Kurozumi K, Date I. Angiogenesis and invasion in glioma. *Brain Tumor Pathol* (2011) **28**:13–24. doi:10.1007/s10014-010-0007-z

7. Qiu L, Wang T, Ge Q, Xu H, Wu Y, Tang Q, et al. Circular RNA signature in hepatocellular carcinoma. *J Cancer* (2019) **10**:3361–72. doi:10.7150/jca.31243

8. Guo X, Wang Z, Deng X, Lu Y, Huang X, Lin J, et al. Circular RNA CircITCH (has-circ-0001141) suppresses hepatocellular carcinoma (HCC) progression by sponging miR-184. *Cell Cycle (Georgetown, Tex)* (2022) **21**:1557–77. doi:10.1080/15384101.2022.2057633

9. Zhan W, Liao X, Chen Z, Li L, Tian T, Yu L, et al. Circular RNA hsa_circRNA_103809 promoted hepatocellular carcinoma development by regulating miR-377-3p/FGFR1/ERK axis. *J Cell Physiol* (2020) **235**:1733–45. doi:10.1002/jcp.29092

10. Yang JX, Xie P, Li YS, Wen T, Yang XC. Osteoclast-derived miR-23a-5p-containing exosomes inhibit osteogenic differentiation by regulating Runx2. *Cell Signal* (2020) **70**:109504. doi:10.1016/j.cellsig.2019.109504

11. Johnstone R, Adam M, Hammond J, Orr L, Turbide C. Vesicle formation during reticulocyte maturation. Association of plasma membrane activities with released vesicles (exosomes). *J Biol Chem* (1987) **262**:9412–20. doi:10.1016/s0021-9258(18)48095-7

12. Wang J, Pu J, Zhang Y, Yao T, Luo Z, Li W, et al. Exosome-transmitted long non-coding RNA SENP3-EIF4A1 suppresses the progression of hepatocellular carcinoma. *Aging* (2020) **12**:11550–67. doi:10.18632/aging.103302

13. Onetti Y, Kälin R, Pitter B, Hou M, Arribas V, Glass R, et al. Deletion of endothelial α-parvin inhibits tumour angiogenesis, reduces tumour growth and induces tumour cell apoptosis. *Angiogenesis* (2022) **25**:155–8. doi:10.1007/s10456-021-09829-y

14. Wang M, Yu F, Li P, Wang K. Emerging function and clinical significance of exosomal circRNAs in cancer. *Mol Ther Nucleic Acids* (2020) **21**:367–83. doi:10.1016/j.omtn.2020.06.008

15. Wang Y, Zou R, Li D, Gao X, Lu X. Exosomal circSTRBP from cancer cells facilitates gastric cancer progression via regulating miR-1294/miR-593-3p/E2F2 axis. *J Cell Mol Med* (2024) **28**:e18217. doi:10.1111/jcmm.18217

16. Chen C, Liu Y, Liu L, Si C, Xu Y, Wu X, et al. Exosomal circTUBGCP4 promotes vascular endothelial cell tipping and colorectal cancer metastasis by activating Akt signaling pathway. *J Exp and Clin Cancer Res* (2023) **42**:46. doi:10.1186/s13046-023-02619-y

17. Xie J, Wei J, Lv L, Han Q, Yang W, Li G, et al. Angiopoietin-2 induces angiogenesis via exosomes in human hepatocellular carcinoma. *Cell Commun Signaling: CCS* (2020) **18**:46. doi:10.1186/s12964-020-00535-8

18. Huang X, Huang Z, Huang J, Xu B, Huang X, Xu Y, et al. Exosomal circRNA-100338 promotes hepatocellular carcinoma metastasis via enhancing invasiveness and angiogenesis. *J Exp and Clin Cancer Res* (2020) **39**:20. doi:10.1186/s13046-020-1529-9

19. Zhu W, Yang M, Shang J, Xu Y, Wang Y, Tao Q, et al. MiR-222 inhibits apoptosis in porcine follicular granulosa cells by targeting the THBS1 gene. *Anim Sci J* (2019) **90**:719–27. doi:10.1111/asj.13208

20. Ma D, Gao X, Liu Z, Lu X, Ju H, Zhang N. Exosome-transferred long non-coding RNA ASMTL-AS1 contributes to malignant phenotypes in residual hepatocellular carcinoma after insufficient radiofrequency ablation. *Cel Prolif* (2020) **53**:e12795. doi:10.1111/cpr.12795

21. Zhang S, Huang Y, Pi S, Chen H, Ye F, Wu C, et al. Autophagy-amplifying nanoparticles evoke immunogenic cell death combined with anti-PD-1/PD-L1 for residual tumors immunotherapy after RFA. *J nanobiotechnology* (2023) **21**:360. doi:10.1186/s12951-023-02067-y

22. Chao J, Zhao S, Sun H. Dedifferentiation of hepatocellular carcinoma: molecular mechanisms and therapeutic implications. *Am J translational Res* (2020) **12**:2099–109.

23. Duda D, Dima S, Cucu D, Sorop A, Klein S, Ancukiewicz M, et al. Potential circulating biomarkers of recurrence after hepatic resection or liver transplantation in hepatocellular carcinoma patients. *Cancers* (2020) **12**:1275. doi:10.3390/cancers12051275

24. Wu Q, Zhou L, Lv D, Zhu X, Tang H. Exosome-mediated communication in the tumor microenvironment contributes to hepatocellular carcinoma development and progression. *J Hematol and Oncol* (2019) **12**:53. doi:10.1186/s13045-019-0739-0

25. Yu M, Yu J, Zhang Y, Sun X, Sun R, Xia M, et al. A novel circRNA-miRNA-mRNA network revealed exosomal circ-ATP10A as a biomarker for multiple myeloma angiogenesis. *Bioengineered* (2022) **13**:667–83. doi:10.1080/21655979.2021.2012553

26. Xu Y, Leng K, Yao Y, Kang P, Liao G, Han Y, et al. A circular RNA, cholangiocarcinoma-associated circular RNA 1, contributes to cholangiocarcinoma progression, induces angiogenesis, and disrupts

vascular endothelial barriers. *Hepatology* (2021) **73**:1419–35. doi:10.1002/hep.31493

27. Li S, Li J, Zhang H, Zhang Y, Wang X, Yang H, et al. Gastric cancer derived exosomes mediate the delivery of circRNA to promote angiogenesis by targeting miR-29a/VEGF axis in endothelial cells. *Biochem biophysical Res Commun* (2021) **560**:37–44. doi:10.1016/j.bbrc.2021.04.099

28. Du E, Li X, He S, Li X, He S. The critical role of the interplays of EphrinB2/EphB4 and VEGF in the induction of angiogenesis. *Mol Biol Rep* (2020) **47**:4681–90. doi:10.1007/s11033-020-05470-y

29. Hou P, Li H, Yong H, Chen F, Chu S, Zheng J, et al. PinX1 represses renal cancer angiogenesis via the mir-125a-3p/VEGF signaling pathway. *Angiogenesis* (2019) **22**:507–19. doi:10.1007/s10456-019-09675-z

30. Li X, Li H, Li Z, Wang T, Yu D, Jin H, et al. TRPV3 promotes the angiogenesis through HIF-1α-VEGF signaling pathway in A549 cells. *Acta Histochem* (2022) **124**:151955. doi:10.1016/j.acthis.2022.151955

31. Chen Z, Chen Y, Li Y, Lian W, Zheng K, Zhang Y, et al. Prrx1 promotes stemness and angiogenesis via activating TGF-β/smad pathway and upregulating proangiogenic factors in glioma. *Cell Death Dis* (2021) **12**:615. doi:10.1038/s41419-021-03882-7

32. Li XP, Jia YL, Duan YQ, Zhao Y, Yin XL, Zhen SM, et al. Circular RNA hsa_circ_0002938 (circCRIM1) promotes the progression of esophageal squamous cell carcinoma by upregulating transcription factor 12. *Neoplasma* (2023) **70**:145–57. doi:10.4149/neo_2023_220823n857

33. Jia C, Chen F, Li W, Zhu X, Wang Y, Guo H, et al. CircCCNB1 knockdown blocks the progression of cervical cancer by acting as competing endogenous RNA in the miR-370-3p/SOX4 pathway. *Ann Clin Lab Sci* (2023) **53**:94–105.

34. Huang C, Deng H, Wang Y, Jiang H, Xu R, Zhu X, et al. Circular RNA circABCC4 as the ceRNA of miR-1182 facilitates prostate cancer progression by promoting FOXP4 expression. *J Cell Mol Med* (2019) **23**:6112–9. doi:10.1111/jcmm.14477

EBM Experimental Biology and Medicine

TYPE Review
PUBLISHED 28 October 2024
DOI 10.3389/ebm.2024.10200

OPEN ACCESS

*CORRESPONDENCE
Fuller W. Bazer,
fuller.bazer@ag.tamu.edu

RECEIVED 15 April 2024
ACCEPTED 30 September 2024
PUBLISHED 28 October 2024

CITATION
Bazer FW, Wu G and Johnson GA (2024) Fructose metabolism is unregulated in cancers and placentae.
Exp. Biol. Med. 249:10200.
doi: 10.3389/ebm.2024.10200

Fructose metabolism is unregulated in cancers and placentae

Fuller W. Bazer[1]*, Guoyao Wu[1] and Gregory A. Johnson[2]

[1]Department of Animal Science, Texas A&M University, College Station, TX, United States, [2]Department of Veterinary Integrative Biosciences, Texas A&M University, College Station, TX, United States

Abstract

Fructose and lactate are present in high concentrations in uterine luminal fluid, fetal fluids and fetal blood of ungulates and cetaceans, but their roles have been ignored and they have been considered waste products of pregnancy. This review provides evidence for key roles of both fructose and lactate in support of key metabolic pathways required for growth and development of fetal-placental tissues, implantation and placentation. The uterus and placenta of ungulates convert glucose to fructose via the polyol pathway. Fructose is sequestered within the uterus and cannot be transported back into the maternal circulation. Fructose is phosphorylated by ketohexokinase to fructose-1-PO4 (F1P) by that is metabolized via the fructolysis pathway to yield dihydoxyacetone phosphate and glyceraldehyde-3-PO4 that are downstream of phosphofructokinase. Thus, there is no inhibition of the fructolysis pathway by low pH, citrate or ATP which allows F1P to continuously generate substrates for the pentose cycle, hexosamine biosynthesis pathway, one-carbon metabolism and tricarboxylic acid cycle, as well as lactate. Lactate sustains the activity of hypoxia-inducible factor alpha and its downstream targets such as vascular endothelial growth factor to increase utero-placental blood flow critical to growth and development of the fetal-placental tissues and a successful outcome of pregnancy. Pregnancy has been referred to as a controlled cancer and this review addresses similarities regarding metabolic aspects of tumors and the placenta.

KEYWORDS

glucose, fructose, lactate, pregnancy, tumor biology, placenta

Introduction

Proliferating cells, such as cancer cells and activated lymphocytes, are metabolically different from nonproliferating cells as they are programmed to utilize either anaerobic or aerobic glycolysis, the Warburg effect, depending on the availability of oxygen [1]. Glucose and fructose are hexose sugars that provide glycolytic intermediates for further metabolism via the pentose cycle, tricarboxylic acid cycle (TCA), one-carbon metabolism and hexosamine biosynthesis pathway. Glycolysis is a physiological response

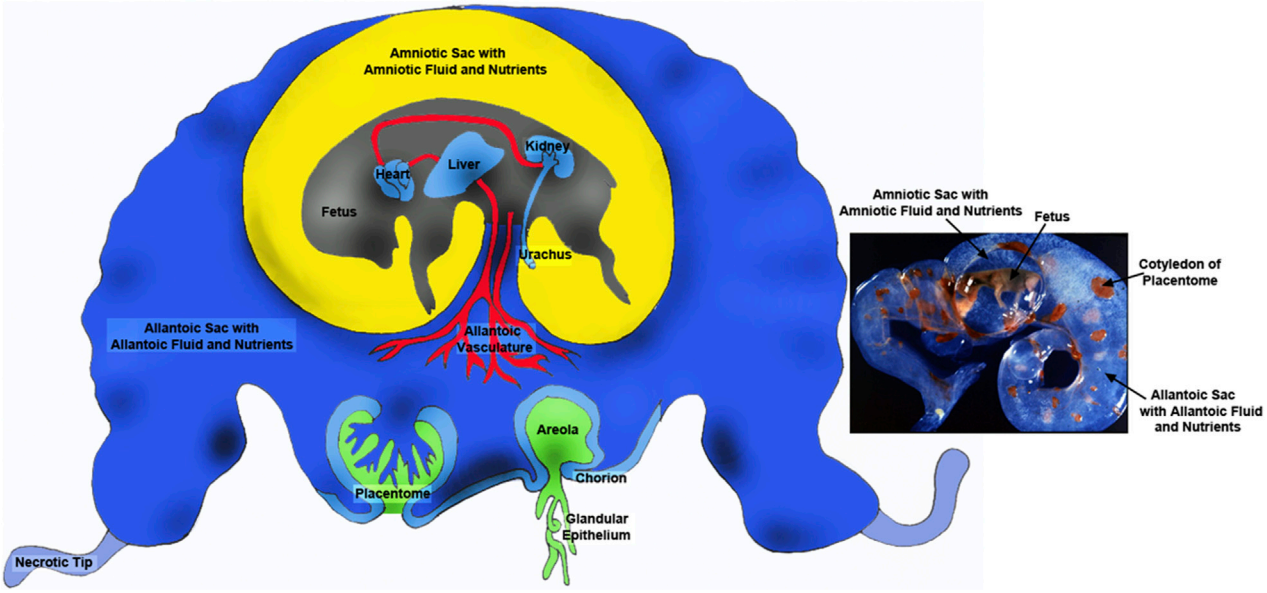

FIGURE 1
Placentae of ungulates include the amnion, allantois and chorion with the latter two membranes forming the chorioallantois. The majority of blood flow is via placentomes composed on the caruncle on the maternal side (green portion) and the cotyledon on the fetal side (blue). There are also areolae associated with the openings of uterine glands that form a "pocket" into which secretions are delivered and transported across the chorioallantois intothe fetal-placental circulation. The amnion is filled with amniotic fluid that is basically isosmotic to fetal serum and contains nutrients such as glucose and fructose. The allantoic sac is filled with allantoic fluid of which changes in are dynamic manner throughout gestation. Although allantoic fluid is hypoosmotic with respect to fetal fluids it is enriched in nutrients transported for support of fetal-placental tissues or cleared through the kidney into the bladder for delivery back into the allantoic sac via the urachus. Thus, allantoic fluid is a nutrient reservoir for the developing conceptus.

of tissues to hypoxia, a low oxygen environment, with cells of tumors taking up glucose and producing intermediate products of glycolysis (including fructose-6-phosphate, F6P) and significant amounts of lactate. By switching from oxidative phosphorylation to glycolysis, cells rapidly generate ATP as compared with oxidation of glucose and activation of the TCA cycle. Further, glycolytic intermediates are substrates for other metabolic pathways required to meet demands for proliferation, migration, and differentiation of cells [2–5].

This review focuses on the metabolism of glucose and fructose, two molecules present in great abundances in conceptuses (embryo and extra-embryonic membranes; fetus and placenta) of ungulates and cetaceans throughout pregnancy [see [6]; Figure 1]. Fructose and lactate have been considered metabolic wastes, so their functional roles in conceptus development have not been established. The following sections of this review evidence for important roles of fructose and lactate in conceptus development. Thus, the focus of this review is on contributions of glucose and fructose to the major metabolic pathways required for development of conceptuses under oxygenated and low oxygen conditions, expression of enzymes for production and metabolism of fructose from glucose, and characterization of lactate synthesis and transport throughout pregnancy.

Another focus of this review is the role of fructose in uncontrolled growth of cancers, as Burton et al. [7] reported similarities between metabolism in placentae and in malignant tumors while acknowledging that growth of the placenta is regulated. They note that the availability of oxygen controls placental development and tumor behavior as both develop in a low oxygen environment, and both need to stimulate vascular development to deliver nutrients and oxygen sufficient to support high rates of cell proliferation. Thus, glycolysis is common in support of growth and development of both placentae and tumors. Glycolysis, rather than oxidative phosphorylation, has the advantage of maintaining carbon skeletons for the synthesis of nucleotides, cell membranes and organelles, as well as protecting the conceptus from adverse effects of free radicals.

Fructose metabolism and cancer (see Krause and Wegner)

The link between cancer and altered glucose metabolism was discovered by Otto Warburg over 100 years ago. A connection between cancer and fructose metabolism was also discovered as fructose, like glucose, affects growth, proliferation, and survival of cancer cells [8, 9]. Cancer cells express solute carrier family

member 5 (SLC2A5), the fructose transporter, and upregulation of SLC2A5 is indicative of a poor prognosis for cancer patients that experienced an increase in cancer cell proliferation, colony growth, and metastasis [10]. There is over-expression of SLC2A5 for glioblastoma, colon, liver, lung, breast, and prostate cancers [11, 12].

The polyol pathway involves two steps for conversion of glucose to fructose [13–15]. Glucose is reduced to sorbitol by aldose reductase (AKR1B1) that requires nicotinamide adenine dinucleotide phosphate hydrogen (NADPH), and sorbitol is oxidized to fructose by sorbitol dehydrogenase (SORD) yielding nicotinamide adenine dinucleotide hydrogen (NADH) from nicotinamide adenine dinucleotide (NAD). The conversion of glucose to fructose may enhance glycolysis with conversion of fructose to fructose-1-PO_4 (F1P) by ketohexokinase (KHK) occurring mainly in the liver [16, 17]. KHK is also frequently expressed in tumors [18–20] that also produce fructose 1-P endogenously from fructose (a product of glucose). This reaction bypasses the rate-limiting step in glycolysis at the level of phosphofructokinase (PFK), which is inhibited by high levels of ATP, citrate and low pH. Naked mole rats also increase the production of fructose and F1P to increase their survival under low oxygen levels and even anoxia because fructose supports glycolysis and generation of ATP and substrates for other major metabolic pathways [21]. Low concentrations of oxygen inhibit oxidative phosphorylation that lowers pH and inhibits PFK. Thus, metabolism of fructose to F1P by KHK bypasses the PFK feedback inhibition by low pH, whereas glaceraldehyde-3-PO_4 (GAP) and dihydroxyacetone-PO_4 (DHAP) enter glycolysis downstream of PFK.

Most tumors develop initially in a hypoxic and acidic environment [22]. A direct link between polyol pathway activity and cancer was reported by Schwab et al. [23] who found a strong correlation between expression of AKR1B1and epithelial-to-mesenchymal transition (EMT) in patients with lung cancer and in an EMT-mediated colon cancer mouse model. They also found that AKR1B1 knockdown decreased EMT in cancers. Knockdown of expression of SORD also suppressed EMT in the cancer cell line. Schwab and colleagues [23] reported that glucose metabolism via the polyol pathway controls EMT via transforming growth factor beta (TGFB) autocrine stimulation and that expression of TGFB decreased following knockdown of AKR1B1 and SORD while EMT markers were rescued by TGFB [23]. There is also a link between the polyol pathway, particularly AKR1B1 overexpression, and development of breast, ovarian, cervical, and rectal cancers [24]. For colorectal cancer cells, AKR1B1 affects cellular proliferation and cell cycle progression, cell motility and expression of nuclear factor kappa-light-chain-enhancer of activated B cells (NFKB) resulting in a poor prognosis for colorectal cancer patients [25].

There is considerable evidence for endogenous production of fructose via the polyol pathway in cancer cells and phosphorylation of fructose to F1P by KHK in tumors of humans. This pathway for glycolysis is clearly advantageous as it bypasses PFK regulation to allow endogenously produced fructose to be used to produce F1P and substrates from the glycolytic pathway to support of cancer cells in a low oxygen, low pH environment that include the hexosamine biosynthesis pathway [26], the pentose cycle (PC) [27], *de novo* lipogenesis [28], one-carbon metabolism [29], and the TCA cycle [29].

The polyol pathway, fructose synthesis, and pregnancy

The polyol pathway involves two steps for conversion of glucose to fructose [13–15] as reviewed in *Fructose Metabolism and Cancer*. But the first report of fructose in tissues of conceptuses was in 1855 by Bernard [30]. Between that time and 1956, numerous reports confirmed the presence or absence of fructose in blood, amniotic fluid and allantoic fluid of ungulates and other species (see Goodwin [31]). Due to confusion about the presence or absence of fructose in fetal blood among species, Goodwin [31] measured fructose in blood from ungulates (ox, goat, horse, pig), cetaceans (fin, humpback and blue whales), and nonungulates (guinea pig, rabbit, rat, dog, cat, ferret) and cited work indicating the absence of fructose in blood from newborn human babies. Thus, he divided common mammals into two groups: those with detectable fructose (ungulates and cetaceans) and those with very low or undetectable fructose in fetal blood (nonungulates and humans). It was also noted that samples of fetal blood and amniotic fluids from ungulates and cetaceans had much greater concentrations of fructose than glucose.

There are species with invasive implantation and either hemochorial (humans, monkeys and rodents) or endotheliochorial (carnivores) placentae with close apposition between maternal and blood and fetal blood for efficient transport of glucose. Species with those types of placentae have little or no fructose in fetal blood or fetal fluids. However, species with noninvasive implantation have either epitheliochorial placentae (pigs, horses, cetaceans) or syndesmochorial placentae (cows, sheep, goats) with five or six layers of cells between maternal and fetal blood. Those species have fructogenic placenta with fructose being the most abundant hexose sugar in blood and fetal fluids of those species. Fructose is present in fluid of the extra-embryonic coelom of human conceptuses in early gestation [32], but it is a minor sugar compared with glucose. Fructose is also a minor sugar in fetal blood and fetal fluids of dogs, cats, guinea pigs, rabbits, rats, and ferrets [31].

Studies of pregnant ewes [see [6, 33, 34]] revealed that: 1) injection of glucose into ewes to make them hyperglycemic

resulted in a rapid increase in fructose in fetal blood; 2) injection of glucose into the fetal vasculature increased glucose in maternal blood and the fetus experienced hyperfructosemia indicating that glucose, but not fructose, could be transported from the fetal-placental vasculature to maternal blood; 3) the placenta is responsible for converting glucose to fructose; and 4) the flux of glucose from maternal blood to fetal blood may reach 70 mg/min in hyperglycemic ewes. Radiolabeled glucose was also shown to be converted to radiolabeled fructose by placentae of pigs. One may speculate about four main points. First, in species with hemochorial and endotheliochorial placenta, the chorion is in very close proximity to maternal blood for highly efficient exchange of glucose and other nutrients, as well as gases. The number of tissue layers separating maternal blood and chorion is three in species with hemochorial placenta, four in species with endotheliochorial placenta, but six in species with syndesmochorial and epitheliochorial placenta. Second, species with hemochorial placenta do not have an allantois as it regresses, like the yolk sac, early in gestation. For carnivores with endotheliochorial placenta, there is an allantoic sac, but it is not well developed. However, for ungulates, a well-developed allantois is characteristic of the placenta. The allantois forms a sac that is a reservoir of water and nutrients (e.g., fructose and glutamine) in storage and available to be recycled into the fetal-placental circulation. Third, the rate of uterine blood flow to support a human pregnancy is estimated to be 0.5 L per minute [35] compared to 2.5 L per minute for pigs [36], 5.95 L per minute for cows [37] and 2 L per minute for sheep during late gestation. The high rates of uterine blood flow for pregnant ungulates are critical for delivery and exchange of sufficient nutrients and gases to support fetal growth and development. Fourth, the placentae of ungulates convert glucose to fructose that is sequestered within the pregnant uterus and unavailable to maternal tissues. Rather, it is metabolized via glycolysis after being phosphorylated at carbon number 1 to F1P. This fructolysis pathway is not inhibited by low pH, citrate or ATP.

Fructose in conceptuses of sheep and pigs has been ignored by fetal physiologist using those animal models in biomedical research although fructose is 15- to 30-fold greater than glucose in allantoic fluid of sheep (see Figure 2), as well as blood of ovine fetuses (data not shown). A review by Battaglia and Meschia [38] on fetal and placental metabolism does not mention fructose. Fructose was considered a waste product since it was not metabolized via the classical glycolytic pathway [38–42] even though it is 11- to 33-times more abundant than glucose in blood and allantoic fluid of fetal lambs [33]. The literature indicates the following: 1) fructose can be used for synthesis of nucleic acids and generation of reducing equivalents in the form of NADPH in fetal pigs [43] and in HeLa cells [44]; 2) neither fructose nor glucose is metabolized via the PC by the ovine placenta [45]; 3) fructose and glucose are equivalent substrates for the synthesis of neutral lipids and phospholipids in heart, liver, kidney, brain, and adipose tissue of fetal lambs [46]; 4) activities of glucose-6-phosphate (G6P) dehydrogenase, malic enzyme, and acetyl-CoA carboxylase in liver are stimulated by glucose to increase lipogenesis [47]; and 5) fructose enters adipocytes by both insulin-independent and insulin-insensitive mechanisms [48]. These lines of evidence indicated that both glucose and fructose are metabolic substrates utilized by mammalian conceptuses.

Unique attributes of fructose as a metabolic substrate supporting growth and development of ungulate and cetacean conceptuses

Fructose is 15- to 30-fold greater in abundance than glucose in fetal fluids and plasma throughout pregnancy in sheep, for example, highlighting the facts that ungulate placentae are fructogenic and that fructose, but not glucose, is sequestered within fetal blood and fetal fluids [[49–51]; Figure 2]. The following are key findings from research on metabolism of fructose in ungulates. First, cell-specific, and temporal changes in expression of enzymes involved in the metabolism of glucose and fructose in ovine and porcine conceptuses throughout pregnancy are well characterized [6, 34, 52–59]. Second, cell-specific and temporal expression of KHK isoforms for conversion of fructose to F1P provide a substrate for metabolism via the fructolysis pathway that bypasses the regulatory step at PFK in glycolysis for unimpeded production of key substrates for the PC (G6P) [54], hexosamine biosynthesis (F6P) [6, 59], one-carbon metabolism and serine synthesis (3-phosphoglycerate) [53], and TCA cycle (pyruvate) [54]. Third, the glycolytic pathway generates abundant lactate that is not likely used for gluconeogenesis by ovine conceptuses as they do not express the required enzymes for gluconeogenesis; glucose-6-phosphatase (G6Pase) or phosphoenolpyruvate carboxykinase (*PCK*) [54]. Fourth, ovine conceptuses do express aldolase, an enzyme that converts glyceraldehyde-3-phosphate (GAP) and dihydroxyacetone phosphate to F-1,6-P. The latter is dephosphorylated to F6P, which is converted to G6P via phosphoglucoisomerase (PGI) for metabolism via the PC and glycogen synthesis [54]. Fifth, there is expression of O-linked N-acetylglucosaminyltransferase (*OGT)* mRNA in placentomes of sheep throughout gestation and OGT glycosylates and activates proteins such as AKT (protein kinase B) to inhibit silencing of TSC2 (tuberous sclerosis complex 2) and activate mechanistic target of rapamycin (mTOR) that stimulates expression of mRNAs and proteins involved in cell proliferation and migration [59]. Sixth, F6P and glutamine are required for synthesis of UDP-GlcNAc (UDP-N-acetyl-D-glucosamine) that uses OGT to activate the mTOR pathway in ovine [59] and porcine [6] conceptuses by transferring a carbohydrate moiety to a serine or a threonine residue [59]. Like fructose, glutamine is also unusually abundant in conceptuses of ungulates. For example, concentrations of

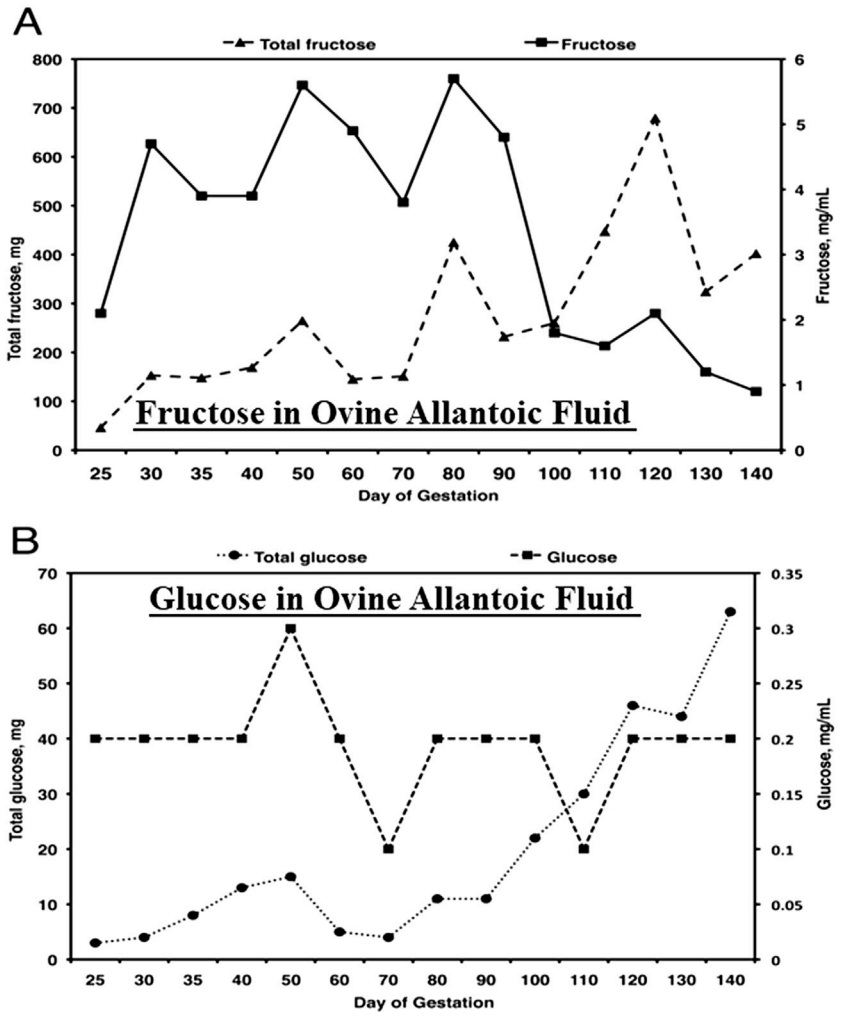

FIGURE 2
Fructose **(A)**, the most abundant hexose sugar in fetal fluids and fetal blood of ungulates such as sheep, is present at concentrations from 4 to 5 mg between Days 30 and 90 of gestation, the period of rapid placental development, as compared to concentrations of glucose **(B)** of about 0.2 mg/mL. Thus, the concentrations of fructose are some 20- to 30-fold greater than for glucose and, as reported, a unique feature of fructose-1-PO4 it its metabolism to yield ATP, as well as substrates for the pentose cycle, serine for one-carbon metabolism and the hexosamine biosynthesis pathway.

glutamine in ovine allantoic fluid are approximately 25 mM at Day 60 of gestation [60].

Fructose synthesis by sheep and pig conceptuses

The period of conceptus development between fertilization and implantation in mammalian species is critical for setting the stage for placental and fetal development. The trophectoderm and endoderm of pre-implantation ovine and porcine conceptuses undergo rapid elongation that involves proliferation, migration, and cytoskeletal modifications of trophectoderm cells. These complex events occur in a low oxygen intrauterine environment supported by nutrients and gases either transported or secreted into the uterine lumen. The conceptus utilizes glucose provided by the mother to initiate metabolic pathways that provide energy and substrates for other metabolic pathways. In ugulates, most available glucose is converted to fructose via the polyol pathway (see Figure 3). As noted previously, even subterranean rodents living in a low oxygen environment, switch to fructose-driven metabolism in very low oxygen environments [21] and cancer cells also produce and metabolize fructose as an adaptation to low oxygen environments [61].

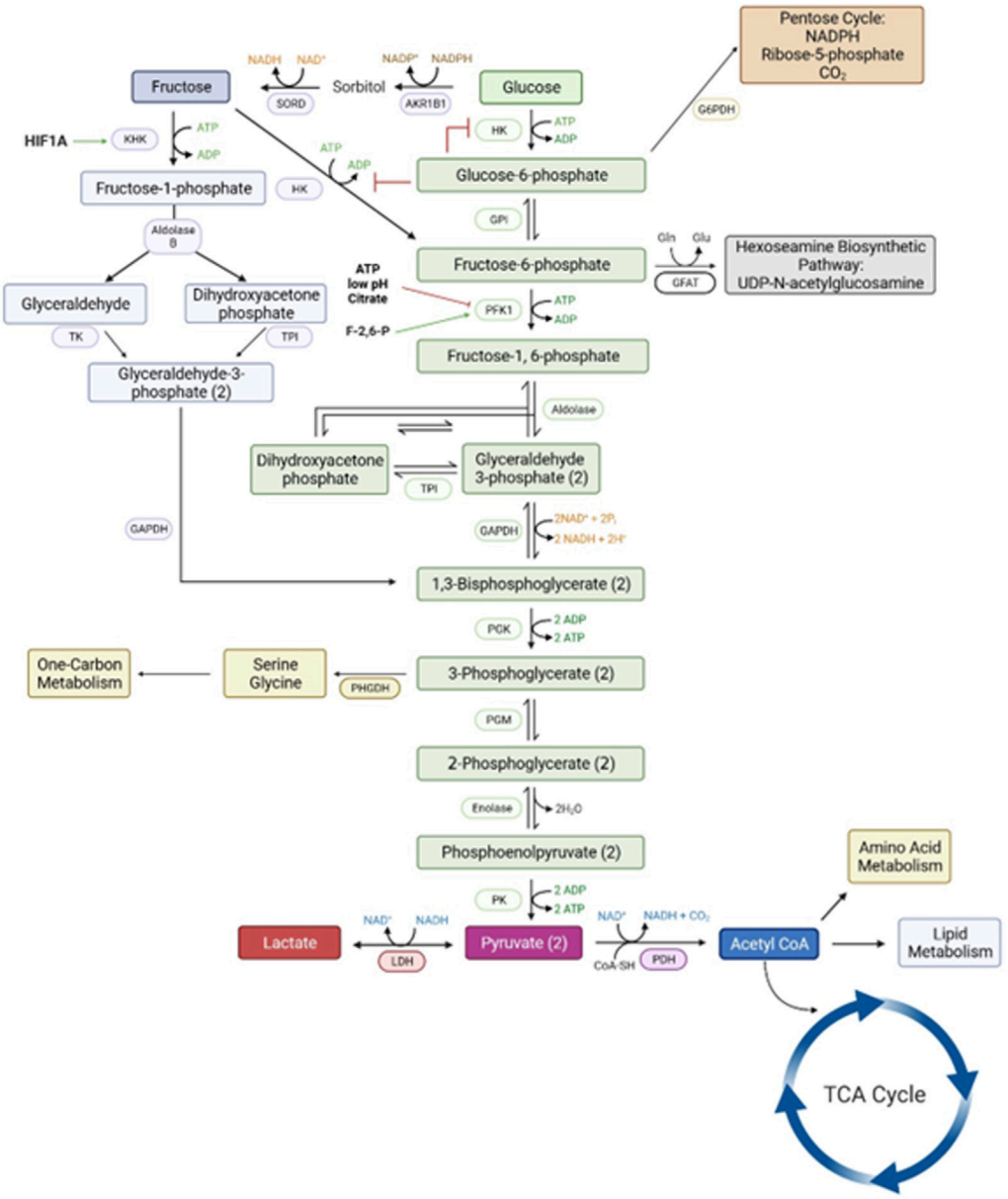

FIGURE 3
The metabolic pathways for a metabolism of glucose via the classical hexosamine pathway has a rate-limiting step at phosphofructose kinase (PFK1) that is inhibited by ATP, low pH and citrate. However, the conversion of glucose to fructose and fructose to fructose-1-PO4 by ketohexokinase allows for an uninhibited pathway for generation of substrates for all major metabolic pathways required for growth and development of the conceptus. Please see the list of abbreviations for each of enzymes noted in this figure [6, 59, 61].

The cell-specific and temporal expression of enzymes required for synthesis and metabolism of fructose in sheep and pig conceptuses include those for the polyol pathway (*SORD* and *AKR1B1*) and glucose and fructose metabolism (*HK1*, *HK2*, *G6PD*, *OGT*, KHK, and *FBP)*, but not those required for gluconeogenesis (*G6Pase* or *PCK*) [52, 57]. Ovine placentomes also express mRNAs for *SORD*, *AKR1B1*, *HK1*, and *OGT*, as well as two isoforms of ketohexokinase, (KHKA and KHKC). The KHKA and KHKC isoforms are expressed in ovine conceptuses from Day 16 of pregnancy and placentomes throughout pregnancy in a cell specific manner. KHKA is most abundant in trophectoderm and cotyledons of placentomes, while KHKC is more abundant in endoderm of Day 16 conceptuses and chorionic epithelium of placentomes. Expression of *KHK* mRNAs in placentomes is greatest at Day 30 of pregnancy in sheep, but not different among days later in gestation.

Fetal fluids and uterine flushings from pigs contain higher concentrations of fructose than glucose, but fructose is not detected in maternal blood. As noted for sheep, fructose is derived from glucose via enzymes of the polyol pathway, AKR1B1 and SORD, transported across cell membranes by solute carriers SLC2A5 and SLC2A8, and converted to F1P by KHK [58]. For pigs, progesterone up-regulates SLC2A8 expression in uterine luminal (LE) and glandular (GE) epithelia during the peri-implantation period of pregnancy and in chorion and blood vessels after Day 30 of gestation. Progesterone up-regulates SLC2A5 mRNA in uterine LE and GE after implantation, and the chorion expresses SLC2A5 between Days 30 and 85 of gestation in pigs. AKR1B1 and SORD are expressed by uterine LE during the peri-implantation period, but expression switches to chorion by Day 20 and is maintained through at least Day 85 of pregnancy. Expression of AKR1B1 mRNA in the uterus is downregulated by estrogen. KHK is expressed by trophectoderm/chorion throughout gestation. Enzymes for conversion of glucose to fructose and for fructose transport are present at the uterine-placental interface of pigs [57, 58]. The shift in expression from uterine LE to chorion during pregnancy suggests that free-floating conceptuses of ungulates are supported initially by fructose synthesized by the uterus, but after implantation, the chorion becomes self-sufficient for fructose synthesis and transport in pigs and sheep [57].

Fructose and the hexosamine biosynthesis pathway

A porcine trophectoderm cell line (pTr1) was used to demonstrate that both fructose and glucose increase cell proliferation by increasing phosphorylated-RPS6K, -EIF4EBP1, and -RPS6 over basal levels within 30 min; an effect sustained for 120 min [6]. Those effects were inhibited by specific inhibitors of RPS6K, EIF4EBP1, PI3K and MTOR. In the same study, the biosynthesis of hyaluronic acid from glucose and fructose was investigated [59]. Inhibition of glutamine-fructose-6-phosphate transaminase 1 (GFPT1) by azaserine (an inhibitor of GFPT1) and GFPT1 siRNA, revealed that MTOR-RPS6K and MTOR-EIF4EBP1 signaling in response to fructose is mediated via GFPT1 activation and the hexosamine pathway. Further, both glucose and fructose are utilized for the production of hyaluronic acid via GFPT1 and the hexosamine biosynthesis pathway. Hyaluronic acid, also known as hyaluronan, is an anionic nonsulfated glycosaminoglycan found as a major component of the extracellular matrix in many tissues, including cancers and in placentae it is known as Wharton's Jelly [62–64]. During placental development hyaluronic acid is an abundant extracellular matrix component responsible for tissue hydration and hydrodynamics, cell migration and proliferation, cell adhesion, supporting blood vessels and enhancing angiogenesis, and it serves as a niche for stem cells [65–67].

Partial degradation products of sodium hyaluronic acid, specifically fragments of 4 and 25 disaccharides in length, elicit angiogenesis in chick chorioallantoic membranes, whereas the intact high molecular weight hyaluronic acid does not induce angiogenesis [68]. Vallet et al. [69] reported that hyaluronic acid in the placenta of pigs increases between Days 25 and 45 of gestation and remains high throughout gestation, while expression of hyaluronoglucosaminidases 1 and 2 also increased with advancing gestation in pigs. Thus, through its role as a substrate for the hexosamine biosynthesis pathway for synthesis of hyaluronic acid, fructose influences angiogenesis and development of microscopic folds of the placenta [69].

Both glucose and fructose can be metabolized to fructose-6-P, as noted previously. Glutamine:fructose-6-P transaminase (GFPT1) then converts glutamine and fructose-6-P into glucosamine-6-P, which is a common substrate for the formation of all aminosugars and glycoproteins in animal cells. Fructose and glucose, in cooperation with glutamine, may affect proliferative behavior of conceptus trophectoderm/chorion via activation of the Akt-TSC2-MTOR signaling cascade. The phosphorylation for activation of this cascade is mediated by O-GlcNAcylation from UDP-N-acetylglucosamine, a primary product of the hexosamine biosynthesis pathway. Key roles of fructose in cellular functions equivalent to those of glucose are to activate integrated cell signaling pathways affecting proliferation of trophectoderm cells through metabolism via the nonoxidative hexosamine biosynthesis pathway to produce GlcN-6-P by GFPT1, increase O-GlcNAcylation of cellular proteins/enzymes by OGT, and increase phosphorylation of the Akt-TSC2-MTOR cell signaling cascade [59]. Fructose and glucose stimulate proliferation of ovine trophectoderm cells at 4 mM, but concentrations of fructose of 11.1–33.3 mM may have much greater effects than glucose at concentrations of only 0.6–1.1 mM. The hexosamine biosynthesis pathway yields UDP-GlcNAc for cytosolic and Golgi-mediated O- linked glycosylation (O-GlcNAcylation) of proteins and glycosylphosphatidylinositol anchors proteins to the outer plasma membrane. The O-GlcNAcylation is the process whereby β-D-N-acetylglucosamine is added to serine or threonine residues of proteins, and OGT is required for this process affecting proliferation and adhesion of oTr1 cells as well as activation of the Akt-TSC2-MTOR signaling cascade. Knockdown of translation of OGT mRNA in oTr1 cells using a morpholino antisense oligonucleotide (MAO) and inhibiting OGT by alloxan both significantly decreased fructose-induced total protein O-GlcNAcylation and cell proliferation and fructose-induced phosphorylation of MTOR, P70S6K, and 4EBP1. In addition, the synthesis of glucosamine-6-P is highly active in tumor cells, which are known to extensively use glutamine for OGT and mTOR activation, as well as cell growth and development (Figure 5) (Akella et al. 2019). Thus,

there is evidence for fructose-induced cell proliferation and activation of MTOR cell signaling being regulated by O-GlcNAcylation.

Fructose metabolism supports the PC and TCA cycle

The culture of ovine conceptus homogenates with ^{14}C-labeled glucose and/or ^{14}C-labeled fructose under oxygenated and low oxygen conditions was conducted to assess contributions of glucose and fructose to the PC, TCA cycle, synthesis of glycoproteins and the synthesis of lipids [54]. Both glucose and fructose contributed carbons to each of those pathways, except for lipid synthesis, and both hexose sugars were metabolized to pyruvate and lactate, with lactate being the primary product of glycolysis under both oxygenated and low oxygen conditions. The ovine conceptus tissue preferentially oxidized glucose over fructose and incorporation of fructose and glucose at 4 mM each into the PC by Day 16 conceptus homogenates was similar in the presence or absence of glucose, but incorporation of glucose into the PC was enhanced by the presence of fructose. The incorporation of fructose into the PC in the absence of glucose was greater under oxygenated conditions, and incorporation of glucose into the PC under low oxygen conditions was greater in the presence of fructose. These results indicate that both glucose and fructose are important metabolic substrates for metabolism via the PC, TCA cycle, and synthesis of glycoproteins [see [34, 54]].

Fructose metabolism supports one-carbon metabolism

Conceptuses of sheep and pigs, for example, undergo incredibly rapid increases in elongation during the peri-implantation period of pregnancy requiring rapid increases in proliferation and migration of trophectoderm that requires equally rapid increases in metabolic reactions that generate nucleic acids for synthesis of DNA and RNA, but also for other vital pathways such as those that generate ATP, reducing agents, or intermediates for subsequent reactions [55, 70, 71]. However, for survival during the peri-implantation period of pregnancy, the conceptus is entirely reliant upon the histotroph secreted and/or transported by uterine epithelia into the uterine lumen including glucose that is rapidly metabolized to fructose. A key amino acid for 1C metabolism is serine, the second most abundant amino acid (following glycine) in uterine flushings from pregnant ewes that increases 6.2-fold between Days 10 and 16 of gestation [60]. Also, with advancing stages of gestation, serine is the most abundant amino acid in fetal blood and allantoic fluid of sheep [72]. Serine can also be synthesized from glucose and/or fructose via the serinogenesis pathway in which 3-phosphoglycerate (3PG, a glycolytic intermediate) is converted to serine by the sequential enzymatic conversions of phosphoglycerate dehydrogenase (PHGDH), phosphoserine aminotransferase 1 (PSAT1), and phosphoserine phosphatase (PSPH) [73]. The conversion of both sugars into serine requires glutamate, a metabolite of glutamine via phosphate-activated glutaminase. The 1C metabolism pathway uses serine as a substrate for transferring 1C units (i.e., methyl groups) linking together the folate cycle that also provides 1C units and the methionine cycle that recycles components of the folate cycle in healthy tissues [74] and cancerous tissue [75]. Ultimately, the production of 1C units via the folate cycle is for the production of formate required for the synthesis of adenine, guanidine, and thymidine nucleotides [76]. Also, 1C metabolism is important for generation of S-adenosylmethionine (SAM) through the methionine cycle and SAM is required for methylation of nucleic acids and proteins for epigenetic modifications [77]. (NADPH generated via 1C metabolism also impacts mitochondrial redox control, particularly under conditions of low oxygen [77].

One-carbon metabolism is critical for metabolism in cancer cells [78, 79]. As cancer cells are highly proliferative under low oxygen conditions like developing conceptuses of ungulates during the peri-implantation period of pregnancy, cancer cells maintain a proliferative state while oxygen deprived by upregulating serine catabolism and 1C metabolism [7, 78]. Therefore, conceptuses of livestock species undergoing extensive cellular proliferation and rapid elongation likely utilize similar metabolic pathways but must rely on extracellular nutrients secreted and/or transported from maternal blood into the uterine lumen, such as glucose, fructose, and serine for 1C metabolism for production of formate during the peri-implantation period of pregnancy.

An experiment was conducted to demonstrate that in addition to free serine available to the conceptus *in utero*, glucose and fructose can generate serine via the serinogenesis pathway in ovine conceptuses for production of formate required for synthesis of purines and thymidine for nucleic acid synthesis [53]. Ovine conceptuses from Day 17 of gestation were cultured in medium containing either: 1) 4 mM D-glucose + 2 mM [U-^{13}C]serine; 2) 6 mM glycine + 4 mM D-glucose + 2 mM [U-^{13}C] serine; 3) 4 mM D-fructose + 2 mM [U-^{13}C]serine; 4) 6 mM glycine + 4 mM D-fructose + 2 mM [U-^{13}C]serine; 5) 4 mM D-glucose + 4 mM D-fructose + 2 mM [U-^{13}C]serine; or 6) 6 mM glycine + 4 mM D-glucose + 4 mM D-fructose + 2 mM [U-^{13}C] serine to determine production of formate. The ovine conceptuses produced both ^{13}C- and ^{12}C-formate, indicating that the [U-^{13}C] serine, glucose, and fructose were utilized to generate formate, respectively. Greater amounts of ^{12}C-formate than ^{13}C-formate were produced, indicating that ovine conceptuses utilized more glucose and fructose than serine to produce formate. These results were the first to demonstrate that both 1C metabolism and serinogenesis are active metabolic

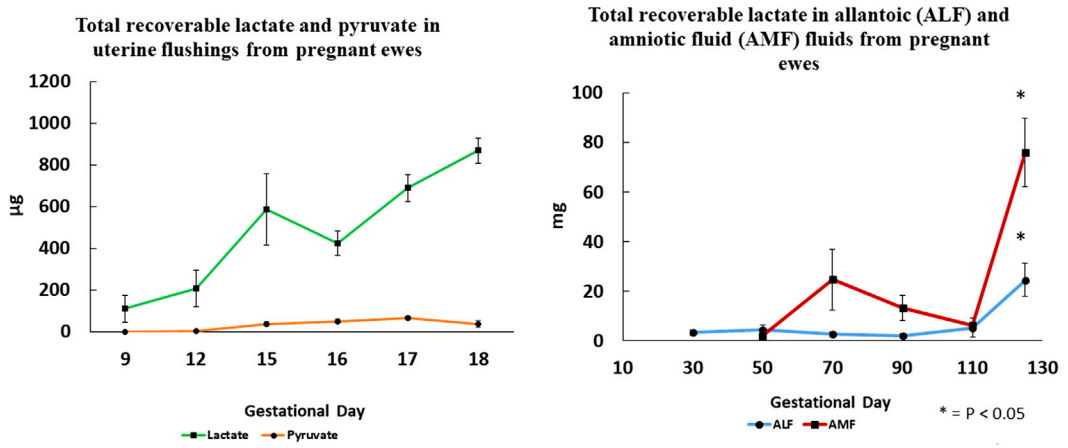

FIGURE 4
Total recoverable lactate in uterine flushings increases significantly between Days 9 and 18 of gestation, while pyruvate is barely detactable suggesting that lactate dehydrogenase A that converts pyruvate to lactate is the most active isoform. Changes in total recoverable lactate in amniotic and allantoic fluids are also shown with respect to day of gestation and fetal fluid compartment.

pathways in ovine conceptuses during the peri-implantation period of pregnancy, and that both glucose and fructose are substrates for generating formate required for synthesis of nucleotides and SAM in rapidly proliferating trophectoderm cells.

Fructose and production of lactate via glycolysis

Lactate, an abundant molecule in fetal fluids and blood of mammalian species is, like fructose, overlooked as a metabolic waste product generated during pregnancy. The metabolism of both glucose and fructose by ovine conceptuses generates significant amounts of lactate. Moses et al. [80] characterized lactate production by ovine conceptuses throughout gestation, as well as expression of mRNAs and proteins involved in lactate metabolism. Lactate in the uterine lumen of sheep increases during the preimplantation period of pregnancy and is significantly more abundant than pyruvate (see Figure 4). Also, concentrations and total amounts of lactate in allantoic and amniotic fluids increase with advancing days of gestation and most abundant on Day 125 of pregnancy. Lactate dehydrogenase (LDH) subunit A (converts pyruvate to lactate) and subunit B (converts lactate to pyruvate) are expressed by ovine conceptuses throughout gestation. Lactate is transported via monocarboxylic acid transporters (MCT) 1 and 4, both of which are expressed by the conceptus throughout gestation. Additionally, the inter-placentomal chorioallantois from Day 126 expresses MCT1 and MCT4 for transport of lactate. Hydrocarboxylic acid receptor 1 (HCAR1) is the receptor for lactate localized to the uterine LE and sGE, as well as conceptus trophectoderm of pregnant ewes throughout gestation [80].

Lactate receptors

The G-protein-coupled receptors for lactate, GPR81 (hydroxycarboxylic receptor 1), GPR109A (hydroxycarboxylic receptor 2) and GPR109B (hydroxycarboxylic receptor 3) share high sequence homology and are designated HCAR1, HCAR2 and HCAR3 [81, 82]. HCAR1 is activated by lactate whereas HCAR2 is activated by the ketone body 3-hydroxy-butyric acid, and HCAR3 is activated by 3-hydoxy-octanoic acid (an intermediate in β-oxidation of octanoate). Lactate binding to HCAR1 stimulates GTPγS-binding with an EC50 of 1.3 mM. However, HCAR1 cloned from tissues of mice, rats, dogs, pigs, cows, monkeys, and Zebra fish responds to physiological concentrations of lactate at 0.5–2.0 mM, as well as 10–20 mM lactate. HCAR1 is expressed in human pituitary, adipocytes, and brown adipose tissue, as well as uterine epithelia and conceptus trophectoderm of sheep [see [80]]. In tumor cells, lactate regulates expression of HCAR1 mRNA via STAT3 (signal transducer and activator of transcription factor 3) cell signaling. In non-immune cells, lactate-HCAR1 cell signaling activates protein kinase A (PKA) and ERK (extracellular signal-related kinases) pathways, and plasmacytoid dendric cells are induced to express interferon alpha (IFNA) in response to calcium mobilization and calcium-calmodulin dependent protein kinase II (CaMKII) and calcineurin (CaN) phosphatase [82]. HCAR1 protein is expressed by uterine LE and sGE, as well as trophectoderm, but not GE, myometrium

from sheep on Day 17 of pregnancy, as well as all cell types of the uterus on Days 30, 70, 90, 110, and 125 of gestation [80].

Lactate as a cell signaling molecule

Expression of hypoxia inducible factor 1 (HIF1A) may occur under both hypoxic and normoxic environments; however, if HIF1A proline residues are hydroxylated by prolyl-4-hydroxylase (PHD) HIF1A is ubiquitinated by the von Hippel-Landeu protein and degraded. But, in the presence of lactate, PHD is inhibited and HIF1A is not subject to degradation [see [83]]. Tumor-derived lactate activates endothelial cells and stimulates angiogenesis through both HIF1A-dependent and HIF1A-independent pathways [84, 85]. In the HIF1A-dependent pathway, MCT1 transports lactate into endothelial cells to inactivate PHDs and stabilize HIF1A that then induces expression of vascular endothelial growth factor (VEGF) to promote angiogenesis in tumor cells under normoxic conditions [86]. Lactate may also induce angiogenesis via a HIF1A-independent mechanism by binding directly to N-Myc downstream-regulated protein (NDRG3) and preventing HIF1A degradation by PHD [87]. NDRG3 promotes angiogenesis under conditions of low oxygen and high concentrations of lactate by binding to c-Raf and activating Raf-ERK signaling in tumor cells to sustain HIF1A activity required for tumorigenesis. Constitutive HIF1A is detectable in non-hypoxic cancer cell lines in response to lactate and pyruvate as evidenced by the accumulation of HIF1A protein in many cancer cell lines due primarily to lactate that prevents degradation of HIF1A [88].

Lactate, HCAR1, and pregnancy

HIF1A is important for the establishment and maintenance of pregnancy in mammals as conceptuses develop in a low oxygen environment and respond to changes in oxygen tension, hormones, and other molecules. For example, expression of HIF1A is upregulated by progesterone in the uterus [89, 90], while HIF2A is upregulated by estrogen [90]. In sheep, HIF1A mRNA is induced by progesterone in the endometrium and HIF2A is upregulated in response to progesterone and IFNT [89]. Lactate is a ligand for HCAR1 in mammary tumors and is designated an orphan G-protein coupled receptor [91]. Lactate interactions with HCAR1 in cancer cells [92] promote angiogenesis [91], tumor growth [93], and chemoresistance [94], and proliferation and migration of normal cells [92]. Lactate produced via glycolysis is used potentially as: 1) an energy source for mitochondrial respiration; 2) gluconeogenic precursor; and 3) cell signaling molecule at physiological concentrations of lactate from 0.5 to 20 mM and when the lactate/pyruvate ratio ranges from 10 to greater than 500 mM under conditions such as vigorous exercise and stress [81]. Lactate acting via HCAR1 in adipocytes inhibits lipolysis by decreasing mitochondrial fatty acid uptake via malonyl-CoA and carnitine palmitoyltransferase I in muscle [84].

The high lactate and low pH environment in the uterine lumen during early pregnancy is created by lactate produced by blastocysts in mice [see [95–97]]. Lactate and low pH increases expression of mRNAs for VEGFA, HCAR1, SLC2A4 (also known as glucose transporter member 4), transcription factor p65 (RELA), MCT1 and snail (SNAI1) involved in epithelial to mesenchymal cell transition in Ishikawa cells. Lactic acid also increases migration of decidualized stromal cells in uteri of mice without changing the extent of decidualization. Further, human umbilical vein endothelial cells (HUVEC) form tubes when treated with 5 mM lactic acid as evidence of an angiogenic effect of lactic acid. Garner [95] reported that mammalian blastocysts use aerobic glycolysis as do cancer cells to create a microenvironment in which the pH is low to increase angiogenesis, vascular permeability, tissue disaggregation through breakdown of the extracellular matrix associated with increases in expression of matrix metalloproteinases 1 and 2 (MMP1 and 2) from blastocysts and MMP9, transforming growth factors beta 1 and 2 (TGFB1, TGFB2), cathepsin B and hyaluronic acid. The increase in hyaluronic acid is suggested to increase hydration of the endometrium due to facilitate implantation. Also, there was a decrease in expression of tissue inhibitors of metalloproteinases (TIMPs) and an increase in NFKB in that study [95]. Lactate also increased Treg cells, conversion of macrophages from M1 (inflammatory) to M2 (anti-inflammatory) phenotypes, and expression of VEGF in macrophages. Gardner [95] suggests that post-implantation conceptuses become more dependent on glycolysis to produce lactate and maintain a low pH environment that mimics hypoxia.

Comline and Silver [98] reported concentrations (mg/100 mL) of lactic acid in fetal umbilical vein blood at 9, 5 and 1 day prepartum to be 16.7, 16.8, and 19.1, respectively, as compared to values in blood from the maternal uterine vein of 11.2, 9.8 and 9.8. In comparison, concentrations (mg/100 mL) of fructose in fetal umbilical vein blood at 9, 5, and 1 day prepartum were 74.3, 77.8, and 67.7, respectively, but not detectable in maternal blood samples. The concentrations of glucose in umbilical vein blood were 13.3, 12.7, and 19.1 mg/100 mL at 9, 5 and 1 day prepartum, respectively as compared to 57.6, 58.0, and 68.0 mg/100 mL in maternal uterine vein blood. Thus, concentrations of fructose in fetal umbilical vein blood were 5- to 6-fold greater than those for glucose in that study [98].

Summary

The literature documents that the intrauterine environment for mammalian conceptuses is hypoxic relative to normal air [95, 99–102] and that is also true for developing tumors [61]. Accordingly, the polyol pathway is active in conceptuses of

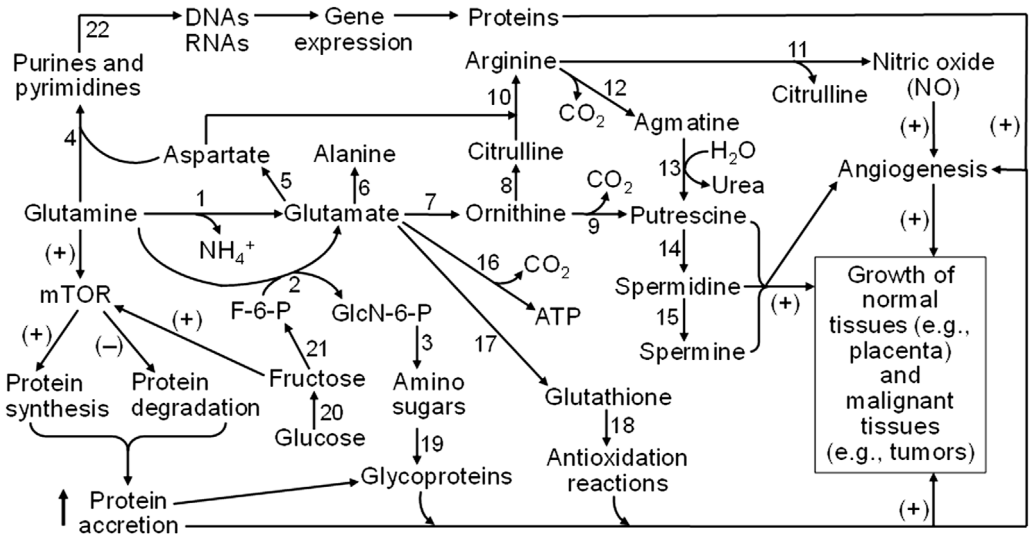

FIGURE 5
Mechanisms responsible for glutamine and fructose metabolism to stimulate the growth of both normal and malignant tissues in humans and animals. Glutamine is degraded via multiple pathways to generate glutamate, aspartate, alanine, ornithine, citrulline, arginine, glucosamine, and CO_2, purines, and pyrimidines. Ornithine and arginine are substrates for the synthesis of polyamines (putrescine, spermidine, and spermine), whereas nitric oxide (NO) is formed from arginine oxidation. Glutamate is required for the production of glutathione as the most abundant low-molecular-weight antioxidant. Amino sugars (which deriving the carbohydrate moiety from fructose-6-phosphate, a product of fructose) are required for the generation of glycoproteins as essential components of membranes, cytoplasm, and the extracellular matrix. Purine and pyrimidine nucleotides are precursors of DNAs and RNAs that are necessary for protein synthesis. Furthermore, both glutamine and fructose activate the mTOR cell signaling pathway to stimulate protein synthesis and inhibit protein degradation, leading to protein accretion in cells. NO (a major vasodilator to promote blood flow and nutrient supply), polyamines, protein accretion, and redox balance are crucial for angiogenesis and the growth of both normal and malignant tissues in humans and animals. Abbreviations: F-6-P, fructose-6-phosphate; GlcN-6-P, N-acetylglucosamine-6-phosphate; mTOR, mechanistic target of rapamycin. The enzymes that catalyze the indicated reactions are: (1) phosphate-activated glutaminase; (2) glutamine: fructose-6-phosphate transaminase; (3) glucosamine-phosphate N-acetyltransferase, phosphoacetylglucosamine mutase, UDP-GlcNAc pyrophosphorylase, and UDP-GlcNAc 4-epimerase; (4) a series of enzymes for purine and pyrimidine syntheses; (5) glutamate-oxaloacetate transaminase; (6) glutamate-pyruvate transaminase; (7) pyrroline-5-carboxylate synthetase and ornithine aminotransferase; (8) ornithine carbamoyltransferase; (9) ornithine decarboxylase; (10) argininosuccinate synthase and argininosuccinate lyase; (11) nitric oxide synthase; (12) arginine decarboxylase; (13) agmatinase; (14) spermidine synthase; (15) spermine synthase; (16) a series of enzymes for glutamate oxidation (including glutamate transaminases and glutamate dehydrogenase); (17) γ-glutamyl-cysteine synthetase and glutathione synthetase; (18) glutathione-dependent antioxidative enzymes (including glutathione peroxidase, glutathione *S*-transferase, and thioltransferase); (19) a series of enzymes for incorporation of amino sugars into proteins; (20) aldose reductase and sorbitol dehydrogenase; (21) fructokinase and hexokinase; and (22) a series of enzymes for DNA and RNA syntheses. The sign (+) and (–) denote activation and inhibition, respectively.

ungulates such as pigs [57] and sheep [54] and even humans [32]. The polyol pathway generates fructose and the metabolism of fructose via frutolysis is sustained for conceptuses of pigs [57] and sheep [33] throughout gestation, but not for human conceptuses [32]. We speculate that species with invasive implantation and hemochorial or hemoendothelial placenta with fewer layers of tissue separating maternal and fetal blood do not require high rates of blood flow to the uterus or a well-developed allantois to serve as a reservoir of nutrients. The various species of ungulates have superficial implantation of the blastocyst/conceptus and high rates of uterine blood flow to ensure a sustained delivery of high amounts of nutrients [concentration of nutrient X uterine blood flow] for transfer to the fetal-placental vasculature, as well as a well-developed allantois in which nutrients not utilized immediately can accumulate and be recycled to ensure that the conceptus is well nourished.

Adaptation of the polyol pathway and fructolysis in the placenta has several advantages for ungulates (see Figure 5). First, the trophectoderm/chorioallantois rapidly converts available glucose to fructose that cannot be transferred to the maternal vasculature, it is a sequestered hexose sugar. Second, fructose is phosphorylated at carbon 1 to F1P that is then committed to the fructolysis pathway for further metabolism to substrates that support the pentose cycle, TCA cycle, hexosamine biosynthesis pathway, and one-carbon metabolism. Third, the fructolysis metabolic pathway is not inhibited by low pH, ATP or citrate as is the case for the hexosamine-dependent pathway for glycolysis. Fourth, the fructose in fetal blood is excreted in urine during the first 24–48 h after birth so that does not cause insulin-insensitivity [102] as piglets fail to survive on synthetic diets containing only fructose [103, 104]. Failure of newborn piglets to survive on fructose-based synthetic diets further validates the unique role of fructose and the fructolysis pathway used by fetal-

placental tissue of ungulates. Further, it is now becoming apparent that lactate, a product of fructose metabolism, likely acts via its own receptor (HCAR1) to influence implantation and placentation, as well as sustain expression of HIF1A and its downstream genes such as KHK and VEGF [105–107]. On-going and future research will further expand knowledge of the roles of fructose and lactate in fetal-placental development and cancer as they represent rapidly developing tissues that share many metabolic profiles.

Author contributions

All authors listed have made a substantial, direct, and intellectual contribution to the work and approved it for publication.

Funding

The author(s) declare financial support was received for the research, authorship, and/or publication of this article. Work in our laboratories was supported by Agriculture and Food Research Initiative Competitive Grants (2018-67015-28093 and 2022-67015-37229) from the USDA National Institute of Food and Agriculture.

Conflict of interest

The author(s) declared no potential conflicts of interest with respect to the research, authorship, and/or publication of this article.

References

1. Andrejeva G, Rathmell JC. Similarities and distinctions of cancer and immune metabolism in inflammation and tumors. *Cell Metab* (2017) **26**:49–70. doi:10.1016/j.cmet.2017.06.004

2. Cruys B, Wong BW, Kuchnio A, Verdegem D, Cantelmo AR, Conradi LC, et al. Glycolytic regulation of cell rearrangement in angiogenesis. *Nat Commun* (2016) **7**:12240. doi:10.1038/ncomms12240

3. Rathmell JC, Heiden MG, Harris MH, Frauwirth KA, Thompson CB. In the absence of extrinsic signals, nutrient utilization by lymphocytes is insufficient to maintain either cell size or viability. *Mol Cell* (2000) **6**:683–92. doi:10.1016/s1097-2765(00)00066-6

4. Wang T, Marquardt C, Foker J. Aerobic glycolysis during lymphocyte proliferation. *Nature* (1976) **261**:702–5. doi:10.1038/261702a0

5. O'Neill LA, Kishton RJ, Rathmell J. A guide to immunometabolism for immunologists. *Nat Rev Immunol* (2016) **16**:553–65. doi:10.1038/nri.2016.70

6. Kim J, Song G, Wu G, Bazer FW. Functional roles of fructose. *Proc Natl Acad Sci U S A* (2012) **109**:E1619–628. doi:10.1073/pnas.1204298109

7. Burton GJ, Jauniaux E, Murray AJ. Oxygen and placental development; parallels and differences with tumour biology. *Placenta* (2017) **56**:14–8. doi:10.1016/j.placenta.2017.01.130

8. Liu H, Heaney AP. Refined fructose and cancer. *Expert Opin Ther Targets* (2011) **15**:1049–59. doi:10.1517/14728222.2011.588208

9. Boroughs LK, DeBerardinis RJ. Metabolic pathways promoting cancer cell survival and growth. *Nat Cell Biol* (2015) **17**:351–9. doi:10.1038/ncb3124

10. Weng Y, Fan X, Bai Y, Wang S, Huang H, Yang H, et al. SLC2A5 promotes lung adenocarcinoma cell growth and metastasis by enhancing fructose utilization. *Cell Death Discov* (2018) **4**(4):38. doi:10.1038/s41420-018-0038-5

11. Godoy A, Ulloa V, Rodríguez F, Reinicke K, Yañez AJ, García Md l A, et al. Differential subcellular distribution of glucose transporters GLUT1–6 and GLUT9 in human cancer: ultrastructural localization of GLUT1 and GLUT5 in breast tumor tissues. *J Cell Physiol* (2006) **207**:614–27. doi:10.1002/jcp.20606

12. Zamora-Leon SP, Golde DW, Concha II, Rivas CI, Delgado-Lopez F, Baselga J, et al. Expression of the fructose transporter GLUT5 in human breast cancer. *Proc Natl Acad Sci USA* (1996) **93**:1847–52. doi:10.1073/pnas.93.5.1847

13. Van Heyningen R. Formation of polyols by the lens of the rat with sugar cataract. *Nature* (1959) **184**:194–5. doi:10.1038/184194b0

14. Kador PF, Kinoshita JH. Role of aldose reductase in the development of diabetes-associated complications. *The Am J Med* (1985) **79**:8–12. doi:10.1016/0002-9343(85)90504-2

15. Kinoshita JH. A thirty-year journey in the polyol pathway. *Exp Eye Res* (1990) **50**:567–73. doi:10.1016/0014-4835(90)90096-d

16. Hayward BE, Bonthron DT. Structure and alternative splicing of the ketohexokinase gene. *Eur J Biochem* (1998) **257**:85–91. doi:10.1046/j.1432-1327.1998.2570085.x

17. Diggle CP, Shires M, Leitch D, Brooke D, Carr IM, Markham AF, et al. Ketohexokinase: expression and localization of the principal fructose-metabolizing enzyme. *J Histochem Cytochem* (2009) **57**:763–74. doi:10.1369/jhc.2009.953190

18. Gao W, Li N, Li Z, Xu J, Su C. Ketohexokinase is involved in fructose utilization and promotes tumor progression in glioma. *Biochem Biophysical Res Commun* (2018) **503**:1298–306. doi:10.1016/j.bbrc.2018.07.040

19. Yang X, Shao F, Shi S, Feng X, Wang W, Wang Y, et al. Prognostic impact of metabolism reprogramming markers acetyl-CoA synthetase 2 phosphorylation and ketohexokinase-A expression in non-small-cell lung carcinoma. *Front Oncol* (2019) **9**:1123. doi:10.3389/fonc.2019.01123

20. Kim J, Kang J, Kang YL, Woo J, Kim Y, Huh J, et al. Ketohexokinase-A acts as a nuclear protein kinase that mediates fructose-induced metastasis in breast cancer. *Nat Commun* (2020) **11**:5436. doi:10.1038/s41467-020-19263-1

21. Park TJ, Reznick J, Peterson BL, Blass G, Omerbašić D, Bennett NC, et al. Fructose-driven glycolysis supports anoxia resistance in the naked mole-rat. *Science* (2017) **356**:307–11. doi:10.1126/science.aab3896

22. Höckel M, Vaupel P. Tumor hypoxia: definitions and current clinical, biologic, and molecular aspects. *JNCI J Natl Cancer Inst* (2001) **93**:266–76. doi:10.1093/jnci/93.4.266

23. Schwab A, Siddiqui A, Vazakidou ME, Napoli F, Böttcher M, Menchicchi B, et al. Polyol pathway links glucose metabolism to the aggressiveness of cancer cells. *Cancer Res* (2018) **78**:1604–18. doi:10.1158/0008-5472.can-17-2834

24. Saraswat MMT, Kumar PU, Suneetha A, Rao R, Srinivasulu M, Reddy B. Overexpression of aldose reductase in human cancer tissues. *Med Sci Monit Int Med J Exp Clin Res* (2006) **12**:CR525–CR529.

25. Taskoparan B, Seza EG, Demirkol S, Tuncer S, Stefek M, Gure AO, et al. Opposing roles of the aldo-keto reductases AKR1B1 and AKR1B10 in colorectal cancer. *Cell Oncol* (2017) **40**:563–78. doi:10.1007/s13402-017-0351-7

26. Chiaradonna F, Ricciardiello F, Palorini R. The nutrient-sensing hexosamine biosynthetic pathway as the hub of cancer metabolic rewiring. *Cells* (2018) **7**:53. doi:10.3390/cells7060053

27. Stincone A, Prigione A, Cramer T, Wamelink MMC, Campbell K, Cheung E, et al. The return of metabolism: biochemistry and physiology of the pentose phosphate pathway. *Biol Rev* (2015) **90**:927–63. doi:10.1111/brv.12140

28. Ameer F, Scandiuzzi L, Hasnain S, Kalbacher H, Zaidi N. *De novo* lipogenesis in health and disease. *Metabolism* (2014) **63**:895–902. doi:10.1016/j.metabol.2014.04.003

29. Nakagawa T, Lanaspa MA, Millan IS, Fini M, Rivard CJ, Sanchez-Lozada LG, et al. Fructose contributes to the Warburg effect for cancer growth. *Cancer Metab* (2020) **8**:16. doi:10.1186/s40170-020-00222-9

30. Bernard C *Lecons de physiologie experimentale*. Paris: Bailliere (1855). 405.

31. Goodwin RFW. Division of the common mammals into two groups according to the concentration of fructose in the blood of the foetus. *The J Physiol* (1956) **132**:146–56. doi:10.1113/jphysiol.1956.sp005509

32. Jauniaux E, Hempstock J, Teng C, Battaglia FC, Burton GJ. Polyol concentrations in the fluid compartments of the human conceptus during the

first trimester of pregnancy: maintenance of redox potential in a low oxygen environment. *The J Clin Endocrinol & Metab* (2005) **90**:1171–5. doi:10.1210/jc.2004-1513

33. Bazer FW, Spencer TE, Thatcher WW. Growth and development of the ovine conceptus. *J Anim Sci* (2012) **90**:159–70. doi:10.2527/jas.2011-4180

34. Moses RM, Kramer AC, Seo H, Wu G, Johnson GA, Bazer FW. A role for fructose metabolism in development of sheep and pig conceptuses. *Adv Exp Med Biol* (2022) **1354**:49–62. doi:10.1007/978-3-030-85686-1_3

35. Vaupel P, Multhoff G. Blood flow and respiratory gas exchange in the human placenta at term: a data update. *Adv Exp Med Biol* (2022) **1395**:379–84. doi:10.1007/978-3-031-14190-4_62

36. Ford SP, Christenson RK. Blood flow to uteri of sows during the estrous cycle and early pregnancy: local effect of the conceptus on the uterine blood supply. *Biol Reprod* (1979) **21**:617–24. doi:10.1095/biolreprod21.3.617

37. Ferrell CL, Ford SP, Prior RL, Christenson RK. Blood flow, steroid secretion and nutrient uptake of the gravid bovine uterus and fetus. *J Anim Sci* (1983) **56**:656–67. doi:10.2527/jas1983.563656x

38. Battaglia FC, Meschia G. Foetal and placental metabolisms: their interrelationship and impact upon maternal metabolism. *Proc Nutr Soc* (1981) **40**:99–113. doi:10.1079/pns19810015

39. Battaglia FC, Meschia G. Principal substrates of fetal metabolism. *Physiol Rev* (1978) **58**:499–527. doi:10.1152/physrev.1978.58.2.499

40. Abrams RM. Energy metabolism. *Semin Perinatol* (1979) **3**:109–19.

41. Bell AW, Ehrhardt RA. Regulation of placental nutrient transport and implications for fetal growth. *Nutr Res Rev* (2002) **15**:211–30. doi:10.1079/nrr200239

42. HaySparks WWJW, Wilkening RB, Battaglia FC, Meschia G, Meschia G. Fetal glucose uptake and utilization as functions of maternal glucose concentration. *Am J Physiology-Endocrinology Metab* (1984) **246**:E237–242. doi:10.1152/ajpendo.1984.246.3.e237

43. White CE, Piper EL, Noland PR, Daniels LB. Fructose utilization for nucleic acid synthesis in the fetal pig. *J Anim Sci* (1982) **55**:73–6. doi:10.2527/jas1982.55173x

44. Reitzer LJ, Wice BM, Kennell DD. Evidence that glutamine, not sugar, is the major energy source for cultured HeLa cells. *J Biol Chem* (1979) **254**:2669–76. doi:10.1016/s0021-9258(17)30124-2

45. Regnault TR, Teng C, de Vrijer B, Galan HL, Wilkening RB, Battaglia FC, et al. The tissue and plasma concentration of polyols and sugars in sheep intrauterine growth retardation. *Exp Biol Med* (2010) **235**:999–1006. doi:10.1258/ebm.2010.009360

46. Scott TW, Setchell BP, Bassett JM. Characterization and metabolism of ovine foetal lipids. *Biochem J* (1967) **104**:1040–7. doi:10.1042/bj1041040

47. Fukuda H, Iritani N, Tanaka T. Effects of high-fructose diet on lipogenic enzymes and their substrate and effector levels in diabetic rats. *J Nutr Sci Vitaminology* (1983) **29**:691–9. doi:10.3177/jnsv.29.691

48. Halperin ML, Cheema-Dhadli S. Comparison of glucose and fructose transport into adipocytes of the rat. *Biochem J* (1982) **202**:717–21. doi:10.1042/bj2020717

49. Bacon JS, Bell DJ. The identification of fructose as a constituent of the foetal blood of the sheep. *Biochem J* (1946) **40**(xlii).

50. Bacon JS, Bell DJ. Fructose and glucose in the blood of the foetal sheep. *Biochem J* (1948) **42**:397–405. doi:10.1042/bj0420397

51. Barklay H, Haas P, Huggett SG, King G, Rowley D. The sugar of the foetal blood, the amniotic and allantoic fluids. *The J Physiol* (1949) **109**:98–102. doi:10.1113/jphysiol.1949.sp004373

52. Moses RM, Stenhouse C, Halloran KM, Sah N, Hoskins EC, Washborn S, et al. Pathways for metabolism of glucose and fructose: I Synthesis and metabolism of fructose by ovine conceptuses. *Biol Reprod* (2024) **111**:148–159. doi:10.1093/biolre/ioae043

53. Halloran KM, Stenhouse C, Moses RM, Kramer AC, Sah N, Seo H, et al. The ovine conceptus utilizes extracellular serine, glucose, and fructose to generate formate via the one carbon metabolism pathway. *Amino Acids* (2023) **55**:125–37. doi:10.1007/s00726-022-03212-x

54. Moses RM, Halloran KM, Stenhouse C, Sah N, Kramer AC, McLendon BA, et al. Ovine conceptus tissue metabolizes fructose for metabolic support during the peri-implantation period of pregnancy. *Biol Reprod* (2022) **107**:1084–96. doi:10.1093/biolre/ioac144

55. Bazer FW, Seo H, Johnson GA, Wu G. One-carbon metabolism and development of the conceptus during pregnancy: lessons from studies with sheep and pigs. *Adv Exp Med Biol* (2021) **1285**:1–15. doi:10.1007/978-3-030-54462-1_1

56. Steinhauser CB, Wing TT, Gao H, Li X, Burghardt RC, Wu G, et al. Identification of appropriate reference genes for qPCR analyses of placental expression of SLC7A3 and induction of SLC5A1 in porcine endometrium. *Placenta* (2017) **52**:1–9. doi:10.1016/j.placenta.2017.02.003

57. Steinhauser CB, Landers M, Myatt L, Burghardt RC, Vallet JL, Bazer FW, et al. Fructose synthesis and transport at the uterine-placental interface of pigs: cell-specific localization of SLC2A5, SLC2A8, and components of the polyol pathway. *Biol Reprod* (2016) **95**:108. doi:10.1095/biolreprod.116.142174

58. Kramer AC, Steinhauser CB, Gao H, Seo H, McLendon BA, Burghardt RC, et al. Steroids regulate SLC2A1 and SLC2A3 to deliver glucose into trophectoderm for metabolism via glycolysis. *Endocrinology* (2020) **161**(8):bqaa098. doi:10.1210/endocr/bqaa098

59. Wang X, Li D, Wu G, Bazer FW. Functional roles of fructose: crosstalk between O-linked glycosylation and phosphorylation of akt-TSC2-MTOR cell signaling cascade in ovine trophectoderm cells. *Biol Reprod* (2016) **95**(5):102. doi:10.1095/biolreprod.116.142281

60. Gao H, Wu G, Spencer TE, Johnson GA, Li X, Bazer FW. Select nutrients in the ovine uterine lumen: I. Amino acids, glucose and ions in uterine lumenal fluid of cyclic and pregnant ewes. *Biol Reprod* (2009) **80**:86–93. doi:10.1095/biolreprod.108.071597

61. Krause N, Wegner A. Fructose metabolism in cancer. *Cells* (2020) **9**:2635. doi:10.3390/cells9122635

62. Fraser JR, Laurent TC, Laurent UB. Hyaluronan: its nature, distribution, functions and turnover. *J Intern Med* (1997) **242**:27–33. doi:10.1046/j.1365-2796.1997.00170.x

63. Stern R, editor. *Hyaluronan in cancer biology*. 1st ed. San Diego, CA: Academic Press/Elsevier (2009).

64. Akella NM, Ciraku L, Reginato MJ. Fueling the fire: emerging role of the hexosamine biosynthetic pathway in cancer. *BMC Biol* (2019) **17**:52. doi:10.1186/s12915-019-0671-3

65. Itano N, Atsumi F, Sawai T, Yamada Y, Miyaishi O, Senga T, et al. Abnormal accumulation of hyaluronan matrix diminishes contact inhibition of cell growth and promotes cell migration. *Proc Natl Acad Sci* (2002) **99**:3609–14. doi:10.1073/pnas.052026799

66. Castellucci M, Kosanke G, Verdenelli F, Huppertz B, Kaufmann P. Villous sprouting: fundamental mechanisms of human placental development. *Hum Reprod Update* (2000) **6**:485–94. doi:10.1093/humupd/6.5.485

67. Higuchi O, Okabe M, Yoshida T, Fathy M, Saito S, Miyawaki T, et al. Stemness of human Wharton's jelly mesenchymal cells is maintained by floating cultivation. *Cell Reprogramming* (2012) **14**:448–55. doi:10.1089/cell.2012.0020

68. West DC, Hampson IN, Arnold F, Kumar S. Angiogenesis induced by degradation products of hyaluronic acid. *Science* (1985) **228**:1324–6. doi:10.1126/science.2408340

69. Vallet JL, Miles JR, Freking BA. Effect of fetal size on fetal placental hyaluronan and hyaluronoglucosaminidases throughout gestation in the pig. *Anim Reprod Sci* (2010) **118**:297–309. doi:10.1016/j.anireprosci.2009.06.019

70. Johnson GA, Bazer FW, Burghardt RC, Wu G, Burghardt RC, Seo H, et al. Cellular events during ovine implantation and impact for gestation. *Anim Reprod* (2018) **15**:843–55. doi:10.21451/1984-3143-ar2018-0014

71. Bazer FW, Johnson GA. Pig blastocyst-uterine interactions. *Differentiation* (2014) **87**:52–65. doi:10.1016/j.diff.2013.11.005

72. Kwon H, Spencer TE, Bazer FW, Wu G. Developmental changes of amino acids in ovine fetal fluids. *Biol Reprod* (2003) **68**:1813–20. doi:10.1095/biolreprod.102.012971

73. Seo H, Johnson GA, Bazer FW, Wu G, McLendon BA, Kramer AC. Cell-specific expression of enzymes for serine biosynthesis and glutaminolysis in farm animals. *Adv Exp Med Biol* (2021) **1285**:17–28. doi:10.1007/978-3-030-54462-1_2

74. Pietzke M, Meiser J, Vazquez A. Formate metabolism in health and disease. *Mol Metab* (2020) **33**:23–37. doi:10.1016/j.molmet.2019.05.012

75. Yang M, Vousden KH. Serine and one-carbon metabolism in cancer. *Nat Rev Cancer* (2016) **16**:650–62. doi:10.1038/nrc.2016.81

76. Field MS, Kamynina E, Stover PJ. MTHFD1 regulates nuclear *de novo* thymidylate biosynthesis and genome stability. *Biochimie* (2016) **126**:27–30. doi:10.1016/j.biochi.2016.02.001

77. Anderson OS, Sant KE, Dolinoy DC. Nutrition and epigenetics: an interplay of dietary methyl donors, one-carbon metabolism and DNA methylation. *The J Nutr Biochem* (2012) **23**:853–9. doi:10.1016/j.jnutbio.2012.03.003

78. Ye J, Fan J, Venneti S, Wan YW, Pawel BR, Zhang J, et al. Serine catabolism regulates mitochondrial redox control during hypoxia. *Cancer Discov* (2014) **4**:1406–17. doi:10.1158/2159-8290.cd-14-0250

79. Pongnopparat T, Tingley G, Gao Y, Brosnan JT, Brosnan ME, Christian SL. Oncogenic ras expression increases cellular formate production. *Amino Acids* (2021) **53**:1589–95. doi:10.1007/s00726-021-03078-5

80. Moses RM, Stenhouse C, Halloran KM, Sah N, Newton MG, Hoskins EC, et al. Metabolic pathways of glucose and fructose: II Spatiotemporal expression of genes involved in synthesis and transport of lactate in ovine conceptuses†. *Biol Reprod* (2024) **111**:159–73. (In Press). doi:10.1093/biolre/ioae047

81. Offermanns S, Colleti LTW, Semple G, Wise A, Ijerman A. International union of basic and clinical pharamcology. LXXXII: nomenclature and classification of hydroxy-carboxilic receptors (GPR81, GPR109A, and GPR109B). *Pharmacol Rev* (2011) **63**:269–90. doi:10.1124/pr.110.003301

82. Payen VL, Mina E, Van Hee VF, Porporato PE, Sonveaux P. Monocarboxylic transporters in cancer. *Mol Metab* (2019) **10**:1016. doi:10.1016/j.molmet.2019.07.006

83. Dillon EL, Knabe DA, Wu G. Lactate inhibits citrulline and arginine synthesis from proline in pig enterocytes. *Am J Physiology-Gastrointestinal Liver Physiol* (1999) **276**:G1079–1086. doi:10.1152/ajpgi.1999.276.5.g1079

84. Brooks GA. Lactate as a fulcrum of metabolism. *Redox Biol* (2020) **35**:101454. doi:10.1016/j.redox.2020.101454

85. Certo M, Marone G, de Paulis A, Mauro C, Pucino V. Lactate: fueling the fire starter. *Wiley Interdisciplinary Reviews Syst Biol Med* (2020) **12**:e1474. doi:10.1002/wsbm.1474

86. Sun H, Zhang D, Yao Z, Lin X, Liu J, Gu Q, et al. Anti-angiogenic treatment promotes triple-negative breast cancer invasion via vasculogenic mimicry. *Cancer Biol & Ther* (2017) **18**:205–13. doi:10.1080/15384047.2017.1294288

87. Lee DC, Sohn HA, Park ZY, Oh S, Kang YK, Lee KM, et al. A lactate-induced response to hypoxia. *Cell* (2015) **161**:595–609. doi:10.1016/j.cell.2015.03.011

88. Courtnay R, Ngo DC, Malik N, Ververis K, Tortorella SM, Karagiannis TC. Cancer metabolism and the Warburg effect: the role of HIF-1 and PI3K. *Mol Biol Rep* (2015) **42**:841–51. doi:10.1007/s11033-015-3858-x

89. Song G, Kim J, Bazer FW, Spencer TE. Progesterone and interferon tau regulate hypoxia-inducible factors in the endometrium of the ovine uterus. *Endocrinology* (2008) **149**:1926–34. doi:10.1210/en.2007-1530

90. Daikoku T, Matsumoto H, Gupta RA, Das SK, Gassmann M, DuBois RN, et al. Expression of hypoxia-inducible factors in the peri-implantation mouse uterus is regulated in a cell-specific and ovarian steroid hormone-dependent manner. *J Biol Chem* (2003) **278**:7683–91. doi:10.1074/jbc.m211390200

91. Lee Y, Shin K, Park S, Park K, Park S, Heo K, et al. G-protein-coupled receptor 81 promotes a malignant phenotype in breast cancer through angiogenic factor secretion. *Oncotarget* (2016) **7**:70898–911. doi:10.18632/oncotarget.12286

92. Brown TP, Ganapathy V. Lactate/GPR81 signaling and proton motive force in cancer: role in angiogenesis, immune escape, nutrition, and Warburg phenomenon. *Pharmacol & Ther* (2020) **206**:107451. doi:10.1016/j.pharmthera.2019.107451

93. Longhitano L, Vicario N, Tibullo D, Giallongo C, Broggi G, Caltabiano R, et al. Lactate induces the expressions of MCT1 and HCAR1 to promote tumor growth and progression in glioblastoma. *Front Oncol* (2022) **12**:871798. doi:10.3389/fonc.2022.871798

94. Liu C, Wu J, Zhu J, Kuei C, Yu J, Shelton J, et al. Lactate inhibits lipolysis in fat cells through activation of an orphan G-protein-coupled receptor, GPR81. *J Biol Chem* (2009) **284**:2811–22. doi:10.1074/jbc.m806409200

95. Gardner DK. Lactate production by the mammalian blastocyst: manipulating the microenvironment for uterine implantation and invasion? *BioEssays* (2015) **37**:364–71. doi:10.1002/bies.201400155

96. Gurner KH, Evans J, Hutchison JC, Harvey AJ, Gardner DK. A microenvironment of high lactate and low pH created by the blastocyst promotes endometrial receptivity and implantation. *Reprod BioMedicine Online* (2022) **44**:14–26. doi:10.1016/j.rbmo.2021.09.012

97. Ma LN, Huang XB, Muyayalo KP, Mor G, Liao AH. Lactic acid: a novel signaling molecule in early pregnancy. *Front Immunol* (2020) **11**:279. doi:10.3389/fimmu.2020.00279

98. Comline RS, Silver M. The composition of foetal and maternal blood during parturition in the Ewe. *The J Physiol* (1972) **222**:233–56. doi:10.1113/jphysiol.1972.sp009795

99. Thompson JGE, Simpson AC, Pugh PA, Donnelly PE, Tervit HR. Effect of oxygen concentration on *in-vitro* development of preimplantation sheep and cattle embryos. *Reproduction* (1990) **89**:573–8. doi:10.1530/jrf.0.0890573

100. Fischer B, Bavister BD. Oxygen tension in the oviduct and uterus of rhesus monkeys, hamsters and rabbits. *Reproduction* (1993) **99**:673–9. doi:10.1530/jrf.0.0990673

101. Barry JS, Anthony RV. The pregnant sheep as a model for human pregnancy. *Theriogenology* (2008) **69**:55–67. doi:10.1016/j.theriogenology.2007.09.021

102. Kaser DJ, Bogale B, Sarda V, Farland LV, Williams PL, Racowsky C. Randomized controlled trial of low (5%) versus ultralow (2%) oxygen for extended culture using bipronucleate and tripronucleate human preimplantation embryos. *Fertil Sterility* (2018) **109**:1030–7.e2. doi:10.1016/j.fertnstert.2018.02.119

103. Becker DE, Ullrey DE, Terrill SW, Notzold RA. Failure of the newborn pig to utilize dietary sucrose. *Science* (1954) **120**:345–6. doi:10.1126/science.120.3113.345.b

104. Aherne FX, Hays VW, Ewan RC, Speer VC. Absorption and utilization of sugars by the baby pigs. *J Anim Sci* (1969) **29**:444–50. doi:10.2527/jas1969.293444x

105. Rosenfeld CR, Morriss FH, Makowski EL, Meschia G, Battaglia FC. Circulatory changes in the reproductive tissues of ewes during pregnancy. *Gynecol Invest* (1974) **5**:252–68. doi:10.1159/000301658

106. Li Z, Wang Q, Huang X, Yang M, Zhou S, Li Z, et al. Lactate in the tumor microenvironment: a rising star for targeted tumor therapy. *Front Nutr* (2023) **10**:1113739. doi:10.3389/fnut.2023.1113739

107. Steele NC, Frobish LT, Miller LR, Young EP. Certain aspects on the utilization of carbohydrates by the neonatal pig. *J Anim Sci* (1971) **33**:983–6. doi:10.2527/jas1971.335983x

EBM Experimental Biology and Medicine

TYPE Original Research
PUBLISHED 02 September 2024
DOI 10.3389/ebm.2024.10048

OPEN ACCESS

*CORRESPONDENCE
Demissew Shenegelegn Mern,
demissew.shenegelegn@i-med.ac.at

RECEIVED 09 November 2023
ACCEPTED 22 August 2024
PUBLISHED 02 September 2024

CITATION
Mern DS and Thomé C (2024) Collagen II enrichment through scAAV6-RNAi-mediated inhibition of matrix-metalloproteinases 3 and 13 in degenerative nucleus-pulposus cells degenerative disc disease and biological treatment strategies.
Exp. Biol. Med. 249:10048.
doi: 10.3389/ebm.2024.10048

Collagen II enrichment through scAAV6-RNAi-mediated inhibition of matrix-metalloproteinases 3 and 13 in degenerative nucleus-pulposus cells degenerative disc disease and biological treatment strategies

Demissew Shenegelegn Mern* and Claudius Thomé

Department of Neurosurgery, Medical University of Innsbruck, Innsbruck, Austria

Abstract

Intervertebral disc (IVD) degeneration damaging the extracellular matrix (ECM) of IVDs is the main cause of spine-associated disorders. Degenerative disc disease (DDD) is a multifaceted disorder, where environmental factors, inflammatory cytokines and catabolic enzymes act together. DDD starts typically due to imbalance between ECM biosynthesis and degradation within IVDs, especially through unbalanced degradation of aggrecan and collagen II in nucleus pulposus (NP). Current treatment approaches are primarily based on conservative or surgical therapies, which are insufficient for biological regeneration. The disintegrins and metalloproteinases with thrombospondin motifs (ADAMTSs) and matrix metalloproteinases (MMPs) are the key proteolytic enzymes for degradation of aggrecan and collagens. Previously, high expression levels of ADAMTS4, ADAMTS5, MMP3 and MMP13, which are accompanied with low levels of aggrecan and collagen II, were demonstrated in degenerative human NP cells. Moreover, self-complementary adeno-associated virus type 6 (scAAV6) mediated inhibitions of ADAMTS4 and ADAMTS5 by RNA-interference (RNAi) could specifically enhance aggrecan level. Thus, MMPs are apparently the main degrading enzymes of collagen II in NP. Furthermore, scAAV6-mediated inhibitions of MMP3 and MMP13 have not yet been investigated. Therefore, we attempted to enhance the level of collagen II in degenerative NP cells by scAAV6-RNAi-mediated inhibitions of MMP3 and MMP13. MRI was used to determine preoperative grading of IVD degeneration in patients. After isolation and culturing of NP cells, cells were transduced with scAAV6-shRNAs targeting MMP3 or MMP13; and analysed by fluorescence microscopy, FACS, MTT assay, RT-qPCR, ELISA and western blotting. scAAV6-shRNRs have no impact on cell viability and proliferation, despite high transduction efficiencies (98.6%) and transduction units (1383 TU/Cell).

Combined knockdown of MMP3 (92.8%) and MMP13 (90.9%) resulted in highest enhancement of collagen II (143.2%), whereby treatment effects were significant over 56 days ($p < 0.001$). Conclusively, scAAV6-RNAi-mediated inhibitions of MMP3 and MMP13 help to progress less immunogenic and enduring biological treatments in DDD.

KEYWORDS

intervertebral disc, collagen II degradation in nucleus pulposus, degenerative disc disease, knockdown of MMP3 and MMP13 using scAAV6-RNAi technology, biological regeneration of intervertebral disc

Impact statement

Degenerative disc disease (DDD) is a common degenerative disorder that starts primarily within the NP. Collagen II, along with aggrecan, is the main and critical ECM components of NP. So far, there are no effective biological treatment strategies available to target the pathological processes of DDD. Current conservative or surgical treatment options, which merely focus on symptomatic interventions, are insufficient for biological restoration of degenerative ECM. Herein we could significantly enhance the level of collagen II in degenerative human NP cells using AAV6-RNAi-mediated inhibitions of MMP3 and MMP13, which are the key degrading enzymes of collagen II in NP. This anti-catabolic biological treatment approach could have a crucial role in suppression of NP degradation and preservation of the ECM. Hence, AAV6-RNAi-mediated inhibitions of MMP3 and MMP13 along with inhibitions of ADAMTS4 and ADAMTS5 enhancing collagen II and aggrecan, could be promising long-term strategies for less immunogenic biological treatments in DDD.

Introduction

Intervertebral discs (IVDs) contribute to essential functions in terms of load resistance and spinal flexibility. They provide flexibility to the spinal column and resist spinal compression by facilitating uniform load spreading on the vertebral bodies; and act as shock absorber for the spine. IVDs are located between adjacent vertebrae in the spinal column and are composed of three distinct regions. They include the centrally localised nucleus pulposus (NP), the peripherally localised anulus fibrosus (AF) and the cranially and caudally localised cartilaginous endplates (CEP). The highly hydrated NP region of a normal IVD contains dominantly proteoglycan and collagen II, which are considered critical to NP homeostasis. The most abundant proteoglycan in NP is aggrecan, which is responsible for the high water content within the NP. Collage II is crucial in forming a network that holds aggrecan and water together. In addition to collagen II, NP contains to a lesser extent, among other collagen types, also collagen XI, which is vital for the assembly of collagen II fibrils. The fibrocartilage AF region of the normal IVD contains primarily the radially aligned collagen I fibrils and considerably less proteoglycan and collagen II. AF contains to a minor degree, among others collagen types, also collagen XI, which forms crosslinks between the adjacent collagen I fibrils. Collagen I and II constitute about 80% of all collagen types in normal IVDs, whereas under physiological conditions collagen II contains more water than collagen I. The relative proportions of collagen I and collagen II vary incrementally and inversely within an IVD; with almost exclusively collagen I at the outermost layers of the AF and almost exclusively collagen II at the innermost layers near to the NP. The collagen fibrils have an alternating pattern and the thickness of their collagen lamellae varies from 200 to 400 μm, which ascends from innermost layers to outermost layers of the AF. The alternating pattern of collagen fibrils in the AF is designed to resist loading forces exerted on the IVDs and tensile forces encountered during twisting and bending. The compressive loading and the swelling of the hydrated NP can be resisted radially by the collagen fibrils of the AF and axially by the vertebral endplates [1–7]. Degeneration of IVDs in humans, especially lumbar disc degeneration, starts sooner in lifetime than degeneration of other connective tissues. During the progression of IVD degeneration the structural integrity and the load-bearing ability decreases gradually, while the dynamic load transfer to adjacent vertebral bodies increases permanently. Thereby damages in the endplates and trabecular bones can occur, and formation of osteophytes can emerge. Moreover, persistent and increasing loading exerted on the facet complex may cause accelerated arthrosis and neural impingement [3, 4]. Lack of structural integrity in the lamellae of the AF (degenerative fissures) can lead to herniation of the NP and cause disc associated pain in some patients. Degeneration of IVDs that results in painful arthritis, disc herniation or spinal stenosis is referred to as degenerative disc disease (DDD).

DDD is one of the most common musculoskeletal disorders and a critical contributor to chronic back pain. It substantially affects the quality of life in terms of disability, social isolation and huge medication costs [8–14]. However, current treatment options are based on either conservative therapies or surgical methods, which can remove only the symptomatic tissue and reconstruct the segment through surgical fusion or disc arthroplasty [15–18]. They do not address the essential

biological restoration of the disc tissues. Therefore, options of biological therapies that can restore or regenerate the damaged IVDs are crucial.

Accelerated DDD involving loss of structural integrity can be caused by different factors, especially by genetic predisposition and environmental influences that lead to imbalanced anabolism and catabolism within IVDs. These include, such as early cellular senescence, decreased ECM production, increased expression of inflammatory cytokines and enhanced activities of degradative enzymes within the avascular IVDs. Cells within IVDs generally acquire nutrients via diffusion through capillaries of CEPs and survive in the oxygen deprived slightly acidic environment. However, with aging the narrowing of the blood vessels near the disc-bone junction of the vertebral body or calcification of the CEPs affect the diffusion of nutrients, and promote more stressful acidic microenvironment within the IVDs. This nutritional deprivation may turn the balance toward accelerated IVD degeneration through early cellular senescence, attenuated ECM formation (anabolism) and increased ECM degradation (catabolism) [19–30].

NP cells play a key role in IVD homeostasis by orchestrating the expressions and activities of anabolic, catabolic, anti-catabolic and inflammatory factors. The degree of imbalances between ECM formation and ECM degradation is highly correlated with the grade of IVD degeneration. High-grade degeneration leading to diminished level of aggrecan and collagen II crucially deteriorate the proper function of IVDs, particularly within the NP. Deregulations of the normal homeostatic mechanism have been repeatedly shown in degenerative NP cells. These involve increased accumulation of selective inflammatory factors (such as TNF-α and IL-1β) and catabolic factors (such as ADAMTSs and MMPs), along with low levels of their natural inhibitors (such as TIMPs) and anabolic factors (such as BMPs, TGF- β and IGF-1) [31–33]. High expression levels ADAMTS4 and ADAMTS5 together with high expression levels of MMP3 and MMP13, which were allied with low levels of aggrecan and collagen II, have been shown in our previous studies of degenerative NP cells [31, 32]. Furthermore, we recently demonstrated that scAAV6-mediated specific inhibition of ADAMTS4 and ADAMTS5 by RNA-interference (RNAi) could enhance the level of aggrecan, without affecting the level of collagen II [34–36]. These findings suggest that MMPs are evidently the main degrading enzymes of collagen II in NP. Therefore, in this study we investigated scAAV6-mediated specific knockdown of MMP3 and MMP13 in degenerative NP cells. Suppression of MMP3 and MMP13 using RNAi-mechanism leading to enhancement of collage II level, without any impact on the level of aggrecan, would be one of the significant therapeutic approaches for inhibition of DDD. Accordingly, developing combinatorial therapeutic strategies, which are able to suppress the designated ADAMTSs and MMPs in NP cells, are crucial for biological restoration of degenerative IVDs.

TABLE 1 IVD samples recruited from sixteen patients showing lumbar disc levels and lumbar disc degeneration grade (DDG) with age and sex.

Sample	Disc level	DDG	Age/Sex
1	L4/L5	IV	40/F
2	L4/L5	IV	42/F
3	L4/L5	IV	43/M
4	L5/S1	IV	46/M
5	L5/S1	IV	48/M
6	L4/L5	IV	50/F
7	L4/L5	IV	52/F
8	L5/S1	IV	55/M
9	L5/S1	IV	58/F
10	L4/L5	IV	59/M
11	L5/S1	IV	60/M
12	L5/S1	IV	63/F
13	L4/L5	IV	64/M
14	L5/S1	IV	65/F
15	L5/S1	IV	66/F
16	L4/L5	IV	69/M

Materials and methods

Ethical considerations in recruiting samples from patients

The local research ethics committee authorized this experimental study (Medical University of Innsbruck: project AN2014-0027 333/4.24). IVD tissues were recruited from patients during lumbar disc surgery. Patients provided their written informed consent to participate in this study. The inclusion criteria for surgery were lumbar disc herniation with nerve root compression detected on MRI, which correlated to primary symptoms that remained unresponsive to non-operative treatment for 6 weeks, or demonstrated progressive neurological deterioration in the face of conservative treatment. Samples from sixteen lumbar discs of sixteen patients, which showed Pfirman disc degeneration grade IV (DDG IV) on MRI, were included in this study [37, 38]. The samples recruited from the sixteen patients are presented in Table 1 (age range: 40–69 years, mean age: 55 years). To determine the DDG of patients, preoperative T2-weighted MRI of the spine was applied. An example of the samples showing a herniated lumbar IVD of DDG IV with nerve root compression is illustrated by using T2-weighted MRI in Figure 1. Lumbar IVD tissues were recruited from the NP sector by nucleotomy and swiftly brought to the

FIGURE 1
T2-weighted MRI image representing the herniated IVDs of DDG IV. T2-weighted MRI image demonstrating a herniated lumbar IVD (L5/S1) of disc degeneration grade IV (DDG IV) with nerve root compression that remained unresponsive to non-operative treatment for 6 weeks. Sixteen patients harboring a herniated lumbar IVD of DDG IV were involved in this study (age range: 40–69 years, mean age: 55 years). The MRI based interobserver reliability agreement for rating of DDG was ascertained with 100% frequency of agreement (κ = 1.00).

laboratory in sterile phosphate buffered saline solution (PBS) for immediate cell isolation.

NP cell isolation and monolayer expansion

IVD tissues that were recruited from patients were immediately brought to the laboratory in PBS and washed at 1,000×g for 2 min. The NP tissues of the IVDs were separated from the AF residual based on their macroscopic morphology (identification of the innermost lamellar rings of the AF). The isolated NP tissues were finely chopped up into small fragments and digested with pronase (0.02% w/v, 37°C, 5% CO_2, 1 h) in 20 mL DMEM (Dulbecco's Modified Eagle's Medium) culture medium, which contained 1% penicillin/streptomycin, 1% glucose and 10% FBS (fetal bovin serum) (Sigma-Aldrich). The samples were then filtered through sterile 75 gm nylon mesh filters (Sigma-Aldrich). The supernatants were centrifuged at 1,000×g for 2 min. Pellets were suspended in 20 mL DMEM and redigested with collagenase II (0.02% w/v) and hyaluronidase (100U) (Sigma-Aldrich) for 180 min (37°C, 5% CO_2). The redigested samples were filtered through sterile 75 gm nylon mesh filters and supernatants were centrifuged at 1,000×g for 2 min. The pellets were resuspended in DMEM culture medium of 10 mL and cultured in 25-cm^2 tissue culture flask (Sigma-Aldrich) for 2 weeks (37°C, 5% CO_2) by changing the culture medium every 2 days. Proliferated NP cells at the confluent of 100% were split in a ratio of 1:2 using trypsin-EDTA (Sigma-Aldrich) for monolayer cell expansion. Expanded NP cells were cryopreserved at −196°C in DMEM culture medium, which contained 30% FBS and 15% dimethyl sulfoxide (DMSO) (Sigma-Aldrich). Cryopreserved NP cells are made available for three-dimensional (3D) cell culture and subsequent analyses.

Alginate based 3D-culture of NP cells

The Alginate-3D-Cell-Culture Kit (AMSBIO) was used based on the instruction guide of the manufacturer (AMS Biotechnology). Briefly, calcium chloride solution (5 mL) was dispensed in a 10-mL sterile glass cup that contained a sterile stir bar. NP cell pellets were prepared from 1×10^5 scAAV6-transduced or non-transduced (untreated) cells in 1.5-mL Eppendorf-tube by harvesting the cells using trypsin-EDTA after 3 days of transduction. Sodium alginate solution (0.5 mL) was then dispensed into each 1.5-mL tube containing the pellet and mixed with a pipette to make a homogeneous cell suspension. The homogeneous cell suspension in each tube was aspirated into a 1-mL syringe that was attached with a plastic flexible needle. In order to drop the cell suspension into the glass cup containing the calcium chloride solution, the plastic flexible needle was removed and a 22G hypodermic needle was attached to the syringe. The cell suspension was dropped into the stirring calcium chloride solution (5 mL) at about two drops per second by holding the syringe in an upright position over the glass cup, and by positioning the tip of the needle about 5 cm above the liquid surface of calcium chloride. Subsequently the beads in calcium chloride solution were stirred about for 10 min until the alginate beads have coagulated and appeared completely white. The calcium chloride solution was removed using a manual pipette without aspirating the beads and then saline solution (10 mL) was added to the beads. The saline solution was removed after 15 min using a manual pipette, the beads were mixed with culture medium (10 mL) and incubated at room temperature (RT) for 10 min. Right after removing the medium, 10 alginate beads were scooped using a sterile spatula and placed

into a separate 24-well plate containing culture medium (2 mL). Cells were cultured in 24-well plates up to 56 days of post-transduction (37°C, 5% CO_2) by changing the culture medium every 2 days. Three independent 3D-cultures of NP cells were performed for each sample.

Recovery of NP cells from alginate beads

After 3D-culture of the NP cells in alginate, the culture medium was removed from each well using a manual pipette. The alginate beads embedding the NP cells were then dissolved by adding sodium citrate solution (1 mL) to each well and mixing for 10 min at RT. The entire mixtures in a 24-well plate were transferred to a 50-mL tube and centrifuged at 1,000×g for 2 min. NP cells were harvested as a precipitated pellet and used for subsequent experimental steps.

Recombinant scAAV6 vector construction

The shuttle plasmid of this study was assembled based on the shuttle scAAV (self-complementary adeno-associated virus) plasmid described before [39, 40]. It contains the expression cassettes of *emerald green fluorescent protein* (emGFP), the shRNA along with the human cytomegalovirus (CMV) promoter and the U6 promoter (a polymerase III promoter). The BLOCK-iT™ RNAi Designer (ThermoFisher) was used to design the shRNAs targeting the mRNAs of MMP3 or MMP13. The corresponding shRNAs were cloned between *BamHI* and *HindIII* restriction sites of the shuttle plasmid. The recombinant shuttle plasmids encoding the shRNAs are termed as plasmid AAV6-MMP3 and plasmid AAV6-MMP13 respectively. The non-target control shRNA is termed as plasmid AAV6-Ctrl. The AAV6 helper plasmid DP6rs was acquired from PlasmidFactory GmbH & Co. KG (Bielefeld, Germany).

The sense sequences of the shRNAs targeting MMP3, targeting MMP13 and the non-target control shRNA are shown below, respectively.

5′- AATGGAGATGCCCACTTTGATTTCAAGAGAATC AAAGTGGGCATCTCCATTTTTTT-3′

5′- AAGACTTCCCAGGAATTGGTGTTCAAGAGACAC CAATTCCTGGGAAGTCTTTTTTT-3′

5′- AATCTTACCGAGCATGACGTTTTCAAGAGAAAC GTCATGCTCGGTAAGATATTTTT-3‘

Production and purification of the recombinant scAAV6 vectors

For the production of the recombinant scAAV6 vectors the human embryonic kidney 293 (HEK293) cells were grown in DMEM containing 1% penicillin/streptomycin, 4.5% glucose and 10% FCS. Prior to transfection the cells were passaged two times at confluent of 90%. 5×10^6 HEK293 cells were cultured in 15-cm culture dish containing 20 mL culture medium until they reached 70–80% confluent. Initially, 96 µg of the helper plasmid (DP6rs) was mixed separately with a 30 µg of the individual shuttle plasmid AAV6-MMP3 or AAV6-MMP13 or AAV6-Ctrl to prepare the transduction medium. Then each mixture of the individual shuttle plasmid was added to a 2.5 mL of 300 mM calcium phosphate (Sigma-Aldrich) and gently mixed with an additional 2.5 mL of two-fold concentrated HEPES Buffered Saline (2 × HBS) (Sigma-Aldrich). After removing the culture medium from the culture dish and the transduction medium was directly pipetted to the culture dish. After incubation (6 h, 37°C, 5% CO_2) the transduction medium was replaced by the culture medium containing 2% FCS. At 72 h of transduction the culture medium was collected, cell pellet was harvested by trypsinization and both together were centrifuged for 5 min at 2000xg. The pellet after centrifugation was suspended in a 2.5 mL serum-free DMEM and the sample was subjected to eight rounds of freeze/thaw cycles by alternating the tube between dry ice-ethanol bath and 37°C water bath. The supernatant containing the recombinant scAAV6 vector was collected by centrifugation at 8000xg (30 min) and stored at −80°C for subsequent purification. The recombinant scAAV6 vectors were then purified as previously described [37]. Shortly, the iodixanol (Sigma-Aldrich) gradient centrifugation was used to purify the recombinant scAAV6 vectors from freeze/thaw-supernatants. Then iodixanol was removed by running the iodixanol fractions through PD10 gel filtration columns (GE Healthcare). Ten fractions of each 1 mL eluate were collected and fractions 4 to 6 were pooled for quantification. The quantitative PCR (qPCR) was used to quantify the purified recombinant scAAV6 vectors: AAV6-MMP3, AAV6-MMP13 and AAV6-Ctrl.

Viral particle quantification of the recombinant scAAV6 vectors

The qPCR was used to quantify the purified recombinant scAAV6 vector particles by using the TaqMan Gene Expression Master Mix (ThermoFisher) and LightCycler 480 (Roche Applied Science). The master mix (1x) supplemented with 200 nM sense and 200 nM antisense primers of 5′-ITR as well as 250 nM ITR-probe and 2 µL of the template DNA was used in the final volume of 20 µL. Hereunder the sequences of the ITR primers and ITR-probe are specified.

5′-ITR-sense: GGAACCCCTAGTGATGGAGTT.

5′-ITR-antisense: CGGCCTCAGTGAGCGAG.

ITR-probe: 6FAM-CACTCCCTCTCTGCGCGCTCG-BHQ1.

As described before [38] the genomic DNA of the shuttle plasmid was used as a standard and three replicates of the standard, negative control and samples were run in 96 well

plate. The applied qPCR program was consisted of an initial denaturation step at 95°C for 10 min followed by 40 cycles with denaturation at 95°C for 15 s and an extension at 60°C for 1 min that included a melt curve stage 65°C–95°C (increment 0.5°C). For the qPCR data analysis, the Applied Biosystems StepOne software v2.1 (Life Technologies) was used and three independent qPCRs were performed for each sample.

Transduction efficiency evaluation of the recombinant scAAV6 vectors

In 24-well plate, 1×10^5 NP cells per well (about 50% confluent) were seeded and cultured for 24 h in 500 µL DMEM containing 1% FCS (37°C, 5% CO_2). The recombinant vectors AAV6-MMP3 or AAV6-MMP13 or AAV6-Ctrl at a dose of 5,000 vector genome copy per seeded cell (5,000 vg/c) were used to transduce the cells. Furthermore, NP cells, which were first transduced with AAV6-MMP3 (5,000 vg/c), were additionally transduced with AAV6-MMP13 (5,000 vg/c) after a day of the first transduction, as a combinatorial transduction (AAV6-MMP3 plus AAV6-MMP13). Using fluorescence microscopy (AxioVert.A, Carl Zeiss) the transduction efficiencies were evaluated every 2 days for the first 16 days and weekly up to 56 days. Flow cytometry-assisted cell sorting (FACS) was also used to evaluate the transduction efficiencies in 3D-cultured cells on day 8, 16, 24, 32, 48, 56 after transduction. MoFlo Cell Sorter (Beckman Coulter) was used for FACS analyses in order to count 1×10^5 cells per sample. The number of GFP-positive cells was quantified according to the manufacturer's protocol. Shortly, the MoFlo Cell Sorter was used with a 100-mm flow cell tip and a flow rate of 12,000 events per second, along with an extension wavelength of 488 nm and a laser power of 110 W. Three independent FACS evaluations with duplicate were performed for each sample.

Transduction units quantification of the recombinant scAAV6 vectors

The number of recombinant scAAV6 vectors internalized into NP cells (transduction units per cell: TU/Cell) was quantified using the qPCR with the 5′-ITR primers and ITR-probe as described above. NP cells were seeded, transduced, 3D cultured and harvested on day 2, 4, 8, 16, 24, 32, 48 and 56 as defined already. Cell pellets were washed three times with PBS to remove the vectors that remained attached to the surface of NP cells. The washed pellets were resuspended in a final volume of 100 µL and subjected to eight rounds of freeze/thaw cycles by alternating the tube between the dry ice-ethanol bath and the 37°C water bath. Following centrifugation at 17,000×g for 5 min, the supernatants were used for titration of the transduction units per cell (TU/Cell) using qPCR. Untreated NP cells and AAV6-Ctrl transduced cells were used as controls, and the shuttle plasmid was used as standard in 10-fold dilutions from 10^6–10^3 copies/µL. Three independent quantifications of TU/Cell were performed for each sample.

Evaluation of NP cell viability and proliferation rate after transduction

The MTT Assay Kit [3-(4, 5-dimethylthiazolyl-2)-2,5-diphenyltetrazolium bromide assay, ThermoFisher] was used to examine the impact of the recombinant scAAV6 vectors on NP cell viability and growth rate. Before transduction as well as on day 2, 4, 8, 16, 24, 32, 48 and 56 after transduction the viability and proliferation rate of transduced and 3D cultured NP cells were quantified. Cells were seeded, transduced, cultured and harvested as described above. The corresponding untreated NP cells and AAV6-Ctrl treated cells were used as controls. After washing the pellets of NP cells two times with PBS, pellets were resuspended in 250 µL culture medium and duplicates of 100 µL were plated into flat-bottomed 96-well plate. Control wells (only with medium alone) were additionally used to provide the blanks for absorbance readings. 10 µL MTT reagent was added to each well after 24 h incubation for recovering (37°C, 5% CO_2), and further incubated for 3 h. After adding 100 µL of the SDS-HCl solution to each well, the samples were further incubated for 4 h. To measure the absorbance of the samples at 570 nm, a microtiter plate reader Infinite 200 (TECAN) was used. The average value of the blank duplicate readings was subtracted from the average values of the sample duplicate readings. A standard curve was used to calculate the number of viable cells. Three independent MTT assays with duplicate were performed for each sample.

Quantification of MMP3 and MMP13 mRNA levels using real-time qRT-PCR

To analyse the impacts of the recombinant scAAV6 vectors (AAV6-MMP3 or AAV6-MMP13 or a combination thereof (AAV6-MMP3 plus pAAV6-MMP13) on the mRNA levels of MMP3 and MMP13, the real-time quantitative reverse transcription PCR (Real-time qRT-PCR) was used. Before transduction as well as on day 2, 4, 8, 16, 24, 32, 48 and 56 after transduction the mRNA levels in transduced and 3D cultured NP cells were quantified. NP cells were seeded, transduced, cultured and harvested as described above. The corresponding untreated NP cells and AAV6-Ctrl treated cells were used as controls. The RNeasy Plus Mini Kit (Qiagen) with DNase I (Sigma-Aldrich) was used to isolate the total RNA without DNA contamination. The amount of total RNA was quantified at 260 nm using a Biospectrometer (Eppendorf). Equal amounts of total RNA were used to perform

reverse transcription (RT), and the TaqMan Reverse Transcription Reagents (ThermoFisher) were used to synthesize the cDNAs. The mRNA levels of MMP3 and MMP13 were quantified by real-time qRT-PCRs using the TaqMan gene expression assays and LightCycler 480 as described above, and β-actin was used as internal standard. The data of relative mRNA levels were numerically presented using the comparative $2^{-\Delta\Delta CT}$ method. Three independent real-time qRT-PCRs with triplicate were performed for each sample. The sense sequences of primers and probes used for the real-time qRT-PCRs are shown below:

MMP3 sense: CTCACTCACAGACCTGACTC
MMP3 antisense: CTCAGAGTGCTGACAGCATC
MMP3 probe: 6FAB-GGCATTCAGTCCCTCTATGG-BHQ1
MMP13 sense: GAATTAAGGAGCATGGCGAC
MMP13 antisense: GTCAAGACCTAAGGAGTGGC
MMP13 probe: 6FAB-GGACAAGTAGTTCCAAAGGC-BHQ1
Beta-actin sense: CAGAAGGACAGCTACGTGGG
Beta-actin antisense: CATGTCGTCCCAGTTGGTCA
Beta-actin probe: 6FAB-GACCCTGAAGTACCCCATCG-BHQ1

Western blot analysis

To investigate the impacts of knockdowns mediated by the recombinant vectors AAV6-MMP3 or AAV6-MMP13 or the combination of both AAV6-MMP3 plus pAAV6-MMP13, the protein expression levels of MMP3, MMP13 and collagen II were evaluated by western blotting. NP cells were seeded, transduced, cultured and harvested on day 8 and 56 as described above. Untreated and AAV6-Ctrl treated NP cells were used as controls. RIPA buffer (radio-immunoprecipitation assay buffer, Sigma-Aldrich, ice-cold) supplemented with protease and phosphatase inhibitors (Sigma-Aldrich) was used for 20 min (4°C) to lyse the harvested NP cells. Lysed cells were centrifuged for 10 min at 14,000×g (4°C) and supernatants containing the total protein were used for western blotting. The concentration of the total protein was determined using BCA Protein Assay Kit (ThermoFisher). Isolated total proteins were separated based on their molecular weight using SDS-PAGE (sodium dodecyl sulfate polyacrylamide gel electrophoresis) and the separated proteins were transferred to polyvinylidene fluoride (PVDF) membrane (ThermoFisher). Anti-MMP3 antibody (ab53015, Abcam), anti-MMP13 antibody (ab39012, Abcam), anti-collagen II antibody (abx013043, Abbexa) and anti-beta-actin antibody (ab8227, Abcam) produced in rabbits were used as primary antibodies. Goat anti-rabbit IgG H&L horseradish peroxidase-conjugated (HRP) secondary antibody (ab205718, Abcam) and Pierce ECL Plus Western Blotting Substrate (32132X3, ThermoFisher) were used to detect interactions between antigens and primary antibodies on the membrane. The detected protein bands were quantitatively compared using ImageJ. Three independent western blot analyses were performed for each sample.

Enzyme-linked immunosorbent assays

To investigate the specificities of the MMP3 and MMP13 knockdowns as well as the enhancement of collagen II that are mediated by AAV6-MMP3 or AAV6MMP-13 or a combination of both AAV6-MMP3 plus AAV6-MMP13, enzyme-linked immunosorbent assay (ELISA) was applied. NP cells were seeded, transduced, cultured and harvested on day 8 and 56 after transduction, and total proteins were isolated and quantified as described above. ELISA was performed for each sample with 100 μg of total protein based on the instruction manuals of the kits (R&D Systems, Uscn Life Science Inc.). Untreated and AAV6-Ctrl treated NP cells were used as controls. Beside the protein levels of MMP3, MMP13 and collagen II, the levels of other vital proteins in NP, such as interleukin-1β (IL-1β) and tumour necrosis factor alpha (TNF-α), ADAMTS4, ADAMTS5 and aggrecan were quantified. To measure the absorbance of the samples, a microplate reader Infinite 200 (TECAN) was used at 450 nm with wavelength correction set to 540 nm. The average values of the blank duplicate readings were subtracted from the average values of the sample duplicate readings. Standard curves were used to calculate the protein concentrations in the samples. Three independent ELISA assays with duplicate were performed for each sample.

Comparative analysis of data

Landis and Koch based interpretations of κ statistics and agreement percentage among two observers were applied to determine the reliability on MRI evaluations of disc degeneration grade [37, 38]. Moreover, the software IBM SPSS Statistics 22 (Armonk, New York, United States) was used for analyses of statistical data. Data of treated and untreated samples were compared by 1-way ANOVA and pairwise comparison. Significance was set at $p < 0.01$. For the relative quantification analyses of the western blot bands the software Image J was used.

Results

MRI evaluation of lumbar disc degeneration grade

The rating of lumbar disc degeneration grade (DDG) based on the T2-weighted MRI, which was carried out by Landis and Koch based interpretations of κ statistics and agreement percentage between two observers, resulted in $\kappa = 1.00$ (frequency of agreement = 100%).

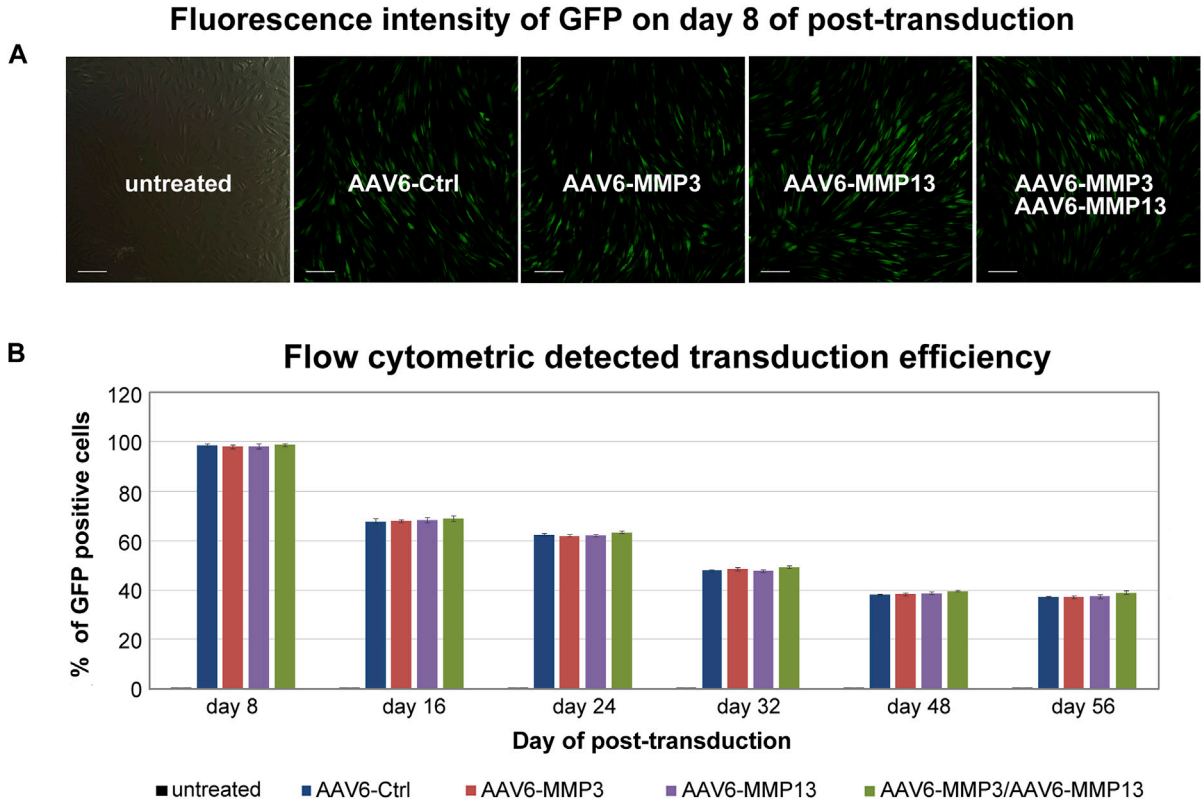

FIGURE 2
Transduction efficiencies determined by fluorescence microscopy and FACS. After culturing of 1×10^5 cells with DMEM (500 µL containing 1% FBS) in 24-well plate, 5,000 vg/c of each GFP packing recombinant scAAV6 vector were used for transduction. The transductions include 5,000 vg/c AAV6-Ctrl (encoding non-targeting control shRNA), 5,000 vg/c AAV6-MMP3 (encoding shRNA targeting MMP3), 5,000 vg/c AAV6-MMP13 (encoding shRNA targeting MMP13) or 5,000 vg/c AAV6-MMP3 plus 5,000 vg/c AAV6-MMP13. Measurement of transduction efficiencies using fluorescence microscopy and FACS showed similar transduction efficiencies for all applied GFP packing vectors ($p \geq 0.315$) **(A)**. Measurement of transduction efficiencies using fluorescence microscopy was performed every 2 days for the first 2 weeks and once a week until 56 days. The highest transduction efficiency was detected on day 8 after transduction **(A)**. For precise measurement of the transduction efficiencies, GFP positive cells were counted using FACS on day 8, 16, 24, 32, 48 and 56 by applying 1×10^5 transduced NP cells per sample to the FACS **(B)**. The data represent mean values with standard deviation of three independent experiments.

qPCR based quantification of recombinant scAAV6 vector genome copy

The recombinant scAAV6 vectors, containing the shRNAs, were produced, purified and quantified as described in the material and method section. 3.5×10^7 HEK293 cells were used for each recombinant vector and using qPCR high final titers (6.4×10^{10}–2.9×10^{11}) of vector genome copies were quantified.

Transduction efficiencies of the recombinant scAAV6 vectors

All recombinant scAAV6 vectors expressing GFP consistently showed similar transduction efficiencies in fluorescence microscopy and in FACS analyses (Figure 2) ($p \geq 0.315$). The highest transduction efficiencies were verified on day 8 after transduction. The highest transduction efficiencies on day 8, as shown by FACS analyses, amounted to the mean values of 98.35% (98,351 ± 837), 97.91% (97,913 ± 790), 98.14% (98,143 ± 994) and 98.61 (98,611 ± 459) for cells transduced with AAV6-Ctrl or AAV6-MMP3 or AAV6-MMP13 or AAV6-MMP3 plus AAV6-MMP13 respectively. Nevertheless, after day 8 of transduction declining numbers of GFP positive cells were persistently detected during the course of 56 days (Figure 2B). At the end of the FACS analyses on day 56, the transduction efficiencies amounted to the mean values of 37.07% (37,072 ± 432), 37.26% (37,261 ± 542), 37.30% (37,301 ± 710) and 38.09% (38,098 ± 732), respectively. For each sample 1×10^5 NP cells (set as 100%) were used for FACS analyses. Age and gender showed no effect.

Evaluation of scAAV6 transduction units and cell proliferation rate

Determining the number of internalized viral copies per cell, also known as transduction units per cell (TU/Cell), is essential to

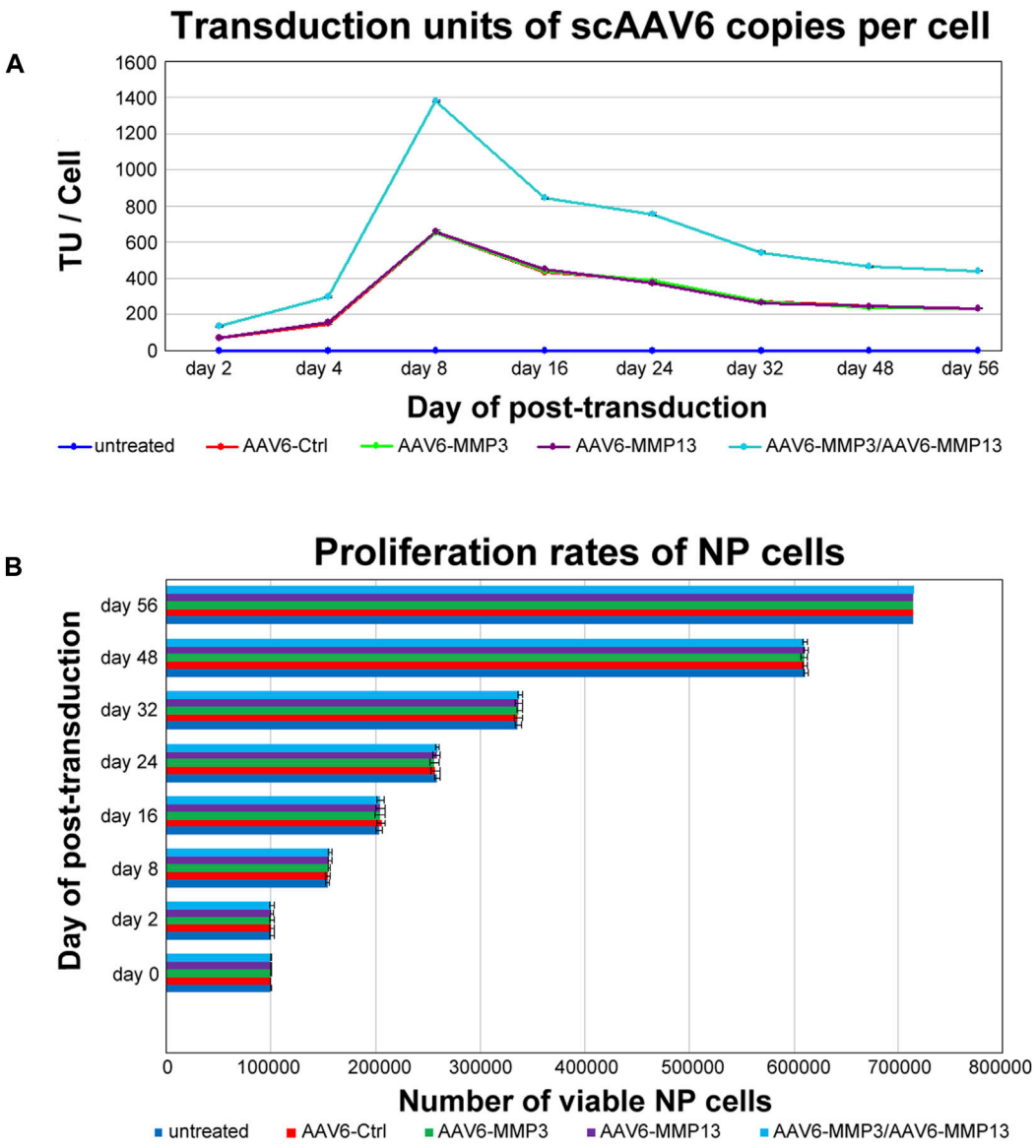

FIGURE 3
Evaluating transduction units and NP cell proliferation rate. After culturing of 1×10^5 NP cells in 24-well plate, cells were transduced either with 5,000 vg/c AAV6-Ctrl (encoding non-targeting control shRNA), 5,000 vg/c AAV6-MMP3 (encoding shRNA targeting MMP3), 5,000 vg/c AAV6-MMP13 (encoding shRNA targeting MMP13) or 5,000 vg/c AAV6-MMP3 plus 5,000 vg/c AAV6-MMP13. qPCR and MTT assay were used to determine the transduction units per cell (TU/Cell) and cell proliferation rates on day 2, 8, 16, 24, 32, 48 and 56. The qPCR analyses showed similar TU/Cell for each single transduction ($p \geq 0.221$), but significantly increased TU/Cell for the successive transduction with AAV6-MMP3 plus AAV6-MMP13 ($p < 0.001$) **(A)**. The MTT assays exhibited similar proliferations rates for all untreated and transduced cells ($p \geq 0.372$) **(B)**. The data represent mean values with standard deviation of three independent experiments.

realize reproducible and practical biological effects, because only a portion of recombinant scAAV6 viral copies, which are attached to the cell surface, are able to get inside the cells. The qPCR was applied to determine the TU/Cell for each recombinant viral vector. The qPCR displayed that transduction with each individual vector constantly reached similar TU/cell ($p \geq 0.221$), and transduction with combined vectors persistently reached augmented TU/Cell ($p < 0.001$). The maximum TU/Cell was detected within 8 days after transduction. On day 8 the mean transduction units of 652 ± 1.70 TU/Cell, 650 ± 5.47 TU/Cell, 656 ± 5.77 TU/Cell, 1,383 ± 2.80 TU/Cell were determined in AAV6-Ctrl, AAV6-MMP3, AAV6-MMP13 or AAV6-MMP3 plus AAV6-MMP13 transduced cells correspondingly. Nevertheless, the TU/Cell was gradually decreasing after day 8 throughout the 56 days of cell culture. On day 56 the TU/Cell was fallen to the mean values of 231 ±

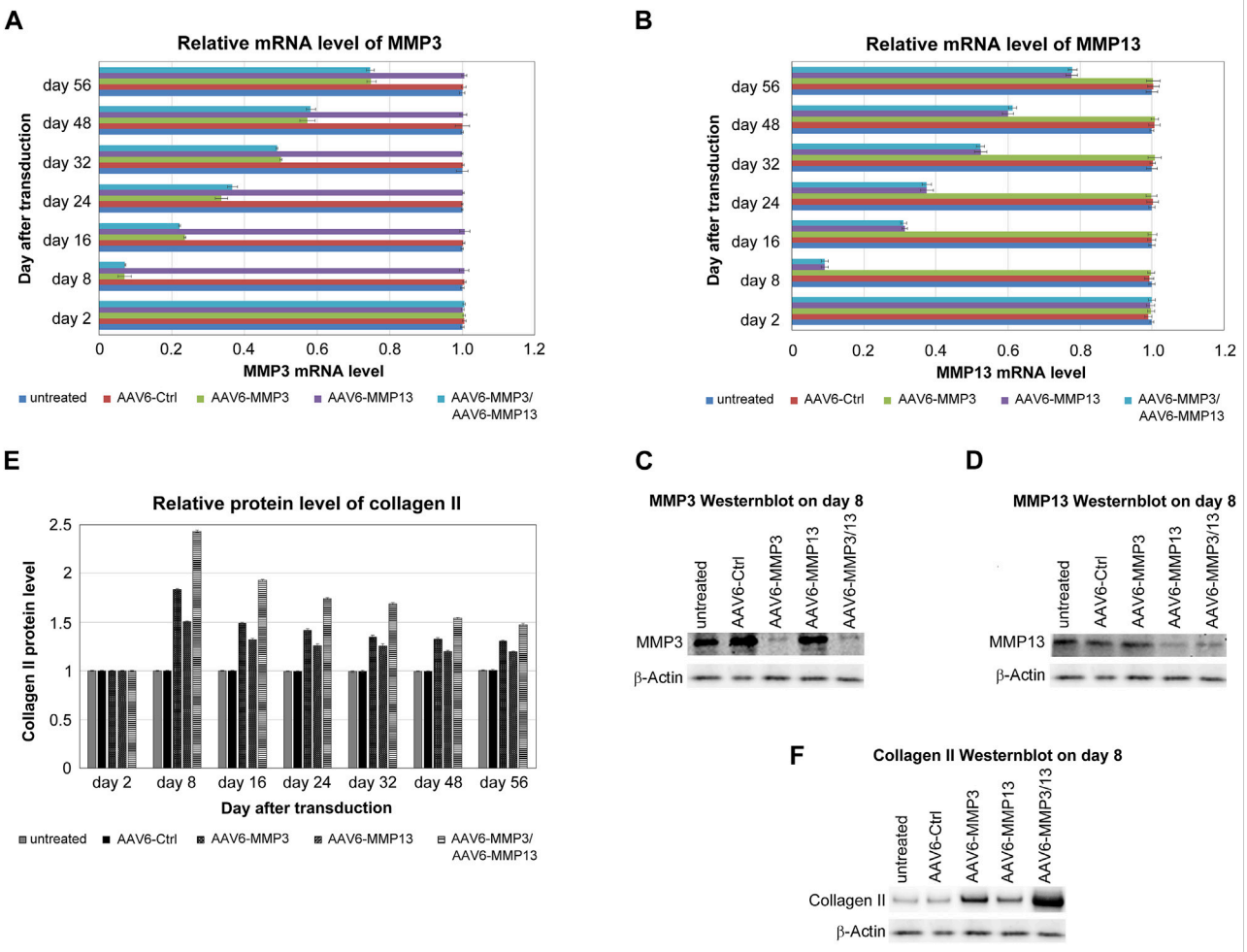

FIGURE 4
Knockdowns of MMP3 and MMP13 associated with collagen II enhancement. For the transduction of 1×10^5 cells either 5,000 vg/c AAV6-Ctrl (encoding non-targeting control shRNA) or 5,000 vg/c AAV6-MMP3 (encoding shRNA targeting MMP3) or 5,000 vg/c AAV6-MMP13 (encoding shRNA targeting MMP13) or a combination thereof (5,000 vg/c AAV6-MMP3 plus 5,000 vg/c AAV6-MMP13) were used. Real-time qRT-PCR and ELISA were performed after harvesting of transduced cells on day 2, 8, 16, 24, 32, 48 and 56, in order to determine the knockdown impacts on MMP3 and MMP13 in related to collagen II enhancement at mRNA and protein level respectively. The relative mRNA levels of MMP3 **(A)** and MMP13 **(B)** as well as the relative protein levels of collagen II **(E)** are depicted. Western blotting was done to show the maximum knockdowns of MMP3 **(C)** and MMP13 **(D)** as well as the maximum enhancement of collagen II **(F)** on day 8 after transduction. The levels in untreated NP cells, which remained unaffected up to 56 days after transduction, represent the arbitrary unit 1.0. The transductions with AAV6-MMP3 or AAV6-MMP13 or a combination thereof depicted efficient and sustainable knockdowns of MMP3 **(A, C)** and MMP13 **(B, D)** ($p < 0.001$), which are associated with the enhancement collagen II level **(E, F)** ($p < 0.001$). The simultaneous knockdown of MMP3 and MMP13 exhibited additional enhancement of collagen II level. Image J analyses of the western blot bands (ratio: Net Protein X/Net Load Ctrl.) showed knockdown effects of 0.11 for MMP3 and 0.13 for MMP13 as well as enhanced expression effects of 1.92, 1,61 and 2.52 for collagen II in AAV6-MMP3 or AAV6-MMP13 or AAV6-MMP3 plus AAV6-MMP13 treated cells respectively ($p < 0.001$). Untreated and AAV6-Ctrl treated NP cells showed unaffected levels of MMP3, MMP13 ($p \geq 0.241$) and collagen II ($p \geq 0.254$). The data represent mean values with standard deviation of three independent experiments.

2.98 TU/Cell, 229 ± 4.50 TU/Cell, 233 ± 3.59 TU/Cell and 439 ± 3.30 TU/Cell correspondingly (Figure 3A). Furthermore, the effects of internalized viral copies on the viability and proliferation rate of NP cells were examined using MTT assays. After seeding of 1×10^5 NP cells in 24-well plate, MTT assays were performed on day 2, 8, 16, 24, 32, 48 and 56 after transduction. Equivalent viabilities and proliferation rates were determined for all transduced and non-transduced cells ($p \geq 0.372$). Moreover, no effect was observed on the morphology of NP cells. These indicate that the internalized viral copies had no any effect on the viability and proliferation rate of NP cells. After 56 days of cell culture, the mean number of viable cells amounted to 715,269 ± 2,552, 714,684 ± 3,303, 715,164 ± 2,762, 714,298 ± 2,664 and 715,592 ± 2,479 for untreated cells and for AAV6-Ctrl, AAV6-MMP3, AAV6-MMP13 or AAV6-MMP3 plus AAV6-MMP13 transduced cells respectively (Figure 3B).

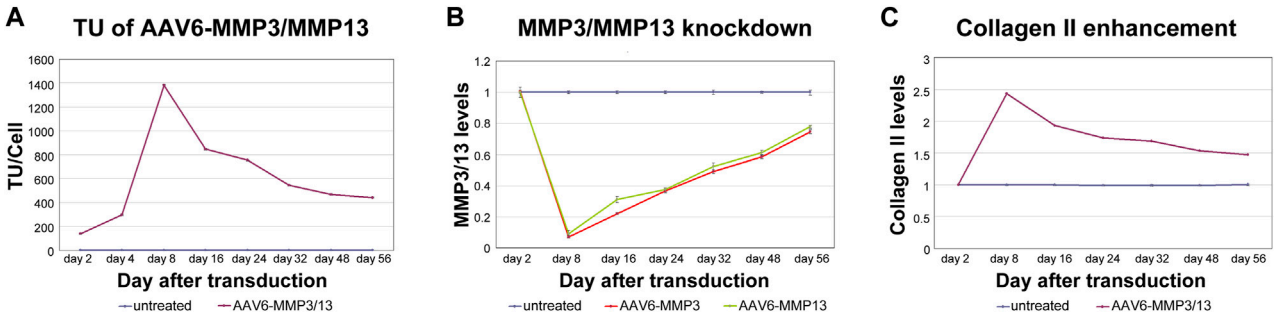

FIGURE 5
Linking between MMP3/MMP13 knockdowns and collagen II enhancement. 5,000 vg/c AAV6-MMP3 and 5,000 vg/c AAV6-MMP13 that encode the shRNAs targeting MMP3 or MMP13 were used to transduce 1×10^5 NP cells. After transduction, the cells were harvested on day 2, 8, 16, 24, 32, 48 and 56. Then the transduction units per cell (TU/Cell), the mRNA levels of MMP3 and MMP13 as well as the protein level of collage II were determined using qPCR, RT-qPCR and ELISA respectively **(A–C)**. A maximum direct correlation between TU/Cell, knockdown impacts on mRNA and enhancement collagen II protein were depicted in successively with AAV6-MMP3/MMP13 transduced cells. There was no any effect in untreated cells and AAV6-Ctrl treated cells regarding knockdown of MMP3 and MMP13 ($p \geq 0.241$) or enhancement of collagen II ($p \geq 0.254$). The levels in untreated cells that remained unaffected up to 56 days represent the arbitrary unit 1.0. The data represent mean values with standard deviation of three independent experiments.

MMP3 and MMP13 knockdown and enhancement of collagen II

The recombinant scAAV6 vectors encoding the shRNAs against MMP3 or MMP13 were functionally tested by using qRT-PCR, western blotting and ELISA. The recombinant scAAV6 plasmids encoding shRNAs against MMP3 (AAV6-MMP3) or against MMP13 (AAV6-MMP13) were separately examined. Moreover, both AAV6-MMP3 and AAV6-MMP13 were successively used for simultaneous knockdown of MMP3 and MMP13. The mRNA expression levels of MMP3 and MMP13 were analysed by qRT-PCR up to 56 days after transduction. The highest knockdown impacts on MMP3 and MMP13 were affirmed on day 8 after transduction. On day 8 the average knockdown impacts of 92.9% for MMP3 and 90.6% for MMP13 were confirmed in AAV6-MMP3 or AAV6-MMP13 treated cells respectively. More importantly, similar average knockdown impacts of MMP3 (92.8%) and MMP13 (90.9%) were confirmed after successive treatment of the cells with both AAV6-MMP3 and AAV6-MMP13. Nevertheless, from day 8 until the end of the examination (day 56) the mRNA knockdown efficiencies were steadily declining. Between day 16 and day 56 the knockdown efficiencies were declined to 76.5% and 25% in AAV6-MMP3 transduced cells as well as to 68.6% and 22.3% in AAV6-MMP13 transduced cells respectively ($p < 0.001$). Furthermore, the mRNA knockdown efficiencies in cells transduced with both AAV6-MMP3 and AAV6-MMP13 were similarly declined to 77.8% and 25.4% for MMP3 as well as to 69.9% and 22% for MMP13 respectively (Figures 4A, B) ($p < 0.001$). Additionally, using western blotting the highest knockdown impacts on MMP3 and MMP13 are shown at protein levels (Figures 4C, D). The relative quantification analyses the western blot bands using the software ImageJ showed repression effects of 0.11 for MMP3 and 0.13 for MMP13 as a ratio of the protein expression level in treated cells relative to the expression level of the same protein in untreated cells (ratio: Net Protein X/Net Load Ctrl.) ($p < 0.001$). Untreated and AAV6-Ctrl treated NP cells showed unaffected levels of MMP3 and MMP13 ($p \geq 0.241$). Furthermore, the impacts of MMP3 and MMP13 knockdown on the enhancement of collagen II were examined using ELISA and western blotting. The results of ELISA also showed that the transduction of NP cells with AAV6-MMP3 or AAV6-MMP13 could enhance the protein levels of collagen II. On day 8 the collagen II levels were enhanced by mean values of 83.4% and 50.2% respectively. Moreover, the successive transduction of NP cells with both AAV6-MMP3 and AAV6-MMP13 showed additive enhancement of collagen II level with the mean value of 143.2% ($p < 0.001$). Nevertheless, the steadily falling knockdown efficiencies of the recombinant vectors on MMP3 and MMP13 during the 56 days of cell culture could also weaken the enhancement of collagen II in a related manner. On day 16 the collagen II levels were enhanced by mean values of just 48.5% in AAV6-MMP3 transduced cells and 32% in AAV6-MMP13 transduced cells, but then by mean value of 92.9% in cells successively transduced with both vectors ($p < 0.001$). On day 56 the collagen II levels were enhanced by mean values of 30.4%, 19.1% and 47.3% respectively (Figure 4E) ($p < 0.001$). Untreated and AAV6-Ctrl treated cells showed unaffected levels of collagen II ($p \geq 0.254$). The maximum enhancement of collagen II on day 8 after transduction is also shown using western blotting (Figure 4F). The ImageJ ratio analyses (Net Protein X/Net

TABLE 2 Specificity of MMP3/MMP13 knockdown and collage II enhancement.

	Untreated [pg/100 µg]	AAV6-Ctrl [pg/100 µg]	AAV6-MMP3 [pg/100 µg]	AAV6-MMP13 [pg/100 µg]	AAV6-MMP3/13 [pg/100 µg]
MMP3/day 8	8,661 ± 75.5	8,685 ± 42.5	624.2 ± 13.3	8,699 ± 65.3	622.4 ± 16.4
MMP3/day 56	8,677 ± 27.5	8,710 ± 48	6,505 ± 64.9	8,671 ± 65.8	6,546 ± 87.7
MMP13/day 8	458.9 ± 3.6	459.6 ± 2.49	456.3 ± 4.74	48.62 ± 0.784	48.84 ± 0.804
MMP13/day 56	452.3 ± 2.18	454.5 ± 2.62	453.9 ± 1.57	358.8 ± 3.73	357.5 ± 3.74
Collagen II/day 8	6320 ± 54	6,312 ± 48.2	11,620 ± 112	9,552 ± 114	15,409 ± 88.8
Collagen II/day 56	6,325 ± 25.9	6,343 ± 37.9	8,255 ± 127	7,557 ± 97.5	9,376 ± 133
IL-1β/day 8	120.4 ± 1.78	120.8 ± 2.14	119.8 ± 1.71	120.6 ± 2.23	119.9 ± 1.38
IL-1β/day 56	122.3 ± 1.63	122.0 ± 2.12	121.4 ± 2	120.7 ± 1.77	121.7 ± 2.16
TNF-α/day 8	109.1 ± 2.23	108.6 ± 2.18	108.4 ± 2.61	109.4 ± 1.77	107.9 ± 1.72
TNF-α/day 56	108.8 ± 2.21	108.9 ± 1.95	107.9 ± 2.38	109 ± 2.32	109.2 ± 1.74
ADAMTS4/day 8	2,953 ± 72.6	2,979 ± 92.6	2,967 ± 96.1	2,930 ± 66.7	2,985 ± 109
ADAMTS4/day 56	2,964 ± 61.6	2,959 ± 77.4	3,001 ± 79.6	2,983 ± 49.4	3,002 ± 97.1
ADAMTS5/day 8	3,785 ± 116	3,809 ± 114	3,797 ± 137	3,794 ± 124	3,816 ± 121
ADAMTS5/day 56	3,802 ± 53.4	3,794 ± 43.1	3,795 ± 69.3	3,770 ± 57.9	3,781 ± 54.5
Aggrecan/day 8	16,321 ± 121	16,291 ± 101	16,314 ± 100	16,338 ± 120	16,304 ± 137
Aggrecan/day 56	16,315 ± 111	16,300 ± 109	16,292 ± 105	16,302 ± 104	16,336 ± 126
	Mean ± SD	Mean ± SD	Mean ± SD	Mean ± SD	Mean ± SD

To demonstrate the specificity of MMP3 and MMP13 knockdown mediated by the recombinant vectors AAV6-MMP3 and AAV6-MMP13 as well as the collage II enhancement, the levels other key NP associated proteins were analysed: such as IL-1β, TNF-α, ADAMTS4, ADAMTS5 and aggrecan. After transduction of 1×10^5 NP cells with either AAV6-MMP3 or AAV6-MMP13, or a combination thereof, the cells were harvested on day 8 and day 56. Total protein was isolated and 100 µg of the protein extract from each probe was used for ELISA. Except the levels of MMP3, MMP13 and collage II, the levels of other tested NP associated proteins remained unaffected ($p \geq 0.271$). MMP3, MMP13 and collagen II levels were affected in all transductions ($p < 0.001$), whereby the combined transduction exhibited further enhancement of collagen II. Data represent mean values of three independent experiments.

Load Ctrl.) of the western blot bands of collagen II on day 8 showed enhanced expression effects with ratios of 1.92, 1,61 and 2.52 in AAV6-MMP3 or AAV6-MMP13 or AAV6-MMP3 plus AAV6-MMP13 treated cells, respectively ($p < 0.001$). Age and gender showed no effect.

MMP3/13 knockdown specificity and correlation with collagen II enhancement

To exhibit the direct correlations between the numbers of internalized recombinant viral vectors (AAV6-MMP3 and AAV6-MMP13) per cell (TU/Cell), the resulted knockdown impacts on the expression levels of MMP3 and MMP13, and the enhancement of collagen II level, we analysed the coherence between their verified values. As shown in Figure 5, we confirmed proportional and direct relationships between the transduction units (Figure 5A), the knockdown impacts on the expressions MMP3/MMP13 (Figure 5B) and the enhancement of collagen II level (Figure 5C). To prove whether the recombinant vectors AAV6-MMP3 and AAV6-MMP13 may influence the levels of other NP relevant proteins, we analysed using ELISA the levels of additional NP critical proteins, such as IL-1β, TNF-α, ADAMTS4, ADAMTS5 and aggrecan, during the course of the study. Their levels in all treated NP cells were comparable to that in untreated NP cells throughout the test time (table 2) ($p \geq 0.271$). Consequently, transduction of NP cells with AAV6-MMP3 or AAV6-MMP13, or a combination thereof might specifically influence the levels of MMP3, MMP13 and collagen II ($p < 0.001$) (Table 2). Age and gender showed no effect.

Discussion

The causes and pathological processes of DDD are multifactorial and complex and are still not well understood. DDD is predominantly induced inside the NP. The current therapeutic measures, which are based on surgical and conservative treatments, are not able to treat the causes and the pathological processes. They might only alleviate the symptoms of the disease, without restoring the biological

structure and function of the ECM. Degradation of the extracellular matrix (ECM) in NP due to the reduction of proteoglycan and collagen contents, mainly aggrecan and collagen II. This reduction exibits an imbalance in the normal physiological events for the maintenance of the ECM, namely, an imbalance in anabolic and catabolic events that can lead to reduced anabolism, enhanced catabolism or a combination thereof [31–36, 39–47]. Previously we have demonstrated in degenerative NP cells very low endogeeous expression levels of growth factors such as TGF-βs, BMPs, IGF-1, bFGF, GDF-5, PDGF and their receptors, which are important anabolic components for the stimulation of ECM synthesis. On the contrary, we recorded significantly increased endogenous expression levels of inflammatory cytokines and their receptors such as IL-1β/IL-1 R and TNF-α/TNF-α R1, where their levels increased with severity of disc degeneration. Moreover, the inflammatory cytokines activated NF-κB/MAPK signaling pathways in the analysed degenrative NP cells could lead as expected to high and increasing endogenous expression of the catabolic factors ADAMTSs and MMPs, especially ADAMTS4, ADAMT5, MMP3 and MMP13. Although these catabolic factors were counteracted by even higher and increasing expression levels of their natural endogeneous inhibitors such as TIMP-1, TIMP-2, TIMP-3 and TIMP-4, we recoded declining levels of aggrecan and collagen II with increased severity of disc degeneration [31, 32, 34–36]. This indicated that the shift of the equilibrium in the direction of ECM collapse needs in additional to the existing endogeous inhibitors also exogeous inhibitors, such as shRNAs, which can specifically target the catabolic factors like MMP3 and MMP13. Consequently, we conducted shRNA based inhibition of MMP3 and MMP13 using AAV6 as gene delivery vehicle. AAV6 mediated knockdown of MMP3 and MMP13 has not yet been attempted. The signal transductions mechanism of DDD is associated with up-regulations of the inflammatory cytokines, especiallyIL-1β and TNF-α, that exhibit vigorous proinflammatory activities. Many molecules that participate in this mechanism have been identified. The inflammasome complex containing the nod-like receptors proteins (NLRPs) is compulsively needed in this signal transduction. Activation of NLRP3 by various stimuli, such as danger-associated molecular patterns (DAMPs) of exogenous and endogenous origin or pathogen-associated molecular patterns (PAMPs) leads to the activation of IL-1β and TNF-α with their receptors IL-1R and TNFR1/TNFR2, through binding to an adapter protein known as myeloid differentiation factor 88 (MyD88). This event can recruit and phosphorylate the IL-1R associated kinase 4 (IRAK4) and TNFR associated factor 6 (TRAF6). IRAK4/TRAF6-mediated signal transduction can subsequently activate the NF-κB or MAPK pathways and deregulate the expression of various catabolic factors, like ADAMTs and MMPs, and aggravate degradation the ECM [48–53]. Hence, AAV6-RNAi-mediated inhibitions of MMP3 and MMP13 that enhanced the collagen II level could be an important treatment approach for the biological restoration of degenerative discs.

In conclusion, our findings support the biology-based regenerative treatment strategies that focus on the deceleration or reversion of DDD though inhibitions of ADAMTSs, MMPs, IL-1β and TNF-α, which are involved in the MAPK and NF-κB signaling pathways [51–53]. The overexpression of MMP3 and MMP13 worsening the decomposition of collagen II could be distinctly and stably decreased by parallel knockdown of the genes using the recombinant scAAV6-shRNA vectors. Hence, the recombinant vectors used for targeting MMP3 and MMP13 could have the potential for pharmaceutical and clinical applications as an effective and safer gene delivery system in DDD. In case of potential off-target effects regarding the clinical applications, various strategies need to be developed to overcome potential limitations that maybe associated with the recombinant AAV vectors. Admittedly, there is a reason for optimism, as the wild type AAVs are not involved in gene therapy as gene delivery vehicles. However, prospective modifications and improvements of AAV vectors can further enhance their potency, specificity and safety for gene-based therapeutic applications in DDD.

Data availability

The original contributions presented in the study are included in the article/supplementary material, further inquiries can be directed to the corresponding author.

Ethics statement

The studies involving humans were approved by Local research ethics committee for Medical University of Innsbruck Innrain 52, 6020 Innsbruck, Tirol Austria. The studies were conducted in accordance with the local legislation and institutional requirements. The participants provided their written informed consent to participate in this study.

Author contributions

DM and CT conceived and designed the manuscript, DM performed the acquisition of data, DM and CT completed the analysis and interpretation of data, DM wrote the manuscript, DM and CT revised and final approved the manuscript. All authors contributed to the article and approved the submitted version.

Funding

The authors declare that no financial support was received for the research, authorship, and/or publication of this article.

Conflict of interest

The authors declared no potential conflicts of interest with respect to the research, authorship, and/or publication of this article.

References

1. Adams MA, Dolan P. Spine biomechanics. *J Biomech* (2005) **38**:1972–83. doi:10.1016/j.jbiomech.2005.03.028

2. Roughley PJ. Biology of intervertebral disc aging and degeneration: involvement of the extracellular matrix. *Spine* (2004) **29**:2691–9. doi:10.1097/01.brs.0000146101.53784.b1

3. Buckwalter JA. Aging and degeneration of the human intervertebral disc. *Spine* (1995) **20**:1307–14. doi:10.1097/00007632-199506000-00022

4. Roberts S, Evans H, Trivedi J, Menage J. Histology and pathology of the human intervertebral disc. *J Bone Jt Surg* (2006) **88**(Suppl. 2):10–4. doi:10.2106/jbjs.f.00019

5. Freemont AJ. The cellular pathobiology of the degenerate intervertebral disc and discogenic back pain. *Rheumatology (Oxford)* (2008) **48**:5–10. doi:10.1093/rheumatology/ken396

6. Walker MH, Anderson DG. Molecular basis of intervertebral disc degeneration. *The Spine J* (2004) **4**(6 Suppl. l):158S–66S. doi:10.1016/j.spinee.2004.07.010

7. Tavakoli J, Elliott DM, Costi JJ. Structure and mechanical function of the interlamellar matrix of the annulus fibrosus in the disc. *J Orthopaedic Res* (2016) **34**(8):1307–15. doi:10.1002/jor.23306

8. Martin BI, Deyo RA, Mirza SK, Turner JA, Comstock BA, Hollingworth W, et al. Expenditures and health status among adults with back and neck problems. *JAMA* (2008) **299**:656–64. doi:10.1001/jama.299.6.656

9. Walker BF. The prevalence of low back pain: a systematic review of the literature from 1966 to 1998. *J Spinal Disord* (2000) **13**:205–17. doi:10.1097/00002517-200006000-00003

10. Stewart WF, Ricci JA, Chee E, Morganstein D, Lipton R. Lost productive time and cost due to common pain conditions in the US workforce. *JAMA* (2003) **290**:2443–54. doi:10.1001/jama.290.18.2443

11. Hart LG, Deyo RA, Cherkin DC. Physician office visits for low back pain. Frequency, clinical evaluation, and treatment patterns from a U.S. national survey. *Spine* (1995) **20**:11–9. doi:10.1097/00007632-199501000-00003

12. Katz JN. Lumbar disc disorders and low-back pain: socioeconomic factors and consequences. *J Bone Jt Surg* (2006) **88**(2 Suppl. l):21–4. doi:10.2106/jbjs.e.01273

13. Kuslich SD, Ulstrom CL, Michael CJ. The tissue origin of low back pain and sciatica:. *Orthop Clin North America* (1991) **22**:181–7. doi:10.1016/s0030-5898(20)31644-8

14. Schwarzer AC, Aprill CN, Derby R, Fortin J, Kine G, Bogduk N. The relative contributions of the disc and zygapophyseal joint in chronic low back pain. *Spine* (1994) **19**:801–6. doi:10.1097/00007632-199404000-00013

15. Berlemann U, Gries NC, Moore RJ. The relationship between height, shape and histological changes in early degeneration of the lower lumbar discs. *Eur Spine J* (1998) **7**:212–7. doi:10.1007/s005860050058

16. Boden SD, Davis DO, Dina TS, Patronas NJ, Wiesel SW. Abnormal magnetic-resonance scans of the lumbar spine in asymptomatic subjects. A prospective investigation. *J Bone & Jt Surg* (1990) **72**:403–8. doi:10.2106/00004623-199072030-00013

17. Freeman BJ, Davenport J. Total disc replacement in the lumbar spine: a systematic review of the literature. *Eur Spine J* (2006) **15**(3 Suppl. l):S439–47. doi:10.1007/s00586-006-0186-9

18. van den Eerenbeemt KD, Ostelo RW, van Royen BJ, Peul WC, van Tulder MW. Total disc replacement surgery for symptomatic degenerative lumbar disc disease: a systematic review of the literature. *Eur Spine J* (2010) **19**:1262–80. doi:10.1007/s00586-010-1445-3

19. Boos N, Weissbach S, Rohrbach H, Weiler C, Spratt KF, Nerlich AG. Classification of age related changes in lumbar intervertebral discs: 2002 Volvo Award in basic science. *Spine* (2002) **27**:2631–44. doi:10.1097/01.brs.0000035304.27153.5b

20. Freemont AJ, Peacock TE, Goupille P, Hoyland JA, O'Brien J, Jayson MI. Nerve ingrowth into diseased intervertebral disc in chronic back pain. *Lancet* (1997) **350**:178–81. doi:10.1016/s0140-6736(97)02135-1

21. Soukane DM, Shirazi-Adl A, Urban JP. Computation of coupled diffusion of oxygen, glucose and lactic acid in an intervertebral disc. *J Biomech* (2007) **40**:2645–54. doi:10.1016/j.jbiomech.2007.01.003

22. Holm S, Maroudas A, Urban JP, Selstam G, Nachemson A. Nutrition of the intervertebral disc: solute transport and metabolism. *Connect Tissue Res* (1981) **8**:101–19. doi:10.3109/03008208109152130

23. Razaq S, Wilkins RJ, Urban JP. The effect of extracellular pH on matrix turnover by cells of the bovine nucleus pulposus. *Eur Spine J* (2003) **12**:341–9. doi:10.1007/s00586-003-0582-3

24. Deyo RA, Bass JE. Lifestyle and low-back pain. The influence of smoking and obesity. *Spine* (1989) **14**:501–6. doi:10.1097/00007632-198905000-00005

25. Wilder DG, Pope MH. Epidemiological and aetiological aspects of low back pain in vibration environments: an update. *Clin Biomech* (1996) **11**:61–73. doi:10.1016/0268-0033(95)00039-9

26. Hirano N, Tsuj H, Ohshima H, Kitano S, Itoh T, Sano A. Analysis of rabbit intervertebral disc physiology based on water metabolism. II. Changes in normal intervertebral discs under axial vibratory load. *Spine* (1988) **13**:1297–302. doi:10.1097/00007632-198811000-00016

27. Holm S, Nachemson A. Nutrition of the intervertebral disc: acute effects of cigarette smoking. An experimental animal study. *Upsala J Med Sci* (1988) **93**:91–9. doi:10.1517/03009734000000042

28. Kurunlahti M, Tervonen O, Vanharanta H, Ilkko E, Suramo I. Association of atherosclerosis with low back pain and the degree of disc degeneration. *Spine* (1999) **24**:2080–4. doi:10.1097/00007632-199910150-00003

29. Kauppila LI. Atherosclerosis and disc degeneration/low-back pain–a systematic review. *Eur J Vasc Endovascular Surg* (2009) **37**:661–70. doi:10.1016/j.ejvs.2009.02.006

30. Roberts S, Urban JP, Evans H, Eisenstein SM. Transport properties of the human cartilage endplate in relation to its composition and calcification. *Spine* (1996) **21**:415–20. doi:10.1097/00007632-199602150-00003

31. Mern DS, Fontana J, Beierfuß A, Thomé C, Hegewald AA. A combinatorial relative mass value evaluation of endogenous bioactive proteins in three-dimensional cultured nucleus pulposus cells of herniated intervertebral discs: identification of potential target proteins for gene therapeutic approaches. *PLoS One* (2013) **8**(11):e81467. doi:10.1371/journal.pone.0081467

32. Mern DS, Beierfuß A, Fontana J, Thomé C, Hegewald AA. Imbalanced protein expression patterns of anabolic, catabolic, anti-catabolic and inflammatory cytokines in degenerative cervical disc cells: new indications for gene therapeutic treatments of cervical disc diseases. *PLoS One* (2014) **9**(5):e96870. doi:10.1371/journal.pone.0096870

33. Le Maitre C, Pockert A, Buttle DJ, Freemont AJ, Hoyland JA. Matrix synthesis and degradation in human intervertebral disc degeneration. *Biochem Soc Trans* (2007) **35**(Pt 4):652–5. doi:10.1042/bst0350652

34. Mern DS, Thomé C. Identification and characterization of human nucleus pulposus cell specific serotypes of adeno-associated virus for gene therapeutic approaches of intervertebral disc disorders. *BMC Musculoskelet Disord* (2015) **16**:341. doi:10.1186/s12891-015-0799-4

35. Shenegelegn Mern D, Tschugg A, Hartmann S, Thomé C. Self-complementary adeno-associated virus serotype 6 mediated knockdown of ADAMTS4 induces long-term and effective enhancement of aggrecan in degenerative human nucleus pulposus cells: a new therapeutic approach for intervertebral disc disorders. *PLoS One* (2017) **12**(2):e0172181. doi:10.1371/journal.pone.0172181

36. Mern DS, Thomé C. Synergetic enrichment of aggrecan in nucleus pulposus cells by scAAV6-shRNA-mediated knockdown of aggrecanase-1 and aggrecanase-2. *Exp Biol Med (Maywood)* (2023):15353702231171905. doi:10.1177/15353702231171905

37. Pfirrmann CW, Metzdorf A, Zanetti M, Hodler J, Boos N. Magnetic resonance classification of lumbar intervertebral disc degeneration. *Spine* (2001) **26**:1873–8. doi:10.1097/00007632-200109010-00011

38. Bangdiwala SI. Graphical aids for visualizing and interpreting patterns in departures from agreement in ordinal categorical observer agreement data. *J Biopharm Stat* (2017) **27**(5):773–83. doi:10.1080/10543406.2016.1273941

39. Wagner A, Röhrs V, Kedzierski R, Fechner H, Kurreck J. A novel method for the quantification of adeno-associated virus vectors for RNA interference applications using quantitative polymerase chain reaction and purified genomic adeno-associated virus DNA as a standard. *Hum Gene Ther Methods* (2013) **24**(6): 355–63. doi:10.1089/hgtb.2013.095

40. Rothe D, Wajant G, Grunert HP, Zeichhardt H, Fechner H, Kurreck J. Rapid construction of adeno-associated virus vectors expressing multiple short hairpin RNAs with high antiviral activity against echovirus 30. *Oligonucleotides* (2010) **20**: 191–8. doi:10.1089/oli.2010.0236

41. Lian C, Gao B, Wu Z, Qiu X, Peng Y, Liang A, et al. Collagen type II is downregulated in the degenerative nucleus pulposus and contributes to the degeneration and apoptosis of human nucleus pulposus cells. *Mol Med Rep* (2017) **16**(4):4730–6. doi:10.3892/mmr.2017.7178

42. Vo NV, Hartman RA, Yurube T, Jacobs LJ, Sowa GA, Kang JD. Expression and regulation of metalloproteinases and their inhibitors in intervertebral disc aging and degeneration. *The Spine J* (2013) **13**(3):331–41. doi:10.1016/j.spinee.2012.02.027

43. Tran CM, Schoepflin ZR, Markova DZ, Kepler CK, Anderson DG, Shapiro IM, et al. CCN2 suppresses catabolic effects of interleukin-1β through α5β1 and αVβ3 integrins in nucleus pulposus cells: implications in intervertebral disc degeneration. *J Biol Chem* (2014) **289**(11):7374–87. doi:10.1074/jbc.m113.526111

44. Xin W, Heilig J, Paulsson M, Zaucke F. Collagen II regulates chondroycte integrin expression profile and differentiation. *Connect Tissue Res* (2015) **56**(4): 307–14. doi:10.3109/03008207.2015.1026965

45. Chiu LH, Chen SC, Wu KC, Yang CB, Fang CL, Lai WF, et al. Differential effect of ECM molecules on re-expression of cartilaginous markers in near quiescent human chondrocytes. *J Cell Physiol* (2011) **226**(8):1981–8. doi:10.1002/jcp.22530

46. Klatt AR, Zech D, Kühn G, Paul-Klausch B, Klinger G, Renno JH, et al. Discoidin domain receptor 2 mediates the collagen II-dependent release of interleukin-6 in primary human chondrocytes. *The J Pathol* (2009) **218**(2): 241–7. doi:10.1002/path.2529

47. Colombier P, Clouet J, Hamel O, Lescaudron L, Guicheux J. The lumbar intervertebral disc. From embryonic development to degeneration. *Jt Bone Spine* (2014) **81**(2):125–9. doi:10.1016/j.jbspin.2013.07.012

48. Mern DS, Beierfuß A, Thomé C, Hegewald AA. Enhancing human nucleus pulposus cells for biological treatment approaches of degenerative intervertebral disc diseases: a systematic review. *J Tissue Eng Regen Med* (2014) **8**(12):925–36. doi:10.1002/term.1583

49. Sakai D, Grad S. Advancing the cellular and molecular therapy for intervertebral disc disease. *Adv Drug Deliv Rev* (2015) **84**:159–71. doi:10.1016/j.addr.2014.06.009

50. Fontana G, See E, Pandit A. Current trends in biologics delivery to restore intervertebral disc anabolism. *Adv Drug Deliv Rev* (2015) **84**:146–58. doi:10.1016/j.addr.2014.08.008

51. Tian Y, Yuan W, Fujita N, Wang J, Wang H, Shapiro IM, et al. Inflammatory cytokines associated with degenerative disc disease control aggrecanase-1 (ADAMTS-4) expression in nucleus pulposus cells through MAPK and NF-κB. *The Am J Pathol* (2013) **182**:2310–21. doi:10.1016/j.ajpath.2013.02.037

52. Wang M, Shen J, Jin H, Im HJ, Sandy J, Chen D. Recent progress in understanding molecular mechanisms of cartilage degeneration during osteoarthritis. *Ann New York Acad Sci* (2011) **1240**:61–9. doi:10.1111/j.1749-6632.2011.06258.x

53. Qi XM, Chen G. p38γ MAPK inflammatory and metabolic signaling in physiology and disease. *Cells* (2023) **12**(13):1674. doi:10.3390/cells12131674

EBM Experimental Biology and Medicine

TYPE Original Research
PUBLISHED 07 August 2024
DOI 10.3389/ebm.2024.10096

OPEN ACCESS

*CORRESPONDENCE
Xinmai Yang,
xmyang@ku.edu

RECEIVED 08 January 2024
ACCEPTED 26 July 2024
PUBLISHED 07 August 2024

CITATION
Subramanian Karthikesh M, Martinez-Rivera N, Rosa-Molinar E, Wang X and Yang X (2024), Ultrasound-assisted laser therapy for selective removal of melanoma cells. *Exp. Biol. Med.* 249:10096. doi: 10.3389/ebm.2024.10096

Ultrasound-assisted laser therapy for selective removal of melanoma cells

Madhumithra Subramanian Karthikesh[1,2], Noraida Martinez-Rivera[3], Eduardo Rosa-Molinar[1,3,4], Xueding Wang[5] and Xinmai Yang[1,2,6]*

[1]Bioengineering Graduate Program, University of Kansas, Lawrence, KS, United States, [2]Institute for Bioengineering Research, University of Kansas, Lawrence, KS, United States, [3]Microscopy and Analytical Imaging Laboratory, University of Kansas, Lawrence, KS, United States, [4]Department of Pharmacology and Toxicology, and Neuroscience, University of Kansas, Lawrence, KS, United States, [5]Department of Biomedical Engineering, University of Michigan, Ann Arbor, MI, United States, [6]Department of Mechanical Engineering, School of Engineering, University of Kansas, Lawrence, KS, United States

Abstract

The current study explores the potential of ultrasound-assisted laser therapy (USaLT) to selectively destroy melanoma cells. The technology was tested on an *ex vivo* melanoma model, which was established by growing melanoma cells in chicken breast tissue. Ultrasound-only and laser-only treatments were used as control groups. USaLT was able to effectively destroy melanoma cells and selectively remove 66.41% of melanoma cells in the *ex vivo* tumor model when an ultrasound peak negative pressure of 2 MPa was concurrently applied with a laser fluence of 28 mJ/cm^2 at 532 nm optical wavelength for 5 min. The therapeutic efficiency was further improved with the use of a higher laser fluence, and the treatment depth was improved to 3.5 mm with the use of 1,064 nm laser light at a fluence of 150 mJ/cm^2. None of the laser-only and ultrasound-only treatments were able to remove any melanoma cells. The treatment outcome was validated with histological analyses and photoacoustic imaging. This study opens the possibility of USaLT for melanoma that is currently treated by laser therapy, but at a much lower laser fluence level, hence improving the safety potential of laser therapy.

KEYWORDS

ultrasound-assisted laser therapy, photo-mediated ultrasound therapy, melanoma treatment, cavitation, selective melanoma treatment

Impact statement

Non-invasive and agent-free therapy is always needed for melanoma. Laser therapies, widely used in melanoma treatment, require an injection of external agents and high laser power. Further, focused ultrasound therapy is another established treatment for melanoma based on hyperthermic effects to induce cell death. This is a pioneer study that uses *Ultrasound-assisted Laser Therapy*, a novel technology based on photo-mediated

ultrasound therapy, a combined laser and ultrasound therapy for treating melanoma at low laser fluence per pulse requiring no external agents.

Introduction

Melanoma is an invasive and aggressive type of cancer most frequently occurring on the skin [1, 2], as well as in the eye [3–5]. The global incidence of newly diagnosed cases of melanoma skyrocketed to 300,000 in 2020 [6]. About 90% of uveal melanoma, the most common eye cancer constituting 3–5% of all melanomas and aggressive cancer with 50% of patients dying from metastasis, is choroidal melanoma [4, 5]. Laser therapies based on thermal effect or release of reactive oxygen species have been used for treating melanoma in both skin and eye [7, 8]. These therapies are advantageous as they are minimally or non-invasive and easy to use [9].

Laser therapies used for melanoma include photothermal therapy (PTT), photo-biomodulation (PBM), transpupillary thermal therapy (TTT), and photo-dynamic therapy (PDT). PTT involves the use of photothermal agents to produce heat upon laser irradiation to treat tumor metastasis through targeted therapy [10]. PTT with a NIR laser at 240 J/cm^2 laser fluence guided by photoacoustic imaging using hyaluronan (HA)-coated FeOOH@polypyrrole (FeOOH@PPy) nanorods as theranostics agent demonstrated anticancer activity in melanoma both *in vitro* and *in vivo* [11]. PTT at 808 nm using functionalized gold nanoparticles on melanoma cells *in vitro* was able to induce apoptosis, necroptosis, and necrosis by controlling the temperature rise through varying laser power from 0.95 W to 1.59 W for 15 min [12]. Another study on dose-dependent PTT using gold nanostars at 808 nm concluded that caspase-3-dependent apoptosis was induced at 720 J/cm^2 laser fluence [13]. Further, a computed tomography-guided synergistic resveratrol-coated gold nanoflowers induced apoptosis and PTT at 808 nm with a laser fluence of 594 J/cm^2 was able to kill cancer cells and showed no recurrence for 16 days *in vivo* [14]. PTT often raises safety concerns as it involves the injection of foreign agents and poses a challenge in completely eliminating the effects of hyperthermia.

PBM is the use of a low-level laser to induce modulation in physiological function without any heating to the cells and tissue [15]. A 660 nm red laser at 150 J/cm^2 was able to inhibit cell migration and reduce VEGF production in the melanoma cells *in vitro,* and also arrest tumor progression with an increased survival rate in mice *in vivo* [16]. Another study with a red light at 635 nm was able to elevate reactive oxygen species and p53 phosphorylation in melanoma cells *in vitro* increasing apoptosis at 1280 J/cm^2 [17]. Red light also inhibits melanoma progression and elevated CD103+ expression of dendritic cells *in vivo* at 2560 J/cm^2. Further, laser therapy at 660 nm with a fluence of 3 J/cm^2, and at 800 nm and 970 nm with a fluence of 6 J/cm^2 demonstrated an increase in type I interferon both *in vitro* and *in vivo* on melanoma [18]. In addition, PBM was able to reduce tumor progression and elevate metabolism *in vitro*. Further, the treated area *in vivo* was surrounded by lymphocytes and dendritic cells, and mature vessels with reduced pro-angiogenic macrophages were observed.

TTT is extensively investigated for laser-based thermal therapy for choroidal melanoma. In TTT, a near-infrared diode laser (810 nm) is used to generate temperatures between 45 and 65°C through heating effect [19]. TTT affects the tumor at 0.7–2 mm depth [20]. TTT at 810 nm demonstrated complete tumor resorption in 29% of the patients with recurrent and residual choroidal melanoma [21]. In addition, TTT also resulted in complications in 44% of patients at 45-month follow-up after three treatment sessions [22]. Further, the tumor recurrence rate in patients was 11% and 15% at 5 and 10 years after TTT, and it was found to be correlated to the high-risk tumor features [23].

PDT is another laser-based therapy used for both skin and choroidal melanoma that is not based on thermal effect. PDT uses photosensitizers to release reactive oxygen species when exposed to visible light [24]. Photosensitizers are substances that can be selectively absorbed by metabolically active tissue like melanoma [25]. The reactive oxygen species induce apoptosis selectively in melanoma. PDT at 673 nm with 10 J/cm^2 using an antibody-metallated phthalocyanine-polyethylene glycol-gold nanoparticle drug conjugate as a photosensitizer demonstrated increased cytotoxic and late apoptotic cell deaths in melanoma cells *in vitro* [26]. PDT at 450 nm using flavin mononucleotide demonstrated apoptosis on melanoma cells at 5 J/cm^2 laser fluence *in vitro* and melanoma xenograft regression at 20 J/cm^2 *in vivo* [27].

Several clinical studies evaluated the potential of PDT for treating choroidal melanoma. A clinical study of muti-dose PDT at 100 J/cm^2 laser fluence for 166s per spot using verteporfin for choroidal melanoma demonstrated tumor reduction in 83% of patients after multiple sessions [28]. Another clinical study involving PDT with verteporfin for choroidal melanoma demonstrated 61.6% complications after years [24]. Another clinical study of three sessions PDT at 50 J/cm^2 with a double duration treatment of 83 s each for choroidal melanoma with verteporfin concluded that 20% of patients failed 5 months post-treatment requiring radiotherapy [29]. The follow-up for this clinical study indicated 62% tumor regression in the 29th month following three sessions of PDT [30]. Another study used fluorinated-functionalized polysaccharide-based nanocomplexes mediated PDT for choroidal melanoma elicited photocytotoxicity through elevation of reactive singlet oxygen at 650 nm for a laser fluence of 100 J/cm^2 for 8 min *in vivo* [31]. Even though PDT is widely used and explored for skin melanoma and choroidal melanoma, the systemic injection of the photosensitizer during PDT makes the skin photosensitive to light after the treatment and requires laser fluence over 50 J/cm^2

for choroidal melanoma. Further, PDT is also limited to a strict treatment window due to the circulation time of the photosensitizer and a challenge with complete elimination from circulation.

The selectivity of laser therapy to treating melanoma can be achieved through selective photo-thermolysis that involves specific targeting of pigmented elements within the target by exposing them to light wavelength corresponding to the peaks of their optical absorption spectrum [32, 33]. Melanin is a pigment present in the melanosome of skin and eye [34]. By using a laser with a wavelength and pulse duration appropriate to the melanin characteristics, pigment destruction of melanin can be induced through selective photo-thermolysis [35]. The shorter wavelength lasers – pulsed dye laser and ruby laser can only treat superficial melanosomes, whereas the ruby laser is minimally absorbed by hemoglobin offering a greater selectivity for melanin [36, 37]. For the melanin pigment, the theoretical optimal optical wavelength ranges from 500 to 600 nm [38]. However, the 500–600 nm range has a limited penetrating depth in the order of 1.5 mm due to high optical absorption [38]. The near-infrared (NIR) laser has also been used in thermal therapy for melanoma, but it often involves localized injection of indocyanine green dye to improve heat generation [39–41]. Further, at longer wavelengths such as 1,064 nm, the laser light can penetrate relatively deeper tissues but at a comparatively higher laser fluence [42–44].

Ultrasound therapies are also widely explored and used for tumor treatment. Focused ultrasound (FUS) technology using a high-intensity focused transducer (HIFU) is increasingly used to non-invasively treat solid tumors [45], including melanoma [46]. Tumor cells are killed in HIFU ablation through thermal effect based on acoustic absorption, or mechanical effect based on cavitation [47]. In the event of bubble collapse, localized tissue damage is induced due to the combined effect of applied ultrasound pressure from FUS, shear stress, and high temperature due to cavitation. However, FUS therapy is not as highly selective as laser therapies because there often exists a sharp optical absorption contrast between different types of tissues.

We have recently developed a combined ultrasound and nanosecond pulsed laser technology, termed photo-mediated ultrasound therapy (PUT), to enhance cavitation activity and demonstrated its high efficiency and excellent selectivity [48–51] to remove micro-vessels. With spatiotemporally synchronized laser pulses and ultrasound bursts, the laser energy and ultrasound amplitude used in PUT are significantly less than the traditional laser-only and ultrasound-only-based technologies.

Based on the same principle, in this study, we presented an ultrasound-assisted laser therapy (USaLT) for melanoma cell removal. Different from previous therapies, such as PTT, PBM, TTT, and PDT, where continuous wave (CW) laser was used, USaLT is based on nanosecond laser pulses with a relatively low fluence per pulse. The possible underlying mechanism of USaLT is to promote cavitation and selectively destroy melanoma cells through mechanical force, rather than thermal effect, by using synchronously applied nanosecond laser pulses and ultrasound bursts. By synergistically applying ultrasound bursts, cavitation activity induced by optical absorbers like melanin during laser therapy can be enhanced [52]. USaLT is advantageous as it is highly precise resulting in high selectivity on the target by exploiting the high optical contrast between endogenous agents like melanin and other tissue in the visible to near-infrared region [52–54]. Further, USaLT is a non-invasive and agent-free technique and is designed to enhance the mechanical effect while suppressing the thermal effects by selecting optimal laser and ultrasound parameters [55].

In this study, we explored the application of USaLT for melanoma cell removal *ex vivo* by using melanin present in melanosomes as an optical absorber for targeted tumor removal. With a novel *ex vivo* melanoma model, we demonstrated that, with the assistance of FUS, laser therapy can destroy melanoma cells selectively with a much lower fluence in comparison with traditional laser therapy, and achieve a treatment depth of at least 3 mm, potentially improving the safety feature of laser therapy.

Materials and methods

Ex vivo USaLT system setup

Figure 1A shows the schematic of the USaLT experimental setup and Figure 1B shows a photograph of the experimental setup. A 500 kHz FUS transducer (H107, Sonic Concepts, Bothell, WA, United States) and an Nd:YAG laser (Surelite SLI-30, Continuum, Santa Clara, CA, United States) were used for USaLT. For the *ex vivo* experiment in a melanoma tumor model on the chicken breast tissue, the laser system, FUS system, and oscilloscope were triggered by a pulse delay generator (Model DG355, Stanford Research Systems, Sunnyvale, CA, United States) at a 30 Hz repetition rate.

Before each experiment, the 500 kHz FUS transducer was first spatially aligned with the laser beam which had a pulse repetition rate of 30 Hz and a pulse duration of 5 ns. During the alignment process, switch 1 position was used, and the photoacoustic (PA) signal generated upon illuminating the target with the laser beam was detected by the FUS transducer. The signal acquisition was then performed using a digital oscilloscope (DPO 3034, Tektronix Inc., Beaverton, OR, United States). The FUS transducer was scanned across the region of interest and fixed at the location where the maximum PA signal was detected, indicating the overlap of the laser and the focal region of the FUS transducer. Through this process, FUS bursts and laser pulses were spatially aligned for each sample.

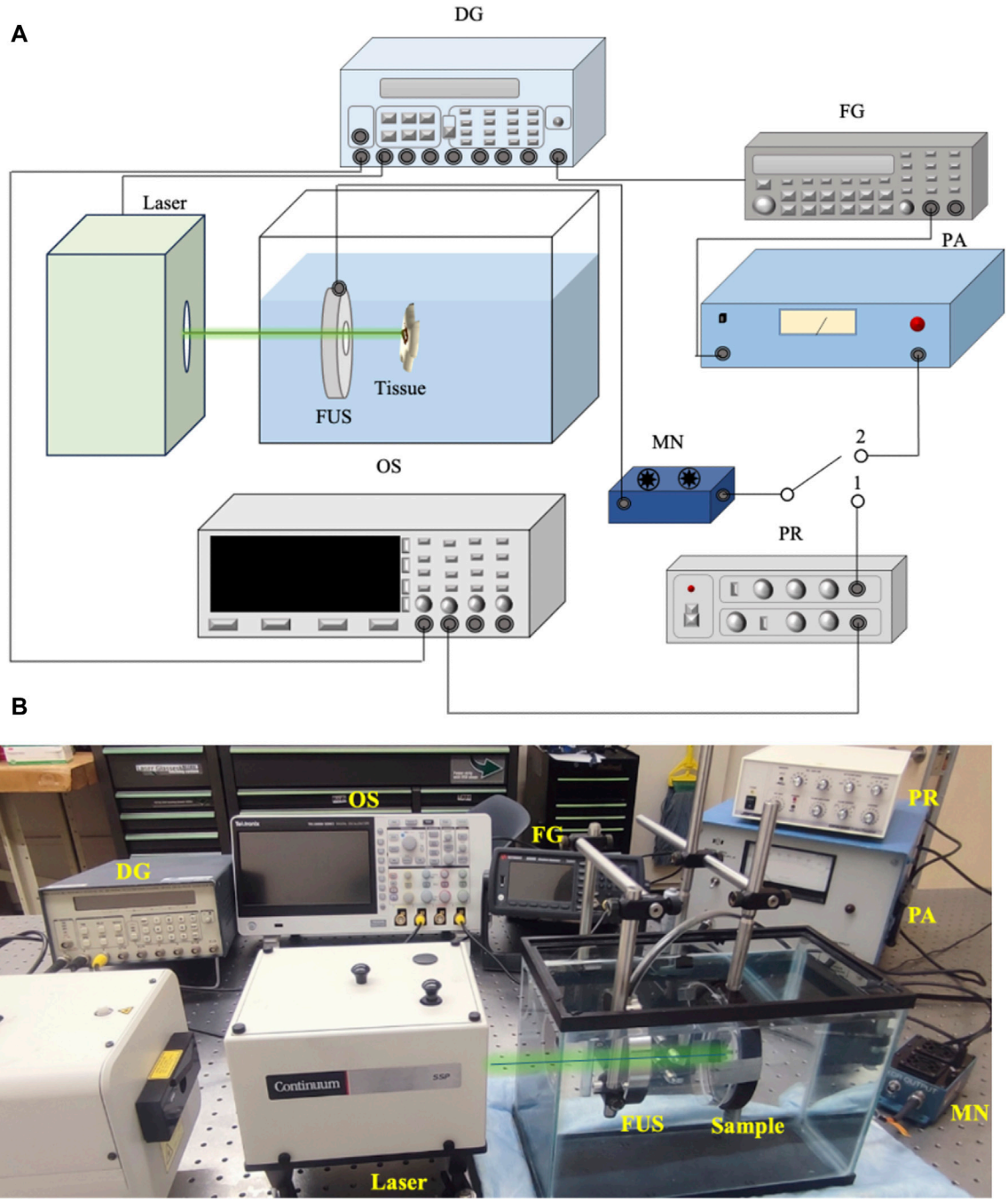

FIGURE 1
(A) Schematic of the system setup for USaLT. Switch position 1 is for alignment. Switch position 2 is for treatment. **(B)** Photograph of the USaLT experimental setup. DG, Delay Generator; OS, Oscilloscope; FG, Function Generator; PR, Pulse Receiver; FUS, Focused ultrasound; PA, Power Amplifier; MN, Matching Network.

Switch 2 position was then used for USaLT. The ultrasound signals were supplied by a function generator (33250A, Agilent Technologies, Santa Clara, CA, United States). The signals were then amplified using a power amplifier (350L RF Power Amplifier, ENI Technology Inc., Rochester, NY, United States) by 50 dB and fed into the FUS transducer via an impedance-matching circuit (Impedance Matching Network H107, Sonic Concepts, Bothell, WA, United States). The FUS transducer focal

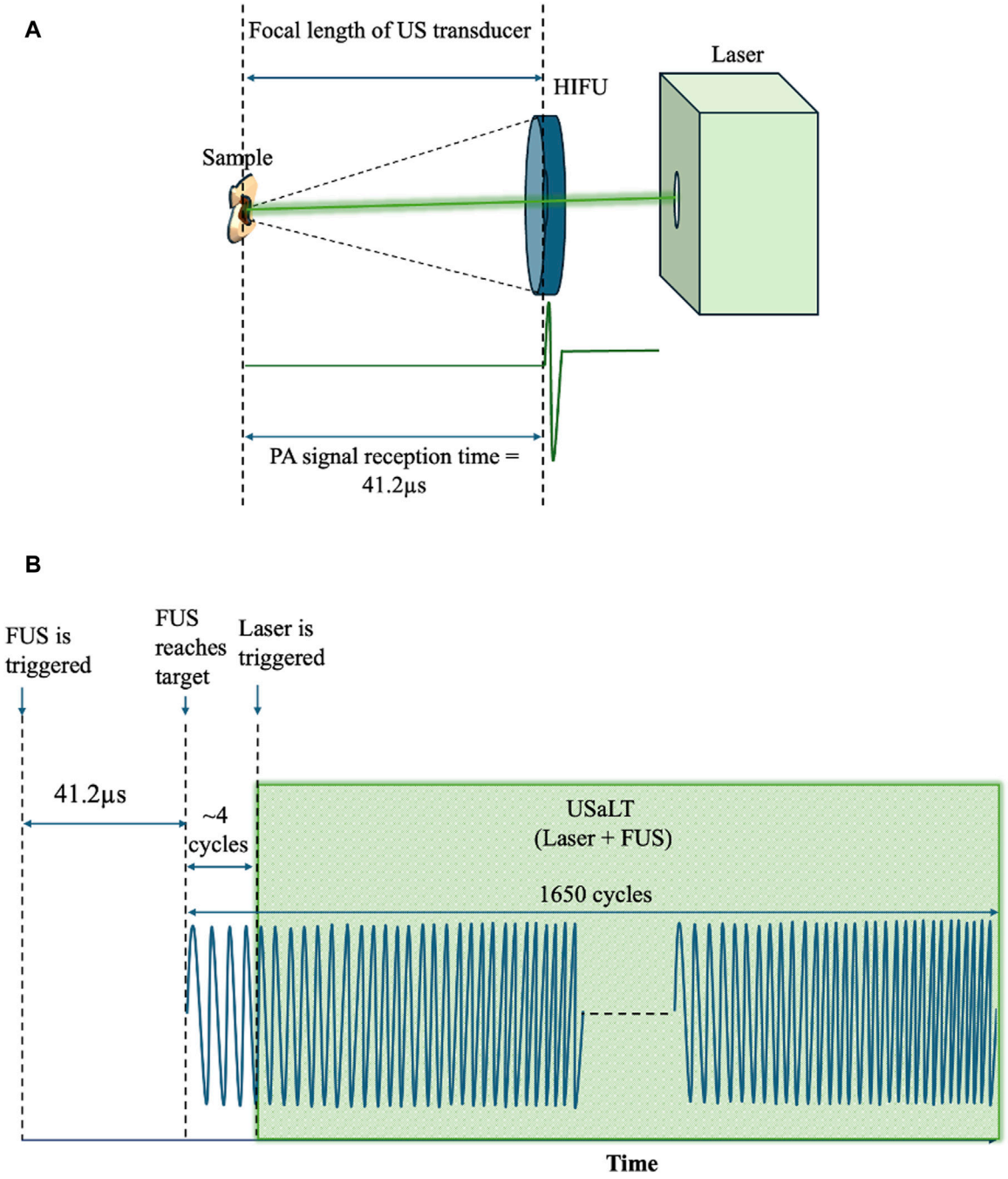

FIGURE 2
(A) Spatiotemporal alignment of laser and ultrasound on the sample. **(B)** FUS and laser pulses triggered during USaLT treatment using the delay generator.

region was focused on the target. The focal length, focal width, and radius of curvature of the FUS transducer are 21.02, 3.02, and 63.2 mm respectively. The ultrasound duty cycle used in this study was 10% to reduce the heat generation with 1,650 cycles at a 30 Hz pulse repetition rate.

For USaLT, laser pulses and ultrasound bursts were synchronously applied by controlling the laser intensity at the surface to maintain the desired laser fluence and using the same ultrasound parameters used for ultrasound-only treatment. By following a previous study [55], the timing sequence of the laser

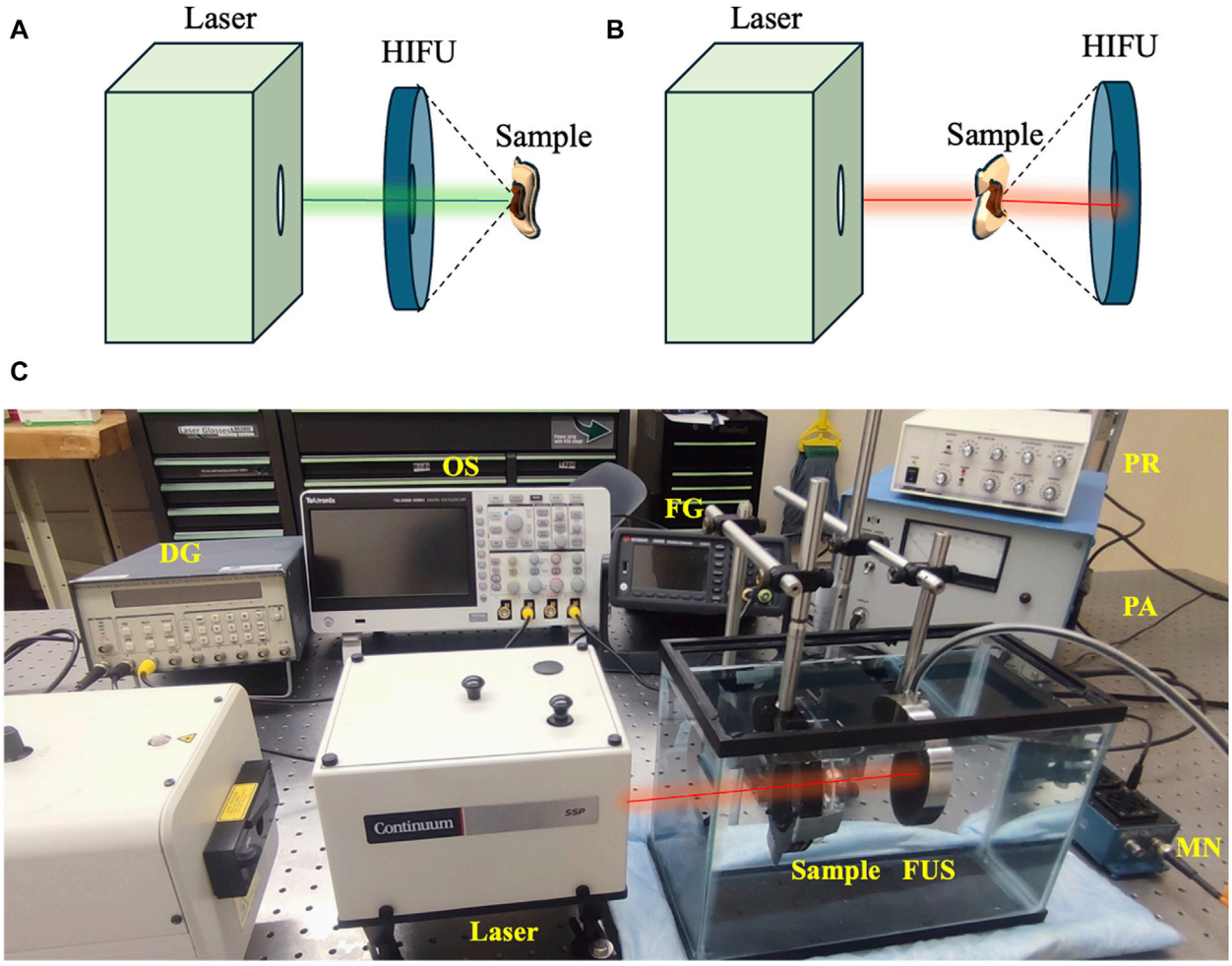

FIGURE 3
Variations in treatment setup for using **(A)** 532 nm and **(B)** 1064 nm. **(C)** USaLT photograph for using 1,064 nm. USaLT photograph for using 532 nm has been shown in Figure 1.

pulses and FUS bursts were precisely controlled by a pulse delay generator as shown in Figure 1. A delay time after each FUS burst was set for triggering each laser pulse such that the FUS burst can propagate to the target before a laser pulse was fired. This delay time was set based on the ultrasound traveling time from the FUS transducer to the target. To measure this traveling time, the FUS transducer was initially used in receiving mode, while a laser pulse was used to generate PA signal from the target (Figure 2A). The measured delay between the laser trigger and the FUS detected PA signal, which is the ultrasound traveling time between the FUS transducer and the target, was precisely calculated and applied to the laser system via the pulse delay generator. As a result of the synchronization, the laser pulse was anticipated to irradiate the target when the negative phase of the FUS burst reached the target, as shown Figure 2B. The diameter of the laser beam used for the laser-only and USaLT was 6 mm for *ex vivo* treatment. The laser power was monitored using an optical power meter before each treatment.

At 532 nm optical wavelength, the laser fluences used for *ex vivo* experiments were 20, 28, and 42 mJ/cm^2, while 150 mJ/cm^2 laser fluence was used for 1,064 nm optical wavelength. These parameters were selected based on a titration process in separate *in vitro/ex vivo* experiments and the availability of the laser sources. Ultrasound peak-negative pressure (PNP) of 2 MPa was used separately for laser-only and ultrasound-only treatment groups and in combination for USaLT groups (n = 5). The treatment time for each sample was 5 min. The variations of system setups for using 532nm and 1,064 nm are shown in Figures 3A, B. Figure 3C shows the photograph of the setup for using 1,064 nm.

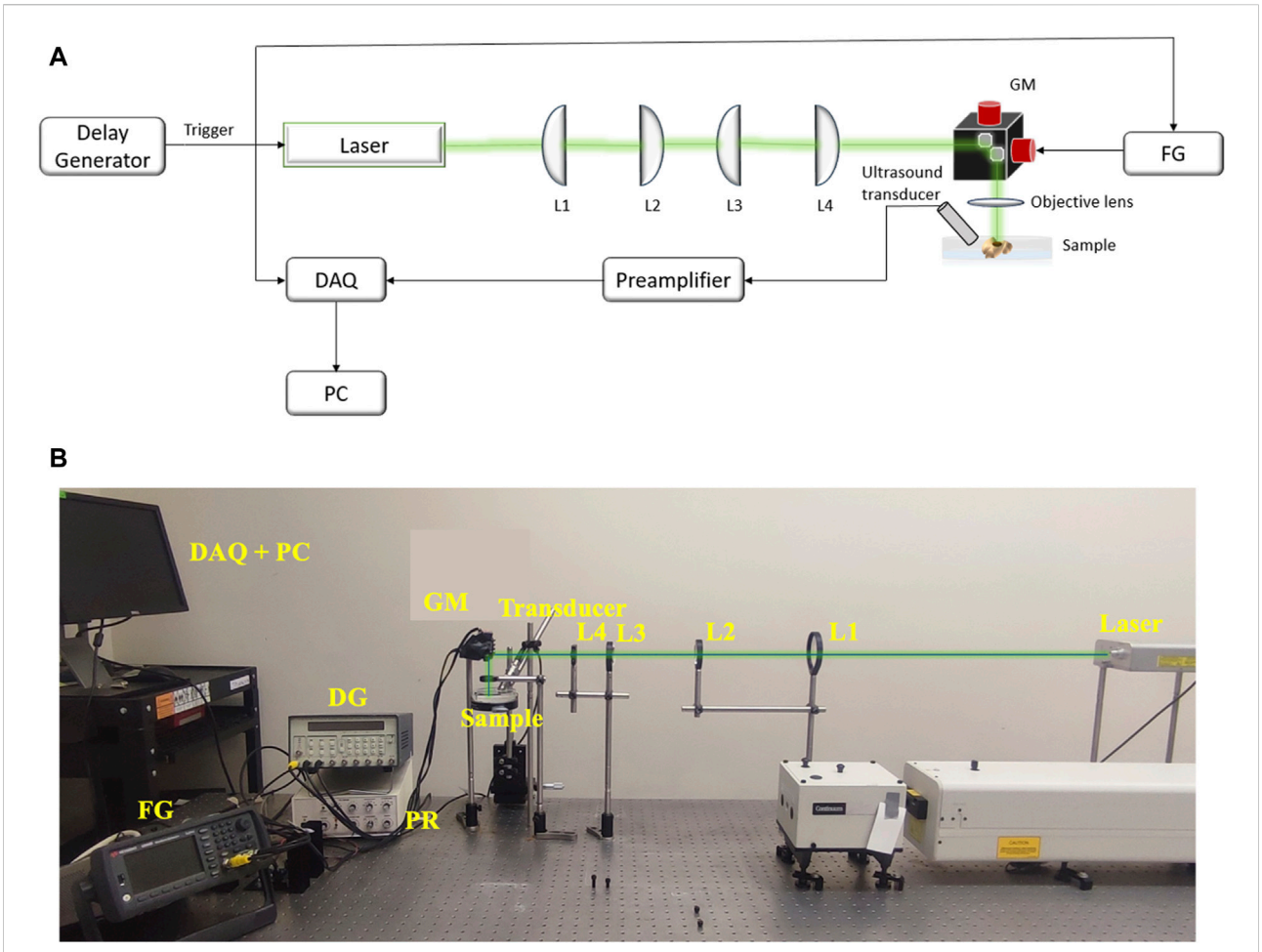

FIGURE 4
(A) The schematic and **(B)** photograph of system setup for PA imaging. FG: Function Generator, DAQ: Data Acquisition Card, PC: Computer, GM: Galvanic mirror, L1 (f = 150 mm), L2 (f = 100 mm), L3 (f = 75 mm), L4 (f = 25.4 mm): Lenses.

Cell culture

Murine melanoma cells B16F10 (ATCC® CRL-6475™) were used. The cells were cultured in complete Dulbecco's Modified Eagle's Medium (DMEM) (ATCC® 30-2002™) supplemented with 10% (v/v) Fetal Bovine Serum (FBS) (ATCC® 30-2020™) and 2% (v/v) penicillin-streptomycin solution (ATCC® 30-2300™) and maintained at 37°C in a humidified incubator (Nunc™, Thermo Scientific, Waltham, MA, United States) with 5% CO_2 in a 75 cm^2 flask. The cells were split into a 1: 10 ratio once 80% confluence was reached.

Ex vivo chicken breast melanoma tumor model

The melanoma cells were grown on chicken breast tissue. The chicken breast was cleaned and cut into pieces 3.5 mm thick. The cells were then injected into the tissue at a concentration of 2 × 10^6 cells/mL. The cell numbers used for melanoma preparation into the tissue were the minimum concentration needed to demonstrate any visible cell growth, analyzed upon optimization through injecting various concentrations. The cells were injected in one shot using a 1 mL syringe with the needle bevel completely inserted facing upwards about 1.75 mm into the tissue at 45°. The tissue injected with the cells was then incubated in the refrigerator for 7 days. The tissue samples were then washed with phenol-red-free DMEM (31053028, Gibco™) before treatment. The samples were placed in a complete cell culture medium for hydration after injection. Further to avoid tissue dehydration and degradation of tissue fat at higher temperatures, samples were placed in a refrigerator during adhesion and growth. The tissue samples were placed in 4% formaldehyde in the medium after treatment until histology procedure.

Photoacoustic imaging for evaluation of treatment effect *ex vivo*

An optical-resolution PA microscopy system (Figure 4) was used to evaluate the treatment outcome on the melanoma cells *ex vivo*. A Q-switched Nd:YAG (532 nm, SPOT-10-100-532, Elforlight, Daventry, UK) laser with a pulse width of 2 ns and pulse repetition rate of 20 kHz pulse repetition was used to produce PA signals. The laser light passed through a series of planoconvex lenses – L1 (f = 150 mm, LA1002-A, Thorlabs, New Jersey, United States), L2 (f = 100 mm, LA1050-A, Thorlabs, New Jersey, United States), L3 (f = 75 mm, LA1145-A, Thorlabs, New Jersey, United States) and L4 (f = 25.4 mm, LA1951-A, Thorlabs, New Jersey, United States). A 2.25 MHz center frequency flat ultrasound transducer (V323-SU, Olympus NDT, Waltham, MA) captured the PA signals generated from the sample. The signal detected by the transducer was delivered to the pre-amplifier (DPR300, Olympus-NDT, Waltham, MA), and finally collected by a personal computer through an A/D data acquisition card (Octopus CS8289: OCT-828-009, GaGe, Lockport, IL) at a sampling rate of 10 MHz. Each sample was placed in degassed water during imaging process, and the PA images of the region of interest were acquired through raster scanning of the laser beam using a galvanic mirror (GVS202, Thorlabs, New Jersey, United States) and focused on the sample through an objective lens (f = 30 mm, LB1757-A, Thorlabs, New Jersey, United States). The laser trigger was used to synchronize the acquisition and the scanning system. A two-dimensional image was reconstructed using the acquired signals from 2D scanning. The images of the *ex vivo* melanoma tumor in each sample were acquired before and after the treatment. The PA intensity was calculated as average over the segmented tumor area as the treatment area of USaLT covered the entire tumor region. The relative change in PA intensity before and after the treatment was used for evaluating the treatment effect. All the quantitative signal analyses were performed on the raw data before any post-processing.

Sample preparation for staining

The samples were fixed in 4% formaldehyde immediately after the treatment. The 4% formaldehyde was prepared by diluting 16% formaldehyde (Sigma Aldrich, Cat. No. P6148, Lot No. MKCD5277) aqueous stock solution. The histology procedure for paraffin embedding was performed using a Pelco BioWave® Pro 36,500 Laboratory Microwave System with a Pelco® Steady Temp™ Pro Thermo Cube (Ted Pella, Inc.). The samples were first dehydrated with increasing concentration of alcohol at 40°C, 5 min each: 50% ethanol, 70% ethanol, 95% ethanol, 1:1 95% EtOH/Isopropanol, and finally at 100% isopropanol before infiltrating with 1: 1 isopropanol/paraffin for 5 min at 70°C. Then, samples were embedded in paraffin (Leica Paraplast Plus®, Cat. No. 39602004, Lot No. 2207122) thrice at 70°C with vacuum for 5 min, 10 min, and 5 min respectively. After 24 h, samples were sectioned using a rotary microtome; sections were ranging between 6 µm and 8 µm thickness. Microscope slides were manually coated with a gelatin solution, in which 1 g of gelatin powder, type A (Electron microscopy Sciences [EMS], Cat. No. 16584, Lot No. 150226) was dissolved in 1L of hot distilled water and then mixed with 0.1 g of chromium (III) potassium sulfate (Sigma-Aldrich, Cat. No. 243361, Lot No. MKBV2677V) once it cooled down. These slides were kept at 4°C until use. The sample sections were then mounted on these coated microscope slides; 3 to 4 sections were mounted per slide.

Sample sections were deparaffinated, hydrated, stained, and dehydrated using a HistoPro® 414 Linear Stainer for paraffin and frozen sections (RUSHABH Instruments, LLC.). The samples were deparaffinated using Histo-clear® II (National Diagnostics, Cat. No. HS-202, Lot No. 11-19-38) for 2 min in the first step, followed by 25 dips in Histo-clear® II two times. The sample sections were then hydrated through 25 dips in the following solutions: 100% ethanol, 100% ethanol, 95% ethanol, 70% ethanol, and in running tap water for 1 min. Figures 5A–C shows the overall workflow for the histology procedure.

Hematoxylin and eosin staining

Sample sections were stained in Harris Hematoxylin (EMS, Cat. No. 26754, Lot No. 211111-04) for 1 min and washed in running tap water for 1 min. This hematoxylin staining was enhanced using Scott's solution next, dipping 25 times; this solution was prepared by adding 2.0 g of sodium bicarbonate (Sigma Life Science, Cat. No. S6014, Lot No. 127K0680) and 20.0 g of magnesium sulfate heptahydrate (Fisher Chemical, Cat. No. M63-500, Lot No. 185221) to 1 L of distilled water. The sample sections were rinsed in DI water, and 95% ethanol was dipped 25 times each and stained with Eosin Y, 1% alcoholic (EMS, Cat. No. 26762-01, Lot No. 211111-05) for 3 min. The sample sections were then initially dehydrated by dipping in the following solution 25 times: 95% ethanol, and 95% ethanol.

Mallory-Heidenhain Azan-Gomori's modification staining

Alternating microscope slides from each sample were selected for Mallory-Heidenhain Azan-Gomori's Modification staining. The sample sections were then stained in 0.1% Azocarmine G (EMS, Cat. No. 26450-01, Lot No. 230725-21) for 30 min at 56°C (staining glass jar was placed inside an oven set at this temperature). Then, sample sections were rinsed with distilled water (25 dips), differentiated in Aniline-Alcohol 1% solution (EMS, Cat. No. 26450-02, Lot No. 230725-22) for 5 min, rinsed with distilled water (25 dips) and transferred to an iron alum solution (Ferric Ammonium Sulfate, 5% aqueous; EMS,

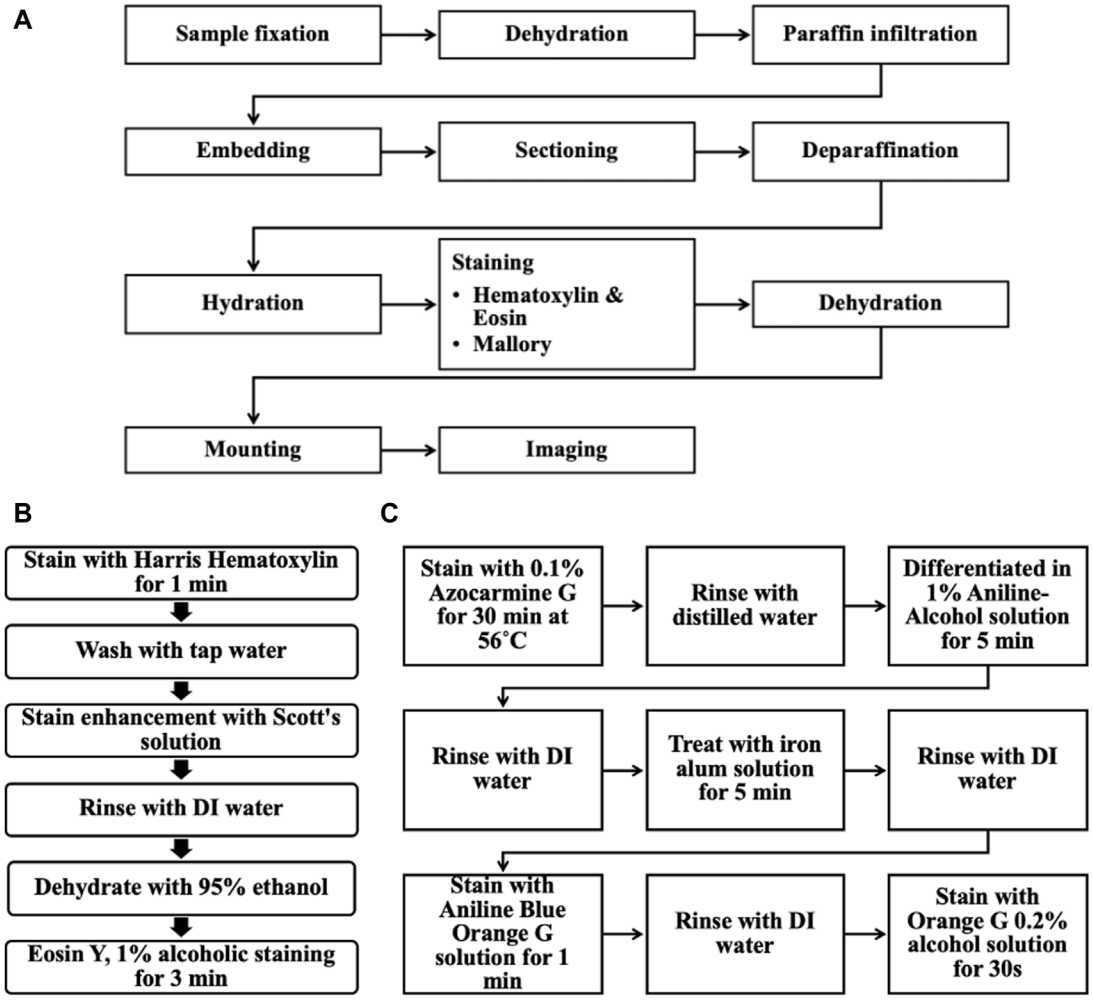

FIGURE 5
(A) Overall workflow of the histological procedure for the *ex vivo* chicken breast melanoma tumor model. **(B)** Steps for Hematoxylin & Eosin staining. **(C)** Steps for Mallory stain.

Cat. No. 26450-03, Lot No. 230724-23) for 5 min, rinsed again (25 dips) and stained with Aniline Blue-Orange G solution (EMS, Cat. No. 26450-04, Lot No. 230725-24) for 1 min. The sample sections were briefly rinsed with distilled water (5 dips) and blotted carefully to then dehydrated completely in 100% ethanol and stained with Orange G 0.2% alcohol solution (EMS, Cat. No. 26450-05, Lot No. 230724-25) for 30 s. This staining protocol was optimized using a mouse pancreas before running these samples (Supplementary Figure S1).

Dehydration and imaging

The sample sections were completely dehydrated by dipping in the following solution 25 times: 100% ethanol, 100% ethanol, Histo-clear® II, and Histo-clear® II. Finally, the samples were placed in Histo-clear® II before mounting and sealed with cover glass using Permount® mounting medium. These sample sections were imaged using a Nikon Eclipse LV100D-U compound bright field upright microscope and images were acquired with Q Capture Pro Version 6.0.0.412 using Q Imaging MicroPublisher 5.0 RTV camera with a pixel resolution of 2560 × 1920 using either a Plan Flour 10X/0.30NA air objective or Plan Flour 20X/0.45NA air objective.

Results

Validation of *ex vivo* tumor model

The Hematoxylin and Eosin staining (H&E), as well as the Mallory staining, was used to confirm and validate the *ex vivo*

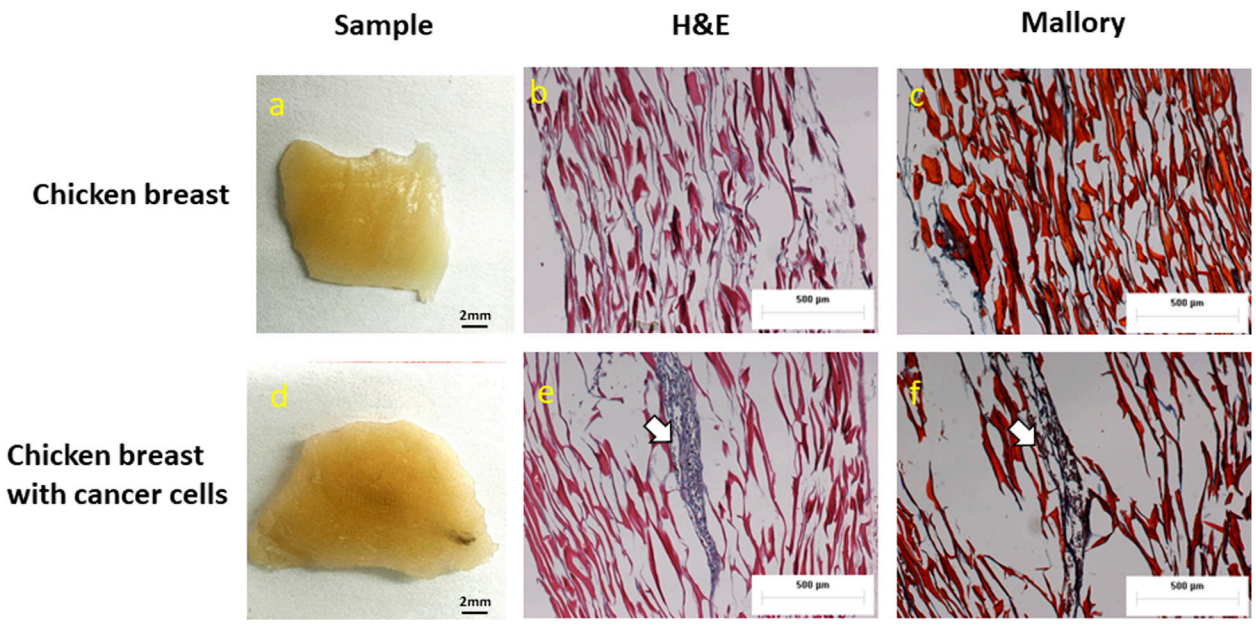

FIGURE 6
Photographs, H&E, and Mallory staining of **(A–C)** Chicken breast only and **(D–F)** *ex vivo* model of chicken breast containing melanoma cells respectively. White arrows indicate the melanoma cancer cells.

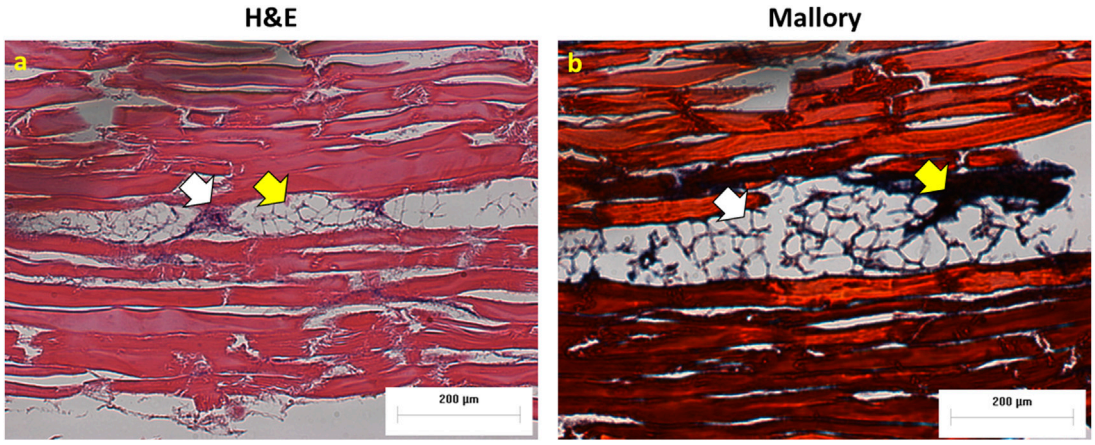

FIGURE 7
Melanoma cells attached to adipose tissue **(A)** H&E and **(B)** Mallory staining. White arrows show cancer cells and yellow arrows indicate adipose tissue.

tumor model after 7 days of melanoma cell incubation in chicken breast tissue (Figure 6). Both H&E and Mallory staining showed a group of melanoma cells holding onto the chicken tissue and forming a network. In the H&E staining, the melanoma cells were dark blue clusters, while with Mallory staining, the cells were present as a dark black cluster. This was validated by comparing them with the chicken breast with no tumor cells. Further, the melanoma cells were also found holding on to the adipose tissue when present. The adipose tissue was indicated by a patterned network using a yellow arrow (Figure 7). These results demonstrated that melanoma cells can successfully grow in *ex vivo* chicken breast tissues with our established protocol in this study.

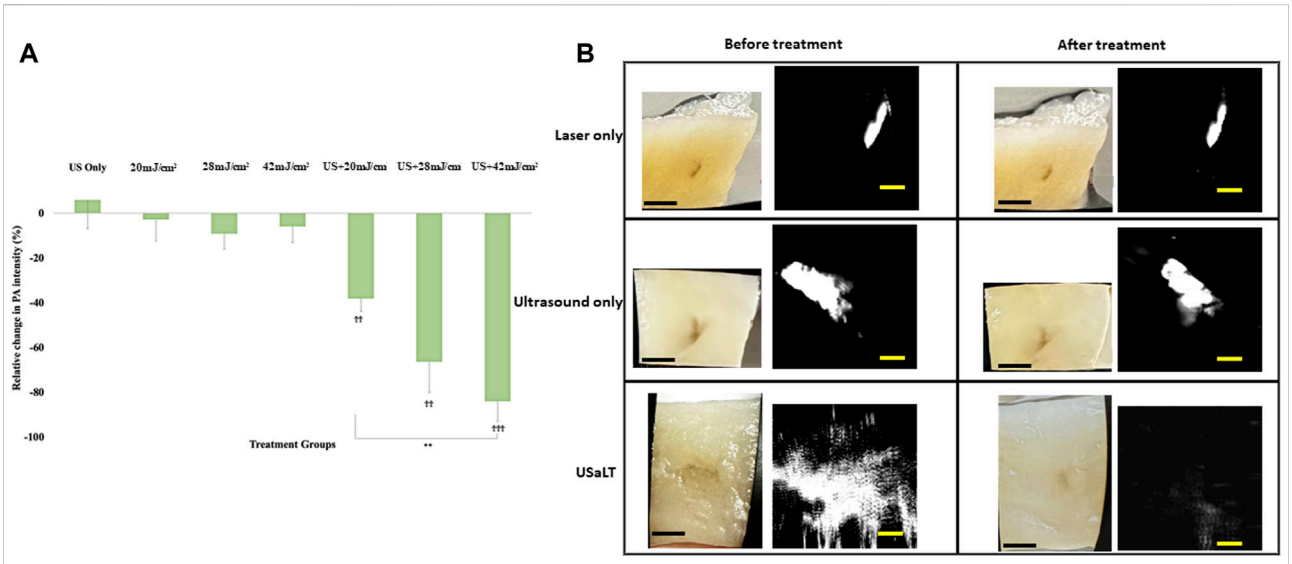

FIGURE 8
(A) Chicken breast photographs and photoacoustic (PA) images. Black scale bar = 2 mm; yellow scale bar = 500 μm. **(B)** Relative change in PA signal intensity for all treatment groups. "††" and "†††" indicate statistical significance of $p < 0.01$ and $p < 0.001$ between control and treatment groups, respectively. "**" indicates statistical significance of $p < 0.01$ between treatment groups respectively. n = 5. Laser only: 42 mJ/cm^2 light fluence at 532 nm wavelength; ultrasound only: 2 MPa PNP ultrasound pressure; USaLT: 42 mJ/cm^2 light fluence at 532 nm wavelength and 2 MPa PNP ultrasound pressure.

USaLT-induced tumor removal on *ex vivo* melanoma model with 532 nm optical wavelength

For all the control groups with ultrasound-only and laser-only treatment, there was no significant removal of melanoma cells at the chosen treatment parameters, as validated by the acquired PA images. However, the relative change in PA intensity was significantly decreased for all USaLT groups with 2 MPa PNP and different laser fluences in comparison with before-treatment PA intensity. The average decrease in PA intensity was 38.17% at 20 mJ/cm^2 ($p = 0.0001$, n = 5), 66.41% at 28 mJ/cm^2 ($p = 0.0013$, n = 5), and 84.03% at 42 mJ/cm^2 ($p < 0.0001$, n = 5) (Figures 8A, B). Furthermore, there was a 120% increase in reduction at 42 mJ/cm^2 ($p = 0.0029$, n = 5) when compared to 20 mJ/cm^2 for the USaLT groups concurrently applying 2 MPa PNP ultrasound. The H&E and Mallory staining showed only a few residual melanoma cells remaining after treatment in the USaLT group (Figure 9), while the ultrasound-only and the laser-only groups had the melanoma clusters intact after the treatment, indicating, at these power levels, ultrasound-only and laser-only were unable to remove melanoma cells, while USaLT can effectively damage melanoma cells. Further, for the USaLT group, while most of the melanoma cells were removed, the surrounding chicken breast tissue structure remained intact, demonstrating the treatment is highly selective.

Depth analysis for USaLT on *ex vivo* melanoma model

The treatment results shown in Figure 8 only demonstrated a treatment depth of ~1 mm due to the use of 532 nm. To treat deep regions, we switched to 1,064 nm optical wavelength, and the experiment was repeated. The melanoma side of sample was placed towards the laser for 532 nm laser. For the depth study, the melanoma side was placed towards the FUS transducer so that the laser beam had to pass through the entire sample of 3.5 mm before reaching the melanoma. We tested the treatment on a range of depths and found that 3.5 mm treatment depth is the maximum depth USaLT can be achieved with a laser fluence of 150 mJ/cm^2 at the top surface (laser side) (Figures 10A, B). Melanoma cells at a depth of 3.5 mm were not significantly removed by the laser-only treatment. However, the USaLT group with 2 MPa PNP ultrasound in combination with 150 mJ/cm^2 at 1,064 nm efficiently removed melanoma cells, resulting in a reduction of 57.96 ± 5.66% (n = 5, $p < 0.001$) in PA intensity (Figure 10A). The H&E and Mallory staining validated the tumor removal during USaLT with only residual melanoma cells and tumor network post-treatment (Figure 11). However, the laser-only treatment group still had the tumor structure present in both staining. Again, the chicken breast tissue structure was intact, demonstrating the treatment is highly selective.

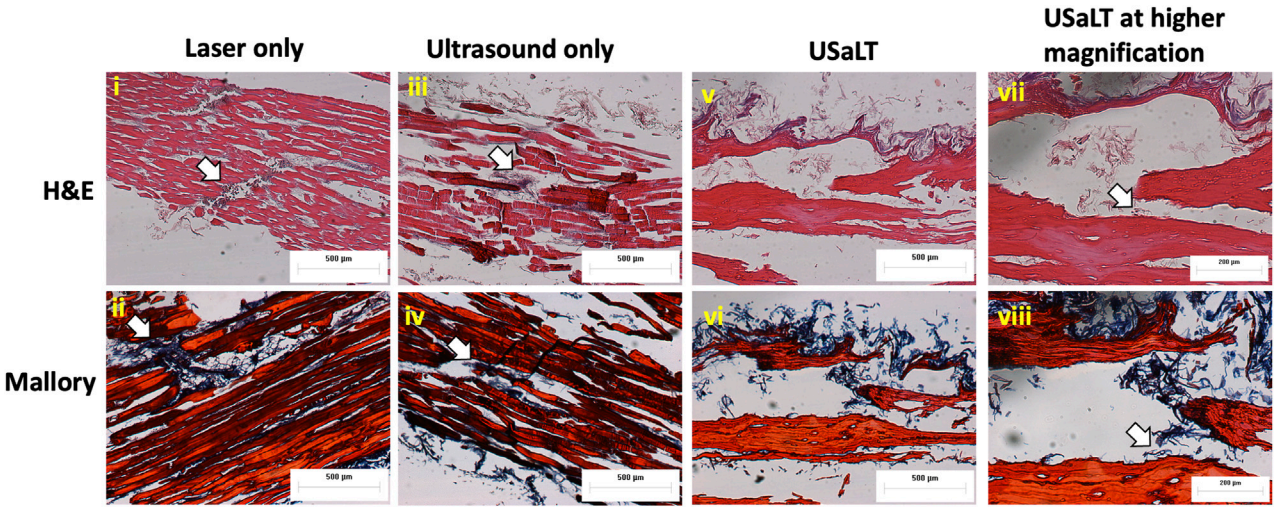

FIGURE 9
H&E and Mallory staining of (i-ii) laser only, (iii-iv) ultrasound only, and (v-viii) USaLT treatment groups. White arrows indicate the melanoma cells. Laser only: 42 mJ/cm^2 light fluence at 532 nm wavelength; ultrasound only: 2 MPa PNP ultrasound pressure; USaLT: 42 mJ/cm^2 light fluence at 532 nm wavelength and 2 MPa PNP ultrasound pressure.

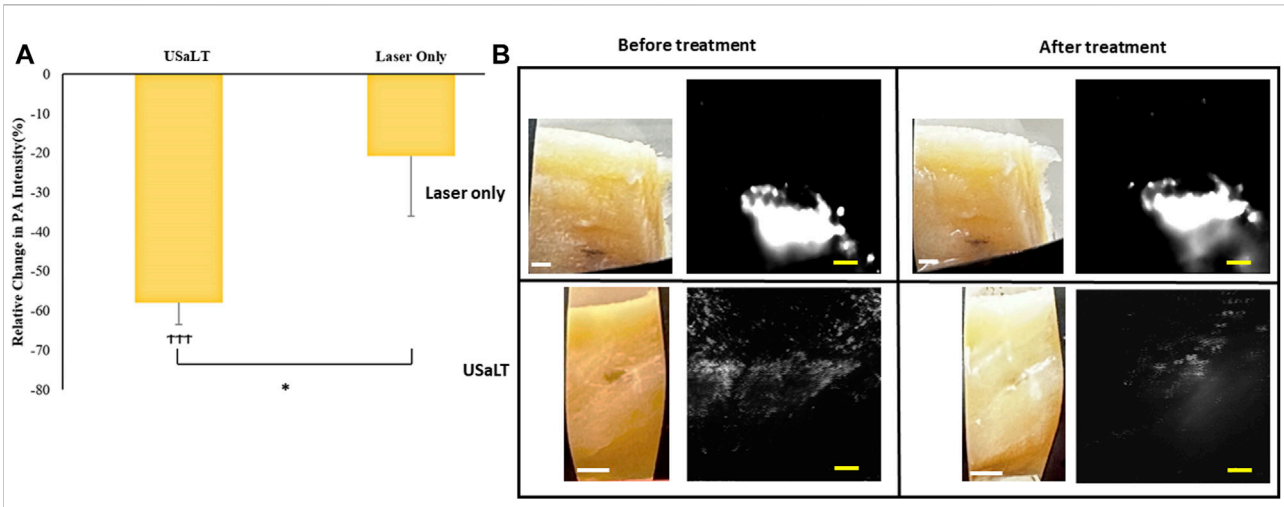

FIGURE 10
(A) Relative change in PA intensity (%) for all treatment groups "†††" indicates statistical significance with $p < 0.0001$ between control and treatment groups. "*" indicates $p < 0.05$ between treatment groups. n = 5. **(B)** Photographs and PA images of samples. Laser only: 150 mJ/cm^2 light fluence at 1,064 nm; USaLT: 150 mJ/cm^2 light fluence at 1,064 nm and 2 MPa PNP ultrasound pressure. White scale bar = 1 mm; yellow scale bar = 250 µm.

Discussion

We demonstrated that USaLT can selectively remove melanoma cells. At 532 nm, USaLT can be effective at as little as 20 mJ/cm^2 laser fluence per pulse, and the ablation efficiency increases as the laser fluence increases. However, due to high attenuation, the treatment depth is only limited to ~1 mm. With the 1,064 nm laser wavelength, where the optical attenuation of tissue is much weaker, USaLT was able to successfully remove the melanoma cells at a depth of about 3.5 mm with a laser surface fluence of about 150 mJ/cm^2 per pulse. During the treatment depth study, the laser beam needed to pass through a ~3 mm thickness of normal tissue before it reached the melanoma cells. The purpose of this study was to examine whether the remaining

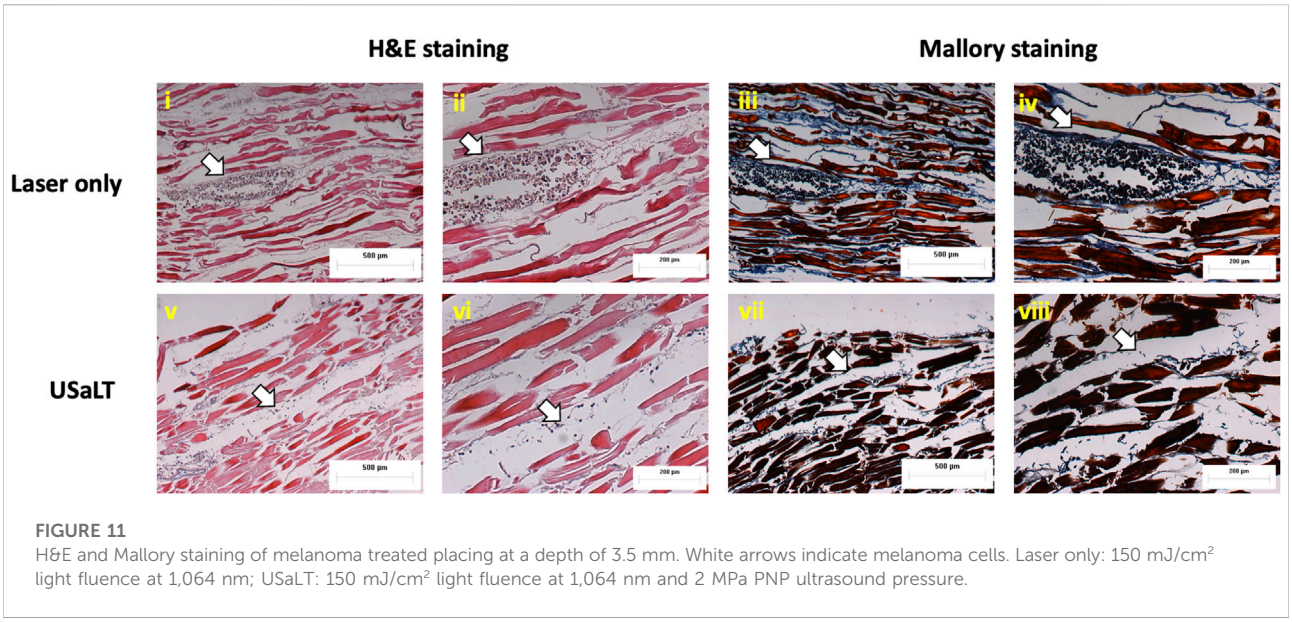

FIGURE 11
H&E and Mallory staining of melanoma treated placing at a depth of 3.5 mm. White arrows indicate melanoma cells. Laser only: 150 mJ/cm^2 light fluence at 1,064 nm; USaLT: 150 mJ/cm^2 light fluence at 1,064 nm and 2 MPa PNP ultrasound pressure.

laser energy would be sufficient for USaLT after the laser beam passed through a layer of tissue. This study did not explore the potential of USaLT treatment with respect to tumor thickness. In a real situation, the melanoma may be removed layer by layer during USaLT. In this case, laser beam will always and only need to pass through normal tissue after the top layer melanoma is selectively removed.

TTT, as a currently available treatment for choroidal melanoma, can efficiently treat at a depth of about 0.7–2 mm when using external agents and laser fluences >100 J/cm^2 [20, 22]. However, TTT causes complications such as superficial petechial and vitreous hemorrhages, macular edema, exudative and rhegmatogenous retinal detachment, retinal vascular occlusion and traction, optic disc atrophy, maculopathy, and extraocular tumor extension [21–23]. In addition, the treatment efficiency in TTT and PDT used for choroidal melanoma are also dependent on the dose of external agents raising safety concerns [13, 28]. In comparison, USaLT can reach 3.5 mm with great selectivity and is free of any external agents. While thermal-based laser therapy destroys all the cells in the heated region, USaLT selectively removes melanoma cells, and the adjacent chicken breast tissue cells remain intact.

As demonstrated in previous studies related to combining laser and FUS therapy such as PUT, the potential underlying mechanism of USaLT is enhanced cavitation. Laser-induced cavitation in high optical absorptive biological tissue, such as melanoma cells, can be further driven by the applied FUS. It is difficult or "tricky" to directly compare the laser fluence between USaLT and other existing laser therapies for melanoma because USaLT utilizes nanosecond pulsed laser while other laser therapies utilize CW lasers. In the current study, we used 5 min treatment duration, which corresponds to 180 J/cm^2 to 1350 J/cm^2 total laser fluence and is in a similar range with fluence used in the existing therapy. However, there is no hyperthermia effect in USaLT because a nanosecond laser is used. With great selectivity and without hyperthermia effect, USaLT can potentially offer safe and precise treatment, which can be significant for treating choroidal melanoma in the eye.

From the laser therapy point of view, this approach can avoid potential unwanted damage to surrounding tissue. From the FUS therapy point of view, ablation becomes much more selective because cavitation is only limited to optical absorptive biological tissues. In the current case, the high optical contrast between melanin and the surrounding tissue was used to achieve high selectivity eliminating the need for injection of any external agents for treatment or selectivity [56].

Similar to PUT, USaLT also involves a synchronous application of pulsed laser and ultrasound [55, 57] as both are dependent on the generation of cavitation bubbles through stress confinement rather than thermal effect and both use a lower laser fluence range. Therefore, USaLT eliminates the possibility of hyperthermic effects and the risk of scarring, which are potential challenges of currently available laser-based thermal therapies for melanoma. Hence, the melanoma destruction was achieved at a laser fluence of 150 mJ/cm^2 per pulse when assisted by ultrasound. As the treatment efficiency for the thermal effect is dependent on the thermal relaxation time, stress confinement is dependent on stress relaxation time. Depending on the size of the melanosomes, the maximum treatment efficiency for thermal therapies could be achieved by using 0.25–1 μs lasers [35]. Moreover, for a 10 nm melanin granule, the stress relaxation time is 7 ps [58]. Hence, in the future, a picosecond laser will be used to facilitate photomechanical disruption for a more efficient melanoma treatment at reduced laser fluence similar to a study

involving a 630 nm PDT-based *in vitro* melanoma treatment with a femtosecond laser, but without requiring any external agents [59].

We also presented a novel *ex vivo* melanoma tumor model in the current study. The *ex vivo* model used here is hypothesized to be feeding on chicken tissue in addition to the cell culture medium for growth. Further, the histological procedure showed that the cancer cells adhered to the adipose tissue and grew on it indicating that it could absorb nutrients that were already present in the tissue. In the future, the cell growth using various dead tissue extracts to get a clear insight. The motivation behind growing the cells in dead tissue is to facilitate the efficacy of cancer-based studies like drug and treatment evaluation when compared to cell-based *in vitro* studies. The nutrients present in the chicken breast tissue including intramuscular fat, collagen, and protein might have aided in the growth of cancer cells on them [60]. Since the model required for this study needed a visible tumor for evaluation, the injection zone is restricted to 1.75 mm from the surface. However, the cells were able to grow when injected deeply into the chicken breast.

All tumor samples were prepared applying the same procedure. Every tumor sample presented in this sample was distinct visually due to metastatic tumor growth, even though the same cell passage and same number of cells were injected and incubated for the same amount of time. In the presented histology results, the tumor was deeper which substantiates the fact that the black tumor spot visible in the photograph is restricted to the surface. Further, the laser beam size was 6 mm in diameter, and the FUS focal spot was 3 mm in diameter. Hence, USaLT, which is dependent on the spatial synchronized laser and FUS, had a treatment region of 3 mm. During all the experiments, the treatment area covered a 3-mm tumor region. The relative PA signal change was calculated for each sample before and after the treatment. These changes were compared between different samples to minimize the effect induced by the size difference between tumor samples.

Since this is the first study reporting the growth of cancer cells in dead tissue, two staining techniques H&E and Mallory were performed to validate tumor growth in the model. H&E is a gold standard histological staining used for cells and tissues; it highlights melanoma cells in brown color. Mallory is used extensively for fibrous tissue and chicken breast tissue is a muscle fiber; in addition, Mallory also stains melanoma cells and was used for substantiation of H&E stain as the model used in this study was novel.

The absorption coefficient of a single melanosome is 550 cm^{-1} at 532 nm and 55 cm^{-1} at 1,064 nm [61, 62]. The absorption coefficient of chicken breast tissue is 0.7 cm^{-1} at 532 nm [63, 64] and 0.01 cm^{-1} at 1,064 nm [65]. The difference in their optical absorption produces contrast in PA imaging and selectivity during treatment. As the difference in optical absorption between melanin and surrounding tissue is used for the selective targeting of melanoma during USaLT, a relatively higher difference will provide better selectivity. Also, it is pertinent to work at a wavelength that can provide high absorption for melanin when compared to blood. The relative absorption of melanin with respect to blood is maximum at 755 nm (54:1), followed by 1,064 nm (16:1) and then 532 nm (2.4:1) [66]. Hence, considering the penetration depth and optical absorption for selectivity 1,064 nm, it might be the ideal wavelength for further *in vivo* studies.

The study reported here is a preliminary study to evaluate the proof-of-concept for using PUT-based USaLT for treating melanoma. In this study, tumor removal using USaLT was confirmed with an *ex vivo* model. The motivation behind using the tumor model is that it allows us to examine the selectivity and depth of treatment of USaLT, which would be otherwise not possible with other *in vitro* studies. Since USaLT is based on PUT, it is hypothesized that the destruction of cells occurs through the mechanical cavitation effect due to the combined effect of laser and ultrasound which at a similar level independently cannot induce any cell damage. Detailed mechanism of action and safety study will need to be carried out *in vivo* in the future, particularly if USaLT is used to treat metastatic melanoma. The potential application of this technique to choroidal melanoma should be evaluated and compared with the current thermal-based laser therapies. Further, while the current study focused on cell death induced by USaLT, other interesting future studies are to examine whether USaLT can stimulate cell metabolism and reproduction, and promote tissue healing. With the improved treatment depth, USaLT can affect cells deeper in tissue than pure optical techniques.

Although the treatment depth can be improved in comparison with pure optical techniques, the most significant limitation of USaLT is still its depth of treatment. The current study demonstrated a treatment depth of up to 3.5 mm through chicken breast tissue. This treatment depth may significantly limit the adoption of USaLT other than for the treatment of choroidal melanoma, where a clear optical path exists.

In the future, a real-time PA image-guided USaLT system may be developed to provide instant feedback on the treatment, and the cavitation mechanism behind cell death should also be further investigated. In addition, in an *in vivo* animal melanoma model, the potential of USaLT to induce immune response should be evaluated.

Conclusion

To summarize, this study is the first study to successfully demonstrate the potential of a PUT-based USaLT technique involving the synchronous application of laser and FUS to destroy melanoma. Initial investigation with 532 nm showed that USaLT could selectively remove melanoma. Further, USaLT showed the selective removal of melanoma cells at relatively low

laser fluence per pulse. Also, at 1,064 nm, a higher optical wavelength, a treatment depth of 3.5 mm could be achieved with USaLT. The histological analysis substantiated that USaLT treatment removed melanoma cells while sparing the surrounding tissue. Further, the laser and ultrasound-only treatment at similar energy levels did not result in the removal of the melanoma. This study demonstrated the potential of PUT-based USaLT for the treatment of melanoma without the need for injection of any external agents into the body.

Data availability

The raw data supporting the conclusions of this article will be made available by the authors, without undue reservation.

Ethics statement

Ethical approval was not required for the studies on animals in accordance with the local legislation and institutional requirements because only commercially available established cell lines were used.

Author contributions

MS: experimental design, experimental investigation, data analysis, writing original draft, review, and editing. XY: conceptualization, experimental design, supervision, data analysis, funding acquisition, writing review and editing. XW: conceptualization, funding acquisition, writing review and editing. ER-M: Histological study design, implementation, data analysis, and supervision, writing review and editing. NM-R: Histological study implementation, data analysis, writing review and editing. All authors contributed to the article and approved the submitted version.

Funding

The author(s) declare financial support was received for the research, authorship, and/or publication of this article. The work is partially supported by R01EY029489 and R01NS118918.

Conflict of interest

The authors declare that the research was conducted in the absence of any commercial or financial relationships that could be construed as a potential conflict of interest.

Supplementary material

The Supplementary Material for this article can be found online at: https://www.ebm-journal.org/articles/10.3389/ebm.2024.10096/full#supplementary-material

SUPPLEMENTARY FIGURE S1
Validation of Mallory stain for muscle fibers with mouse pancreas.

References

1. George J, Nihal M, Singh CK, Zhong W, Liu X, Ahmad N. Pro-proliferative function of mitochondrial sirtuin deacetylase SIRT3 in human melanoma. *J Invest Dermatol* (2016) **136**:809–18. doi:10.1016/j.jid.2015.12.026

2. Viale PH. The American Cancer Society's facts & figures: 2020 edition. *J Adv Pract Oncol* (2020) **11**:135–6. doi:10.6004/jadpro.2020.11.2.1

3. Soliman N, Mamdouh D, Elkordi A. Choroidal melanoma: a mini review. *Medicines* (2023) **10**:11. doi:10.3390/medicines10010011

4. Krantz BA, Dave N, Komatsubara KM, Marr BP, Carvajal RD. Uveal melanoma: epidemiology, etiology, and treatment of primary disease. *Clin Ophthalmol* (2017) **11**:279–89. doi:10.2147/opth.s89591

5. Violanti SS, Bononi I, Gallenga CE, Martini F, Tognon M, Perri P. New insights into molecular oncogenesis and therapy of uveal melanoma. *Cancers* (2019) **11**:694. doi:10.3390/cancers11050694

6. Ferlay J, Colombet M, Soerjomataram I, Parkin DM, Piñeros M, Znaor A, et al. Cancer statistics for the year 2020: an overview. *Int J Cancer* (2021) **149**:778–89. doi:10.1002/ijc.33588

7. Novikova IN, Potapova EV, Dremin VV, Dunaev AV, Abramov AY. Laser-induced singlet oxygen selectively triggers oscillatory mitochondrial permeability transition and apoptosis in melanoma cell lines. *Life Sci* (2022) **304**:120720. doi:10.1016/j.lfs.2022.120720

8. Khorsandi K, Kianmehr Z, Hosseinmardi Z, Hosseinzadeh R. Anti-cancer effect of gallic acid in presence of low level laser irradiation: ROS production and induction of apoptosis and ferroptosis. *Cancer Cel Int* (2020) **20**:18–4. doi:10.1186/s12935-020-1100-y

9. Aaberg TM, Jr. Laser for choroidal melanoma. *Int Ophthalmol Clin* (2006) **46**:15–26. doi:10.1097/01.iio.0000195857.38947.37

10. Zou L, Wang H, He B, Zeng L, Tan T, Cao H, et al. Current approaches of photothermal therapy in treating cancer metastasis with nanotherapeutics. *Theranostics* (2016) **6**:762–72. doi:10.7150/thno.14988

11. Phan TTV, Bui NQ, Cho S-W, Bharathiraja S, Manivasagan P, Moorthy MS, et al. Photoacoustic imaging-guided photothermal therapy with tumor-targeting HA-FeOOH@PPy nanorods. *Scientific Rep* (2018) **8**:8809. doi:10.1038/s41598-018-27204-8

12. Zhang Y, Zhan X, Xiong J, Peng S, Huang W, Joshi R, et al. Temperature-dependent cell death patterns induced by functionalized gold nanoparticle photothermal therapy in melanoma cells. *Scientific Rep* (2018) **8**:8720. doi:10.1038/s41598-018-26978-1

13. Xu P, Ning P, Wang J, Qin Y, Liang F, Cheng Y. Precise control of apoptosis via gold nanostars for dose dependent photothermal therapy of melanoma. *J Mater Chem B* (2019) **7**:6934–44. doi:10.1039/c9tb01956a

14. Yang T, Ren H, Zhang W, Rong L, Zhang D. Resveratrol-coated gold nanoflowers for CT imaging and apoptosis/photothermal synergistic therapy of malignant melanoma. *ACS omega* (2023) **8**:34629–39. doi:10.1021/acsomega.3c03538

15. Heiskanen V, Hamblin MR. Photobiomodulation: lasers vs. light emitting diodes? *Photochemical Photobiological Sci* (2018) **17**:1003–17. doi:10.1039/c8pp00176f

16. de Souza Contatori CG, Silva CR, de Toledo Pereira S, Rodrigues MFSD, de Lima Luna AC, Marques MM, et al. Responses of melanoma cells to

photobiomodulation depend on cell pigmentation and light parameters. *J Photochem Photobiol B: Biol* (2022) **235**:112567. doi:10.1016/j.jphotobiol.2022.112567

17. Austin E, Huang A, Wang JY, Cohen M, Heilman E, Maverakis E, et al. Red light phototherapy using light-emitting diodes inhibits melanoma proliferation and alters tumor microenvironments. *Front Oncol* (2022) **12**:928484. doi:10.3389/fonc.2022.928484

18. Ottaviani G, Martinelli V, Rupel K, Caronni N, Naseem A, Zandonà L, et al. Laser therapy inhibits tumor growth in mice by promoting immune surveillance and vessel normalization. *EBioMedicine* (2016) **11**:165–72. doi:10.1016/j.ebiom.2016.07.028

19. Houston SK, Wykoff CC, Berrocal AM, Hess DJ, Murray TG. Lasers for the treatment of intraocular tumors. *Lasers Med Sci* (2013) **28**:1025–34. doi:10.1007/s10103-012-1052-0

20. Maheshwari A, Finger PT. Laser treatment for choroidal melanoma: current concepts. *Surv Ophthalmol* (2023) **68**:211–24. doi:10.1016/j.survophthal.2022.05.002

21. Saakian S, Val'skiĭ V, Semenova E, Amirian A. Transpupillary thermotherapy in the treatment of recurrent and residual choroidal melanomas: preliminary results. *Vestnik Oftalmologii* (2009) **125**:11–5.

22. Chojniak MM, Chojniak R, Nishimoto IN, Allemann N, Erwenne CM. Primary transpupillary thermotherapy for small choroidal melanoma. *Graefe's Archive Clin Exp Ophthalmol* (2011) **249**:1859–65. doi:10.1007/s00417-011-1733-6

23. Mashayekhi A, Shields CL, Rishi P, Atalay HT, Pellegrini M, McLaughlin JP, et al. Primary transpupillary thermotherapy for choroidal melanoma in 391 cases: importance of risk factors in tumor control. *Ophthalmology* (2015) **122**:600–9. doi:10.1016/j.ophtha.2014.09.029

24. Roelofs KA, Fabian ID, Arora AK, Cohen VM, Sagoo MS. Long-term outcomes of small pigmented choroidal melanoma treated with primary photodynamic therapy. *Ophthalmol Retina* (2021) **5**:468–78. doi:10.1016/j.oret.2020.08.019

25. Austin E, Mamalis A, Ho D, Jagdeo J. Laser and light-based therapy for cutaneous and soft-tissue metastases of malignant melanoma: a systematic review. *Arch Dermatol Res* (2017) **309**:229–42. doi:10.1007/s00403-017-1720-9

26. Naidoo C, Kruger CA, Abrahamse H. Targeted photodynamic therapy treatment of *in vitro* A375 metastatic melanoma cells. *Oncotarget* (2019) **10**:6079–95. doi:10.18632/oncotarget.27221

27. Akasov RA, Sholina N, Khochenkov D, Alova A, Gorelkin P, Erofeev A, et al. Photodynamic therapy of melanoma by blue-light photoactivation of flavin mononucleotide. *Scientific Rep* (2019) **9**:9679. doi:10.1038/s41598-019-46115-w

28. Rundle P. Treatment of posterior uveal melanoma with multi-dose photodynamic therapy. *Br J Ophthalmol* (2014) **98**:494–7. doi:10.1136/bjophthalmol-2013-304432

29. Fabian I, Stacey A, Papastefanou V, Al Harby L, Arora A, Sagoo M, et al. Primary photodynamic therapy with verteporfin for small pigmented posterior pole choroidal melanoma. *Eye* (2017) **31**:519–28. doi:10.1038/eye.2017.22

30. Fabian ID, Stacey AW, Harby LA, Arora AK, Sagoo MS, Cohen VM. Primary photodynamic therapy with verteporfin for pigmented posterior pole cT1a choroidal melanoma: a 3-year retrospective analysis. *Br J Ophthalmol* (2018) **102**:1705–10. doi:10.1136/bjophthalmol-2017-311747

31. Li J, Xue Y, Tian J, Liu Z, Zhuang A, Gu P, et al. Fluorinated-functionalized hyaluronic acid nanoparticles for enhanced photodynamic therapy of ocular choroidal melanoma by ameliorating hypoxia. *Carbohydr Polym* (2020) **237**:116119. doi:10.1016/j.carbpol.2020.116119

32. Goldberg D, Kothare A, Doucette M, Kaur A, Ronan S, Fromowitz J, et al. Selective photothermolysis with a novel 1726 nm laser beam: a safe and effective solution for acne vulgaris. *J Cosmet Dermatol* (2023) **22**:486–96. doi:10.1111/jocd.15602

33. Anderson RR, Parrish JA. Selective photothermolysis: precise microsurgery by selective absorption of pulsed radiation. *Science* (1983) **220**:524–7. doi:10.1126/science.6836297

34. Le L, Sirés-Campos J, Raposo G, Delevoye C, Marks MS. Melanosome biogenesis in the pigmentation of mammalian skin. *Integr Comp Biol* (2021) **61**:1517–45. doi:10.1093/icb/icab078

35. Bukvić Mokoš Z, Lipozenčić J, Čeović R, Štulhofer Buzina D, Kostović K. The first international congress 'current state in corrective dermatology: lasers and fillers' zagreb, october 1-2, 2010. *Acta dermatovenerologica Croatica: ADC* (2010) **18**(0-0):315–6.

36. Tanzi EL, Lupton JR, Alster TS. Lasers in dermatology: four decades of progress. *J Am Acad Dermatol* (2003) **49**:1–34. doi:10.1067/mjd.2003.582

37. Lee JD, Oh MJM. Q-switched ruby laser, absorption coefficient, and spot size effect. In: *Lasers in dermatology: parameters and choice: with special reference to the asian population*. Springer (2023). p. 49–55.

38. John HE, Mahaffey PJ. Laser ablation and cryotherapy of melanoma metastases. *J Surg Oncol* (2014) **109**:296–300. doi:10.1002/jso.23488

39. Li X, Naylor MF, Le H, Nordquist RE, Teague TK, Howard CA, et al. Clinical effects of *in situ* photoimmunotherapy on late-stage melanoma patients: a preliminary study. *Cancer Biol Ther* (2010) **10**:1081–7. doi:10.4161/cbt.10.11.13434

40. Naylor MF, Chen WR, Teague TK, Perry L, Nordquist RE. *In situ* photoimmunotherapy: a tumour-directed treatment for melanoma. *Br J Dermatol* (2006) **155**:1287–92. doi:10.1111/j.1365-2133.2006.07514.x

41. St Pierre SA, Rommel J, Ciurea A, Fife D, Yoo SS, Martini M, et al. *In situ* photoimmunotherapy: a surgery-and limb-sparing approach to the treatment of cutaneous metastases in advanced melanoma. *Arch Dermatol* (2010) **146**:831–4. doi:10.1001/archdermatol.2010.181

42. Ash C, Dubec M, Donne K, Bashford T. Effect of wavelength and beam width on penetration in light-tissue interaction using computational methods. *Lasers Med Sci* (2017) **32**:1909–18. doi:10.1007/s10103-017-2317-4

43. Mineroff J, Austin E, Jagdeo J. Cutaneous effects of photobiomodulation with 1072 nm light. *Arch Dermatol Res* (2022) **315**:1481–6. doi:10.1007/s00403-022-02480-7

44. Kaub L, Schmitz C. Comparison of the penetration depth of 905 nm and 1064 nm laser light in surface layers of biological tissue *ex vivo*. *Biomedicines* (2023) **11**:1355. doi:10.3390/biomedicines11051355

45. Zhang L, Orsi F, Arnone P, Chen W. High intensity focused ultrasound ablation: a new therapeutic option for solid tumors. *J Cancer Res Ther* (2010) **6**:414–20. doi:10.4103/0973-1482.77064

46. Li H, Yuan SM, Yang M, Zha H, Li XR, Sun H, et al. High intensity focused ultrasound inhibits melanoma cell migration and metastasis through attenuating microRNA-21-mediated PTEN suppression. *Oncotarget* (2016) **7**:50450–60. doi:10.18632/oncotarget.10433

47. Malietzis G, Monzon L, Hand J, Wasan H, Leen E, Abel M, et al. High-intensity focused ultrasound: advances in technology and experimental trials support enhanced utility of focused ultrasound surgery in oncology. *Br J Radiol* (2013) **86**:20130044. doi:10.1259/bjr.20130044

48. Hazlewood D, Yang X. Enhanced laser surface ablation with an integrated photoacoustic imaging and high intensity focused ultrasound system. *Lasers Surg Med* (2019) **51**:616–24. doi:10.1002/lsm.23072

49. Zhang H, Xie X, Li J, Qin Y, Zhang W, Cheng Q, et al. Removal of choroidal vasculature using concurrently applied ultrasound bursts and nanosecond laser pulses. *Scientific Rep* (2018) **8**:12848. doi:10.1038/s41598-018-31045-w

50. Li S, Qin Y, Wang X, Yang X. Bubble growth in cylindrically-shaped optical absorbers during photo-mediated ultrasound therapy. *Phys Med Biol* (2018) **63**:125017. doi:10.1088/1361-6560/aac7bc

51. Hu Z, Zhang H, Mordovanakis A, Paulus Y, Liu Q, Wang X, et al. High-precision, non-invasive anti-microvascular approach via concurrent ultrasound and laser irradiation. *Scientific Rep* (2017) **7**:40243. doi:10.1038/srep40243

52. Cui H, Zhang T, Yang X. Laser-enhanced cavitation during high intensity focused ultrasound: an *in vivo* study. *Appl Phys Lett* (2013) **102**:133702. doi:10.1063/1.4800780

53. Hu Z, Zhang H, Mordovanakis A, Paulus YM, Liu Q, Wang X, et al. High-precision, non-invasive anti-microvascular approach via concurrent ultrasound and laser irradiation. *Scientific Rep* (2017) **7**:40243–12. doi:10.1038/srep40243

54. Cui H, Yang X. Enhanced-heating effect during photoacoustic imaging-guided high-intensity focused ultrasound. *Appl Phys Lett* (2011) **99**:231113. doi:10.1063/1.3669441

55. Qin Y, Yu Y, Xie X, Zhang W, Fu J, Paulus Y, et al. The effect of laser and ultrasound synchronization in photo-mediated ultrasound therapy. *IEEE Trans Bio-medical Eng* (2020) **67**:3363–70. doi:10.1109/tbme.2020.2985648

56. Jacques SL. Optical properties of biological tissues: a review. *Phys Med Biol* (2013) **58**:R37–R61. doi:10.1088/0031-9155/58/11/r37

57. Subramanian Karthikesh M, Wu S, Singh R, Paulus Y, Wang X, Yang X. Effect of photo-mediated ultrasound therapy on nitric oxide and prostacyclin from endothelial cells. *Appl Sci* (2022) **12**:2617. doi:10.3390/app12052617

58. Jacques SL, Oraevsky AA, Thompson CR, Gerstman BS. Working theory and experiments on photomechanical disruption of melanosomes to explain the threshold for minimal visible retinal lesions for sub-ns laser pulses. *Laser-tissue Interaction V; Ultraviolet Radiat Hazards: SPIE* (1994) 54–65. doi:10.1117/12.182967

59. Kars MD, Yıldırım G, Gündoğdu Y, Gönce F, Ayan E, Kılıç HŞ. Revealing the therapeutic effects of aminolevulinate mediated femtosecond laser induced photochemotherapy in different cancer cells. *Eurobiotech J* (2020) **4**:207–15. doi:10.2478/ebtj-2020-0024

60. Chen Y, Qiao Y, Xiao Y, Chen H, Zhao L, Huang M, et al. Differences in physicochemical and nutritional properties of breast and thigh meat from crossbred chickens, commercial broilers, and spent hens. *Asian-australasian J Anim Sci* (2015) **29**:855–64. doi:10.5713/ajas.15.0840

61. Jacques SL, McAuliffe DJ. The melanosome: threshold temperature for explosive vaporization and internal absorption coefficient during pulsed laser irradiation. *Photochem Photobiol* (1991) **53**:769–75. doi:10.1111/j.1751-1097.1991.tb09891.x

62. Jacques SL. Melanosome absorption coefficient. *Oreg Med Laser Cent* (1998) **7**.

63. Marquez G, Wang LV, Lin S-P, Schwartz JA, Thomsen SL. Anisotropy in the absorption and scattering spectra of chicken breast tissue. *Appl Opt* (1998) **37**:798–804. doi:10.1364/ao.37.000798

64. Raymond JL, Cleveland RO, Roy RA. HIFU-induced changes in optical scattering and absorption of tissue over nine orders of thermal dose. *Phys Med Biol* (2018) **63**:245001. doi:10.1088/1361-6560/aaed69

65. Adams MT, Cleveland RO, Roy RA. Modeling-based design and assessment of an acousto-optic guided high-intensity focused ultrasound system. *J Biomed Opt* (2017) **22**:017001. doi:10.1117/1.jbo.22.1.017001

66. Tanghetti Md E, Jennings J. A comparative study with a 755 nm picosecond Alexandrite laser with a diffractive lens array and a 532 nm/1064 nm Nd: YAG with a holographic optic. *Lasers Surg Med* (2018) **50**:37–44. doi:10.1002/lsm.22752

EBM Experimental Biology and Medicine

TYPE Original Research
PUBLISHED 14 October 2024
DOI 10.3389/ebm.2024.10119

OPEN ACCESS

*CORRESPONDENCE
Xuemei Zhang,
zhangxuemei@cqmu.edu.cn

RECEIVED 22 February 2023
ACCEPTED 27 September 2024
PUBLISHED 14 October 2024

CITATION
Xiao J, Liu B, Yin Y and Zhang X (2024) Immunization with recombinant *Streptococcus pneumoniae* PgdA protects mice against lung invasion. *Exp. Biol. Med.* 249:10119. doi: 10.3389/ebm.2024.10119

Immunization with recombinant *Streptococcus pneumoniae* PgdA protects mice against lung invasion

Jiangming Xiao[1,2], Bichen Liu[2], Yibing Yin[2] and Xuemei Zhang[2]*

[1]Department of Laboratory Medicine, Chongqing General Hospital, Chongqing University, Chongqing, China, [2]Department of Laboratory Medicine, Key Laboratory of Diagnostic Medicine (Ministry of Education), Chongqing Medical University, Chongqing, China

Abstract

Current pneumococcal vaccines, including the pneumococcal polysaccharide (PPV23) and conjugate (PCV13) vaccines, offer protection against specific serotypes but pose risks of serotype replacement that can alter the composition of the nasopharyngeal microbiota. To address this challenge, a novel strategy has been proposed to provide effective protection without disrupting the colonization of other bacterial populations. In our study, we found that subcutaneous immunization with recombinant peptidoglycan N-acetylglucosamine deacetylase A (rPgdA) elicited robust humoral and cellular immune responses, significantly reducing the invasion of *Streptococcus* pneumoniae in the lungs without affecting nasopharyngeal carriage. Furthermore, rPgdA antisera were shown to diminish bacterial invasion of lung epithelial cells *in vitro*. Notably, sera from patients with invasive pneumococcal infections exhibited higher levels of antibodies against the PgdA protein compared to sera from healthy adults, suggesting that a natural immune response to this protein occurs during infection. These results suggest a promising new target for the development of pneumococcal vaccines.

KEYWORDS

***Streptococcus* pneumoniae, PgdA, vaccine candidate, novel strategy, colonization**

Impact statement

Long-term vaccination strategies against *Streptococcus pneumoniae* have focused on eliminating asymptomatic carriage and disease, leading to changes in the colonizing microbiota with unknown future consequences. As a result, a novel strategy for providing effective protection while allowing potential bacterial populations, such as *S. pneumoniae*, to colonize has been proposed. In this context, we show that PgdA immunization can significantly reduce pneumococcal invasion of the lungs without affecting carriage. These findings may provide a new candidate protein vaccine for the development of new immunization strategies for pneumococcal diseases.

Introduction

Streptococcus pneumoniae is a natural component of human nasopharyngeal microbiota, but it is also an important pathogen of various respiratory tract illnesses and invasive diseases, including community-acquired pneumonia, sepsis, meningitis, sinusitis and otitis media [1, 2]. Pneumococcal illness affects over one million children under the age of five annually around the world, and the mortality rate is roughly 200,000 [2]. Additionally, *S. pneumoniae* is one of the most significant drug-resistant bacteria in the world and is in urgent need of novel treatments, according to the World Health Organization. Due to the potential life threat of *S. pneumoniae* and the increase of its drug resistance, vaccination has become the most effective method to prevent pneumococcal diseases.

Current vaccines based on the capsular polysaccharide of *S. pneumoniae*, including the 23-valent pneumococcal polysaccharide vaccine (PPV23) and pneumococcal conjugate vaccines (PCVs), have successfully reduced the incidence of invasive pneumococcal diseases and the transmission of vaccine serotypes, providing substantial benefits to public health. However, numerous epidemiological studies have shown that while the introduction of PCVs significantly decreased the nasopharyngeal carriage rate of vaccine-covered serotypes, it also led to a significant increase in the carriage rate of non-vaccine serotypes [3–7]. Additionally, the prevalence of other bacteria, such as *Haemophilus influenzae* and *Staphylococcus aureus*, tends to rise with the introduction of PCVs [8–11]. Research has also demonstrated that the nasopharyngeal microbiota, including *S. pneumoniae*, can prevent the spread of potentially more dangerous pathogens like *Streptococcus pyogenes* and *S. aureus* through competitive rejection [12, 13]. These studies suggest that an indirect effect of PCV vaccination might be the disruption of the nasopharyngeal microbiota, leading to various clinical issues that cannot be disregarded. Consequently, some researchers have proposed a novel immunization strategy to combat pneumococcal disease: a vaccine candidate that can elicit an immune response and prevent the occurrence and development of pneumococcal disease while having no impact on the colonization of potential bacteria in the nasopharynx [14, 15]. Greene et al. verified the potential feasibility of this strategy using pneumococcal surface protein A (PspA) in a pneumococcal disease model caused by influenza virus [14]. Therefore, we aim to explore whether other pneumococcal proteins might have similar protective functions.

Peptidoglycan N-acetylglucosamine deacetylase (PgdA), encoded by the *pgdA* gene, can deacetylate peptidoglycan and make pneumococcus more resistant to host lysozyme, thus increasing the virulence of *S. pneumoniae* [16, 17]. The importance of PgdA for virulence has also been demonstrated in other pathogens, such as *Listeria*, *Enterococcus faecalis*, *Streptococcus suis*, and *Streptococcus iniae* [16, 18–21]. The *pgdA* variants have also been shown to be involved in penicillin resistance [22]. Therefore, some researchers have taken PgdA as an antibacterial target to search for inhibitors that inhibit the activity of PgdA [23, 24]. A recent study showed that PgdA immunization could not reduce the colonization of *S. pneumoniae* TIGR4 strain in the nasopharynx due to capsule factors. However, whether PgdA immunization can protect against invasive pneumococcal disease remains unclear. In addition, our previous study showed that *pgdA* is an *in vivo* inducible gene, and its expression is markedly elevated during lung tissue infection [25], suggesting that it is crucial to the pathogenesis of *S. pneumoniae*. Therefore, in this study, we subcutaneously inoculated recombinant PgdA into mice to study whether the vaccine can effectively prevent the invasive disease of *S. pneumoniae* without impacting the colonization of *S. pneumoniae* in the nasopharynx.

Materials and methods

Construction of rPgdA expression plasmid

Since full-length membrane proteins are difficult to obtain, we chose the extracellular domains for expression. The transmembrane region of PgdA was predicted by TMHMM[1], and amino acids of the extracellular domain at positions 39 to 463 were selected as the sequence of the recombinant protein. The corresponding gene fragment of *pgdA* was amplified by PCR from chromosomal DNA isolated from *S. pneumoniae* TIGR4 with the primers TAGCTCTTCAAAGCTTTGAAGATCTAC CAGCAAAAAAG and TACTCGAGTTATTCATCACGACTA TAGTACA using the PrimeSTAR PCR reagent kit (Takara). The following conditions were used for amplification: 94°C for 10 min, 34 cycles of 94°C for 30 s, 58°C for 30 s, 72°C for 10 min, and one final extension step of 72°C for 10 min. Then the PCR fragments were digested with NdeI/XhoI enzymes and cloned into the corresponding restriction sites in pPAL7 with T4 DNA Ligase (New England BioLabs) to generate plasmid pPAL7-PgdA, forming a sequence that encodes a fusion protein of profinity eXact tag-PgdA. The expression vector was finally identified by sequencing.

Protein expression and purification

The recombinant PgdA (rPgdA) was obtained and purified according to the instruction manual of Profinity eXact™ Protein Purification System (BIORAD). Briefly, the expression plasmid was transformed into BL21 (DE3) for protein expression. The

1 http://www.cbs.dtu.dk/services/TMHMM/

monoclonal colony was selected and cultured in 5 mL of LB supplemented with 100 μg/mL ampicillin until OD_{600} = 0.5 at 37°C with shaking at 180 rpm. Then the activated bacterial solution was added into 500 mL of LB containing 100 μg/mL ampicillin and the mixture was further cultured at 37°C with shaking at 180 rpm until OD_{600} = 0.5. The target protein was induced by shaking at 20°C for about 10 h at a concentration of 0.5 mM isopropyl-β-D-thiogalactopyranoside (IPTG). The cells were harvested by centrifugation followed by wash twice and resuspended with 25 mL of Wash Buffer (0.1 M sodium phosphate, pH 7.2). The bacteria were then destroyed by 25% strength ultrasonic (10 s ON and 10 s OFF) in the ice bath. The supernatant containing the protein was collected by centrifugation followed by sterile filtration with 0.22 μm Millex-GP Filter Unit (Millipore). The chilled (4°C) cell lysate was then loaded into the column packed with 4 mL of Profinity eXact resin and washed with Wash Buffer for three times. After that, the column was incubated at 4°C for overnight with 5 mL of Elution Buffer (0.1 M sodium phosphate, 0.1 M sodium fluoride, pH 7.2) before the tag-free protein was eluted and collected. Endotoxin was removed by the ToxinEraser™ Endotoxin Removal Kit (GenScript). SDS-PAGE and Coomass Bright Blue staining were used to identify protein size and purity.

Animals

Female 6–8-week-old C57BL/6J mice used in this study were purchased from and raised at Chongqing Medical University, Chongqing, China. All animal experiments involved in this paper were approved by the Animal Care and Use Committee of the Chongqing Medical University.

Bacterial strains and growth conditions

S. pneumoniae type 2 strain D39 was purchased from the National Collection of Type Cultures (London, United Kingdom). *S. pneumoniae* type 4 strain TIGR4 was obtained from the American Type Culture Collection (ATCC; Manassas, VA, United States). The other *S. pneumoniae* strains including serotype 1 (CMCC 31109), serotype 3 (CMCC 31203), serotype 6B (CMCC 31207), serotype 7F (CMCC 31507), serotype 9V (CMCC 31216), serotype 14 (CMCC 31614), serotype 18C (CMCC 31687), serotype 19F (CMCC 31693), serotype 23F (CMCC 31759), were obtained from the China Medical Culture Collection (CMCC; Beijing, China) center. All *S. pneumoniae* strains were grown on Columbia sheep blood agar plates (Chongqing Pangtong, China) or semisynthetic casein hydrolysate medium supplemented with 0.5% yeast extract (C + Y medium) at 37°C with 5% CO_2. The CFU of pneumococci were calculated by plating on blood agar. The 50% lethal doses (LD50s) of D39 in C57BL/6J mice have been determined to be approximately 50 CFU.

Immunization and sera collection

Mice were subcutaneously injected with either 35 μg of rPgdA mixed with an equal volume of Inject Alum Adjuvant (Thermo Scientific) or with adjuvant only for three times with an interval of 14 days. Sera were collected before each vaccination and 1 week after the final vaccination and stored at −80°C until further use.

ELISA

The 96-well plates were coated with 5 μg/mL of rPgdA protein at 4°C for overnight. The plates were then blocked with 2% bovine serum albumin at 37°C for 2 h after being washed 3 times with PBS/T (containing 0.05% Tween-20). After three PBS/T rinses, gradient-diluted antiserum was added to the wells, and the plates were then incubated at 37°C for 1 hour. The HRP-labeled secondary antibody was added at a ratio of 1:5000 after five PBS/T washes. After 45 min of continuing incubation, the plates were washed with PBS/T for 6 times and TMB substrate was added to develop color for 15 min. The absorbance of 450 nm was read after stop solution was added, with 2.1 times of blank control as the threshold. HRP-labeled goat anti-mouse IgG and goat anti-human IgG were purchased from KPL (Gaithersburg, MD, United States). HRP-labeled goat anti-mouse IgG1, IgG2a, IgG2b, and IgG3 subtypes were purchased from Santa Cruz (Santa Cruz Biotechnology, Santa Cruz, CA).

Western blot analysis

A total of 11 different serotypes of *S. pneumoniae* were collected and lysed by 0.5% deoxycholic scid sodium salt. Whole-cell lysates were separated with 10% SDS-PAGE and transferred to *Immobilon* membranes (Immobilon P, Millipore) electrophoretically. Membranes were blocked for 2 h at room temperature in TBS with 0.1% tween 20 (TBS-T) and 5% skim milk powder. The membranes were washed three times in TBS-T at room temperature and then incubated for overnight in antisera (1: 2000 dilution) at 4°C. Then the membranes were washed with TBS-T and incubated with HRP-conjugated goat anti-mouse secondary antibody diluted to 1:5000 in TBS-T containing 5% skim milk powder. After the membranes were washed with TBS-T, the membranes were developed with HRP substrate luminol reagent (Millipore, MA).

Bacterial adhesion and invasion of A549 epithelial cells

A549 cells were seeded at 2×10^5 cells per well in a 24 well plate overnight. Pooled sera from the control or rPgdA groups were mixed with TIGR4 bacteria and incubated on a rotator at room temperature for 1 h. After removing the medium from the plate, bacteria (2×10^7) were added to each well and incubated at 37°C with 5% CO_2. For the adhesion experiment, after 30 min of incubation, the wells were then washed with PBS to remove unattached bacteria. For the invasion experiment, after 2 h of incubation, the wells were then washed with PBS before being treated with penicillin (10 μg/mL) and gentamicin (200 μg/mL) for 15 min to kill extracellular bacteria, after which the cells were washed with PBS again and lysed by adding 100 μL of distilled water to the wells. After serial dilution and plating onto blood agar plates, samples were examined for viable counts after overnight incubation.

Cytokine assays

Two weeks after the final immunization, the spleens of mice were collected, homogenized and passed through 70-μm cell sieve to yield single spleen cell suspension, and red blood cells were dissolved with red blood cell lysate. Spleen cells were re-suspended in 10% inactivated FBS RPMI-1640 medium supplemented with 100 U/mL of penicillin G and 100 U/mL of streptomycin sulfate. Cells were counted and cultured (5×10^6 cells/well) in 24-well plates and stimulated with rPgdA (5 μg/mL) or concanavalin A (5 μg/mL) at 37°C with 5% CO2. At the time of 72 h, the cell supernatant was collected and the levels of cytokines IFN-γ, IL-4, IL-17a, and IL-10 were detected by ELISA kit (BioLegend) according to the instructions.

Challenge

In the colonization model, bacterial challenge was conducted 2 weeks after the final immunization. Mice were anesthetized with pentobarbital and intranasally challenged with the serotype 19F strain (1×10^8 CFU, 30 μL per nostril). Three days post-challenge, nasal cavity lavage fluid and lungs were collected, serially diluted, and plated on blood agar to count the colonies.

To further evaluate the protective effect of rPgdA against invasive diseases, we utilized both sepsis and pneumonia models. Two weeks after the last immunization, mice in each group were challenged with the D39 strain. In the sepsis model, mice were challenged intraperitoneally with approximately 600 CFU of D39 in 100 μL of sterilized PBS. In the pneumonia model, mice were anesthetized with pentobarbital and challenged intranasally with approximately 1×10^8 CFU of D39 in 30 μL of sterilized PBS. Mouse survival was monitored every 24 h for 21 consecutive days post-challenge.

Detection of antibodies to rPgdA in human sera

Serum samples from 54 healthy adults and 26 patients with acute pneumococcal pneumonia were collected from the First Affiliated Hospital of Chongqing Medical University. The study excluded people with human immunodeficiency virus, hepatitis B or C virus infection, acute diseases, and severe chronic diseases. The titers of PgdA-specific IgG antibodies in all serum samples were detected by ELISA (as shown in above). This study was approved by the ethics committees of Chongqing Medical University and First Affiliated Hospital of Chongqing Medical University. The informed consent of all participants has been obtained.

Statistical analysis

All statistical analyses were performed with Graph-Pad Prism 8.0 software. Antibody titers were compared by Mann-Whitney *U* test (two-tailed). Comparisons of the cytokine levels and numbers of CFU were performed with the two-tailed Student's *t*-test. Survival data were analyzed with the use of the log rank (Mantel–Cox) test. Significant difference was defined as $P < 0.05$.

Results

Antibody response in mice immunized with rPgdA

To evaluate the immunogenicity and the antigen-specific responses of recombinant rPgdA, we first obtained the unlabeled rPgdA protein by affinity purification and determined the molecular weight of rPgdA to be approximately 49 kDa by SDS-PAGE (Figure 1A). Subcutaneous immunization with rPgdA in combination with Alum adjuvant produced a higher IgG antibody titer than adjuvant alone (Figure 1B), demonstrating the activation of humoral immune response. Figure 1C shows that the IgG isotypes produced by rPgdA immunization are mainly IgG1 and IgG2b. These results suggest that rPgdA has good immunogenicity *in vivo*.

To determine whether rPgdA antisera can recognize PgdA antigens, we performed a western blot assay to detect PgdA expression in different serotypes of *S. pneumoniae*. The results showed that rPgdA antisera could specifically recognize the PgdA protein in various *S. pneumoniae* serotypes (Figure 1D). This demonstrates that PgdA is highly conserved across different strains, suggesting that immunization with rPgdA could potentially provide broad protection.

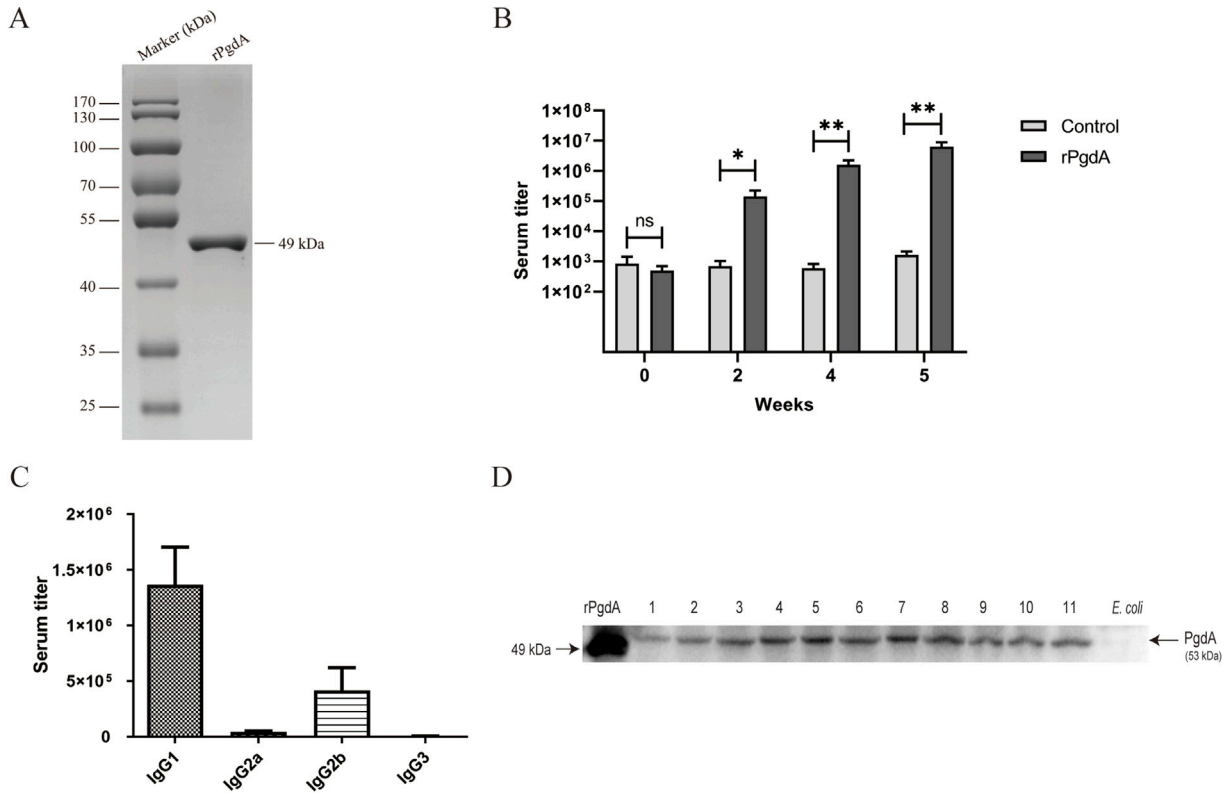

FIGURE 1
Protein expression and antibody response. **(A)** Analysis of the rPgdA protein by SDS-PAGE. **(B)** The titer of rPgdA-specific total IgG. Sera were collected before each vaccination and 1 week after the last vaccination, and its titer was determined by ELISA. **(C)** The IgG subtypes of rPgdA antiserum were detected by ELISA at 1 week after the final immunization. **(D)** Determination of PgdA in different serotypes of *Streptococcus pneumoniae* by Western blot. Lane 1, serotype 1; lane 2, serotype 2; lane 3, serotype 3; lane 4, serotype 4; lane 5, serotype 6B; lane 6, serotype 7F; lane 7, serotype 9V; lane 8 serotype 14; lane 9, serotype 18C; lane 10, serotype 19F; and lane 11, serotype 23F. The data are presented as means ± SDs, and statistical significance was determined using the Mann-Whitney U test. $*p < 0.05$; $**p < 0.01$; ns, not significant.

Effect of rPgdA antisera on bacterial adhesion and invasion to A549 cells

In order to evaluate whether the rPgdA antisera has a certain protective function, we investigated whether the antisera can block the adhesion and invasion of pneumococcus to lung epithelial cells. The results showed that although rPgdA antisera had no significant effect on reducing the adhesion of TIGR4 to A549 cells, it could significantly reduce the TIGR4 bacterial invasion of A549 cells (Figures 2A, B).

Cytokine production by mouse splenocytes

To study the cytokine response induced by rPgdA vaccination, the spleen cells of immunized mice were obtained and stimulated with rPgdA, and the cellular immune responses was evaluated by detecting the production of IFN-γ, IL-4, IL-17a, and IL-10. The results showed that after rPgdA stimulation, significant production of IFN-γ, IL-10, and IL-17a was observed compared with the control group (Figures 3A, B, D). In contrast, no significant change in IL-4 was detected (Figure 3C). These results suggesting that immunization of rPgdA can specifically induce Th1, Th17 as well as regulatory T cell type immune responses.

Capacity of rPgdA to elicit protection

We used the colonization model induced by serotype 19F to evaluate the protective effect of rPgdA on invasive diseases. As shown in Figure 4A, the nasal bacterial burden was comparable between the rPgdA vaccination group and the control group. However, rPgdA-immunized mice had significantly fewer pneumococci in their lungs compared to the adjuvant-treated mice (Figure 4B).

To further evaluate the protective ability of rPgdA, we employed a mouse model of invasive pneumococcal infection. After intraperitoneal challenge with the D39 strain, the survival rate of mice inoculated with rPgdA did not differ substantially from the control group (Figure 4C). In the pneumonia model,

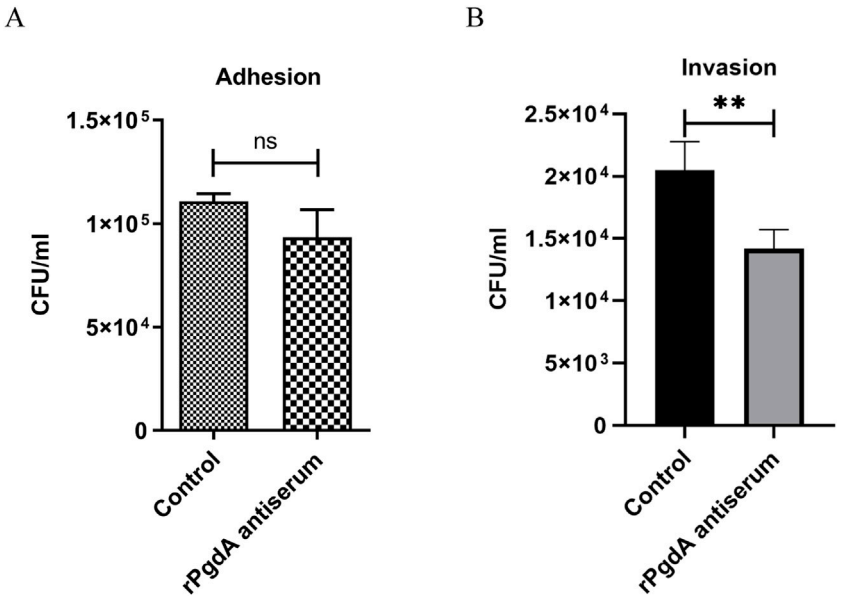

FIGURE 2
Effect of rPgdA antisera on pneumococcal adhesion **(A)** and invasion **(B)** to A549 lung epithelial cells. TIGR4 bacteria were opsonized with pooled sera from mice vaccinated with adjuvanted rPgdA and then incubated with A549 cells. Sera from mice inoculated with the adjuvant alone served as the control. Error bars represent the results from at least three independent experiments using the same sera. Statistical analysis was analyzed by Student's *t*-test. $^{**}p < 0.01$; ns, not significant.

mice inoculated with rPgdA and challenged with D39 exhibited improved survival compared to control mice, with survival rates of 50% in the immunized group versus 25% in the control group (Figure 4D). Although this increase in survival rate was not statistically significant, it suggests that rPgdA immunization may reduce the invasion of pneumococci into the lungs without affecting colonization in the nasal cavity.

Human sera contain antibodies to rPgdA

A previous study showed that the antisera from healthy adults could react with PgdA [26]. To further investigate the immune response to PgdA in humans, we assessed the levels of PgdA-specific IgG in the sera of both healthy adults and patients with acute pneumococcal pneumonia. As illustrated in Figure 5, the geometric mean titer of serum IgG antibodies against PgdA was significantly higher in patients with acute pneumococcal pneumonia compared to healthy adults. This finding suggests that a natural immune response to PgdA is elicited during pneumococcal infection.

Discussion

In this study, our results demonstrated that rPgdA has good immunogenicity, and immunization with rPgdA can induce robust systemic immune response in mice. In addition, we found that subcutaneous immunization of mice with rPgdA did not significantly affect the colonization of pneumococcus in the nasopharynx, but could significantly reduce the invasion of pneumococcus in the lung. More importantly, we found that PgdA antibodies may play a role in the prevention of pneumococcal disease in humans.

Previous studies have shown that incorporation of affinity tag to a recombinant protein may alter its structure, change its immunogenicity, and cause non-specific reactions [27–30]. To reduce these negative effects, we used the Profinity eXact protein purification technology in this study, which helps to purify recombinant proteins with natural N-terminus. Through subcutaneous immunization of mice with unlabeled rPgdA, we can obtain antibodies that recognize the PgdA protein of multiple pneumococcal serotypes, which indicates that the recombinant PgdA protein may possess broadly conserved epitopes, potentially providing extensive protection.

In the colonization model, we found no significant difference in the colonization level of 19F after rPgdA inoculation compared with the adjuvant group alone, but a significant reduction in the bacterial burden in the lungs. We reason that the lack of protective effect of rPgdA immunization on colonization may be due to the blocking effect of pneumococcal capsular polysaccharide on antibodies, which has been demonstrated by Zangari, T., et al. [31]. However, it

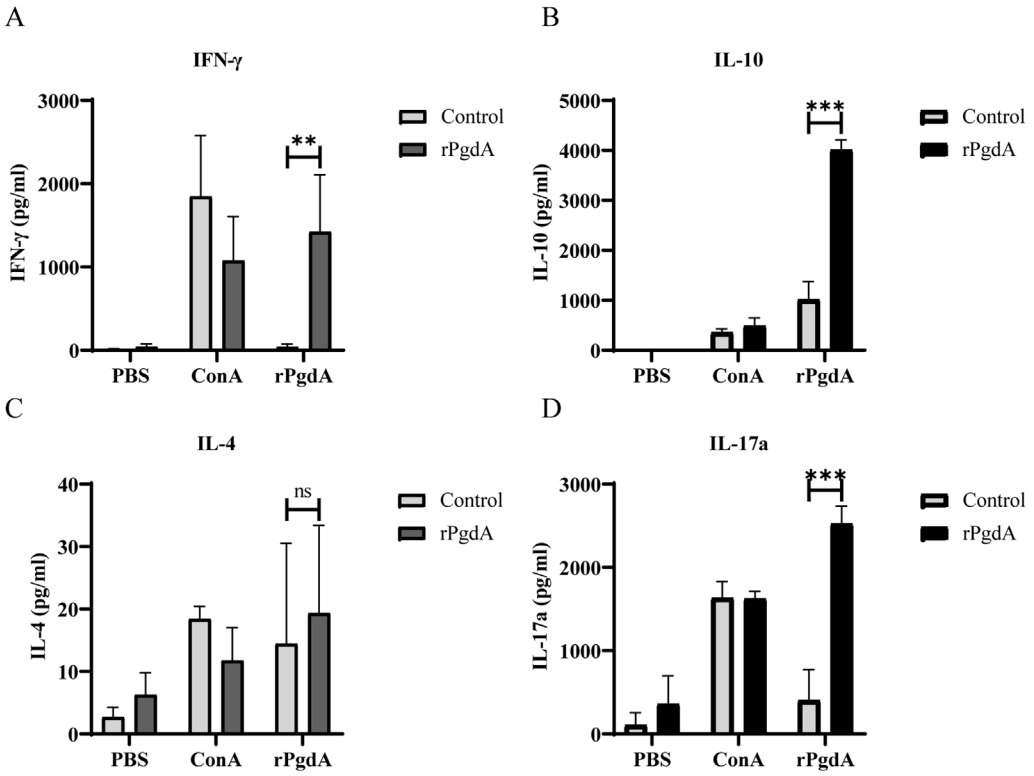

FIGURE 3
The impact of subcutaneous immunization with rPgdA on cytokine production in murine splenocytes was assessed. Splenocytes were isolated from mice immunized with either adjuvanted rPgdA or adjuvant alone (Control) and analyzed for the levels of IFN-γ **(A)**, IL-10 **(B)**, IL-4 **(C)**, and IL-17a **(D)** using ELISA on day 14 following the final vaccination. The isolated splenocytes were subsequently stimulated with PBS, Concanavalin A (ConA), or rPgdA, with ConA serving as the positive control and PBS as the negative control. The results are presented as means ± SDs. Statistical significance was performed by Student's *t*-test. $^{**}p < 0.01$; $^{***}p < 0.001$; ns, not significant.

has a protective effect on lung colonization, which may be due to the following reasons. Firstly, a previous study showed that in order to effectively invade cells, *S. pneumoniae* will reduce the content of capsular polysaccharide to fully expose adhesion molecules [32]. At the same time, one of our previous studies showed that PgdA would be induced to express in the lungs [25], thus the expression of PgdA is increased during invasion. The above factors can increase the chance of PgdA antigen exposure and recognition by its antisera. Secondly, our results suggest that rPgdA antisera can reduce pneumococcal invasion of lung epithelial cells. Finally, we cannot ignore the role of cellular immune responses, as our cytokine analysis showed that the levels of IL-17A, IL-10, and IFN-γ were significantly increased in splenocytes stimulated with rPgdA. As other researchers have shown, these cellular immune responses are critical for defense against pneumococcal infections, and a comprehensive immune response is necessary for effective elimination of *S. pneumoniae* [33–36].

Th17 responses are crucial for controlling nasal colonization and preventing invasive disease in pneumococcal infections. Th17 cells play a significant role in clearing *S. pneumoniae* from the nasopharynx by enhancing neutrophil recruitment and promoting local inflammation [37]. Despite the robust Th17 responses observed in mice vaccinated with rPgdA, these animals did not show a reduction in nasal colonization. Several factors may contribute to this discrepancy. First, although rPgdA vaccination induces a Th17 response, this response alone may be insufficient to counteract the specific mechanisms facilitating pneumococcal colonization. The vaccine might stimulate effective immunity against invasive disease but be less adept at targeting nasal colonization due to the complex interactions between pneumococcal surface proteins and the host immune system [38, 39]. Additionally, *S. pneumoniae* has evolved various immune evasion mechanisms, such as modulating surface antigens and evading phagocytosis, which allow it to persist in the nasopharynx [40–42]. Even with a robust Th17 response, these evasion strategies could enable pneumococci to maintain colonization. Therefore, the rPgdA vaccine might not fully address these evasion mechanisms, leading to persistent nasal colonization despite the Th17 response.

In the survival challenge model, rPgdA inoculation did not exhibit a protective effect against an intraperitoneal challenge, but there was an improvement in survival in the pneumonia model, although this increase was not statistically significant.

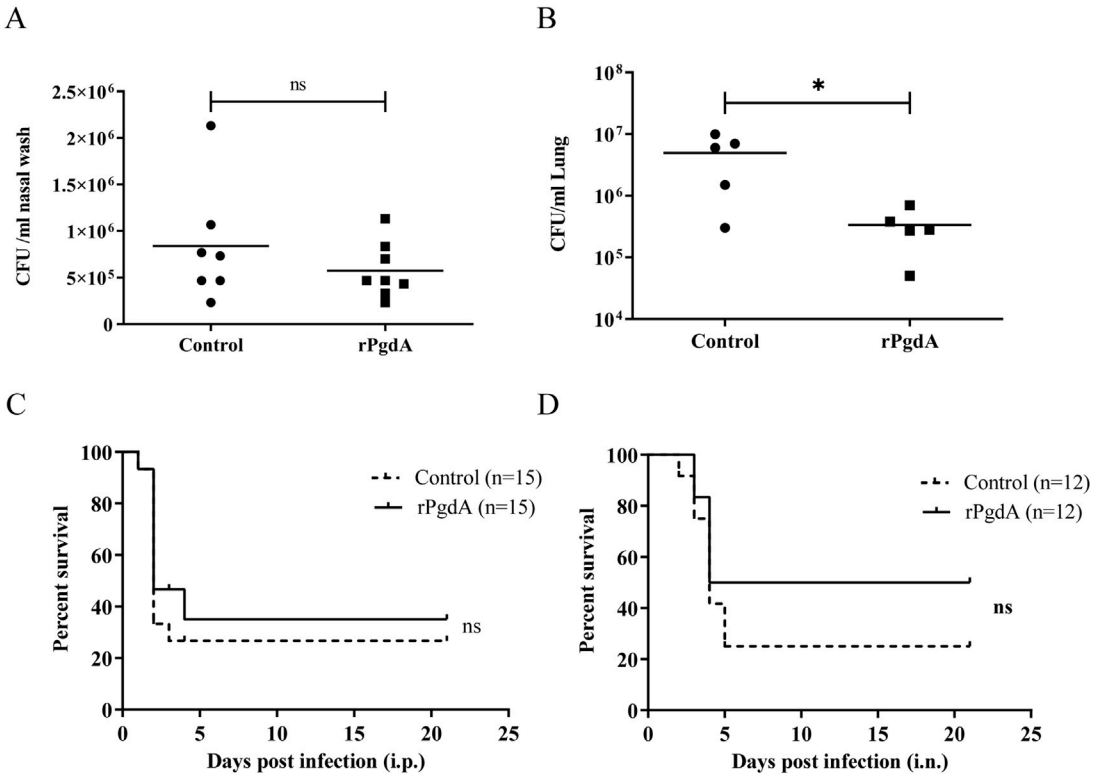

FIGURE 4
Effect of rPgdA vaccination on pneumococcal challenge. Levels of bacterial load in nasopharynx **(A)** and lungs **(B)** of mice challenged intranasally with *Streptococcus pneumoniae* 19F. The CFUs of nasal colonization and lung invasion were calculated by plating serial dilutions of pneumococci recovered from the nasal washes or lungs, respectively. Each point represents the number of CFU recovered from a mouse. The horizontal line symbolizes the median of each group. Mice immunized with adjuvanted rPgdA or adjuvant alone were challenged with D39 via intraperitoneal **(C)** or intranasal **(D)** route at a dose of 600 CFU and 1×10^8 CFU, respectively, and the survival rates were recorded daily. Statistical significance of survival was analyzed by the log rank (Mantel-Cox) test. $*p < 0.05$; ns, not significant.

Adequate protection was not observed in this study, potentially due to the pneumococcal capsule's ability to block antibody function, as suggested by a recent study [31]. Another factor could be the differing immune environments in the abdominal cavity and lungs. The abdominal cavity, primarily a sterile environment, lacks the mucosal immune components found in the lungs, which are constantly exposed to various inhaled pathogens and particles. This disparity in immune environments might affect the efficacy of the vaccine, with the lungs being better equipped to mount a robust local immune response.

We analyzed serum samples from adults with invasive pneumococcal infections and found that antibody titers against PgdA were significantly higher compared to those in healthy adults. This suggests that PgdA may be involved in the pneumococcal infection process. The elevated levels of anti-PgdA antibodies in patients with invasive pneumococcal infections imply that the immune response to PgdA could play a role in combating or preventing such infections.

In conclusion, subcutaneous immunization with rPgdA can induce humoral and cellular immunity, which can reduce the

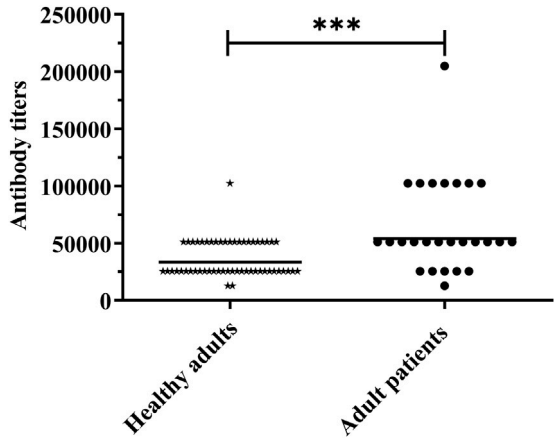

FIGURE 5
Human serum samples were detected for antibody titer against rPgdA by ELISA. The horizontal line symbolizes the geometric mean of the antibody titer, and each point represents the data of an individual. The significance of the difference was calculated using the Student's *t*-test. $***p < 0.001$.

invasion of *S. pneumoniae* to the lung. Simultaneously, no discernible effect on colonization was observed in our experimental setting. Considering the limited improvement in survival, we recommend its use in combination with other proteins for better prevention of pneumococcal infection under the new strategy.

Author contributions

JX and XZ conceived and designed the study; JX and BL performed the experiment; YY and XZ provided important insights in experimental design and performing; JX and BL performed the data analysis; JX and XZ wrote the paper; YY revised the paper. All authors contributed to the article and approved the submitted version.

Data availability statement

The original contributions presented in the study are included in the article/supplementary material, further inquiries can be directed to the corresponding author.

Ethics statement

The studies involving humans were approved by the ethics committees of Chongqing Medical University and First Affiliated Hospital of Chongqing Medical University. The studies were conducted in accordance with the local legislation and institutional requirements. The participants provided their written informed consent to participate in this study. The animal study was approved by the Animal Care and Use Committee of the Chongqing Medical University. The study was conducted in accordance with the local legislation and institutional requirements.

Funding

The author(s) declare financial support was received for the research, authorship, and/or publication of this article. This study was supported by the National Natural Science Foundation grants of China (Grant numbers 81571622).

Acknowledgments

We would like to thank Te Chen and Professor Dapeng Chen for their help in collecting clinical samples.

Conflict of interest

The author(s) declared no potential conflicts of interest with respect to the research, authorship, and/or publication of this article.

References

1. Bogaert D, De Groot R, Hermans PW. Streptococcus pneumoniae colonisation: the key to pneumococcal disease. *The Lancet Infect Dis* (2004) **4**:144–54. doi:10.1016/s1473-3099(04)00938-7

2. van der Poll T, Opal SM. Pathogenesis, treatment, and prevention of pneumococcal pneumonia. *The Lancet* (2009) **374**:1543–56. doi:10.1016/s0140-6736(09)61114-4

3. Rose MA, Laurenz M, Sprenger R, Imohl M, van der Linden M. Nasopharyngeal carriage in children after the introduction of generalized infant pneumococcal conjugate vaccine immunization in Germany. *Front Med (Lausanne)* (2021) **8**:719481. doi:10.3389/fmed.2021.719481

4. Chang B, Akeda H, Nakamura Y, Hamabata H, Ameku K, Toma T, et al. Impact of thirteen-valent pneumococcal conjugate vaccine on nasopharyngeal carriage in healthy children under 24 months in Okinawa, Japan. *J Infect Chemother* (2020) **26**:465–70. doi:10.1016/j.jiac.2019.12.009

5. van Gils EJ, Veenhoven RH, Hak E, Rodenburg GD, Bogaert D, Ijzerman EP, et al. Effect of reduced-dose schedules with 7-valent pneumococcal conjugate vaccine on nasopharyngeal pneumococcal carriage in children: a randomized controlled trial. *JAMA* (2009) **302**:159–67. doi:10.1001/jama.2009.975

6. Brandileone MC, Zanella RC, Almeida SCG, Cassiolato AP, Lemos APS, Salgado MM, et al. Long-term effect of 10-valent pneumococcal conjugate vaccine on nasopharyngeal carriage of Streptococcus pneumoniae in children in Brazil. *Vaccine* (2019) **37**:5357–63. doi:10.1016/j.vaccine.2019.07.043

7. Chan KC, Subramanian R, Chong P, Nelson EA, Lam HS, Li AM, et al. Pneumococcal carriage in young children after introduction of PCV13 in Hong Kong. *Vaccine* (2016) **34**:3867–74. doi:10.1016/j.vaccine.2016.05.047

8. Brandileone MC, Zanella RC, Almeida SCG, Brandao AP, Ribeiro AF, Carvalhanas TRM, et al. Effect of 10-valent pneumococcal conjugate vaccine on nasopharyngeal carriage of Streptococcus pneumoniae and Haemophilus influenzae among children in Sao Paulo, Brazil. *Vaccine* (2016) **34**:5604–11. doi:10.1016/j.vaccine.2016.09.027

9. Spijkerman J, Prevaes SM, van Gils EJ, Veenhoven RH, Bruin JP, Bogaert D, et al. Long-term effects of pneumococcal conjugate vaccine on nasopharyngeal carriage of S. pneumoniae, S. aureus, H. influenzae and M. catarrhalis. *PLoS One* (2012) **7**:e39730. doi:10.1371/journal.pone.0039730

10. Camilli R, Vescio MF, Giufre M, Daprai L, Garlaschi ML, Cerquetti M, et al. Carriage of Haemophilus influenzae is associated with pneumococcal vaccination in Italian children. *Vaccine* (2015) **33**:4559–64. doi:10.1016/j.vaccine.2015.07.009

11. Angoulvant F, Cohen R, Doit C, Elbez A, Werner A, Bechet S, et al. Trends in antibiotic resistance of Streptococcus pneumoniae and Haemophilus influenzae isolated from nasopharyngeal flora in children with acute otitis media in France before and after 13 valent pneumococcal conjugate vaccine introduction. *BMC Infect Dis* (2015) **15**:236. doi:10.1186/s12879-015-0978-9

12. Lewnard JA, Huppert A, Givon-Lavi N, Pettigrew MM, Regev-Yochay G, Dagan R, et al. Density, serotype Diversity, and fitness of Streptococcus pneumoniae in upper respiratory tract cocolonization with nontypeable Haemophilus influenzae. *J Infect Dis* (2016) **214**:1411–20. doi:10.1093/infdis/jiw381

13. Biesbroek G, Wang X, Keijser BJ, Eijkemans RM, Trzcinski K, Rots NY, et al. Seven-valent pneumococcal conjugate vaccine and nasopharyngeal microbiota in healthy children. *Emerg Infect Dis* (2014) **20**:201–10. doi:10.3201/eid2002.131220

14. Greene CJ, Marks LR, Hu JC, Reddinger R, Mandell L, Roche-Hakansson H, et al. Novel strategy to protect against influenza virus-induced pneumococcal disease without interfering with commensal colonization. *Infect Immun* (2016) **84**:1693–703. doi:10.1128/iai.01478-15

15. Li Y, Hill A, Beitelshees M, Shao S, Lovell JF, Davidson BA, et al. Directed vaccination against pneumococcal disease. *Proc Natl Acad Sci U S A* (2016) **113**: 6898–903. doi:10.1073/pnas.1603007113

16. Vollmer W, Tomasz A. Peptidoglycan N-acetylglucosamine deacetylase, a putative virulence factor in Streptococcus pneumoniae. *Infect Immun* (2002) **70**: 7176–8. doi:10.1128/iai.70.12.7176-7178.2002

17. Vollmer W, Tomasz A. The pgdA gene encodes for a peptidoglycan N-acetylglucosamine deacetylase in Streptococcus pneumoniae. *J Biol Chem* (2000) **275**:20496–501. doi:10.1074/jbc.m910189199

18. Boneca IG, Dussurget O, Cabanes D, Nahori MA, Sousa S, Lecuit M, et al. A critical role for peptidoglycan N-deacetylation in Listeria evasion from the host innate immune system. *Proc Natl Acad Sci U S A* (2007) **104**:997–1002. doi:10.1073/pnas.0609672104

19. He´bert L, Courtin P, Torelli R, Sanguinetti M, Chapot-Chartier MP, Auffray Y, et al. *Enterococcus faecalis* constitutes an unusual bacterial model in lysozyme resistance. *Infect Immun* (2007) **75**:5390–8. doi:10.1128/iai.00571-07

20. Fittipaldi N, Sekizaki T, Takamatsu D, de la Cruz Dominguez-Punaro M, Harel J, Bui NK, et al. Significant contribution of the pgdA gene to the virulence of Streptococcus suis. *Mol Microbiol* (2008) **70**:1120–35. doi:10.1111/j.1365-2958.2008.06463.x

21. Milani CJ, Aziz RK, Locke JB, Dahesh S, Nizet V, Buchanan JT. The novel polysaccharide deacetylase homologue Pdi contributes to virulence of the aquatic pathogen Streptococcus iniae. *Microbiology* (2010) **156**:543–54. doi:10.1099/mic.0.028365-0

22. Tait-Kamradt AG, Cronan M, Dougherty TJ. Comparative genome analysis of high-level penicillin resistance in Streptococcus pneumoniae. *Microb Drug Resist* (2009) **15**:69–75. doi:10.1089/mdr.2009.0891

23. Bui NK, Turk S, Buckenmaier S, Stevenson-Jones F, Zeuch B, Gobec S, et al. Development of screening assays and discovery of initial inhibitors of pneumococcal peptidoglycan deacetylase PgdA. *Biochem Pharmacol* (2011) **82**: 43–52. doi:10.1016/j.bcp.2011.03.028

24. DiFrancesco BR, Morrison ZA, Nitz M. Monosaccharide inhibitors targeting carbohydrate esterase family 4 de-N-acetylases. *Bioorg & Med Chem* (2018) **26**: 5631–43. doi:10.1016/j.bmc.2018.10.008

25. Meng JP, Yin YB, Zhang XM, Huang YS, Lan K, Cui F, et al. Identification of Streptococcus pneumoniae genes specifically induced in mouse lung tissues. *Can J Microbiol* (2008) **54**:58–65. doi:10.1139/w07-117

26. Croucher NJ, Campo JJ, Le TQ, Liang X, Bentley SD, Hanage WP, et al. Diverse evolutionary patterns of pneumococcal antigens identified by pangenome-wide immunological screening. *Proc Natl Acad Sci U S A* (2017) **114**:E357-E366–E66. doi:10.1073/pnas.1613937114

27. Khan F, Legler PM, Mease RM, Duncan EH, Bergmann-Leitner ES, Angov E. Histidine affinity tags affect MSP1(42) structural stability and immunodominance in mice. *Biotechnol J* (2012) **7**:133–47. doi:10.1002/biot.201100331

28. Singh M, Sori H, Ahuja R, Meena J, Sehgal D, Panda AK. Effect of N-terminal poly histidine-tag on immunogenicity of Streptococcus pneumoniae surface protein SP0845. *Int J Biol Macromolecules* (2020) **163**:1240–8. doi:10.1016/j.ijbiomac.2020.07.056

29. Wu J, Filutowicz M. Hexahistidine (His6)-tag dependent protein dimerization: a cautionary tale. *Acta Biochim Pol* (1999) **46**:591–9. doi:10.18388/abp.1999_4131

30. Chant A, Kraemer-Pecore CM, Watkin R, Kneale GG. Attachment of a histidine tag to the minimal zinc finger protein of the Aspergillus nidulans gene regulatory protein AreA causes a conformational change at the DNA-binding site. *Protein Expr Purif* (2005) **39**:152–9. doi:10.1016/j.pep.2004.10.017

31. Zangari T, Zafar MA, Lees JA, Abruzzo AR, Bee GCW, Weiser JN. Pneumococcal capsule blocks protection by immunization with conserved surface proteins. *NPJ Vaccin* (2021) **6**:155. doi:10.1038/s41541-021-00413-5

32. Hammerschmidt S, Wolff S, Hocke A, Rosseau S, Müller E, Rohde M. Illustration of pneumococcal polysaccharide capsule during adherence and invasion of epithelial cells. *Infect Immun* (2005) **73**:4653–67. doi:10.1128/iai.73.8.4653-4667.2005

33. Vuononvirta J, Peltola V, Ilonen J, Mertsola J, He Q. The gene polymorphism of IL-17 G-152a is associated with increased colonization of Streptococcus pneumoniae in young Finnish children. *Pediatr Infect Dis J* (2015) **34**:928–32. doi:10.1097/inf.0000000000000691

34. Ramos-Sevillano E, Ercoli G, Brown JS. Mechanisms of naturally acquired immunity to Streptococcus pneumoniae. *Front Immunol* (2019) **10**:358. doi:10.3389/fimmu.2019.00358

35. Colino J, Snapper CM. Opposing signals from pathogen-associated molecular patterns and IL-10 are critical for optimal dendritic cell induction of *in vivo* humoral immunity to Streptococcus pneumoniae. *The J Immunol* (2003) **171**: 3508–19. doi:10.4049/jimmunol.171.7.3508

36. Wilson R, Cohen JM, Jose RJ, de Vogel C, Baxendale H, Brown JS. Protection against Streptococcus pneumoniae lung infection after nasopharyngeal colonization requires both humoral and cellular immune responses. *Mucosal Immunol* (2015) **8**: 627–39. doi:10.1038/mi.2014.95

37. Wang Y, Jiang B, Guo Y, Li W, Tian Y, Sonnenberg GF, et al. Cross-protective mucosal immunity mediated by memory Th17 cells against Streptococcus pneumoniae lung infection. *Mucosal Immunol* (2017) **10**:250–9. doi:10.1038/mi.2016.41

38. Ogunniyi AD, LeMessurier KS, Graham RM, Watt JM, Briles DE, Stroeher UH, et al. Contributions of pneumolysin, pneumococcal surface protein A (PspA), and PspC to pathogenicity of Streptococcus pneumoniae D39 in a mouse model. *Infect Immun* (2007) **75**:1843–51. doi:10.1128/iai.01384-06

39. Weiser JN, Ferreira DM, Paton JC. Streptococcus pneumoniae: transmission, colonization and invasion. *Nat Rev Microbiol* (2018) **16**:355–67. doi:10.1038/s41579-018-0001-8

40. Mathew BJ, Gupta P, Naaz T, Rai R, Gupta S, Gupta S, et al. Role of Streptococcus pneumoniae extracellular glycosidases in immune evasion. *Front Cell Infect Microbiol* (2023) **13**:1109449. doi:10.3389/fcimb.2023.1109449

41. Gil E, Noursadeghi M, Brown JS. Streptococcus pneumoniae interactions with the complement system. *Front Cell Infect Microbiol* (2022) **12**:929483. doi:10.3389/fcimb.2022.929483

42. Andre GO, Converso TR, Politano WR, Ferraz LF, Ribeiro ML, Leite LC, et al. Role of Streptococcus pneumoniae proteins in evasion of complement-mediated immunity. *Front Microbiol* (2017) **8**:224. doi:10.3389/fmicb.2017.00224

EBM Experimental Biology and Medicine

TYPE Original Research
PUBLISHED 28 October 2024
DOI 10.3389/ebm.2024.10171

OPEN ACCESS

*CORRESPONDENCE
Zhiqiang Yu,
120yuzhi@163.com
Jin Xu,
doctorjinjin@163.com

†These authors share first authorship

RECEIVED 17 March 2024
ACCEPTED 11 October 2024
PUBLISHED 28 October 2024

CITATION
Yu Z, Chen X, Liu Z, Ding R and Xu J (2024) Subunit-specific mechanisms of isoflurane-induced acute tonic inhibition in dentate gyrus granule neuron.
Exp. Biol. Med. 249:10171.
doi: 10.3389/ebm.2024.10171

Subunit-specific mechanisms of isoflurane-induced acute tonic inhibition in dentate gyrus granule neuron

Zhiqiang Yu[1*†], Xiaodan Chen[1†], Zheng Liu[1], Ran Ding[2] and Jin Xu[3*]

[1]Department of Anesthesiology, Tianjin Central Hospital for Gynecology and Obstetrics, Tianjin, China, [2]Tianjin Research Institute of Anesthesiology and Department of Anesthesiology, Tianjin Medical University General Hospital, Tianjin, China, [3]Department of Anesthesiology, Tianjin Hospital, Tianjin, China

Abstract

Prolonged exposure to volatile anesthetics may raise the risk of developing cognitive impairment by acting on gamma-a Aminobutyric acid A receptors (GABAAR). The dentate gyrus plays an important role in the hippocampus and has a high potential for neural plasticity. However, it is unknown whether prolonged anesthesia induces a change in acute phasic or tonic inhibition in dentate gyrus granule cells (DGGCs) by acting on GABAAR. In order to verify the effects of volatile anesthetics on the current in DGGCs, a whole-cell patch was applied to record acute brain slices, and this study indicated that 4 h but not 2 h of isoflurane (ISO) exposure induced significantly larger tonic currents in DGGCs other than hippocampal CA1 pyramidal and thalamic relay neurons. Furthermore, this study demonstrated that the increased tonic current in DGGCs was dependent on the δ subunit-containing GABAARs by using transgenic δ subunit knockout mice. In conclusion, the δ subunit specific GABAAR is the key element that increased acute tonic inhibition in DGGCs of mice after prolonged ISO exposure, which may be one of the mechanisms of ISO neurotoxicity to the developing brain.

KEYWORDS

dentate gyrus, isoflurane, tonic current, GABAA receptor, knockout

Impact statement

To verify the effect of long-term general anesthesia on neurotoxicity by studying the subunit specific mechanism of acute ankylosing inhibition of dentate gyrus granule neurons induced by isoflurane.

Introduction

Millions of surgical procedures are performed annually under general anesthesia. There is a growing concern that prolonged general anesthetic exposure might result in brain disorders in young children and geriatric patients and increase the risk of cognitive impairments [1, 2]. Although conclusive evidence of general anesthetic neurotoxicity in humans has not yet been confirmed, many animal researches have indicated that exposure to general anesthetics during early postnatal life impairs neurocognitive function. The cellular and molecular mechanisms underlying this potential hazard of general anesthetics remain poorly understood.

The mechanism by which general anesthetics impair cognition may involve a decrease in hippocampal neurogenesis [3, 4]. Rodent models have shown that alterations in hippocampal neurogenesis induced by volatile anesthetics contribute to brain impairment, such as numerous deficits in learning and memory [4–6]. Postnatally, learning, memory, and cognitive ability are closely correlated with neurogenesis and neurodevelopment, especially in newly generated mature dentate gyrus granule cells (DGCs) [7]. Considerable evidence from rodents and nonhuman primates has demonstrated that the neurogenesis of granule neurons in the dentate gyrus (DG) can be influenced by volatile anesthetics such as isoflurane (ISO) and sevoflurane [8–12]. However, the mechanism by which volatile anesthetics affect the neurogenesis of granular neurons in the DG remains unclear.

GABA type A receptors (GABAARs) generate rapid inhibitory neuronal transmission and are critical for regulating memory, mood, sleep, and nervous system excitability. GABAARs mediate two different types of inhibition: phasic inhibition mediated by postsynaptic receptors and tonic inhibition mediated by extrasynaptic receptors located outside the synapse [13, 14], which induces in variations in GABAergic conductance across different brain areas and neuron types [15]. In the past 20 years, the relationship between dysfunctional GABAergic system and the neurotoxicity of volatile anesthetics is one of the most explored topics. Tonic inhibition and phasic inhibition are crucial for maintaining a balance between the inhibitory and excitatory systems. Volatile general anesthetics are positive allosteric modulators (PAMs) of GABAARs and are widely used for analgesia and sedation. ISO is one of the most widely used volatile anesthetics. Based on current evidence, prolonged exposure to ISO [16, 17] has been confirmed as a possible risk factor in interrupting the function of dentate gyrus granule cells (DGGCs) [3, 18–20]. However, whether prolonged ISO exposure induces a change in acute phasic inhibition and tonic inhibition in DGGCs by acting on GABAAR remains unclear.

Further more, γ2-subunit predominantly contribute to phasic GABAAR-mediated currents in DGCs, α5 and δ subunits predominantly contribute to tonic GABAAR-mediated currents in DGCs. In order to verify the effects of volatile anesthetics on phasic and tonic currents, and observe the effects of volatile anesthetics on the currents dependent on γ2, α5 and δ subunit-containing GABAARs, we used a whole-cell patch to observe the effects of ISO exposure on acute phasic inhibition and tonic inhibition in DGGCs. Specific antagonists of the subunits and transgenic subunit knockout mice are used to observe the effects of ISO exposure on the γ2, α5 and δ subunit-containing GABAARs currents in DGGCs.

Materials and methods

Mice

The use of animals in all experiments were approved by Animal Ethics Committee of Tianjin Central Hospital of Gynecology and Obstetrics according to the National Institutes of Health guidelines. Male or female mice are both suitable to use, and male mice were used in this study. C57BL/6 (Beijing Weitonglihua Experimental Animal Technology Co., Ltd; Beijing; China) and Gabrd KO mice, 3 weeks, 10–15 g, were used in this study. The Gabrd KO mice were shared by professor Hui Shen of Tianjin Medical University. The Gabrd KO mice were derived from C57BL/6 mice, and the mice have been backcrossed to C57BL/6J for ten generations. The mice were weaned and genotyped at postnatal day 21 (P21). Quantitative real-time PCR was used to analyze the transcriptional profile of the GABAAR subunits, and the information of sequences of the primers were provided in the Supplementary Material. To minimize bias, the birth time are similar, the mice age, gender and feeding environment are same between Control group (C57BL/6) and Gabrd KO mice group. All mice were bred in the temperature-fixed, humidity-controlled animal colony with a 12 h light/dark circle (7:00 a.m. to 7:00 p.m.). All mice used in the experiments were housed in several cages, and provided with sufficient food and water throughout the study.

Exposure of mice to ISO

The mice were randomly divided to the following three groups: Control group (no ISO exposure, Control), ISO 2 h group (exposed to 1.5% ISO for 2 h, ISO 2 h), and ISO 4 h group (exposed to 1.5% ISO for 4 h, ISO 4 h). ISO was delivered using a pour-fill vaporizer group (RWD R500), whereas the animals in the Control group were exposed to 21% O_2 for 30 min. During exposure to ISO, the chamber temperature was kept at approximately 39°C with a custom-made heating pad. The respiration was monitored visually, and the rectal temperature of mice was monitored and maintained between 36.5 and 37.5°C throughout the experiments.

Electrophysiological recording

Whole-cell voltage-clamp recordings were recorded in the DGGCs in the Control, ISO 2 h, and ISO 4 h groups. Mouse hippocampal and thalamic slices were prepared as previous study described [21]. Briefly, animals were quickly decapitated under ISO anesthesia, and the brains were dissected in ice and oxygenated artificial cerebrospinal fluid (ACSF) containing 125 mM NaCl, 4.5 mM KCl, 1.25 mM NaH_2PO_4, 26 mM $NaHCO_3$, 1 mM $MgCl_2$, 2 mM $CaCl_2$, and 20 mM glucose (pH 7.4 when bubbled with 95% oxygen and 5% CO_2). Coronal slices (350–380 μm) containing the bilateral hippocampus CA1/DG and thalamus were prepared incubated at 34°C in an oxygenated sucrose-based ACSF for at least 45 min and subsequently, all slices were kept at room temperature to recover for another 30 min before performing whole-cell voltage-clamp. A single slice was placed in a recording chamber, where it was continuously perfused (2 mL min/L) with ACSF saturated with 95% O_2/5% CO_2 at room temperature, which was placed on the fixed stage of an upright Olympus BX50WI microscope (Olympus, Tokyo, Janpan). The currents in acute cortical slices of pyramidal neurons in the hippocampal CA1/DG and thalamic relay neurons were recorded by Whole-cell patch-clamp.

The recording glass pipettes with resistance 4–6 MΩ were full of an intracellular solution, which containing: 10 mM HEPES, 130 mM CsCl, 5 mM QX314, 8 mM NaCl, 0.3 mM Na-GTP, 4 mM Mg-ATP, and 0.2 mM EGTA; pH: 7.3. To record and observe the tonic GABAAR currents, 50 μM DNQX, 5 μM CGP 52432 and 50 μM APV were regularly added into the bath electrolyte to block the B type GABA receptors and ionotropic glutamate. To reveal the total tonic GABA current, local perfusion of 10 μM bicuculline (BIC, sigma) was used to block all GABAA-Rs and change the holding current. To reveal the tonic current mediated by α5-containing GABAARs, local application of 100 nM L-655,708 (Tocris) was used, which is a selective inverse agonist for α5 GABAARs. The membrane potential was kept at −70 mV. Spontaneous miniature inhibitory postsynaptic currents (mIPSCs) were pharmacologically separated by bath application of NBQX (50 μM), D-AP5 (50 μM), and TTX (1 μM), and all slices were measured at −60 mV of voltage clamp mode. Access resistance was regulated before and after each recording. Series resistance was typically 10–20 MΩ. Neurons were abandoned when the parameter was higher than 30 MΩ or varied more than 20%. An Axon 700B amplifier (Molecular Devices, LLC., San Jose, CA, United States) was applied to record electrical signals. All data were filtered at 10 kHz and digitized at 20 kHz using a Digidata-1550B system with clampfit 10.6 software (Molecular Devices, LLC., San Jose, CA, United States).

Data analysis and statistics

Tonic GABAAR currents were defined as the amplitude change following BIC perfusion and measured as previous studies described [22, 23]. The frequency and amplitude of sIPSCs were analyzed offline using clampfit 10.6 (Molecular Devices, LLC., San Jose, CA, United States) and GraphPad Prism software v6. Differences of the tonic currents and the sIPSC parameters were analyzed by one-way analysis of variance (ANOVA) followed by Sidak *post hoc* t-test. Unless otherwise stated, data were represented as mean ± standard deviation. An unpaired t-test was applied to the independent samples. A P-value of <0.05 was considered that the difference was statistically significant.

Results

Prolonged ISO exposure induced the tonic GABAAR current in DGGCs

The results revealed that the tonic currents of the ISO 2 h group were comparable to those of the Control group ($P = 0.84$, Figures 1A–C). However, in the ISO 4 h group, tonic GABAAR currents were significantly larger than those of the Control group and ISO 2 h group (F [2, 13] = 64.67, $P < 0.001$; Figures 1B, C). Next, to investigate whether other brain regions exhibited enhanced tonic GABAAR currents following ISO exposure, hippocampal CA1 pyramidal neurons and thalamic relay neurons were recorded by whole-cell voltage-clamp under the same conditions as the DGGCs. The tonic GABAAR currents in the two brain areas were not altered by ISO exposure (F [2, 28] = 2.532, $P = 0.10$; F [2, 28] = 2.774, $P = 0.08$; Figures 2A, B), implying that ISO exposure preferentially increased tonic GABAA receptor currents in the DG but not in other examined brain regions. These results suggest that acute inhibitory tonic GABAAR currents were time-and location-dependent in DGGCs.

Prolonged ISO exposure did not change the phasic inhibitory postsynaptic transmission

Furthermore, whole-cell voltage-clamp recordings were used to determine whether ISO exposure changed the basal phasic postsynaptic inhibitory transmission in DGGCs. After blocking the excitatory postsynaptic currents and action potentials, mIPSCs were isolated and recorded from DGGCs of juvenile animals. A variation in mIPSC amplitude suggests a variation in the number of ionic GABAA receptors at postsynaptic sites, whereas a variation in mIPSC frequency implies a change in the synapse number or presynaptic vesicle release odds. There was no

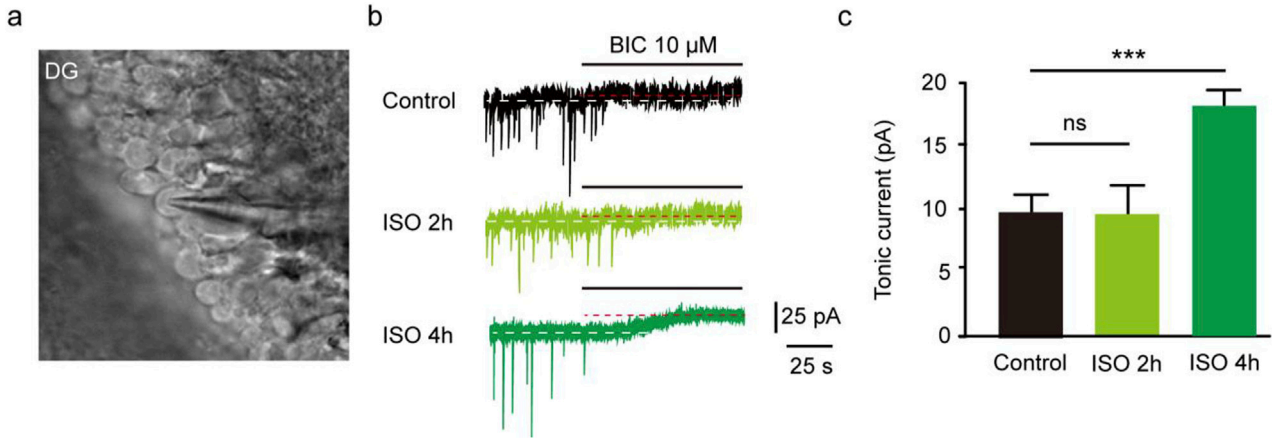

FIGURE 1
Exposed ISO for 4 h induced tonic current in DGGCs. **(A)** Image of brain slice. **(B)** Samples of the tonic current recording in Control, ISO 2 h, and ISO 4 h group. **(C)** Mean change in tonic current in Control, ISO 2 h and ISO 4 h group (Control, 8.75 ± 0.75 pA, n = 6 cells, one cell per mouse; ISO 2 h, 8.42 ± 1.04 pA, n = 5 cells, one cell per mouse; ISO 4 h, 17.90 ± 1.01 pA, n = 5 cells, one cell per mouse; one-way ANOVA, F [2, 13] = 64.67, ***p < 0.001, ns, not significant).

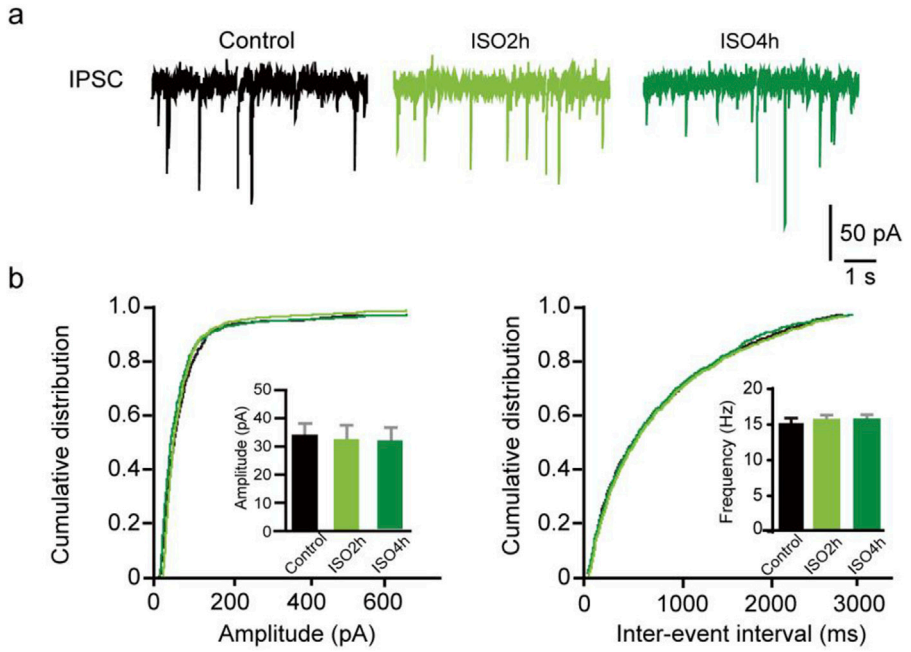

FIGURE 2
ISO do not change the phasic mIPSC frequency and amplitude in DGGCs. **(A)** Representative traces of mIPSCs recorded from dentate granule cells of adult mice. **(B)** Quantifications of mIPSC amplitude and cumulative distributions of the inter-event intervals. mIPSC amplitudes are comparable between Control and ISO group (Control, 31.06 ± 4.64 pA, n = 11 cells, one cell per mouse; ISO 2h, 32.85 ± 4.31 pA, n = 10 cells, one cell per mouse; ISO 4h, 35.84 ± 5.65 pA; n = 10 cells, one cell per mouse; one-way ANOVA, F [2, 28] = 2.532, P = 0.10). Quantifications of mIPSC frequency and cumulative distributions of the mIPSC inter-event interval. mIPSC inter-event interval are comparable between control and ISO group (Control, 16.45 ± 4.05 Hz, n = 11 cells, one cell per mouse; ISO 2h, 20.44 ± 3.82 Hz, n = 10 cells, one cell per mouse; ISO 4h, 18.30 ± 3.74 Hz, n = 10 cells, one cell per mouse; one-way ANOVA, F [2, 28] = 2.774, p = 0.08).

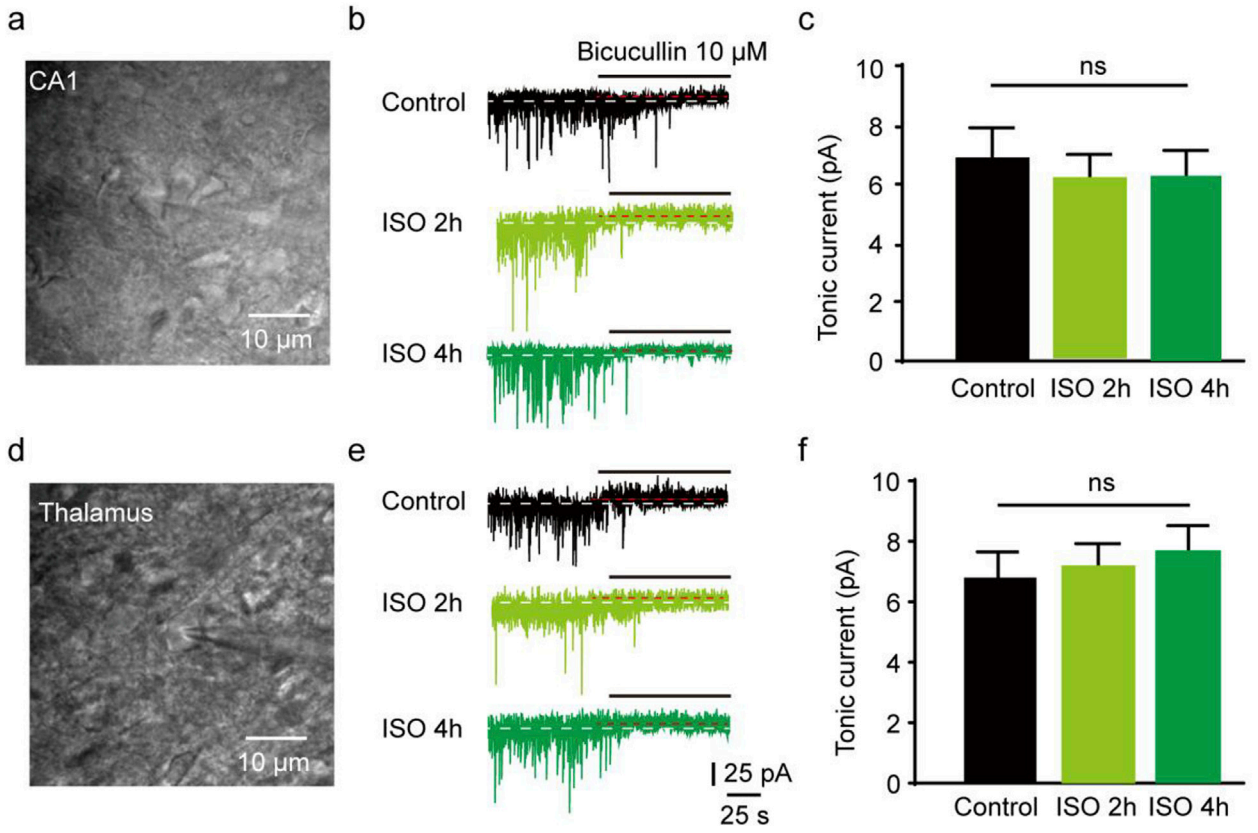

FIGURE 3
Hippocampus CA1 and thalamus relay cells showed no enhanced tonic current by 2 and 4 h ISO exposure revealed by GABAAR antagonist BIC, compared with Control group respectively. **(A)** Example of image, hippocampus CA1 pyramidal neuron. **(B)** Samples of the tonic current recording from CA1 pyramidal neuron. **(C)** The average amplitude of tonic current (pA) in Control, ISO 2h, and ISO 4 h group (Control, 6.89 ± 0.72 pA, n = 7 cells, one cell per mouse; ISO 2h, 6.11 ± 0.70 pA, n = 8 cells, one cell per mouse; ISO 4h, 6.23 ± 0.75 pA, n = 8 cells, one cell per mouse, one-way ANOVA, F [2, 20] = 2.44, p = 0.11). **(D)** Example of image, thalamus relay neuron, scale bar 10 μM. **(E)** Samples of the tonic current recording from thalamus relay neurons. **(F)** The average amplitude of tonic current (pA) in Control, ISO 2h, and ISO 4 h group (Control, 6.87 ± 0.72 pA, n = 7 cells, one cell per mouse; ISO 2h, 7.19 ± 0.65 pA, n = 8 cells, one cell per mouse; ISO 4h, 7.56 ± 0.64 pA, n = 8 cells, one cell per mouse; one-way ANOVA, F [2, 20] = 2.01, p = 0.16).

difference in the mIPSC amplitude in the Control, ISO 2h, and ISO 4 h groups, suggesting 4 h ISO exposure does not regulate the postsynaptic GABAA receptor number (F [2, 20] = 2.44, P = 0.11; Figures 3A–C). There was no obvious difference in mIPSC frequency among the control, ISO 2h, and ISO 4 h groups (F [2, 20] = 2.01, P = 0.16; Figures 3D–F). These results demonstrated that 2 h and 4 h of ISO exposure did not change the phasic postsynaptic inhibitory transmission in dentate granule cells.

Prolonged ISO exposure induced acute tonic current dependent on δ other than α5 subunit-containing GABAA receptor

In the CNS, some subunits exhibit restricted expression profiles. α5 subunit is abundantly expressed in the hippocampus and DG [14, 24], and the excessive function of extrasynaptic α5-containing GABAAR after general anesthesia has been found [25]. δ subunits are also located at extrasynaptic sites where GABAAR are activated by ambient GABA [13, 14, 26]. To examine whether extrasynaptic α5-containing GABAAR was associated with the acute tonic current induced by prolonged ISO exposure, a selective inverse agonist for α5 GABAARs (L-655,708) was used. Our study showed that the tonic current blocked by L-655,708 in the control group was comparable to that in the ISO 4 h group in DGGCs (t = 1.64, df = 12, P= 0.13; Figures 4A, B). Meanwhile, the total tonic current blocked by BIC in the ISO 4 h group was nearly double that in the control group (t = 8.52, df = 12, P < 0.001; Figures 4A, C), which is consistent with the previous values (Figure 1C). However, up to now, there was no suitable δ subunit GABAAR antagonist; the tonic currents were recorded in δ subunit knockout mice in DGGCs. Identified with our prediction, using the δ subunit knockout mice, we found tonic inhibition currents comparable to the control group (t = 1.54, df = 12, P = 0.15; Figures 4D, E).

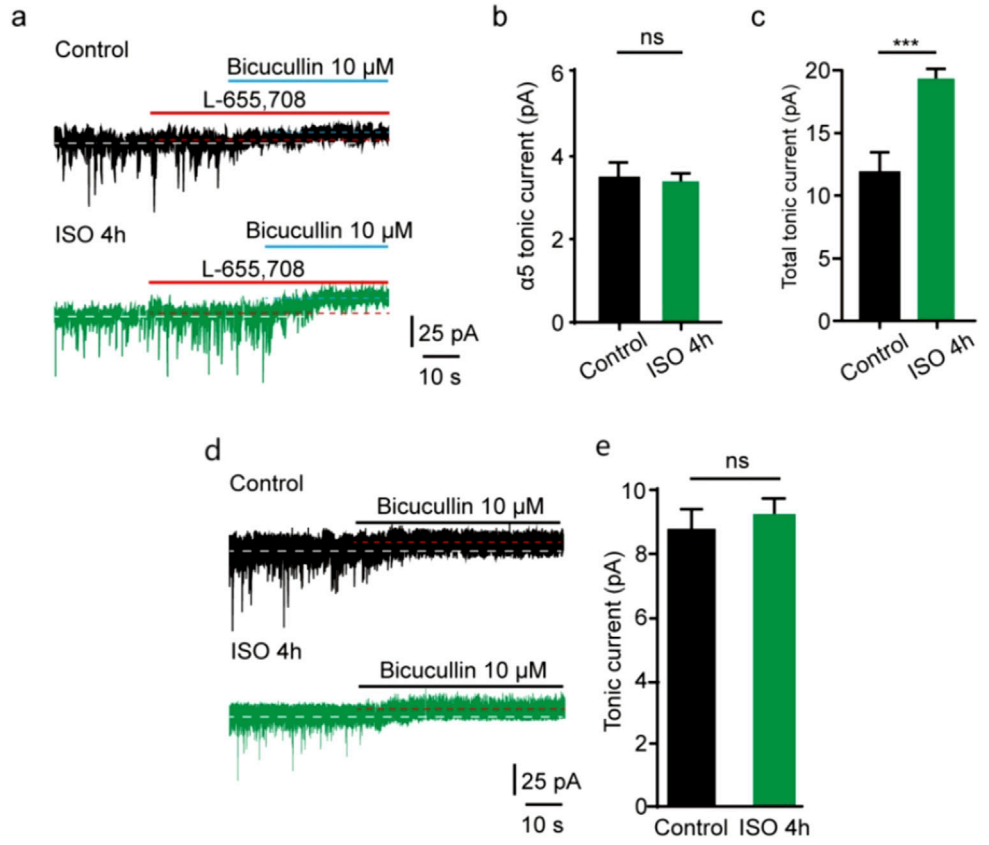

FIGURE 4
ISO-induced tonic current did not change by α5 subunit antagonist. **(A)** Representative tonic current recordings (Up, Control; Middle, ISO 4 h; Down, ISO 4 h + α5 subunit antagonist). **(B)** Statistics of the average amplitude tonic current by α5 subunit antagonist L-665,708 (Control, 3.51 ± 0.53 pA, n = 7 cells, one cell per mouse; ISO 4 h, 3.11 ± 0.36 pA, n = 7 cells, one cell per mouse; Unpaired t-test, t = 1.64, df = 12, $p = 0.13$) **(C)** The average amplitude of total tonic current (pA) in control and ISO 4 h group (Control, 12.23 ± 1.46 pA, n = 7 cells, one cell per mouse; ISO 4h, 19.21 ± 1.60 pA, n = 7 cells, one cell per mouse; Unpaired t-test, t = 8.52, df = 12, ***$p < 0.001$. ns, not significant). **(D)** Samples of tonic current. Up, control; Down, 4 h ISO pretreatment. **(E)** Mean change in tonic current (pA) in control and ISO 4 h group (Control, 8.80 ± 0.83 pA, n = 7 cells, one cell per mouse; ISO 4h, 9.70 ± 1.30 pA, n = 7 cells, one cell per mouse; Unpaired t-test, t = 1.54, df = 12, Control vs. ISO 4h, $p = 0.15$).

Discussion

We found that prolonged ISO exposure induced larger tonic GABAAR currents in DGGCs, but not in the hippocampal CA1 and thalamus. Additionally, prolonged ISO exposure did not change the phasic mIPSC frequency and amplitude in DGGCs. Meanwhile, we indicated that the increased tonic current after prolonged ISO exposure in the DGGCs was mediated by the δ subunit-containing GABAARs.

Prolonged ISO exposure increased acute tonic current in DGGCs

As key mediators of inhibitory signals in the brain, GABAARs comprise dozens of highly heterogeneous subtypes regarding their pharmacological properties, subunits and subcellular location [27]. Among these receptors, some GABAARs are known to be located postsynaptically and extrasynaptically and account for phasic and tonic inhibition in many different brain regions. This study discovered that the tonic current in DGGCs was significantly increased when ISO exposure was up to 4 h but not 2 h. However, ISO exposure did not change phasic inhibitory postsynaptic transmission in DGGCs. Our results showed that 4 h of ISO exposure did not increase the tonic current in the hippocampal CA1 or thalamus. δ-containing GABAARs tonic currents contribute critically to inhibition in DGGCs but not in hippocampal CA1 and thalamic relay neurons.

Prolonged ISO exposure increased acute tonic current dependent on δ other than α5 subunit-containing GABAA receptor

Tonic inhibition regulates neuronal excitability, δ-GABARs are localized to the extrasynaptic and perisynaptic membrane of DGCs, and the tonic GABAAR current in DGGCs is mainly

mediated by δ subunit-containing receptors [28]. Low ambient GABA levels in the extracellular space could generate tonic inhibition in DG that expressed δ-containing GABAARs. The α5-containing GABAARs that make up 25% of the receptor subtype are located in the learning and memory-related region of the brain. In addition to exhibiting synaptic phasic inhibition, the extrasynaptic α5-containing receptors mediate tonic inhibition [26, 29]. The tonic inhibition that mediated by α5-containing GABAAR in the DG plays an significant role in cognitive function [30–32].

In this study, prolonged ISO exposure induced larger tonic GABAAR currents in DGGCs, and the amplitude values of tonic inhibition with the α5 subunit antagonist L-655,708 [33] were comparable to the 4 h ISO exposure group, which indicated that the increased tonic current was not dependent on the α5 subunit-containing GABAARs. Furthermore, whether the increased tonic current induced by prolonged ISO exposure depended on the δ subunit-containing GABAARs in DGGCs was considered in this study. Although many drugs selectively enhance-unk-containing GABAARs, no specific blocker can be used. We exposed δ subunit knockout mice to ISO for 4 h and found that tonic current values were comparable to the control levels. Hence, our findings have thus far shown that the δ-containing GABAARs have key roles in contributing to DGGCs tonic inhibition by ISO exposure.

Effects of the increased acute tonic current in DGGCs on neuronal development and cognitive function

The DG is the main entrance to the hippocampus and plays a important role in emotion, learning, and memory. The DG, as an important part of the hippocampus, has a high potential for neural plasticity, and the maturation and neurogenesis of DGCs in the postnatal life in the subgranular zone is conducive to the capability of the DG to transform [34]. Therefore, factors that potentially affect the development and maturation of neurons in the DG may have long-lasting effects on brain function. Some studies have indicated the effects of general anesthetics exposure on cognitive function; one common feature is that anesthesia exposure disrupts the generation and development of DGCs in the hippocampus [7, 35, 36]. A previous study demonstrated that hippocampal DGCs are very vulnerable to ISO-induced neurotoxicity in juvenile mice [37]. Tonic inhibition of DGGCs negatively regulates neuronal development and neurocognitive function. We found that the tonic current in DGGCs was increased by prolonged ISO exposure. Hence, we inferred that prolonged ISO exposure may impair neuronal development and cognitive function by increasing the acute tonic current in DGGCs.

δ-containing GABAARs paly an important role in inhibitory network in mediating acute brain impairment, and δ receptors have been defined are associated with consciousness, mood disorders, epilepsy, and schizophrenia. Tonic inhibitory current is generated by activating extrasynaptic GABAA receptors. δ subunit-containing receptors of GABAAR mediate tonic current in DGGCs, which inhibits learning and memory and modulates the function of DGCs. By pharmacologically isolating δ-containing receptors, this study demonstrated that tonically activated δ-containing GABAARs are strongly modulated by prolonged ISO exposure because of their contribution to IPSCs in DGCs. Hence, prolonged ISO exposure may impair neuronal development and cognitive function by increasing the acute tonic current dependent on δ subunit specific GABAAR in DGGCs.

This study had a few limitations. First, there are several subunit-containing receptors of GABAAR-mediated tonic current in DGGCs, but we only selected δ and α5, two common subunit-containing receptors, to observe the effects of prolonged ISO exposure on tonic current in DGGCs. Second, we only observed an acute tonic current in the DGGCs but did not observe whether the increased tonic current was persistent. Third, we did not evaluate the cognitive function of the mice using long-term potentiation or water maze. Fourth, the knockout and control mice were derived from distinct litters in the present study, which may induce potential bias due to differences in genetic background, fetal neurodevelopment, and/or maternal behaviors between the two groups. Therefore, further studies are warranted.

Conclusion

Our data suggest that δ subunit specific GABAAR is the key element of the acute tonic inhibition in juvenile mice in DGGCs by prolonged ISO exposure.

Author contributions

RD designed the experiments and guided the electrophysiological experiments. JX analyzed the data. ZL, XC, and RD performed isoflurane exposure experiments. ZY and JX wrote the manuscript after discussing with all authors. All authors contributed to the article and approved the submitted version.

Data availability

The datasets presented in this study can be found in online repositories. The names of the repository/repositories and accession number(s) can be found in the article/Supplementary Material.

Ethics statement

The animal study was approved by the Animal Ethics Committee of Tianjin Central Hospital of Gynecology and Obstetrics. The study was conducted in accordance with the local legislation and institutional requirements.

Funding

The author(s) declare that financial support was received for the research, authorship, and/or publication of this article. This study was funded by the Natural Science Fund of Tianjin City (19JCQNJC11000) and the Tianjin Municipal Health Commission (TJWJ2022MS042), China.

Acknowledgments

Thank for the sharing of Gabrd KO mice by professor Hui Shen.

Conflict of interest

The author(s) declared no potential conflicts of interest with respect to the research, authorship, and/or publication of this article.

Supplementary material

The Supplementary Material for this article can be found online at: https://www.ebm-journal.org/articles/10.3389/ebm.2024.10171/full#supplementary-material

References

1. Erasso DM, Camporesi EM, Mangar D, Saporta S, Saporta S. Effects of isoflurane or propofol on postnatal hippocampal neurogenesis in young and aged rats. *Brain Res* (2013) **1530**:1–12. (Electronic)). doi:10.1016/j.brainres.2013.07.035

2. Monk TG, Weldon B, Fau - Garvan CW, Garvan CF-DDE, Dede DF-van der AMT, van der Aa Mt Fau - Heilman KM, et al. Predictors of cognitive dysfunction after major noncardiac surgery. *Anesthesiology* (2008) **108**(1):18–30. doi:10.1097/01.anes.0000296071.19434.1e

3. Kim JL, Bulthuis NE, Cameron HA. The effects of anesthesia on adult hippocampal neurogenesis. *Front Neurosci* (2020) **14**:588356–4548. (Print)). doi:10.3389/fnins.2020.588356

4. Huang J, Jing S, Chen X, Bao X, Du Z, Li H, et al. Propofol administration during early postnatal life suppresses hippocampal neurogenesis. *Mol Neurobiol* (2016) **53**(2):1031–44. doi:10.1007/s12035-014-9052-7

5. Jiang Y, Tong D, Fau - Hofacer RD, Hofacer Rd Fau - Loepke AW, Loepke Aw Fau - Lian Q, Lian Q, et al. Long-term fate mapping to assess the impact of postnatal isoflurane exposure on hippocampal progenitor cell productivity. *Anesthesiology* (2016) **125**(6):1159–70. doi:10.1097/ALN.0000000000001358

6. Wang N, Lu Y, Wang K, Li WS, Lu P, Lei S, et al. Simvastatin attenuates neurogenetic damage and improves neurocognitive deficits induced by isoflurane in neonatal rats. *Cell Physiol Biochem* (2018) **46**(2):618–32. doi:10.1159/000488630

7. Tong D, Ma Z, Su P, Wang S, Xu Y, Zhang LM, et al. Sevoflurane-induced neuroapoptosis in rat dentate gyrus is activated by autophagy through NF-κB signaling on the late-stage progenitor granule cells. *Front Cell Neurosci* (2020) **14**:590577. doi:10.3389/fncel.2020.590577

8. Fang F, Xue Z, Cang J. Sevoflurane exposure in 7-day-old rats affects neurogenesis, neurodegeneration and neurocognitive function. *Neurosci Bull* (2012) **28**(5):499–508. doi:10.1007/s12264-012-1260-4

9. Li Q, Mathena R, Fau - Xu J, Xu J, Fau - Eregha ORN, Eregha On Fau - Wen J, et al. Early postnatal exposure to isoflurane disrupts oligodendrocyte development and myelin formation in the mouse Hippocampus. *Anesthesiology* (2019) **131**(5):1077–91. doi:10.1097/ALN.0000000000002904

10. Sohn HM, Kim HY, Park S, Han SH, Kim JHA-O. Isoflurane decreases proliferation and differentiation, but none of the effects persist in human embryonic stem cell-derived neural progenitor cells. *J Anesth* (2017) **31**(1):36–43. doi:10.1007/s00540-016-2277-z

11. Hirotsu A, Iwata Y, Tatsumi K, Miyai Y, Matsuyama T, Tanaka T. Maternal exposure to volatile anesthetics induces IL-6 in fetal brains and affects neuronal development. *Eur J Pharmacol* (2019) **863**;172682. doi:10.1016/j.ejphar.2019.172682

12. Goyagi T. Dexmedetomidine reduced sevoflurane-induced neurodegeneration and long-term memory deficits in neonatal rats. *Int J Developmental Neurosci* (2019) **75**:19–26. doi:10.1016/j.ijdevneu.2019.04.002

13. Brickley SG, Mody I. Extrasynaptic GABA(A) receptors: their function in the CNS and implications for disease. *Neuron* (2012) **73**(1):23–34. doi:10.1016/j.neuron.2011.12.012

14. Belelli D, Harrison Nl Fau - Maguire J, Maguire J, Fau - Macdonald RL, Macdonald R, Fau - Walker MC, et al. Extrasynaptic GABAA receptors: form, pharmacology, and function. *J Neurosci* **29** (41):12757–63. doi:10.1523/JNEUROSCI.3340-09.20

15. Olsen RW, Sieghart W. International Union of Pharmacology. LXX. Subtypes of gamma-aminobutyric acid(A) receptors: classification on the basis of subunit composition, pharmacology, and function. Update. *Pharmacol Rev* (2008) **60**(3):243–60. doi:10.1124/pr.108.00505

16. Rudolph U, Antkowiak B. Molecular and neuronal substrates for general anaesthetics. *Nat Rev Neurosci* (2004) **5**(9):709–20. doi:10.1038/nrn1496

17. Orser BA, Wang DS. GABAA receptor theory of perioperative neurocognitive disorders. *Anesthesiology* (2019) **130**(4):618–9. doi:10.1097/aln.0000000000002562

18. Zhu C, Gao J, Fau - Karlsson N, Karlsson N, Fau - Li Q, Li Q, et al. Isoflurane anesthesia induced persistent, progressive memory impairment, caused a loss of neural stem cells, and reduced neurogenesis in young, but not adult, rodents *J Cereb Blood Flow Metab* (2010;**30**(5):1017–30. doi:10.1038/jcbfm.2009.274

19. Erasso DM, Chaparro Re Fau - Quiroga Del Rio CE, Quiroga Del Rio Ce Fau - Karlnoski R, Karlnoski RF-CEM, Camporesi Em Fau - Saporta S, Saporta S. Quantitative assessment of new cell proliferation in the dentate gyrus and learning after isoflurane or propofol anesthesia in young and aged rats. *Brain Res* (2012);**1441**:38–46. doi:10.1016/j.brainres.2011.11.025

20. Tung A, Herrera S, Fau - Fornal CA, Fornal Ca Fau - Jacobs BL, Jacobs BL. The effect of prolonged anesthesia with isoflurane, propofol, dexmedetomidine, or ketamine on neural cell proliferation in the adult rat. *Anesth Analg* (2008);**106**(6):1772–7. doi:10.1213/ane.0b013e31816f2004

21. Rammes G, Starker Lk Fau - Haseneder R, Haseneder R, Fau - Berkmann J, Berkmann J, Fau - Plack A, et al. Isoflurane anaesthesia reversibly improves cognitive function and long-term potentiation (LTP) via an up-regulation in NMDA receptor 2B subunit expression. *Neuropharmacology* (2009);**56**(3):626–36. doi:10.1016/j.neuropharm.2008.11.002

22. Krook-Magnuson EI, Li P, Fau - Paluszkiewicz SM, Paluszkiewicz Sm Fau - Huntsman MM, Huntsman MM. Tonically active inhibition selectively controls feedforward circuits in mouse barrel cortex. *J Neurophysiol* (2008);**100**(2):932–44. doi:10.1152/jn.01360.2007

23. Bright DP, Smart TG. Methods for recording and measuring tonic GABAA receptor-mediated inhibition. *Front Neural Circuits* (2013);**7**:193. doi:10.3389/fncir.2013.00193

24. Martenson JS, Yamasaki T, Chaudhury NH, Albrecht D, Tomita SA-OX. Assembly rules for GABA(A) receptor complexes in the brain. *eLife* (2017) **6**:27443. doi:10.7554/elife.27443

25. Wang DS, Kaneshwaran K, Fau - Lei G, Lei G, Fau - Mostafa F, Mostafa F, et al. Dexmedetomidine prevents excessive gamma-aminobutyric acid type A receptor function after anesthesia. *Anesthesiology* (2018);**129**(3):477–89. doi:10.1097/ALN

26. Glykys J, Mann Eo Fau - Mody I, Mody I. Which GABA(A) receptor subunits are necessary for tonic inhibition in the hippocampus? *J Neurosci* (2008);**28**(6):1421–6. doi:10.1523/JNEUROSCI.4751-07.2008

27. Sigel E, Steinmann ME. Structure, function, and modulation of GABA(A) receptors.*J Biol Chem* (2012);**287**(48):40224–31. doi:10.1074/jbc.R112.386664

28. Stell BM, Brickley Sg Fau - Tang CY, Tang Cy Fau - Farrant M, Farrant M, Fau - Mody I, Mody I. Neuroactive steroids reduce neuronal excitability by selectively enhancing tonic inhibition mediated by delta subunit-containing GABAA receptors. *Proc Natl Acad Sci U S A* (2003);**100**(24):14439–44. doi:10.1073/pnas.2435457100

29. Mohamad FH, Has AA-O. The α5-containing GABA(A) receptors-a brief summary.*J Mol Neurosci* (2019);**67**(2):343–51. doi:10.1007/s12031-018-1246-4

30. Engin E, Zarnowska ED, Benke D, Tsvetkov E, Sigal M, Keist R, et al. Tonic inhibitory control of dentate gyrus granule cells by α5-containing GABAA receptors reduces memory interference. *J Neurosci* (2015);**35**(40):13698–712. doi:10.1523/JNEUROSCI.1370-15.2015

31. Fatemi SH, Reutiman T, Fau - Folsom TD, Folsom T, Fau - Rooney RJ, Rooney R, et al. mRNA and protein levels for GABAAalpha4, alpha5, beta1 and GABABR1 receptors are altered in brains from subjects with autism. *J Autism Dev Disord* (2010;**40**(6):743–50. doi:10.1007/s10803-009-0924-z

32. Mendez MA, Horder J, Fau - Myers J, Myers J, Fau - Coghlan S, Coghlan S, et al. The brain GABA-benzodiazepine receptor alpha-5 subtype in autism spectrum disorder: a pilot [(11)C]Ro15-4513 positron emission tomography study. *Neuropharmacology* (2013);**68**:195–201. doi:10.1016/j.neuropharm.2012.04.008

33. Wu Z, Guo Z, Gearing M, Chen G. Tonic inhibition in dentate gyrus impairs long-term potentiation and memory in an Alzheimer's [corrected] disease model. *Nat Commun* (2014);**5**:4159. doi:10.1038/ncomms5159

34. Aniol V, Manolova A, Gulyaeva N. Early life events and maturation of the dentate gyrus: implications for neurons and glial cells. *Int J Mol Sci* (2022) **23**(8):4261. doi:10.3390/ijms23084261

35. Kang E, Jiang D, Ryu YK, Lim S, Kwak M, Gray CD, et al. Early postnatal exposure to isoflurane causes cognitive deficits and disrupts development of newborn hippocampal neurons via activation of the mTOR pathway. *Plos Biol* (2017) **15**(7):e2001246. doi:10.1371/journal.pbio.2001246

36. Wei K, Liu Y, Yang X, Liu J, Li Y, Deng M, et al. Bumetanide attenuates sevoflurane-induced neuroapoptosis in the developing dentate gyrus and impaired behavior in the contextual fear discrimination learning test. *Brain Behav* (2022) **12**(11):e2768. doi:10.1002/brb3.2768

37. Jiang Y, Tong D, Hofacer RD, Loepke AW, Lian Q, Danzer SC. Long-term fate mapping to assess the impact of postnatal isoflurane exposure on hippocampal progenitor cell productivity. *Anesthesiology* (2016) **125**(6):1159–70. doi:10.1097/aln.0000000000001358

EBM Experimental Biology and Medicine

TYPE Correction
PUBLISHED 19 September 2024
DOI 10.3389/ebm.2024.10348

OPEN ACCESS

*CORRESPONDENCE
Jay R. Ebert,
jay.ebert@uwa.edu.au

RECEIVED 19 August 2024
ACCEPTED 06 September 2024
PUBLISHED 19 September 2024

CITATION
Ebert JR, Magi A, Unt E, Prans E, Wood DJ and Koks S (2024) Corrigendum: Genome-wide association study identifying variants related to performance and injury in high-performance athletes.
Exp. Biol. Med. 249:10348.
doi: 10.3389/ebm.2024.10348

Corrigendum: Genome-wide association study identifying variants related to performance and injury in high-performance athletes

Jay R. Ebert[1]*, Agnes Magi[2,3], Eve Unt[2,3], Ele Prans[4], David J. Wood[5] and Sulev Koks[6,7]

[1]School of Human Sciences (Exercise and Sport Science), The University of Western Australia, Crawley, WA, Australia, [2]Department of Sports Medicine and Rehabilitation, Institute of Clinical Medicine, Faculty of Medicine, University of Tartu, Tartu, Estonia, [3]Sports Medicine and Rehabilitation Clinic, Tartu University Hospital, Tartu, Estonia, [4]Department of Anaesthesiology and Intensive Care, Tartu University Hospital, Tartu, Estonia, [5]School of Surgery, The University of Western Australia, Crawley, WA, Australia, [6]Perron Institute for Neurological and Translational Science, QEII Medical Centre, Nedlands, WA, Australia, [7]Centre for Molecular Medicine and Innovative Therapeutics, Murdoch University, Murdoch, Perth, WA, Australia

KEYWORDS

genome-wide association, genetics, DNA, lower limb musculoskeletal injury

A Corrigendum on
Genome-wide association study identifying variants related to performance and injury in high-performance athletes

by Ebert JR, Magi A, Unt E, Prans E, Wood DJ and Koks S (2023). Exp Biol Med (Maywood). 248(20):1799–1805. doi: 10.1177/15353702231198068

In the published article, there was an error in Figure 1 as published. While the Figure legend is correct, the image is incorrect. The corrected Figure 1 and its caption appear below.

In the published article, there was an error in Figure 2 as published. While the Figure legend is correct, the image is incorrect. The corrected Figure 2 and its appear below.

The authors apologize for these errors and state that this does not change the scientific conclusions of the article in any way.

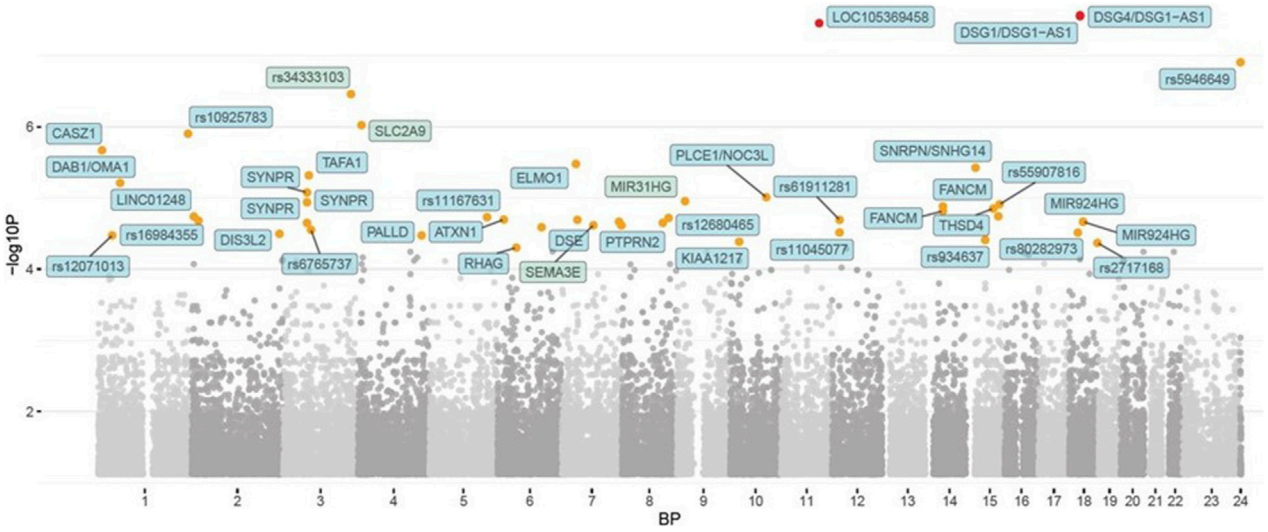

FIGURE 1
Manhattan plot representing the *p* values of the genome-wide association in reaching the podium (medalist) or not. The orange dots represent $p < 10^{-5}$ while the red dots represent $p < 10^{-8}$ (i.e., strong genome-wide significance).

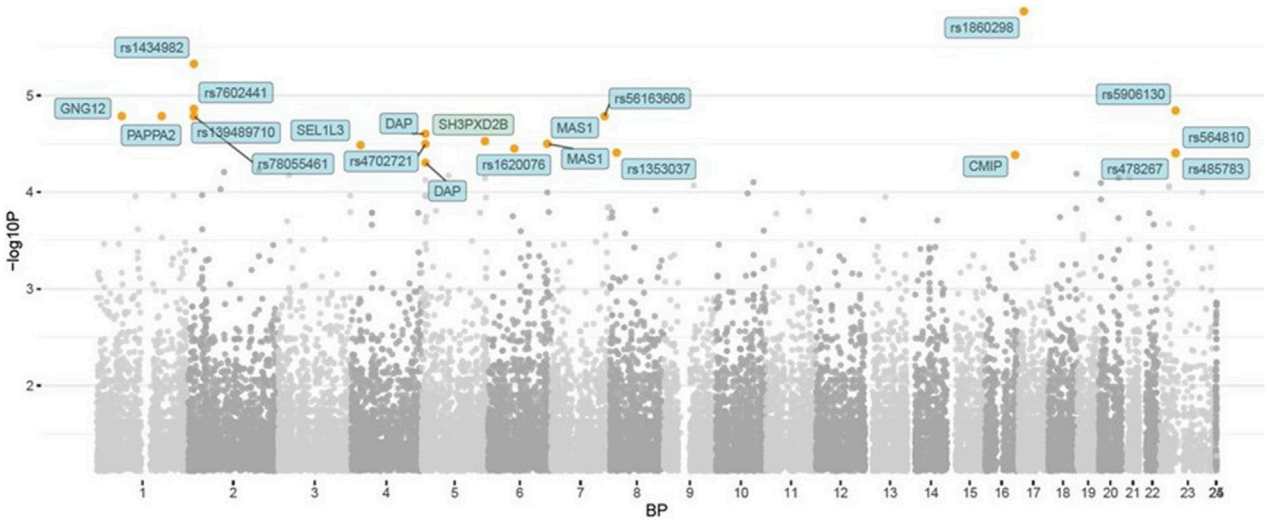

FIGURE 2
Manhattan plot representing the *p* values of the genome-wide association in being injured or not. The orange dots represent $p < 10^{-5}$ while the red dots (N/A) represent $p < 10^{-8}$ (i.e., strong genome-wide significance).

Scope

Experimental Biology and Medicine (EBM) is a global, peer-reviewed journal dedicated to the publication of multidisciplinary and interdisciplinary research in the biomedical sciences. The journal covers the spectrum of translational research from T0, basic research, to T4, population health. Articles in EBM represent cutting edge research at the overlapping junctions of the biological, physical and engineering sciences that impact upon the health and welfare of the world's population. EBM is particularly appropriate for publication of papers that are multidisciplinary in nature, are of potential interest to a wide audience, and represent experimental medicine in the broadest sense of the term. However, manuscripts reporting novel findings on any topic in the realm of experimental biology and medicine are most welcome.

EBM publishes Research, Reviews, Mini Reviews, and Brief Communications in the following categories.

- Anatomy/Pathology
- Artificial Intelligence/ Machine Learning Applications to Biomedical Research
- Biochemistry and Molecular Biology
- Bioimaging
- Biomedical Engineering
- Bionanoscience
- Cell and Developmental Biology
- Clinical Trials
- Endocrinology and Nutrition
- Environmental Health/Biomarkers/ Precision Medicine
- Genomics, Proteomics, and Bioinformatics
- Immunology/Microbiology/Virology
- Mechanisms of Aging
- Neuroscience
- Pharmacology and Toxicology
- Physiology and Pathophysiology
- Population Health
- Stem Cell Biology
- Structural Biology
- Synthetic Biology
- Systems Biology and Microphysiological Systems
- Translational Research

EBM Experimental Biology and Medicine

EBM is the official journal of the Society for Experimental Biology and Medicine

Led by Dr Steven Goodman, Experimental Biology and Medicine (EBM) is a global, peer-reviewed journal dedicated to the publication of multidisciplinary and interdisciplinary research in the biomedical sciences.

Discover more of our Special Issues

See more →

Contact

development@ebm-journal.org

See more

ebm-journal.org

publishingpartnerships.frontiersin.org/our-partners